Experimentele analyse van het post-breukgedrag van gelamineerd glas onder impact- en schokbelasting

Experimental Analysis of the Post-Fracture Response of Laminated Glass under Impact and Blast Loading

Sam Van Dam

Promotoren: prof. dr. ir. Wim Van Paepegem, dr. ir. David Lecompte
Proefschrift ingediend tot het behalen van de graad van
Doctor in de Ingenieurswetenschappen: Bouwkunde

Vakgroep Materialen, Textiel en Chemische proceskunde
Voorzitter: prof. dr. Kiekens
Faculteit Ingenieurswetenschappen en Architectuur
Academiejaar 2017-2018

UNIVERSITEIT
GENT

ISBN: XXX-XX-XXXX-XXX-X
NUR: XXX
Wettelijk depot: D/2017/XX.XXX/XX

Promotors:

Prof. dr. ir. Wim Van Paepegem
Ghent University
Faculty of Engineering and Architecture
Department of Materials, Textiles and Chemical Engineering

Dr. ir. David Lecompte
Royal Military Academy
Polytechnical faculty of the Royal Military Academy
Department of Civil and Materials Engineering

Examination Committee:

Prof. dr. ir. Luc Taerwe (*Chairman*)	Ghent University
Prof. dr. ir. Wim Van Paepegem (*Promotor*)	Ghent University
Dr. ir. David Lecompte (*Promotor*)	Royal Military Academy
Prof. dr. ir. Jan Belis	Ghent University
Prof. dr. ir.-arch. Nathan Van den Bossche	Ghent University
Dr. ir. Ives De Baere	Ghent University
Prof. dr. ir. Hugo Sol	Vrije Universiteit Brussel
Prof. dr. ir. John Vantomme	Royal Military Academy
Dr. ir. Pol D'Haene	Eastman

Research Institute:

Ghent University
Department of Materials, Textiles and Chemical Engineering
Mechanics of Materials and Structures
Technologiepark-Zwijnaarde 903
9052 Zwijnaarde
Belgium
Tel. +32 9 331 04 44
Sam.VanDam@UGent.be

This research was funded by VLAIO.

“Zwangvolle Plage!
Müh’ ohne Zweck!”

- Mime, “Siegfried” (Act I), R. WAGNER

ACKNOWLEDGMENTS

This PhD would not have been possible without my supervisor, Wim, who believed in me and guided me through this challenging opportunity. It is incredible how you manage to give all your PhD students plenty of time and guidance, knowing you have so many of them. Your suggestions during our regular meetings had a crucial impact on the outcome of this work. I also want to explicitly thank you for your support during the darkest hours of my PhD-writing.

My gratitude also goes toward my co-promoter David Lecompte of the Royal Military Academy for guiding me through the blast tests. In the second month of my PhD he took me along to a Royal Air Force test site near the Scottish border, in the freezing cold and pouring rain, to witness a large-scale explosion test. I will never forget the 'instrumentation' we applied together, and the one that fell off.

Another big thank you goes to John Vantomme of the RMA, head of the COBO department, but who at first was my Master thesis supervisor at the Vrije Universiteit Brussel and made it possible for me to do a PhD at Ghent University. He wrote to several colleagues of his in Ghent saying he had a student interested in doing a PhD there, and also suggested I should apply for an IWT grant.

Getting that IWT grant meant that we could bring a second researcher on board. This led to the division of the topic in an experimental and numerical PhD, the second of which was taken up by my colleague Joren Pelfrene. I think one plus one certainly equalled more than two in our case.

A mostly experimental PhD would be impossible without the support of excellent technical staff, so I would like to thank Luc and Pascal for bearing with me, making last-minute changes to test set-ups and building several larger-scale set-ups. They, together with Martine, also made the morning coffee breaks highly entertaining. In the underground bunker at the RMA, Bruno provided me with lots of knowledge and tips & tricks about performing blast tests, for which I am very grateful.

The former head of our department, Joris, although not directly involved in my research, did contribute much to it, not in the least by his mindset of validated experimental-numerical research, a constant quest for answers (resulting in more questions) and a sense for detail.

From our industrial partners, I want to thank Pol D'Haene, Leen Billiet and Bob Theeten, as well as Jeroen Bonamie and the other lab assistants of Eastman,

Solutia, for providing us with the means to make hundreds of samples free of charge. Without their support, the scale of this research would have been decimated. Their input during meetings also helped in shaping this research. I look forward to continuing my research with them. At AGC, my gratitude goes toward Bertrand Mathy and François Lecolley.

For helping me to get started with the DIC technique, I want to thank Bachir Belkassem (RMA) and Ken Sprangers (VUB). As a large part of my tests were conducted at the RMA, I would like to thank my 'colleagues' there as well, in particular Raouf for letting me use his shock tube. From the VUB, I would like to single out prof. Hugo Sol and Massimo for doing the resonalyser tests. In addition, my former class mates and teachers always made it feel a bit like coming home, when I visited the department when I happened to be in Brussels.

The time I had at our department was made very enjoyable by my colleagues. Some of the people I want to thank in particular are Mathias, my first office buddy, for sharing his diverse music; Frederik, for the excellent company in London; Mathijs and Siebe for being the driving forces behind so many fun activities; Diederik, for always helping out, even if he didn't have time; The girls (and Tom) of the Metallurgy department for the after-work activities; Joachim, for joining me to those activities; Dorien, for giving me the opportunity to create my first wedding dress; Klaas and Jana, my fellow Ingenieursproject 1 assistants and Geert, for his joyous and improvisational take on life.

A separate paragraph is due to Ives. This post-doc researcher has so much practical knowledge, I don't think I had one experimental campaign where Ives did not make a contribution, directly or indirectly, big or small.

A lot of work in this book is to be accredited to my thesis students, or 'my little minions' as I liked to call them: Lisa, Annabel, Sahin, Bert, Colin, Roel, Glenn, Guillaume, Simon, Stef, Magali and Renaat.

Of course, I owe much to my parents and grand-parents. Thank you for supporting me throughout my academic career. Also a shout-out to my little sister, Maurane.

Finally, I would like to thank my friends, who have welcomed me into this beautiful city and helped me relax after writing, in particular Tom & Jasper, also for proof-reading this document; Roel & Jelle, Pieter and Joeri for the bubbles; Michael, Bolle, Ruben and Kristof C, for movie nights and parties; Kristof DW & Kjell, for supplying mojito's at the Gentse Feesten; Rein, Bart and Karel, for sharing my theatrical passion and Quinten my operatic passion.

Sam Van Dam
November 2017, Ghent

SUMMARY

Laminated glass consists of two or more glass plates, bonded together by a polymer interlayer, designed to give the laminate post-breakage residual strength. This is necessary, as the sudden fracture of monolithic glass and the resulting sharp fragments flying around at high speeds, typically cause the most injuries during impact or blast events.

The most common type of interlayer is based on a plasticized polyvinyl butyral (PVB) polymer. It does not disintegrate upon fracture but keeps the glass shards together, preventing them from harming bystanders. Hence, laminated glass has residual load-bearing capacity and thus the necessary redundancy for structural use. Typical thicknesses for glass in automotive applications range from 1.2 to 2 mm and from 4 to 6 (even up to 10) mm for architectural applications. PVB interlayers are produced in multiples of 0.38 mm, up to 1.52 mm.

Adhesion between glass and the PVB interlayer is mainly achieved by hydrogen bonds. The bonding strength is very important with regard to the post-breakage behaviour of laminated glass. For low adhesion the impact resistance is high because the residual projectile energy after breakage of the glass is absorbed by delamination between the glass and PVB interlayer and the resulting additional deformation of the interlayer. However, too low adhesive bonding strength may compromise safety due to complete delamination/debonding of dangerous glass shards and negatively influences the long term stability of the laminate. For high adhesion levels much less energy can be absorbed by the interlayer itself and therefore projectiles can more easily penetrate it. However, high adhesion prevents that dangerous glass fragments are detached after glass fracture and ascertains long term stability. Thus, a compromise has to be found for the adhesion level based on the application and desired outcome.

The work, in three parts, presented here deals with assessing the mechanical behaviour of laminated glass – with different adhesion levels – to impact and blast loading. The reader is encouraged to take a look at the work of Joren Pelfrene, whose PhD *"Numerical Analysis of the Post-Fracture Response of Laminated Glass under Impact and Blast Loading"* (2016) describes the Finite Element Analysis of most tests presented in this work.

The goal of this research is threefold: i) to expand the fundamental knowledge about the mechanical behaviour of laminated glass subjected to dynamic loading and the role the interlayer has in this behaviour, ii) to improve upon the governing standards by developing test set-ups which are extensively instrumented so we can obtain a maximum of information about this post-fracture behaviour and iii) to interact with the numerical work of Pelfrene, by supplying data for either the development of finite element models or their validation.

The first part of this dissertation serves as an introduction, with a description of the mechanical behaviour of the constituent materials of laminated glass (glass & PVB) and the adhesion between both.

First, the bending behaviour of monolithic glass is investigated, using both a four-point and axisymmetric bending set-up. Finite element analysis is applied to calculate the stress at which the glass fractures for both set-ups and a Weibull analysis is performed to check the influence of the air and tin side. Scatter on the results is very high but this is in accordance with literature.

Tensile tests, both quasi-static and dynamic, are performed on PVB specimens, yielding data to build material laws.

Analytical formulas to calculate the deflection of a laminated specimen under four-point bending are developed, and checked with finite element analysis and an experimental campaign. The deflection is shown to be dependent on the cantilever length of specimens beyond their supports. In contrast with elastic beam theory, the stresses along the cantilever section of the beam are not zero. After reaching a minimum compressive stress at the bearing point, it only drops to zero, following a linear course, at the free end of the cantilevered beam. Furthermore, the stress is not constant between the loading points. After reaching a maximum at the load introduction points, it decreases towards the middle of the beam. Strain measurements confirm these conclusions.

Through-crack-tension specimens are used to investigate Mode II delamination. Several parameters, such as interlayer thickness and adhesion level, and loading rate, are examined. Images of the moving delamination fronts are post-processed in order to calculate the strains and strain energies present in the different interlayers. Steady state is most often achieved for specimens with a high loading rate. Whereas the steady state force is hardly influenced by the adhesion level, the tearing behaviour clearly is. Also the strains and strain energy show a difference.

Mode I failure was investigated with pull-off adhesion tests. For all three tested adhesion levels, a similar failure stress is found.

The second part deals with impact behaviour of laminated glass. In a first test campaign, a small-scale drop weight (SSDW) set-up is used to test both square and circular samples with varying properties and different indentor types. Within a

single test series and for fixed testing conditions, the test specimens exhibit quasi-identical pre-fracture behaviour, meaning the test set-up is capable of producing reproducible results. Fracture occurs first for the bottom glass plate, and is characterized by a significant drop in the force signal.

Further processing of the data and high-speed images is automated. A method is found to quantify impact damage of laminates. Difference in behaviour due to differing adhesion levels could not be achieved as the specimens are not loaded severely enough.

In a second test campaign, a set-up conforming to the European Standard EN 12600 is employed. The tyres that are part of the pendulum are characterised in great detail. Tensile and compression tests on several configurations of the tyres, or parts of them, are executed. A pressure plate is used to measure the impact pressure and force exerted by the twin-tyre pendulum. Deflections and strains of laminated glass specimens are determined and the adhesion level is shown to have an influence on the tearing behaviour.

An EN 356 set-up is designed and constructed but only preliminary testing is performed on it.

The third and final part focuses on blast loading. Several small-scale test series where laminated glass panels are subjected to blast loads are performed. In a first test series, the laminates cannot be subjected to a severe enough blast loading, due to the limited clamping area. Too high a charge weight and the panels are blown out of the frame in one piece. A wider clamping ring is designed but even then no difference between samples with different adhesion can be discerned. Using high charge weights at a small distance also results in unpredictable pressures, due to local effects. A small shock tube is used to mitigate these problems, but this results in a too much localized force, and flying glass particles impede correlation of the high-speed images. However, tearing of the interlayer can be achieved and it seems dependent on adhesion level.

A final set-up with a larger shock tube is designed which finally yields good results. A clear difference in behaviour is observed between specimens with higher adhesion and with lower adhesion, where the high adhesion specimens are more prone to tearing of the interlayer. This is to be expected because the low delamination results in higher strains in the interlayer in order to bridge the cracks in the fractured glass.

Pressure tests are performed both for the initial (open air) and final (shock tube) set-up. They prove the shock waves are reproducible, and planar in case of the shock tube.

Twelve large-scale blast tests are conducted on laminated glass panels, of which nine are successful. A medium adhesion ‘standard ’interlayer and a high adhesion stiff interlayer are tested. The tests are reproducible in the initial phase, which attests the quality of the set-up. From the moment the glass fracture and subsequent PVB tearing start to play a role, the results differ. The combination of the stiffness and the high adhesion to the glass causes the interlayer to tear quickly at the edges by the incoming shock wave. In four of the five tests, the whole laminated glass panel is blown out of the frame, leaving only the clamped edges in place. On the contrary, the standard interlayer is clearly more flexible. Of the other four plates, the interlayer of three plates is torn. However, the way in which the panels deformed differs from the stiff interlayer ones. Except for small glass shards, no parts are torn from the panel.

In conclusion, the dependency of the post-fracture behaviour of laminated glass on the adhesion level is clearly demonstrated. Several test set-ups have been developed or improved to investigate the mechanical response of laminated glass as a whole, as well as its constituent materials, to (dynamic) loading. Through the interaction with finite element modelling, deeper insight in the subject has been achieved.

NEDERLANDSE SAMENVATTING

Gelamineerd glas bestaat uit twee of meer glaspanelen, die aan mekaar worden gebonden door een polymeer tussenlaag, ontworpen om het laminaat na glasbreuk residuele sterkte te geven. Dit is nodig omdat het plotselinge falen van monolitisch glas en de resulterende scherpe fragmenten die aan hoge snelheid rondvliegen, de oorzaak zijn van de meeste verwondingen bij impact- of schokbelasting.

Het meest gebruikte type tussenlaag is gebaseerd op een geplastizeerd polyvinyl butyral (PVB) polymeer. Bij impact valt het niet uiteen maar houdt het de glasstukken samen, daarbij verwondingen aan omstaanders vermijdend. Bijgevolg heeft gelamineerd glas een residuele lastdragende capaciteit en dus de nodige redundantie voor structureel gebruik van het materiaal. Typische diktes voor glas in automobiele toepassingen liggen tussen 1.2 en 2 mm en tussen 4 en 6 (tot zelfs 10) mm voor architecturale toepassingen. PVB tussenlagen worden geproduceerd in veelvouden van 0.38 mm, tot 1.52 mm.

Adhesie tussen het glas en de PVB tussenlaag wordt voornamelijk gerealiseerd door waterstofbruggen. De bindsterkte is zeer belangrijk voor het gedrag na breuk van gelamineerd glas. Voor lage adhesie is de impactweerstand hoog, omdat de overblijvende energie van het projectiel na glasbreuk geabsorbeerd wordt door delaminate tussen glas en PVB en de resulterende verdere vervorming van de tussenlaag. Maar een te lage adhesie kan de veiligheid compromitteren door het volledig delamineren van gevaarlijke glasscherven, en het beinvloedt op negatieve wijze de lange-termijn stabiliteit van het laminaat. Voor hoge adhesie kan veel minder energie geabsorbeerd worden door de tussenlaag en alzo kunnen objecten makkelijker de tussenlaag penetreren. Echter voorkomt hoge adhesie het loskomen van gevaarlijke glasfragmenten en verzekert het de lange termijn stabiliteit. Een compromis moet aldus gevonden worden voor het adhesieniveau, gebaseerd op de applicatie en gewenste uitkomst.

Het werk, in drie delen, dat hier gepresenteerd wordt, gaat over het inschatten van het mechanisch gedrag van gelamineerd glas – met verschillende adhesieniveau's – onder impact- en schokbelasting. De lezer wordt aangeraden om het werk van Joren Pelfrene door te nemen, wiens doctoraat *"Numerieke analyse van het gedrag na breuk van gelamineerd glas onder impact- en schokbelasting"* (2016) de numerieke simulaties beschrijft van de meeste proeven gepresenteerd in dit werk.

Het doel van dit onderzoek is drieledig: i) het uitbreiden van de fundamentele kennis over het mechanische gedrag van gelamineerd glas bij schokbelasting en de rol die de tussenlaag hierin speelt, ii) het verbeteren van de standaarden door het ontwikkelen van uitgebreid geïnstrumenteerde testopstellingen om een maximum aan informatie over die post-breuk gedrag te verkrijgen en iii) het interageren met het numeriek werk van Pelfrene door data te leveren voor enerzijds de ontwikkeling van numerieke modellen en anderszijds voor hun validatie.

Het eerste deel dient tot introductie, met een beschrijving van het mechanisch gedrag van de samenstellende materialen van gelamineerd glas (glas & PVB) en de adhesie tussen beide.

Eerst wordt het buiggedrag van monolitisch glas onderzocht, met zowel een vierpunts- als axisymmetrische buigopstelling. De eindige elementen methode wordt gebruikt om de spanning te berekenen waarbij het glas breekt, en een Weibull-analyse wordt uitgevoerd om de invloed van de tin- en luchtzijde te controleren. De spreiding op de resultaten is zeer hoog maar dit stemt overeen met de theorie.

Trektesten, zowel quasi-statisch als dynamisch, worden uitgevoerd op PVB proefstukken, om data te bekomen om materiaalmodellen te bouwen.

Analytische formules om de deflectie van een gelamineerd proefstuk bij vierpuntsbuiging te berekenen worden ontwikkeld, en gecontroleerd met numerieke simulaties en een testcampagne. Het wordt aangetoond dat de deflectie afhankelijk is van de uitkraging van de proefstukken, voorbij de opleggingen. In tegenstelling tot wat de elastische balk theorie zegt, zijn de spanningen in deze uitkragende secties niet nul. Na het bereiken van een minimale compressiespanning ter hoogte van de oplegging, daalt de spanning lineair tot nul aan het vrije uiteinde van de uitkragende balk. Bovendien is de spanning niet constant tussen de punten van krachtinleiding. Na het bereiken van een maximum ter hoogte van deze punten, daalt de spanning langzaam naar het midden van de balk. Rekmetingen bevestigen deze conclusies.

Through-crack-tension (“trek-door-breuk”) proefstukken worden gebruikt om delaminatie in Mode II te onderzoeken. Verscheidene parameters, zoals dikte van de tussenlaag en adhesieniveau, en belastingssnelheid, worden onderzocht. Beelden van het voortschrijdende delaminatiefront worden gepostprocessed om de rek en rekenergie te bepalen van de verschillende tussenlagen. Een stationaire plateaufase wordt het vaakst behaald voor proefstukken met een hoge belastingssnelheid. De kracht in die plateaufase blijkt niet gevoelig voor het adhesieniveau, maar het breukgedrag wel. Ook de rek en rekenergieën tonen een verschil aan.

Faling in Mode I wordt onderzocht met eenvoudige “pull-off” adhesietesten. Voor alle drie adhesieniveau’s wordt een gelijkaardige breuksterkte gevonden.

Het tweede deel handelt over het gedrag bij impact van gelamineerd glas. In een eerste testreeks wordt een kleinschalige valopstelling met verschillende indentoren gebruikt om vierkante en ronde platen met verschillende eigenschappen te testen. In eenzelfde testreeks en voor vastgelegde testcondities, vertonen de proefstukken quasi-identiek gedrag voor breuk, wat betekent dat de opstelling capabel is reproduceerbare resultaten te geven. Break trad eerst op voor de onderste glasplaat, en wordt gekenmerkt door een significante daling van het krachtsignaal.

Verdere processing van de data en hogesnelheidsbeelden verloopt geautomatiseerd. Een methode is gevonden om de schade aan de laminaten te kwantificeren. Verschillen in gedrag door een verschil in adhesieniveau konden niet ontdekt worden omdat de proefstukken niet zwaar genoeg belast worden.

In een tweede testreeks wordt een opstelling gebruikt conform aan de Europese EN 12600 norm. De banden die deel uitmaken van de pendulum worden in groot detail gekarakteriseerd. Trek- en druktesten op verschillende configuraties van de banden, of delen van de banden, worden uitgevoerd. Een drukplaat meet de impactdruk en –kracht uitgeoefend door de pendulum. De doorbuigingen en rekken van gelamineerde proefstukken worden bepaald en het wordt aangetoond dat het adhesieniveau een invloed heeft op het breukgedrag.

Een EN 356 opstelling wordt ontworpen en gebouwd, maar slechts enkele preliminaire tests worden er op uitgevoerd.

Het derde, laatste deel focust op schokbelasting. Verscheidene kleinschalige testreeksen waarbij gelamineerde glaspanelen worden onderworpen aan schokbelasting worden uitgevoerd. In een eerste testreeks kunnen de platen niet onderworpen worden aan een hoge last, door de beperkte inklemming. Bij een te hoge lading vliegen ze in hun geheel uit de opstelling. Een bredere klemring wordt ontworpen maar dan nog kan geen verschil tussen adhesieniveau's opgemerkt worden. Zware ladingen op een korte afstand resulteren ook in onvoorspelbare drukken door lokale effecten. Een kleine shock tube moet deze problemen oplossen, maar dit resulteert in een te gelocaliseerde kracht waardoor rondvliegende glaspartikels de correlatie van de hogesnelheidsbeelden hinderen. Echter, het scheuren van de tussenlaag kan bekomen worden en lijkt afhankelijk van het adhesieniveau.

Een laatste opstelling met een grotere shock tube wordt ontworpen die eindelijk goede resultaten oplevert. Een duidelijk verschil in gedrag wordt geobserveerd tussen proefstukken met een hoge en lage adhesie, waarbij de proefstukken met hoge adhesie meer geneigd zijn tot scheuren. Dit is te verwachten omdat de lage delaminate resulteerd in hogere rekken in de tussenlaag om de breuken in het glas te overbruggen.

Drukproeven worden uitgevoerd voor zowel de initiële (in open lucht) als de finale (shock tube) opstelling. Deze tonen aan dat de schokgolven reproduceerbaar zijn, en vlak in het geval van de shock tube.

Twaalf schokproeven op grote schaal worden uitgevoerd op panelen gelamineerd glas, waarvan 9 succesvol zijn. Een ‘standaard’ tussenlaag met medium adhesie en een stijvere tussenlaag met hogere adhesie worden beproefd. De testen zijn reproduceerbaar in de initiële fase, wat de kwaliteits van de opstelling bevestigd. Vanaf het moment dat het glas breekt en derhalve het scheuren van de PVB een rol begint te spelen, wijken de resultaten af. De combinatie van een stijve tussenlaag en hoge adhesie veroorzaakt het snelle scheuren van de tussenlaag langs de ingeklemde randen door de inkomende schokgolf. In vier van de vijf testen wordt het paneel in zijn geheel uit de inklemming geworpen, waardoor enkel de ingeklemde randen op hun plaats blijven. De standaard tussenlaag is, in tegenstelling, duidelijk flexibeler. Van deze vier platen scheurt de tussenlaag bij drie platen. Maar de wijze waarop ze vervormen is verschillend van de panelen met stijvere tussenlaag. Behalve enkele kleine stukjes, worden geen stukken van de panelen gescheurd.

In conclusie, kan gesteld worden dat de afhankelijkheid van het gedrag na breuk van gelamineerd glas van het adhesieniveau duidelijk is aangetoond. Verschillende testopstellingen die de mechanische respons van gelamineerd glas als een geheel, of van de samenstellende materialen, onderzoeken zijn ontwikkeld of verbeterd. Door de interactie met de eindige elementen methode kon een dieper inzicht in de materie bekomen worden.

CURRICULUM VITAE

Sam Van Dam was born on November 17, 1988 in Boom, Belgium. In 2011, he received his Master of Science degree in Civil Engineering from the Vrije Universiteit Brussel, Belgium.

Immediately after his graduation he started his PhD at the Mechanics of Materials and Structures research group of the Department of Materials Science and Engineering (now Materials, Textiles and Chemical Engineering). His research work focused on an experimental approach to characterise laminated glass materials and assess the post-fracture performance of laminated glass under dynamic loading, in close collaboration with Joren Pelfrene, who handled the numerical part of the subject.

In the meantime, he has started working on a new project at Eastman Chemical Company (Ghent) on multilayered PVB interlayers for use in laminated glass.

Sam Van Dam is author of 3 scientific publications in international peer-reviewed journals, of which 1 as the first author, and has contributed to 9 publications in international conference proceedings. During his PhD study he supervised the work of 13 thesis students.

LIST OF PUBLICATIONS

Publications in international journals of the Science Citation Index – A1

[1] **Van Dam, Sam**, Joren Pelfrene, Stijn De Pauw, and Wim Van Paepegem. 2014. "Experimental Study on the Dynamic Behaviour of Glass Fitted with Safety Window Film with a Small-scale Drop Weight Set-up." *International Journal of Impact Engineering* 73: 101–111.

[2] Pelfrene, Joren, **Sam Van Dam**, and Wim Van Paepegem. 2015. "Numerical Analysis of the Peel Test for Characterisation of Interfacial Debonding in Laminated Glass." Ed. Robert Adams. *International Journal of Adhesion and Adhesives* 62: 146–153.

[3] Pelfrene, Joren, Johannes Kuntsche, **Sam Van Dam**, Wim Van Paepegem, and Jens Schneider. 2016. "Critical Assessment of the Post-breakage Performance of Blast Loaded Laminated Glazing: Experiments and Simulations." *International Journal of Impact Engineering* 88: 61–71.

Conference proceedings available in ISI Proceedings, (WOS) – P1

[1] **Van Dam, Sam**, Joren Pelfrene, Wim Van Paepegem, Joris Degrieck, David Lecompte, and John Vantomme. 2013. "A New Experimental Test Set-up for Investigating Impact Resistance of Laminated Glass." In *COST ACTION TU0905: MID-TERM CONFERENCE ON STRUCTURAL GLASS*, ed. Jan Belis, Christian Louter, and Danijel Mocibob, 359–366. Leiden, The Netherlands: CRC Press/Balkema.

[2] **Van Dam, Sam**, Frederik Allaeys, Wim Van Paepegem and Joris Degrieck. 2015. "Accurately measuring 2D position using a composed grid pattern and DTFT." In *OPTICAL MEASUREMENT TECHNIQUES FOR STRUCTURES & SYSTEMS III*, ed. Joris Dirckx, 313-319. Maastricht, The Netherlands: Shaker Publishing BV.

[3] Pelfrene, Joren, **Sam Van Dam**, Joris Degrieck, and Wim Van Paepegem. 2013. "Numerical Simulation of Elastic, Fracture and Post-failure Response of Monolithic and Laminated Glass Under Impact Loading." In *COST ACTION TU0905: MID-TERM CONFERENCE ON STRUCTURAL GLASS*, ed. Jan Belis, Christian Louter, and Danijel Mocibob, 413–420. Leiden, The Netherlands: CRC Press/Balkema.

Publications in international conference proceedings – C1

[1] **Van Dam, Sam**, and Joren Pelfrene. 2012. "Study on the Mechanical Response of Glass Facades Under Air Blast Loading." In *Proceedings of Recent, Current & Near-Future Research on Structural Glass*, ed. Jan Belis, 39–44. Ghent, Belgium: University Press.

[2] **Van Dam, Sam,** Joren Pelfrene, Ken Spranghers, David Lecompte and Wim Van Paepegem. 2013. "Digital Image Correlation technique applied to laminated glass plates under free air blast loading." In Conference Proceedings of the 21st DYMAT Technical Meeting, High speed imaging for dynamic testing of materials and structures. 43-46. London, United Kingdom:

[3] **Van Dam, Sam,** Joren Pelfrene, Wim Van Paepegem and David Lecompte. 2014. "Mechanical response of laminated glass plates subjected to impact loading." In *Proceedings of Challenging Glass 4 & COST Action TU0905 Final Conference*, ed. Jan Belis, Christian Louter, Freek Bos, and Jean-Paul Lebet, 473–480. London, UK: Taylor & Francis Group.

[4] Pelfrene, Joren, **Sam Van Dam**, Ruben Sevenois, Francisco Antonio Gilabert Villegas, and Wim Van Paepegem. 2016. "Fracture Simulation of Structural Glass by Element Deletion in Explicit FEM." In *Challenging Glass 5 (CGC5) Conference on Architectural and Structural Applications of Glass*, ed. Jan Belis, Freek Bos, and Christian Louter, 439–454. Ghent, Belgium: Ghent University.

[5] Pelfrene, Joren, **Sam Van Dam**, and Wim Van Paepegem. 2014. "Numerical and Experimental Study of the Peel Test for Assessment of the glass-PVB Interface Properties in Laminated Glass." In *Proceedings of Challenging Glass 4 & COST Action TU0905 Final Conference*, ed. Jan Belis, Christian Louter, Freek Bos, and Jean-Paul Lebet, 513–520. London, UK: Taylor & Francis Group.

[6] Pelfrene, Joren, **Sam Van Dam**, Johannes Kuntsche and Wim Van Paepegem. 2016. "Numerical simulation of the EN12600 pendulum test for structural glass." In *Challenging Glass 5 (CGC5) Conference on Architectural and Structural Applications of Glass*, ed. Jan Belis, Freek Bos, and Christian Louter, 439–454. Ghent, Belgium: Ghent University.

Conference abstracts – C3

[1] Pelfrene, Joren, **Sam Van Dam**, and Wim Van Paepegem. 2012. "Simulating Dynamic Glass Fracture in an Air Blast Event." In *13th FEA PhD Symposium, Abstracts*. Ghent University. Faculty of Engineering and Architecture.

[2] Pelfrene, Joren, **Sam Van Dam** and Wim Van Paepegem. 2014. "Numerical simulation of the 'human impact' pendulum test for structural glass." In *SIMULIA Benelux User's Meeting*.

CONTENTS

PART II – Impact

ANNEXES

Chapter 1 INTRODUCTION

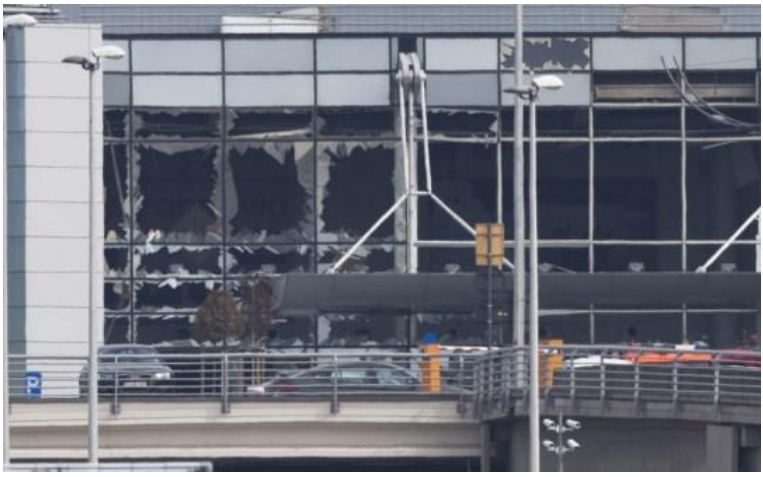

Overview

This chapter presents a general overview of the performed research. A short introduction about the subject matter – dynamic loading of laminated glass – is given as well as why the research is relevant, both from an academic and industrial point of view. Next, the background of the project this PhD is part of, is briefly summarized. The objectives of the study are listed and, to conclude, an overview of the different parts and chapters comprising this work is given.

1.1 BACKGROUND OF THE PROBLEM

1.1.1 What is laminated glass?

Laminated glass is composed out of two or more glass panes bonded by one or more interlayers. The most common type of interlayer is polyvinyl butyral (PVB).

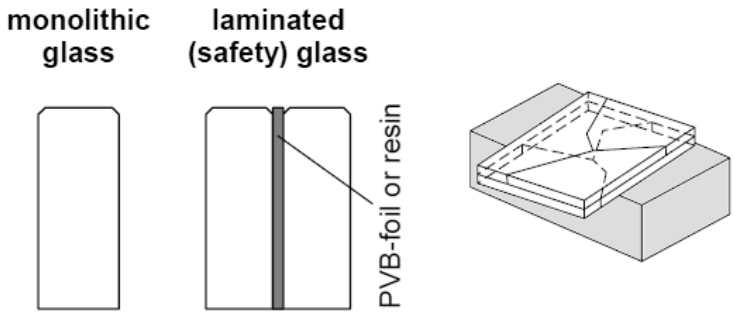

Figure 1-1 **Comparison monolithic and laminated glass (left) and post breakage behaviour of laminated glass (right) (adapted from [1]).**

Fracture of monolithic glass can occur without any warning, with very little deformation and in a split second. Due to this brittle behaviour and the associated safety risks, it cannot be used for structural or safety applications. These great disadvantages are avoided when using laminated glass. Laminated glass does not disintegrate upon fracture but the glass shards are kept together by the interlayer, preventing them from harming bystanders. Hence the material has residual load-bearing capacity and thus the necessary redundancy for structural use.

1.1.2 Impact and blast on laminated glass facades

Ever more facades are built using laminated glass [1]. The main reasons for this are the increased (awareness of) threats of terrorist attacks and natural disasters (like hurricanes and earthquakes) and the unfavourable role glass plays in the sometimes extensive loss of life and property caused by these events. For instance, the most severe injuries in blast victims are caused by flying glass fragments [2]. In urban environments glass fragments are responsible for 80% of total injuries, and up to 55% of the injuries at 120m from the blast are glass-related [3, 4].

Often these buildings house strategic companies or federal services and are thus prone to attacks from malevolent individuals. Buildings adjacent to them can sustain severe collateral damage (Figure 1-2). Accidental industrial explosions also induce peak loading on for example the control room overlooking a chemical

process. The use of laminated glass dramatically reduces the risk of injury by ensuring glass fragments stay adhered to a highly elastic interlayer.

When a charge is detonated, stored energy is rapidly released with an audible blast. The wave propagates with supersonic velocity until it hits an obstacle, such as a glass facade. If this is not capable of withstanding the dynamic overpressure, the glass will break. Current design guidelines are quite simplistic and do not consider this post-failure response. When certification tests are conducted, neither intensive instrumentation nor detailed numerical modelling is considered. International designers rely on guidelines from the US authorities [5] such as Wingard software and ASTM standards [6].

Figure 1-2 **Blast damage to glass facades on buildings adjacent to the Australian Embassy in Jakarta, Indonesia, 2004 [7].**

1.2 JUSTIFICATION OF THE RESEARCH

Although laminated glass has been around for decades and is often used to mitigate blast or impact loading, the mechanical behaviour is not very well known. Thus, calculations are often simplified and results are processed with very high safety factors. This leads to very conservative estimates resulting in thick laminate assemblies which are also not very economical.

Several standards exist to test laminated glass but they only classify the behaviour of the laminates in discrete categories. Little or no instrumentation is implemented during such tests. This prevents a thorough understanding of the underlying mechanical behaviour of their products. Post-failure response is not taken into account.

When developing a new laminated glass assembly, expensive testing campaigns according to these standards have to be performed in order to obtain the qualification required by the customer. Basic numerical models exist, but they are often empirical-based (e.g. Wingard) or employ a high level of simplification (e.g. SJ Mepla). This means that changing even a single parameter requires a new test campaign to investigate the laminate's behaviour.

Since the fundamental knowledge about the mechanical behaviour of laminated glass under dynamic loading remains limited, despite attempts from the industry to expand it, it is certainly justified to perform such research in an academic environment.

Also, literature on the subject is quite limited and most often confined to conference papers. Journal articles dealing with dynamic loading of laminated glass also lack instrumentation during the very limited number of tests they report.

1.3 CONTEXT OF THIS RESEARCH

This research project originated as a combination of two previously completed doctoral studies in the same research department. In his PhD, Sivakumar Palanivelu did research on the crushing behaviour of metal beverage cans and composite tubes under blast loading, which was the first PhD in the department dealing with that type of highly dynamic loading [8]. Stijn De Pauw, on the other hand, worked simultaneously but independently, on the impact behaviour of window glass fitted with safety window film [9]. Both researchers used a mixed experimental-numerical approach. In 2010, they successfully defended their thesis.

Subsequently, prof. Van Paepegem, promoter of both aforementioned PhDs, decided to combine the blast loading part of Palanivelu with the safety glass part of De Pauw, albeit laminated instead of retrofitted with safety window film. A BOF grant was awarded and the author commenced on this project, September 2011, intending to do both experimental and numerical research. However, some months later the author was awarded a personal IWT grant and thus the BOF grant could be used to hire a second researcher. Following previous successful projects conducted in the same manner, it was decided to have one researcher focussing on experiments, and the other one on simulations. Joren Pelfrene chose the latter [10] and the author of this thesis chose the experimental approach.

Because of their expertise concerning explosives, The Royal Military Academy in Brussels, was approached as partner for the blast tests, as they were for Palanivelu's research. John Vantomme, head of the COBO department, and major David Lecompte would follow up the blast part of the research.

Keeping in mind the arguments from the previous section, Solutia, a subsidiary of Eastman Chemical Company and world market leader in producing the PVB interlayer for laminated glass and AGC Glass Europe, the world's largest glass producing company, were interested to join this project to obtain a fundamental understanding of how laminated glass works under such conditions and to gain insight into which parameters influence this behaviour.

The main objective of this whole project is to build versatile validated models to predict the mechanical behaviour of laminated glass under dynamic loading, based on highly instrumented experiments.

1.4 OBJECTIVES

The aim of this PhD research can be summarized in three objectives which are given below.

1.4.1 Expand fundamental knowledge

The first objective is to gain an insight in what parameters influence the mechanical behaviour of laminated glass under dynamic loading, in what way and what the underlying mechanisms are. Special attention will go to how the properties of the interlayer and its interaction with the glass will influence this behaviour. First, the basic constituents of a laminated glass assembly will be characterized individually, including the interface. This characterization is vital in understanding the underlying mechanisms and in providing the necessary data for the numerical simulations. Next, the complete construction will be characterized as a whole.

For this purpose, we will conduct an extensive range of experiments, static as well as dynamic, on the basic materials and combinations of these materials.

1.4.2 Instrumented set-ups

It is clear that the standards used in the industry are inadequate to provide detailed information about the mechanical behaviour of laminated glass under dynamic loading. These standards are to be improved or new set-ups are to be conceived which can provide this information. When looking at literature, often the tests are also not properly instrumented and only a few tests are conducted. Instrumentation and how to apply this are of the utmost importance, since blast tests are very expensive and a maximum of data must be extracted from a single test to justify the expense.

The results of these tests will serve as input for the numerical simulation models.

1.4.3 Interaction with numerical modelling

As described above, the research was split in an experimental and numerical part, with each part being conducted by a different researcher. The focus of this PhD will thus obviously lie on the experimental part, but whenever relevant, paragraphs describing the numerical work of my colleague Joren Pelfrene and how his work resulted in an interaction with the experiments are added to the chapters. These paragraphs will be clearly marked. Each chapter presenting experimental results will also end with an overview of the relevant associated numerical simulations.

Many of the experiments were done specifically to obtain information necessary for the finite element models. Others were used to validate the models.

1.5 STRUCTURE OF THIS WORK

This work is structured into 3 large parts and one concluding chapter. Part one serves as an introduction and describes in detail the properties of the constituent materials as reported in literature (Chapter 2). Chapter 3 deals with the characterisation of the constituent materials and interface, mostly in a quasi-static manner but already some dynamic tests are introduced, such as high-speed tensile tests on the interlayer.

Part 2 deals with impact loading of laminated glass. An introduction which includes a literature review and discussion about the standards is presented in Chapter 4. Next, two types of impact each get their own chapter. Small specimens were tested with a small-scale drop weight (SSDW) set-up (Chapter 5). A set-up often used in industry is the standardised EN 12600 set-up, which loads larger panels of glass with two inflated tyres to simulate human impact (Chapter 6).

Again, Part 3 starts with an introductory chapter with a literature review and discussion of standards, albeit this time about blast loading of laminated glass (Chapter 7). Chapter 8 comprises two sections. First, the small-scale blast tests conducted in the underground bunker of the RMA are described. These were free air-blast tests where the shockwave is allowed to expand without being forced in a certain direction. The second section describes similar tests but this time not with an open air blast, but using a shock tube instead. This part concludes with large-scale blast tests (Chapter 9) performed at an open-air military domain. The final Chapter 10 gives an overview of the conclusions drawn from the whole of this work, followed by an outlook for future research.

A theoretical background for the Digital Image Correlation technique can be found in Annex A. Part of the post-processing of the SSDW results (see Chapter 5) is detailed in Annex B. The design of an EN 356 set-up and a description of some preliminary tests are presented in Annex C.

1.6 REFERENCES

[1] M. Haldimann, A. Luible, and M. Overend, *Structural Use of Glass*. Zürich: International Association for Bridge and Structural Engineering, 2008.

[2] E. E. Hinmann, "Lessons from ground zero," American society for Industriel Safety & Security Management, 1995, pp. 26-35.

[3] Smith, D. Glazing for injury alleviation under blast loading – UK Practice. In Proceedings of Glass Processing Days 2001, 18-21 June, Tampere, Finland. 2001.

[4] H. S. Norville, N. Harvill, E. J. Conrath, S. Shariat, and S. Mallonee, "Glass-related injuries in Oklahoma City bombing," *Journal of Performance of Constructed Facilities*, pp. 50-56, 1999.

[5] Interagency Security Committee (ISC) security design criteria for new federal office buildings and major modernization projects, National Research Council, 2001.

[6] N. F. Johnson, "International standards for blast resistant glazing," *Journal of ASTM International*, vol. 3, pp. 1-16, 2006.

[7] M. D. Netherton and M. G. Stewart, "The effects of explosive blast load variability on safety hazard and damage risks for monolithic window glazing," *International Journal of Impact Engineering*, vol. 36, pp. 1346-1354, Dec 2009.

[8] S. Palanivelu, "Energy Absorption of crushable Tubes for Protective Structures under Static, Impact and Blast Loading," Doctor in de Ingenieurswetenschappen: Werktuigkunde-elektrotechniek, PhD, Department of Material Science and Engineering, Mechanics of Materials and Structures, Ghent University, Ghent, 2011.

[9] S. De Pauw, "Experimental and Numerical Study of Impact on Window Glass Fitted with Safety Window Film," Doctor in de Ingenieurswetenschappen: Werktuigkunde-Elektrotechniek, PhD, Department of Material Science and Engineering, Mechanics of Materials and Structures, Ghent University, Ghent, 2010.

[10] J. Pelfrene, "Numerical analysis of the post-fracture response of laminated glass under impact and blast loading," Doctor in de Ingenieurswetenschappen: Werktuigkunde-Elektrotechniek, PhD, Department of Material Science and Engineering, Mechanics of Materials and Structures, Ghent University, Ghent, 2016.

PART I – INTRODUCTION & MATERIAL CHARACTERIZATION

This part contains a further introduction to the materials and techniques used in this study, as well as a first characterization of the constituent materials of laminated glass.

Chapter 2 MATERIAL SELECTION AND MECHANICAL PROPERTIES

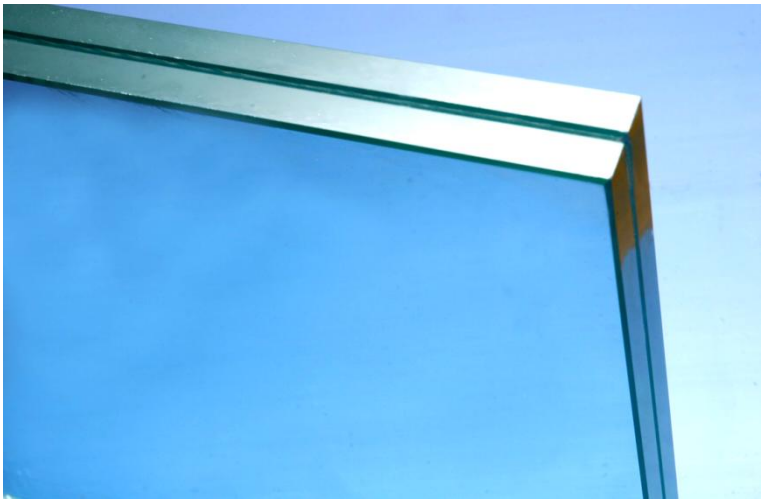

Overview

In this chapter the basic constituents of laminated glass – glass and a polymer interlayer – are discussed as well as the interface between both. Their basic mechanical properties are given and some background information about how they are produced and how this can affect the research. The behaviour and production of laminated glass as a whole is discussed in the final sections. Where appropriate the necessary choices concerning the materials to be tested are made.

2.1 GLOBAL STRUCTURE OF THE LAMINATED GLASS CONSTRUCTION

Laminated glass, in the broadest sense, consists of a stacking of minimum 2 glass plies with minimum one polymer interlayer sandwiched in between every two glass panels. The most common interlayer is PolyVinyl Butyral or PVB.

Figure 2-1 Possible laminate configurations.

The composition of a standard laminate (such as the first and third configuration in Figure 2-1) is determined by a number in an "*xy.z*" format with "x" and "y" the nominal thickness of the glass plies in mm and "z" the number of interlayers (with a standard thickness of 0.38 mm). For example a laminate with 2 glass plies of nominally 4 mm and a 0.76 mm PVB layer has a composition number of 44.2.

Architectural glazing is most often made with 2 glass panels of 3 to 6 mm and with 1 to 4 0.38 mm layers of PVB. Automotive windshield glazing uses thinner glass. Bulletproof glass will have a high number of different glass panels and interlayers, resulting in a very bulky and heavy configuration.

2.2 GLASS

Glass is an inorganic amorphous solid, which is obtained by cooling its molten, liquid phase in such a way that it solidifies without crystallization [1].

The glass most frequently used for architectural purposes is flat soda-lime silica glass (SLSG) which is manufactured according to the float process. The end product of the float process can be addressed as annealed float glass (ANG). The main advantage of annealed float glass is that the residual stresses are very small and its surfaces are parallel and smooth. This allows for easy cutting and drilling of the glass pane. Because annealed float glass is produced in such large quantities, it is an economical solution for laminating companies.

2.2.1 Glass composition

As the name predicts the three main resources used for this type of glass are: sodium oxide (soda), calcium oxide (limestone) and silica (sand).

Silica is the base material for the production of glass, soda is added to lower its melting temperature and calcium exhibits chemically stabilizing properties. Furthermore, mechanical properties and colour are adjusted by adding small quantities of metal oxides.

Table 2-1 Chemical composition of soda lime silicate glass [2].

Chemical component	Mass percentage
Silicon dioxide (SiO_2)	69% to 74%
Calcium oxide (CaO)	5% to 14%
Sodium oxide (Na_2O)	10% to 16%
Magnesium oxide (MgO)	0% to 6%
Aluminium oxide (Al_2O_3)	0% to 3%
Others	0% to 5%

2.2.2 Glass production

Flat soda-lime-silica glass is manufactured following the float-process (schematized in Figure 2-2). This process is continuous and starts with heating up the ingredients listed in Table 2-1 in a furnace up to 1550°C. The mixture is now relatively viscous which allows it to be spread out over a bath of molten tin at 1000°C. Due to the fact that the density of tin is higher than that of the glass, the glass melt floats over the tin surface. The flatness of the glass is guaranteed by the great difference in surface tension of the two materials. Tin, however, forms tin oxide under atmospheric conditions. To avoid SnO_2 adhering to the glass, an overpressure is applied as well as a protective atmosphere consisting of a mixture of nitrogen and hydrogen.

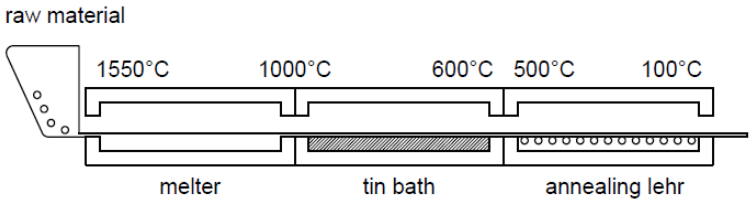

Figure 2-2 Production process for float glass [3].

The thickness of the glass is controlled by edge rollers; each speed leads to an equilibrium thickness of the glass melt. Over the length of the tin bath the glass melt is allowed to cool slowly until it reaches approximately 600°C, then it is solidified enough for transportation over rollers. These rollers transport the glass ribbon into the annealing lehr in which it cools down very slowly to minimize residual stress build-up caused by non uniform solidification and shrinking. The glass leaving the annealing lehr is automatically inspected to detect flaws after which it is cut to a standard size of 6 by 3.21 m. These plates are also called jumbo-plates.

2.2.2.a Influence of air/tin side

The two faces of glass sheets are not identical, because only one of them comes into contact with the tin bath. This results in a small amount of diffusion of tin(oxide) in this surface [4]. The strength of this tin side is said to be marginally lower than that of the air side [4-6]. However, this is most likely to be attributed to the transport rollers the tin side comes into contact with, resulting in larger surface flaws. It also has an influence on adhesive bonding (see 2.4.3).

The tin side can be detected by illuminating it with ultraviolet radiation (e.g. from a common UV lamp). This will cause the tin to fluorescence and turn a milky white. The air side does not display this behaviour.

Figure 2-3 Milky white gleam of tin side (left) and violet gleam of air side (right).

2.2.3 Glass properties

2.2.3.a Physical properties

The density of glass is 2500 kg/m^3 [7]. The most obvious optical property is its high transparency within the visible range of wavelengths. However, long-wave infrared radiation is blocked, resulting in the green-house effect. The coefficient of thermal expansion is 9.10^{-6}/K [2].

2.2.3.b Mechanical properties

Glass behaves almost perfectly elastic and isotropic up to its point of failure, which is very brittle. No plastic deformation whatsoever takes place. This prevents local stress concentrations from being reduced by redistribution of stresses as would be the case for e.g. steel. This is also the reason why the fracture strength of glass is several orders of magnitude lower than its theoretical strength, which is exceptionally high. Though its failure strength is a point of debate because of the large scatter, there exists a broad consensus for the elastic properties of glass which are presented in Table 2-2.

Table 2-2 Elastic properties of glass.

Reference	E [GPa]	ν [-]
EN 572-1 [2]	70	0.2
DIN 1249-10 [8]	73 (for annealed), 70 (for tempered)	0.23
EN 1288-1 [9]	/	0.23

The theoretical tensile strength of glass can be calculated starting from the bonds on molecular scale, which form a covalent network, assuming that the predominating bond is silicon-oxygen. Based on the molecular bonding energy the theoretical tensile strength of glass is 21-32 GPa [3, 10].

In reality the tensile strength of glass is significantly lower, considerably less than 100 MPa even. The reason for this behaviour is the presence of structural flaws, mostly situated on the surface and the edges of the glass [11]. The most common flaws are: scratches, bubbles, inhomogeneities and inclusions [12]. All of these flaws are inherent to the production process and are unavoidable. Scratches however can also find their origin after the production process. The latter are the most frequent and biggest flaws present in the glass. Furthermore, they only occur on the surface of the glass. Due to their irregularity, stresses are concentrated and built up around these flaws. These local stresses are much larger than the average stress distribution and can quickly reach the ultimate tensile strength of the material and thereby cause failure of the material.

In Figure 2-4 a relationship is given for the tensile strength in function of the surface flaw depth. The compressive strength of glass is remarkably higher; this is due to the fact that when compressed, surface flaws are not being opened but are pressed together. There is still the effect of stress concentration in compression, but the intensity is far smaller. Typical values for compressive strength are 700 MPa – 900 MPa [7]. However, due to the Poisson effect glass never fails in compression but always in tension, as some flaws will inevitably experience tensile stress.

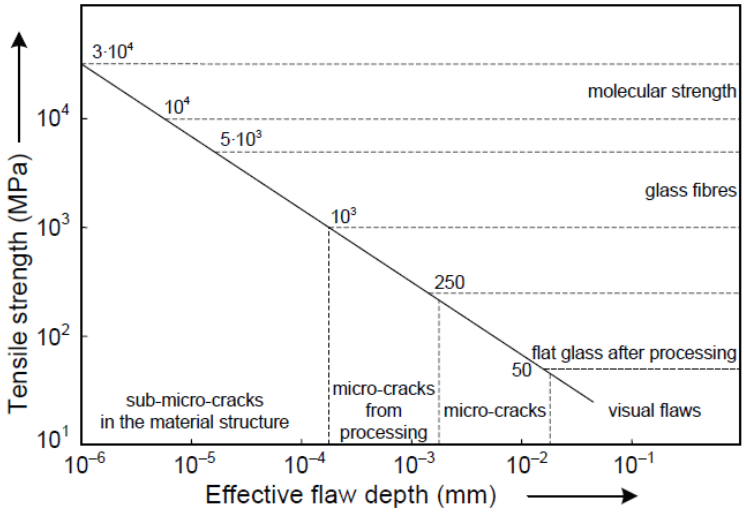

Figure 2-4 **Typical short-term strengths as a function of the flaw depth (adapted from [11]).**

The failure strength of glass is dependent of many factors [9], including but not limited to: the surface condition, the stressed surface area [13], the ambient medium [14], the age of the glass panel, the rate and duration of loading and, to a lesser extent, temperature.

Because this research will include static up to highly dynamic loading of glass the influence of the loading rate deserves a closer look [15-19]. When loading a brittle material at a relatively slow rate, failure will be initiated by the most critical flaw. This behaviour is addressed as the weakest link regime. When loading happens rapidly, stress is built up very fast causing failure in multiple flaws simultaneously. There is an averaging effect which narrows the stochastic distribution of the material strength and results in higher flexural strength. The latter phenomenon is referred to as the multiple fragmentation regime.

As a rule of thumb for the failure strength, one can apply the values given in EN 527-1 [2] and DIN 1249-10 [7] which is 45 MPa. This is not an average value but a 5% fractile value with a 95% confidence level. The average would be higher but because of the large scatter a conservative value is needed for design purposes.

2.2.4 Thermal treatments [3]

Because annealed float glass is cooled very gradually, the residual stresses are quite low. However, sometimes the presence of residual stresses can be favourable for the glass strength. These stresses can be re-introduced with a thermal treatment of a specimen. Several gradations are possible, but the most prominent stresses arise in so-called fully tempered glass (FTG). All processing of the specimen has to be completed before this further thermal treatment and the edges have to be ground and chamfered.

First the cleaned glass panes are heated up to approximately 650°C, this is some 100°C above the glass transition temperature of glass. At this temperature the glass behaves more as a rubber like material. After this process the glass is quenched by 20°C jets of air.

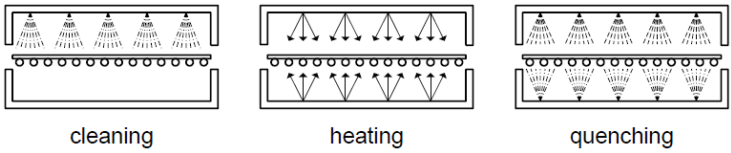

Figure 2-5 Tempering process.

The process of quenching assures rapid cooling of the glass surface which creates a thermal gradient from the glass body to the surface. When the glass surface cools down and solidifies, it shrinks unhindered because the glass body is still behaving plastic. After that, the body cools down but now shrinkage is impeded by the already solidified glass surface. Thus internal stresses are being built up, creating compression of the surface and tension in the body.

During the heat treatment, the glass panes are propelled by rollers which compromise the flatness of the glass at the glass transition temperature. The resulting ripples are called “roller waves”. Additionally, deformations can arise from the internal stress distribution.

The flaws at the surface are closed under the action of compression, avoiding the risk for high stress concentrations around the flaw tips. The tensile flexural strength of the glass is thereby increased greatly, amounting to 120 MPa [1] (5% fractile, compare to the earlier 45 MPa of annealed float glass). Furthermore this process prevents the development of sub critical crack growth; whilst the glass surface is under compression, no static fatigue [20] will occur.

However, it can still break but when it does so, fully tempered glass shatters into thousands of small pieces. The additional benefit of fully tempered glass is that it poses less risk of injuring people upon breakage and that the resistance to

temperature variations is larger. The downside is that drilling, milling and cutting cannot be done on tempered glass without fracturing it. Another problem is that fully tempered glass does not possess any residual strength after breakage, whilst the shards in annealed glass can still bear loads, especially when laminated.

Heat-strengthened glass is similar to fully tempered glass in every aspect, but the quenching is less severe resulting in lower residual stresses and thus a lower failure strength at 70 MPa [1] (5% fractile).

A totally different method to increase the failure strength by introducing compressive stresses on the surface is chemical tempering. It does not involve thermal effects but relies on the exchange of sodium ions in the glass surface with potassium ions which are about 30% bigger. This affects only a very thin layer. A comparison of the stress profiles resulting from thermal and chemical tempering is presented in Figure 2-6.

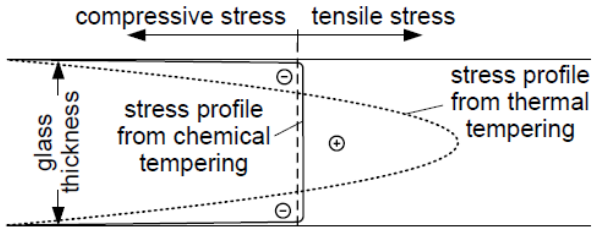

Figure 2-6 **Comparison of the stress profiles obtained by thermal and chemical tempering.**

Chemical tempering is very expensive and is therefore not often applied in structural applications of glass.

2.2.5 Glass processing

Though difficult, it is possible to perform some operations on glass such as hole drilling, edge working and cutting it to a variety of shapes and sizes. Other treatments can include curving of the glass, applying coatings or modification of the surface for decoration purposes (etching).

2.2.5.a Cutting to size

The normal procedure to cut glass is to first score the surface using a diamond wheel cutter dipped in glass cutting oil. The pane can then be easily cut by breaking it along this groove (Figure 2-7). However, this process introduces severe flaws along the cutting edge which influence the glass strength. Moreover, this damage is

confined to the cutting side of the glass (Figure 2-8). This unwanted asymmetrical behaviour [21] can be mitigated by applying a side finish such as described in DIN 1249-11 [8].

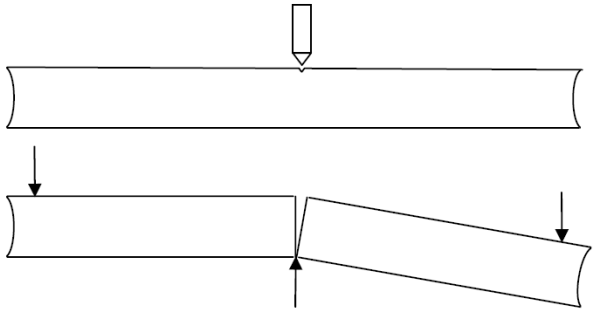

Figure 2-7 **Glass cutting [1].**

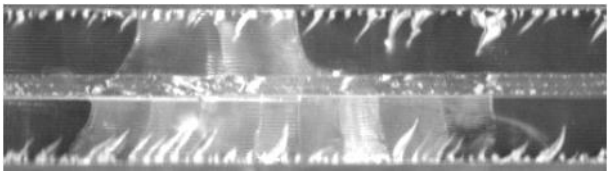

Figure 2-8 **Typical damage arising at laminated glass sides due to cutting (cutting surfaces are the outer surfaces of this laminated sample).**

Other techniques resulting in less damage are water jet and laser cutting.

2.3 PVB

The most common interlayer material is PolyVinyl Butyral or PVB, a thermoplastic polymer exhibiting visco-elastic behaviour. Trade names include Saflex (Solutia Eastman), Butacite (DuPont), Trosifol (Kuraray Europe GmbH) etc.

Thermoplastics are polymers that become soft and eventually melt when heated, thus they can be remodelled and reformed by applying heat and subsequently cooling them. The polymer structure is composed out of long monomer chains with strong covalent bonds. These monomer chains are interconnected by relatively weak Van Der Waals bonds which break when heat is applied and reform when cooled down again. Because of its visco-elastic behaviour, temperature, loading rate and loading duration are important parameters that influence its mechanical behaviour.

PVB foils are mostly produced with a standard thickness of 0.38 mm but thicker films of 0.76 mm are also available. The combination of several films (up to 6 for curved or tempered laminates) results in a single interlayer.

2.3.1 PVB composition

A PVB interlayer ready for use is a mixture of PVB resin and plasticizers, together with other additives such as UV-stabilizers, adhesion controlling agents, colour pigments and a percentage of recycled PVB interlayer.

2.3.1.a PVB resin

The PVB resin acts as a thermoplast making it ideal for the extrusion process. The chemical structure of the polymer is shown in Figure 2-9.

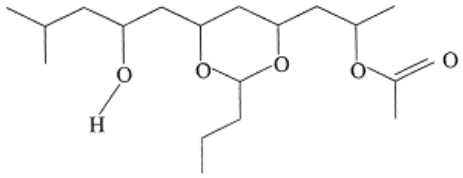

Figure 2-9 Chemical structure of PVB (adapted from [22]).

It contains alcohol groups (left structure), acetyl groups (middle structure) and acetate groups (right structure). The degree to which every group is present depends on the production circumstances.

PVB is derived from vinyl acetate. The entire reaction process is out of scope for this research. It suffices to say that the number of alcohol groups is an important parameter to determine adhesion characteristics.

Due to the presence of a large number of functional groups, PVB is highly compatible with a range of additives like plasticizers, who can affect the properties of PVB in several ways.

2.3.1.b Additives

Plasticizers are added because without them PVB would be quite brittle in the temperature range of most applications. They lower the glass transition temperature making the interlayer more workable. An optimal amount has to be added depending on the desired properties. Indicative values range from 20 to 25 parts of plasticizer per 100 parts of PVB [22, 23]. Usually, dibutyl sebacate is used as plasticizer, an ester.

Should one extrude a film composed of only resin and plasticizer, one would get a maximal adhesion. However, a laminate made with this interlayer would have a very low impact resistance (see 2.4.3 about adhesion). Hence, adhesion control agents are added. These are salts that impede the formation of hydrogen bonds between the OH-groups of the film and the silanol groups of the glass.

A third additive is a UV-stabilizer, necessary to withstand the constant exposure to sunlight which most architectural and automotive glazing experiences. Without it, the polymer would dissolve, discolour and become brittle.

2.3.2 PVB production [24]

The actual production of the interlayer is done by means of a continuous extrusion process. The basic components are fed into a mixer. The homogenous mixture is led into the extruder. With a revolving screw the mass is pressurized, making it melt. The resulting paste is forced through a thin rectangular nozzle, resulting in a continuous interlayer. From this point on, the interlayer is pulled forward by a complex set of rolls. It passes through several zones including a relaxation zone, a warm and cold water bath and inspection zones. Before the interlayer is rolled up, the edges are trimmed and fed back into the mixer. Finally, the roll of film is packaged in an aluminium bag and stored beneath 10°C.

A complete schematic of the different steps is presented in Figure 2-10.

2.3.3 PVB properties

PVB is characterized by an amorphous molecular structure, this means that the monomer chains are distributed randomly like cooked spaghetti. The density of PVB is slightly higher than that of water at 1070 kg/m^3 [25].

When temperature rises or load duration increases, the interconnection of the monomer chains weakens and the material behaves softer. Thus the Young's modulus E and the shear modulus G drop with increasing temperature and load duration whilst the Poisson's ratio ν nears to its theoretical maximum value of 0.5. In Figure 2-11 relaxation curves for PVB are displayed.

Like glass, thermoplastics have a glass transition temperature. For PVB the glass transition temperature is situated between 12°C-18°C. According to [26] this transition range is situated between 5°C-40°C. At this temperature the intermolecular bonds start to break. Of course this is not a sudden reaction but it takes place over a certain temperature range called the glass transition zone. In the glass transition zone the material can be modelled as visco-elastic. On the left (or faster/colder) side of Figure 2-11 the material is in a vitreous state which can be modelled as purely elastic whilst on the right (or slower/warmer) side the material is

rubbery and more viscous. Because the glass transition temperature of PVB situates at room temperature, it manifests visco-elastic behaviour in most applications.

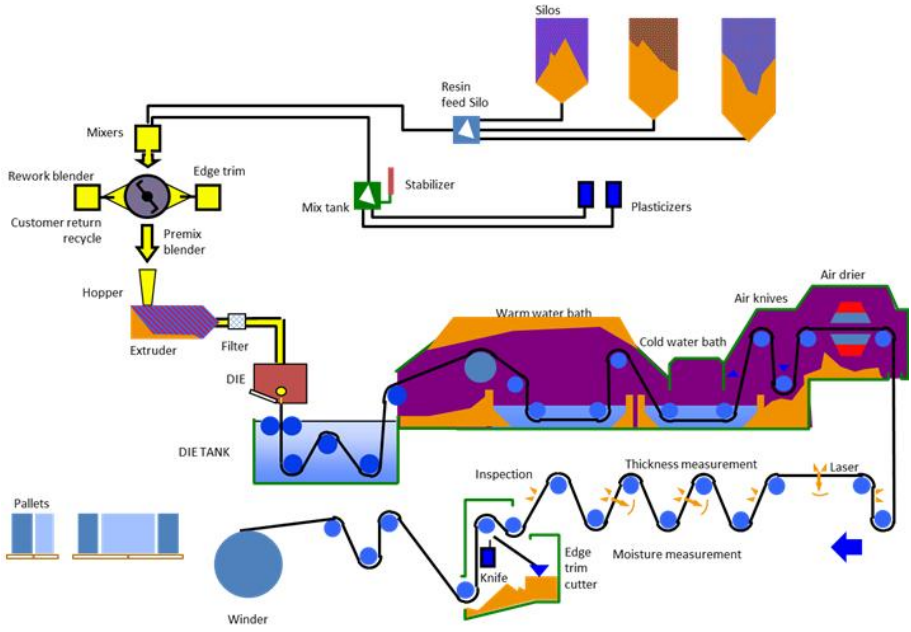

Figure 2-10 Production process PVB interlayer.

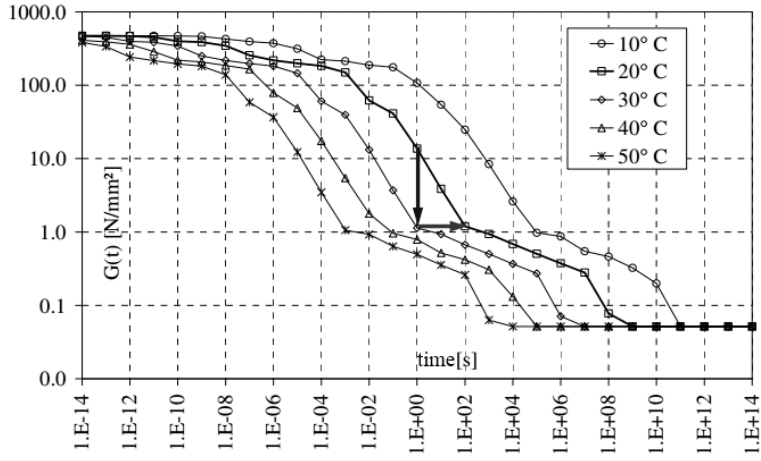

Figure 2-11 Relaxation curves of PVB [25].

Data regarding PVB interlayer properties in literature is quite limited and the conditions under which it was gathered are often not well documented. Furthermore, it shows a large scatter on results. Hence, it will be necessary to perform our own series of tests to get the data needed for the numerical simulations.

That being said, Eastman does provide customers with the following data sheet containing the basic properties of PVB (Table 2-3). But it should be clear that the behaviour of PVB cannot be described with a single modulus value at a certain temperature and loading rate, but it can be an indicative value to compare different types of interlayers.

Table 2-3 Basic properties of Saflex® RB41 PVB interlayer [24].

Property		**Saflex®**		**Conditions**
Density	ρ	1070	kg/m^3	23°C
Shear modulus	G	20.6	MPa	23°C / 25%RH
Poisson's ratio	ν	0.50		23°C / 25%RH
Tensile strength	f_t	27	MPa	23°C / 25%RH
Strain at failure	ε_t	205	%	23°C / 25%RH
Young's modulus	E	1.56	MPa	60°C / 1Hz

2.3.4 Alternatives

The newly developed materials EVA (EthylVinyl Acetate) and TPU (Thermoplastic PolyUrethane) have the advantage of being highly adhesive to materials other than glass, more translucent and less moisture dependent. However, their manufacturing cost is many times higher than for conventional PVB. Therefore these materials are mainly used for architectural purposes (not automotive) and for photovoltaic module encapsulation (solar panels).

SentryGlas Plus® or SGP is an ionoplast interlayer material that has the advantage that its glass temperature is well above room temperature. Therefore it acts much stiffer than conventional PVB at a given temperature and/or load duration [27]. However, this higher stiffness can make the lamination of such interlayers difficult. A stiffer PVB has been developed which exhibits similar behaviour. Such stiff interlayers are most often employed in high-end markets such as aviation and military applications and in free edge balustrades.

2.4 LAMINATED GLASS

2.4.1 Production (laminating)

The procedure described in this section is the procedure developed at the Quality Control Lab of Eastman Solutia in their Ghent plant for making small-scale specimens. All specimens used in this research were made there using this procedure, unless stated otherwise. The procedure is very labour-intensive and requires many small steps, often with a bottle-neck characteristic. This explains the high cost of small samples of laminated glass.

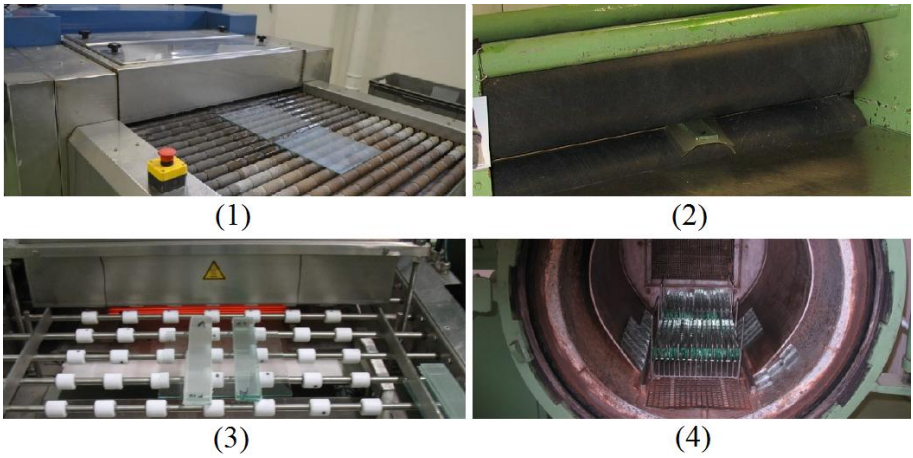

Figure 2-12 **Several steps in producing laminated glass samples: (1) industrial glass washer, (2) rubber pressing rolls, (3) infrared oven and (4) autoclave.**

The PVB is first cut to size manually, a little bigger than the glass specimen will be. The type of PVB is indicated in a corner using an alcohol marker. The individual sheets are then hung in a climate chamber for a minimum of 3 hours. This chamber, with a temperature of 40°C and a relative humidity of 26% ensures the PVB does not contain too much moisture, which affects adhesion. In this state the PVB is opaque.

In the meanwhile, the float glass is cut to size manually (this could also be automated). Next, the tin side is determined using a UV lamp and this is marked on a glass corner using a diamond tip pen. The glass is then washed and dried (Figure 2-12 (1)). The water used is demineralised water with a conductivity of less than 10 µS and it has been heated to approx. 60°C. This step is very important because each particle left on the glass surface will have a negative effect on the adhesion. The

glass is stored upright and separated from each other (to prevent adhesion) and placed for half an hour in the same conditioning chamber as the PVB.

For small samples (e.g. four-point bending beams) the glass and PVB are stacked inside this climate chamber. First, a glass pane is placed with its air side upwards after which one or two interlayer films (according to the specified test series) are laid over the glass pane. It has to be ensured that the interlayer film is completely covering the glass pane and that its test series mark is placed within the glass geometry. Last, a second glass pane is placed above the interlayer film with its air side downwards in such a way that the edges of the upper pane coincide with those of the lower pane. The interlayer is preferably adhered to the air side because this ensures a higher level of adhesion (2.4.3).

The samples are then pushed through rubber pressing rolls before cutting away the excess interlayer material from the edges (Figure 2-12 (2)). Next, they are heated in an infrared oven to approximately 80°C (Figure 2-12 (3)). This helps in removing trapped air when the samples are pushed through the rubber pressing rolls a second time. The PVB has already become a bit transparent after this step.

For larger samples the stacking of the laminate is performed outside the climate chamber. The edges are trimmed immediately after stacking and the laminate is heated in an infrared oven and subsequently pushed a single time through the rubber pressing rolls.

Next, for all types of specimens, follows an autoclave cycle (Figure 2-12 (4)). During a 70-minute cycle, the samples are heated to 143°C at a pressure of 13 bar. This ensures that any remaining air is removed from the samples. The samples should be placed vertically in the autoclave, instead of one on top of the other, which would cause the bottom plate to have a thinner interlayer because of the weight.

2.4.2 Bending and post-breakage behaviour

The shear modulus G of the interlayer is the most important parameter in determining the behaviour of laminated glass upon bending. This response to loading may vary between two extreme cases [28, 29]. If the shear modulus of the interlayer had the same order of magnitude as the shear modulus of the glass, laminated glass should behave as a monolithic material upon bending (Figure 2-13(a)). However, the shear modulus of glass is ca. 29 GPa whilst the shear modulus of PVB at room temperature is in the order of a few MPa. This means that the glass plates are able to bend separately from each other, deforming the interlayer in the process.

For very short load times, the shear modulus of the PVB will be significantly higher, resulting in a more monolithic-like behaviour.

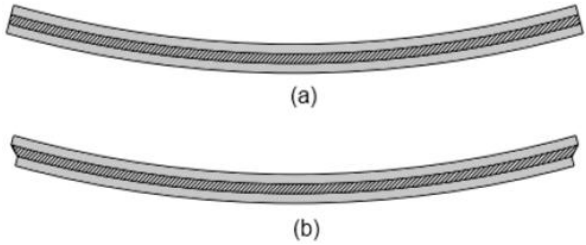

Figure 2-13 **Bending of laminated glass: (a) $G_{interlayer} \approx G_{glass}$ (b) $G_{interlayer} <<< G_{glass}$.**

One of the main advantages of laminated glass is its behaviour after breakage compared to ordinary glass. The fractured glass pieces stay adhered to the interlayer, which can deform significantly before tearing. This prevents glass fragments from flying away, possibly injuring people, as would be the case with monolithic glass.

This is especially true when it is used as a structural member where there must be redundancy present in the system. However, contrary to popular belief, laminated glass composed of fully tempered glass plates does not guarantee this post-breakage stability because the highly fragmented panels are unable to achieve an arching or locking action which would be the case for annealed glass panels [30].

Three stages of flexural behaviour in laminated glass are shown in Figure 2-14. In the first stage both glass sheets are intact. In the second stage the bottom sheet has fractured and the top sheet is carrying all the loads. In a third stage, the top sheet is also fractured but because the fragments lock together in compression and the interlayer is in tension, some further post-breakage resistance is achieved.

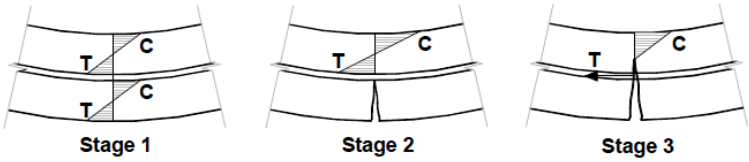

Figure 2-14 **Three stages of flexural behaviour in laminated glass showing the post-breakage stress distribution [3].**

2.4.3 Glass-PVB adhesion

Bonding between glass and PVB is mainly achieved by hydrogen bonds [11]. These bonds form between the polar vinyl alcohol groups present in the PVB and the polar silanol groups (Si-OH) on the glass surface. Additionally, true chemical bonds are also formed to some extent.

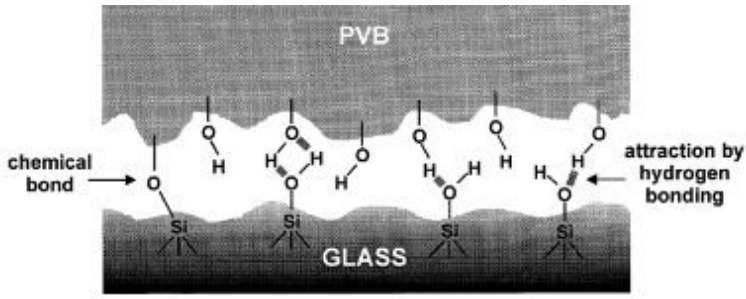

Figure 2-15 PVB-glass bonding mechanism [31].

Due to the surface roughness of the contact surfaces of both materials, these weak bonds do not form sufficiently without further treatment. Therefore an autoclave is needed which operates at a temperature of 143°C and a pressure of 13 bar. Here the PVB is softened and pressed on the rough surfaces of the glass, adopting their shape.

The bonding strength or adhesion between glass and PVB depends on several other factors as well. Alkali (earth) metal salts, originating from the cleaning water can severely reduce the adhesion. Potassium for example attracts residual moisture from the PVB, this leads to water clustering which hinders hydrogen bond formation. The earth metals calcium and magnesium interact directly with the vinyl alcohol groups: decommissioning them for further bonding. Therefore demineralised water is used for cleaning the glass, the purity is indicated by its conductivity (μS).

Tin particles show no affinity towards the vinyl alcohol groups present in the PVB, therefore tin side bonding is considered weaker than air side bonding.

PVB is a hygroscopic material which constantly tries to increase its moisture level by extracting it from the surrounding environment. As mentioned earlier, the presence of water decreases the adhesive bonding strength. The optimum moisture content of the PVB is situated around 0.4%, corresponding to a relative ambient humidity of ca. 25%. This is why the PVB is conditioned before lamination.

The adhesive bonding strength is important with regard to the post-fracture behaviour of laminated glass. It is observed on Figure 2-16 that the impact resistance of laminated glass is inversely proportional to the adhesion between glass and PVB.

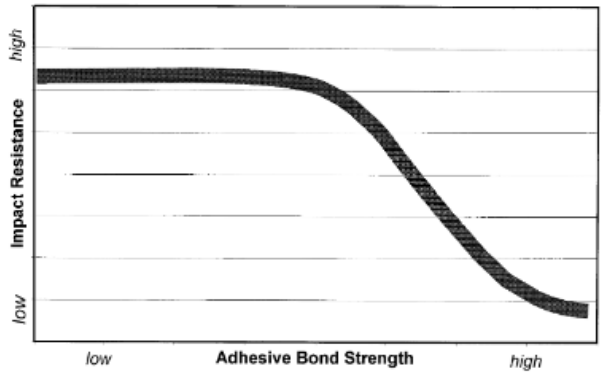

Figure 2-16 **Impact resistance as a function of adhesive bond strength [31].**

This can be explained by the following. For low adhesion, the PVB can delaminate from the glass, dissipating energy by doing so, and a relatively large area of PVB can stretch to accommodate the laminate's deflection under loading. For high adhesion, however, the PVB will not delaminate, causing only a very small strip of interlayer (along the glass crack) to stretch, resulting in very high strains and ultimately failure by tearing of the PVB (Figure 2-17).

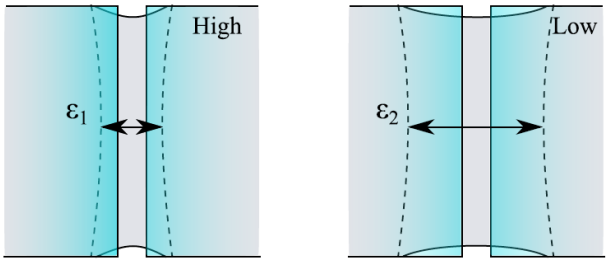

Figure 2-17 **Delamination of interlayer from glass around a crack with a given opening width for high adhesion (left) and low adhesion (right).**

Thus, for low adhesion the impact resistance is high because the residual projectile energy after breakage of the glass is absorbed by delamination and the resulting additional deformation of the interlayer. However, too low adhesive bonding strength may compromise safety due to complete delamination of dangerous glass shards. For high adhesion levels much less energy can be absorbed by the interlayer itself and therefore projectiles can more easily penetrate. However, high adhesion ensures that dangerous glass fragments will not be detached after glass breakage.

Thus, a compromise has to be found for the adhesion level based on the application and desired outcome.

2.4.3.a Measurement of adhesion

The adhesion itself can be measured with various testing methods. The most common are the Pummel test, Compressive Shear Test (CST), Through Cracked Tension test (TCT) and the Peel test.

In the industry the most widely accepted procedure for testing and evaluating the adhesion level between PVB interlayers and the glass substrate to which it is laminated is the Pummel test (Figure 2-18). Square specimens are hit repeatedly with a hammer and afterwards the remaining shards of glass are compared to 'standardized' samples. The specimen is then rated from 1 to 10 with 1 the highest adhesion and 10 the lowest. It should be clear to the reader that this method is very subjective and does not give quantitative data.

Figure 2-18 Preparation of the specimen for the Pummel test (left) and comparison to standardized sample (right) [24].

A schematic of the experimental setup of the Compressive Shear Test is shown in Figure 2-19. The specimen is put between a lower trolley which is free to translate in the horizontal direction and an upper block that moves vertically under the applied load. The specimen experiences a combined state of compression and shear under this loading. The polymer undergoes large rubber-like shear strains. A crack will nucleate at the free edge of the specimen along one of the interfaces. Processing of the acquired load and displacement data will result in an adhesion value.

The principles of the peel test and Through Cracked Tension (TCT) test will be explained in Chapter 3 together with experimental results from those tests.

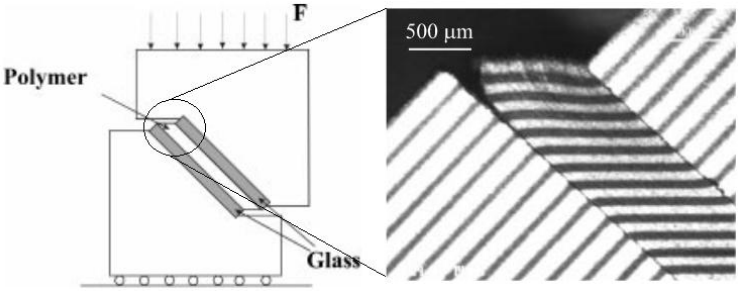

Figure 2-19 **Schematic drawing of CST (left) and detailed view of delaminating sheared interlayer (right) [32].**

2.5 CONCLUSIONS

It is clear that both materials that make up a laminated glass assembly exhibit very different behaviour. Furthermore, this behaviour is already very varied for the material itself. On the one hand there is the elastic, brittle nature of glass with a large scatter on flexural strength and a low failure strain, on the other hand there is the visco-elastic behaviour of PVB which can strain immensely, with its glass transition temperature around room temperature. This results in extreme conditions for experimental work.

From a modelling point of view, this applies even more, because both material models could not be more different. This underlines the importance of being careful with experimental data.

The influence of adhesion between both materials can be summarized as follows. For a low adhesion level, the PVB is allowed to delaminate from the edges of the fractured glass pieces, resulting in a lower average strain of the interlayer between the cracks in the glass. On the contrary, for a high adhesion level, this delamination is hindered resulting in a locally very high strain causing the interlayer to tear.

However, the adhesion level cannot be too low, as then the glass fragments will delaminate as a whole, defying the actual purpose of laminated glass in preventing injuries due to propulsed glass fragments.

In this research, only laminates made with annealed float glass will be tested, along with a variety of PVB interlayers including three different levels of adhesion, a stiffer variant, and of several thicknesses.

2.6 REFERENCES

[1] J.-D. Wörner, J. Schneider, and A. Fink, *Glasbau - Grundlagen, Berechnung, Konstruktion*: Springer, 2001.

[2] CEN, EN 572-1:2004. Glass in building - Basic soda lime silicate glass products - Part 1: Definitions and general physical and mechanical properties, 2004.

[3] M. Haldimann, A. Luible, and M. Overend, *Structural Use of Glass*. Zürich: International Association for Bridge and Structural Engineering, 2008.

[4] M. H. Krohn, J. R. Hellmann, D. L. Shelleman, C. G. Pantano, and G. E. Sakoske, "Biaxial flexure strength and dynamic fatigue of soda-lime-silica float glass," *Journal of the American Ceramic Society*, vol. 85, pp. 1777-1782, Jul 2002.

[5] ASTM C158-02 (2002): Standard Test Methods for Strength of Glass by Flexure (Determination of Modulus of Rupture).

[6] A. A. Wereszczak, K. E. Johanns, and T. P. Kirkland, "Strength And Contact Damage Responses In A Soda-Lime-Silicate And A Borosilicate Glass," Oak Ridge National Laboratory, Oak Ridge2006.

[7] DIN 1249-10:1990 Glass For Use In Building Construction - Part 10: Chemical And Physical Properties.

[8] Glass in building, glass sides, concept, characteristics of side types and finishes," in *DIN 1249 Part 11*, 1986.

[9] EN 1288-1:2000 Glass in building - Determination of the bending strength of glass - Part 1: Fundamentals of testing glass.

[10] M. Overend, G. A. R. Parke, and D. Buhagiar, "Predicting failure in glass - A general crack growth model," *Journal of Structural Engineering-Asce*, vol. 133, pp. 1146-1155, Aug 2007.

[11] M. Hegger, V. Auch-Schwelk, M. Fuchs, and T. Rosenkranz, *Baustoff Atlas*: Birkhäuser, 2006.

[12] X. Brajer, P. Forquin, R. Gy, and F. Hild, "The role of surface and volume defects in the fracture of glass under quasi-static and dynamic loadings," *Journal of Non-Crystalline Solids*, vol. 316, pp. 42-53, Feb 2003.

[13] D. Oakley, "An empirical study of the effect of stressed area on the strength of float glass surfaces," *Journal of Non-Crystalline Solids*, vol. 196, pp. 134-138, MAR 1996 1996.

[14] S. M. Wiederhorn and L. H. Bolz, "Stress Corrosion and Static Fatigue of Glass," *Journal of the American Ceramic Society*, vol. 53, pp. 543-&, 1970.

[15] F. H. Zhou and J. F. Molinari, "Stochastic fracture of ceramics under dynamic tensile loading," *International Journal of Solids and Structures*, vol. 41, pp. 6573-6596, Nov 2004.

[16] F. H. Zhou and J. F. Molinari, "On the rate-dependency of dynamic tensile strength of a model ceramic system," *Computer Methods in Applied Mechanics and Engineering*, vol. 194, pp. 1693-1709, 2005.

[17] O. Miller, L. B. Freund, and A. Needleman, "Modeling and simulation of dynamic fragmentation in brittle materials," *International Journal of Fracture*, vol. 96, pp. 101-125, 1999.

[18] C. Denoual and F. Hild, "Dynamic fragmentation of brittle solids: a multi-scale model," *European Journal of Mechanics a-Solids*, vol. 21, pp. 105-120, Jan-Feb 2002.

[19] F. Hild, C. Denoual, P. Forquin, and X. Brajer, "On the probabilistic-deterministic transition involved in a fragmentation process of brittle materials," *Computers & Structures*, vol. 81, pp. 1241-1253, May 2003.

[20] M. Vandebroek, J. Belis, C. Louter, and R. Caspeele, "Influence of the load history on the edge strength of glass with arrised and ground edge finishing," *Engineering Fracture Mechanics*, vol. 104, pp. 29-40, May 2013.

[21] F. A. Veer and J. Zuidema, "The strength of Glass, Effect of Edge Quality," presented at the Glass Processing Days, 2003.

[22] A. K. Dhaliwal and J. N. Hay, "The characterization of polyvinyl butyral by thermal analysis," *Thermochimica Acta*, vol. 391, pp. 245-255, Aug 12 2002.

[23] C. V. G. Vallabhan, Y. Das, and M. Ramasamudra, "Properties of PVB Interlayer Used in Laminated Glass," *Journal of Materials in Civil Engineering*, vol. 4, pp. 71-76, 1992.

[24] Internal document Solutia, Eastman Chemical Company

[25] J. Belis, "Kipsterkte van monolithische en gelamineerde glazen liggers," Ghent University, 2005.

[26] P. A. Hooper, B. R. K. Blackman, and J. P. Dear, "The mechanical behaviour of poly(vinyl butyral) at different strain magnitudes and strain rates," *Journal of Materials Science*, vol. 47, pp. 3564-3576, Apr 2012.

[27] L. Biolzi, S. Cattaneo, and G. Rosati, "Progressive damage and fracture of laminated glass beams," *Construction and Building Materials*, vol. 24, pp. 577-584, Apr 2010.

[28] H. S. Norville, K. W. King, and J. L. Swofford, "Behavior and strength of laminated glass," *Journal of Engineering Mechanics-Asce*, vol. 124, pp. 46-53, Jan 1998.

[29] M. Z. Asik and S. Tezcan, "A mathematical model for the behavior of laminated glass beams," *Computers & Structures*, vol. 83, pp. 1742-1753, Aug 2005.

[30] A. Kott and T. Vogel, "Safety of laminated glass structures after initial failure," presented at the Proceedings of the IABSE Symposium, Shanghai, 2004.

[31] U. Keller and H. Mortelmans, "Adhesion in Laminated Safety Glass - What makes it work?," presented at the Glass Processing Days, 1999.

[32] P. Rahul-Kumar, A. Jagota, S. J. Bennison, and S. Saigal, "Interfacial failures in a compressive shear strength test of glass/polymer laminates," *International Journal of Solids and Structures*, vol. 37, pp. 7281-7305, Nov-Dec 2000.

Chapter 3 MATERIAL CHARACTERISATION

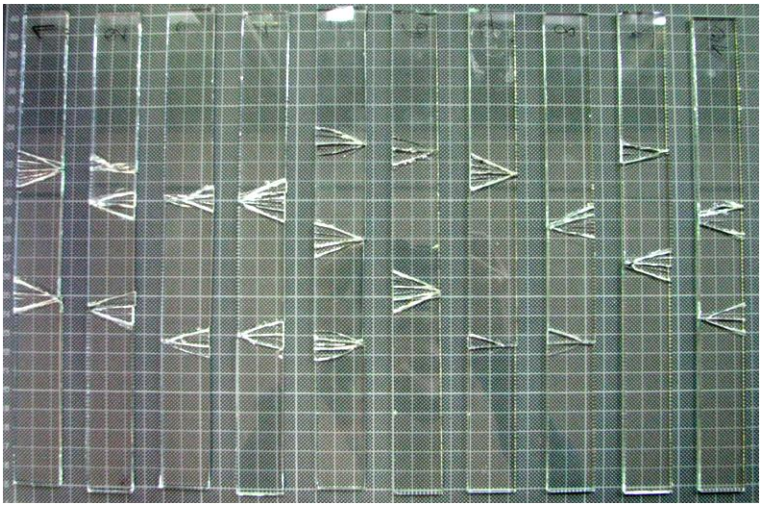

Overview

In this chapter the constituent materials of laminated glass are characterised, mostly in a quasi-static manner. First, bending tests (both four-point and axisymmetrical bending) are performed on monolithic glass samples to assess their failure strength. Next, tensile tests on PVB are described, both static and dynamic, to determine the visco-elastic and hyperelastic behaviour needed for numerical material models. Bending tests are then continued, this time on laminated samples. In a final part, the interface between glass and PVB is characterised, using Through-Cracked-Tension and pull-off tests.

3.1 GLASS

At present, knowledge about the relationship between induced edge flaw severity and glass edge strength is insufficient [1] although extensive research on this topic is currently performed by Vandebroek *et al.* [2, 3].

Therefore, test setups eliminating the edge influence can result in better values for the inherent strength of glass as a material. Such knowledge is needed when looking at dynamic loading of glass panes, such as during impact loading. Then crack initiation will most often start in the centre of the specimen and thus be independent of edge quality, resulting in strength values up to one order of magnitude larger than static values, affected by the edge effect [4].

When determining glass strength for use in dynamic design based on quasi-static tests, it is, therefore, crucial to eliminate the edge effects during such tests. Also, cracks need time to grow and when they do not have that time due to a high loading rate, glass strength might increase by a factor of 3 [5] during impact loading. The stressed area is of equal importance, as the statistical distribution of surface defects has a direct effect on glass strength [6].

An often quoted example [7, 8] to demonstrate the vast influence that the presence of surface flaws can have, is the much higher tensile strength of glass fibres (2000 MPa), which, due to their minute dimensions – a diameter of circa 10 μm – just do not have any, or only very small, flaws.

Several types of tests can be used to determine glass tensile strength, each one resulting in different values. This is why the used test method and standard must always be specified when comparing glass strengths.

The simplest one is of course a basic tensile test, where a rectangular or dumbbell specimen is subjected to uniaxial tension but such tests are rarely carried out on ceramic materials. Furthermore, glass is hardly ever applied in pure tension, most of structural glass being subjected to bending. For flexural strength determination four-point bending and ring-on-ring or ball-on-ring methods are used with the coaxial double ring test method being the preferred one in Europe to obtain glass strength data [1].

Determining the flexural strength with a four-point bending test is described in the European standard EN 1288-3 [9] and its American counterpart ASTM C 158-02 [10]. Biaxial flexure test methods are described in standards EN 1288-1[4], EN 1288-2 [11], EN 1288-5 [12] and ASTM C 1499-09 [13].

It is difficult to compare results because they are dependent on the followed test procedure (see above) and statistical analysis interpreting the results. Often results seem contradictory [14-17].

The general statistical procedure consists of fitting a two-parameter Weibull distribution [18, 19] to the experimental failure stress data. Though highly dependent on age, load history and surface flaws, a widely accepted [20] (5% fractile) value for the strength of annealed glass is 45 MPa whereas for the mean, values between 60 and up to 100 MPa are found, depending on the source [18, 20-22]. An overview can be found in [23]. For a permanent load, however, designing with a value as low as 7 MPa [1] could be mandatory, due to susceptibility of glass to stress corrosion cracking or static fatigue [24].

However, giving glass a 'better' edge quality does, rather contradictorily, not always result in a higher design strength, because of a larger scatter and subsequent lower 5%-fractile value obtained when processing the data according to some statistical distribution, despite a higher mean value [1, 25]. This larger scatter can be understood as polishing removes the macroscopic defects but introduces many more microscopic defects with a larger scatter.

3.1.1 Four-point bending

3.1.1.a Standards

According to the European standard EN 1288-3 [9], the flexural strength can be determined, including the effect of the edges by using a four-point bending test. Indeed, over the central span delimited by the bending rollers the bottom surface of the specimen as well as its longitudinal edges are subjected to the same maximum longitudinal stress, which based on simple beam theory is assumed to be uniform and uniaxial.

The dimensions of the glass specimens are prescribed as 1100 mm by 360 mm. To hold the glass fragments together and facilitate the determination of the fracture origin, an adhesive film is fixed to the surface of the specimen facing the bending rollers, which are set 200 mm apart. The supporting rollers are set 1000 mm apart. Between the rollers and the specimen rubber strips are placed for a more distributed load introduction. The load rate is specified as 2 MPa/s, meaning the displacement rate is dependent on the specimen thickness. A correction factor k is introduced to take into account the fact that for the rather wide beams (l/b approx. 3) used in this test, simple beam theory is no longer applicable and the longitudinal stress can no longer be regarded as uniform across the width.

ASTM C158-02 [10] differs from the European standard in the following manner. The support and the indentor consist of pivoting cylindrical edges (with approximately 3 mm radius) and no rubber strips are used. In addition to this, the dimensions are much smaller. The size of the glass specimens is prescribed as 250

mm by 38.1 mm. The loading lines are set to a distance of 100 mm while the bearing lines have a 200 mm separation. Also the load rate is lower: 1.1 MPa/s.

3.1.1.b Experiments

The main focus of the four-point bending test campaign was on laminated glass (see §3.3.2), so for pure glass, only one type of monolithic glass specimens was tested. Consequently, for a description and discussion of these tests, the author refers to the section about four-point bending on laminated glass samples (3.3.2), where the results of the monolithic samples have been incorporated. Besides, as the fracture is edge-dominated for these tests, comparison with the axisymmetrical bending tests in the next section is limited. It suffices to say the average failure stress for the monolithic test specimens under four-point bending was 64.4 ± 27.6 MPa.

3.1.2 Axisymmetrical bending

3.1.2.a Standards

In EN 1288-1 the principle of the coaxial double ring test is explained. By ensuring that only a limited area of the surface of the specimen, not including the edges, is subjected to maximum tensile stressing, the edge effects are suppressed to a large extent. By using a ring-shaped indentor, the tensile stresses in this circular shaped, middle area of the specimen are intended to be uniform.

Nevertheless some complications appear. EN 1288-1 states that when the deflections are relatively small (the precise limit depends on the ring geometry) the central surface area is subjected to uniform tensile stresses. Moreover, in the case of round glass specimens the radial and the tangential stress are then of equal size. If, however, the deflections become larger this leads to localized increases in stress below the edge of the loading ring, the extent of which increases as the load rises. Also at this stage of the loading the tangential and radial stresses change differently.

This standard also states that in the case of the large test surface area this increase in stress below the edge of the loading ring can be avoided by applying a gas pressure in the ring-shaped indentor against the surface of the glass specimen. The gas pressure then has to be optimized in such a way that either the radial or tangential tensile stress develops almost uniformly within the loading ring. This of course requires a complex control system.

ASTM C 1499-09 describes a test method for the equibiaxial flexural strength of ceramics which macroscopically exhibit isotropic, homogeneous and continuous behaviour. It uses a coaxial double ring loading configuration similar to that of the test methods described in EN 1288. As in the EN 1288 the specimens can

be round or square. Unlike the EN 1288 this standard does not impose specific dimensions for the loading fixtures nor for the specimens. It only requires the dimensions to be attuned so that simple plate theory can be applied (equations to enforce this condition are provided). Also, ASTM C 1499-09 recommends a much higher load rate (>30 MPa/s) than the load rate of 2 MPa/s prescribed by EN 1288.

3.1.2.b Test set-up

The test set-up is an in-house design, albeit with the European EN 1288 standard in mind. The major difference between our test setup and the one described in the standard is that a spherical indentor is used instead of a loading ring. The loading ring has the advantage of producing uniform bending stresses in the central area on the glass. However, since dynamic impact tests with a spherical indentor will be conducted in this same research (Chapter 6), there was opted for the use of a similar indentor. A 5 mm-radius spherical polished steel indentor and a 100 mm-diameter steel supporting ring were made to our specifications. A schematic overview is given in Figure 3-1. The tests were performed on an Instron tensile tester with a 10 kN-range load cell. The displacement rate was set to 1 mm/min. The complete setup is depicted in Figure 3-2.

From the tensile test machine the maximum force was obtained; the LVDT delivered the maximum bending displacement in the centre of the glass. As the displacements caused by the bending of the relatively stiff glass are very small, they could be inaccurate if derived from the crosshead displacement of the machine. This is due to the local deformation of the glass and the displacement of the indentor relative to the crosshead. Therefore, a linear variable differential transformer (LVDT) was set up under the middle of the specimen to measure only the displacement due to the bending of the glass at this point.

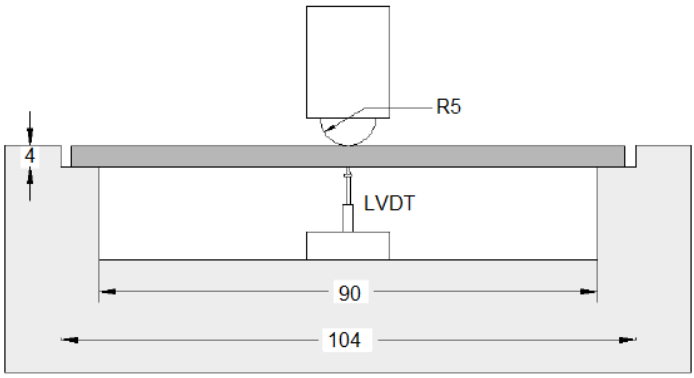

Figure 3-1 Axisymmetrical bending geometry.

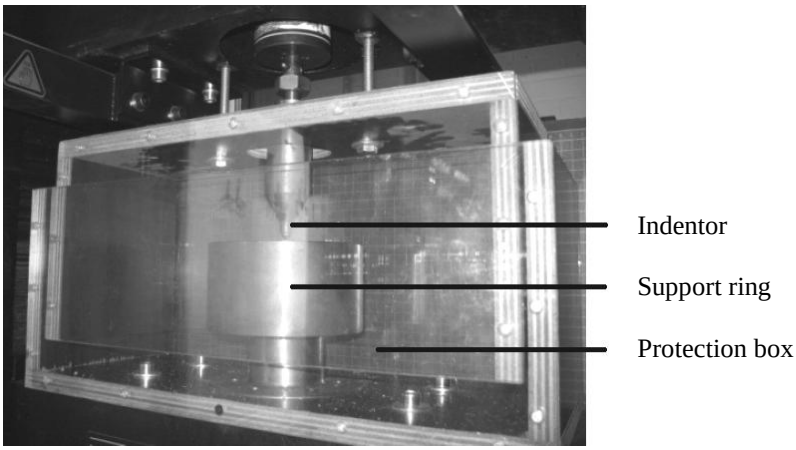

Figure 3-2 Axisymmetrical bending set-up.

3.1.2.c Finite element processing

No analytical solution can be found to relate the force applied to/by the indentor and the stress in the centre of the bottom surface of the glass specimen, directly underneath it. For a detailed study about this, including several methods to try and approximate this solution, the author refers to De Pauw's PhD [26].

Thus, a finite element model of the glass specimen, its supporting ring and the indentor was built in Abaqus/Standard 6.11. Because of the axial symmetry a two-dimensional axisymmetric model could be constructed to save calculation time. The glass was modelled as a pure elastic isotropic material, with the material constants determined as E = 74.18 GPa and ν_{12}= 0.23. Both indentor and supporting ring were modelled as being analytically rigid, because modelling them as deformable steel bodies proved no advantage, resulting only in larger computation times. The geometry is the same as the experimental one (pictured in Figure 3-1), with the addition of a 1 mm chamfer on the bearing line. Between the indentor and glass as well as between the glass and supporting ring, a "hard" normal contact was defined as well as a tangential friction penalty value of 0.5. As for the boundary conditions, the supporting ring is encastred and the horizontal translation and in-plane rotation of the indentor are set to 0. Instead of applying a load on the indentor, a vertical displacement, corresponding to the average value measured over all experiments was imposed. The element used, CAX8, is an 8-node biquadratic axisymmetric quadrilateral element with full integration. A mesh size of 0.39 mm was adopted as

then the results exhibited a good convergence. Near the loading and bearing points, the element size was decreased to 0.078 mm. The model assembly is shown in Figure 3-3.

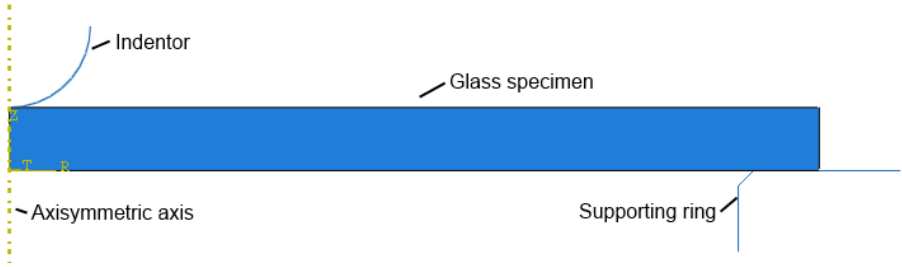

Figure 3-3 Abaqus FE model of axisymmetric bending test.

The outputs of interest are the reaction force in the indentor, maximum principal stress at the bottom centre of the plate (= flexural strength) and the displacement of this point, for comparison with the displacement measured by the LVDT. For a given measured maximum force, the corresponding numerically determined flexural strength and displacement were calculated based on the reaction force obtained at the average displacement in Abaqus. The average difference between calculated and measured displacement is 2.67% (as opposed to an average difference of 17% by De Pauw [26], see also Table 3-1 a bit further), due mainly to the addition of friction between the supporting ring and glass specimen.

The maximum in-plane principal stress along a radial line on the bottom of the specimen is shown in Figure 3-4. For easy comparison, the values are normalized; a mere 2 mm away from the centre, the stress has already dropped by 25%. After 5 mm the values are halved. This helps explain why the critical defect always has to be in close vicinity of the centre of the specimen. Along the bearing line, due to the discrete introduction of reaction forces, a small peak stress occurs, however, it does not affect the results near the middle of the specimen.

In Figure 3-5, a contour plot of the maximal principal stresses in the radial direction (σ_{rr}) is shown. A very high local compression stress occurs beneath the indentor.

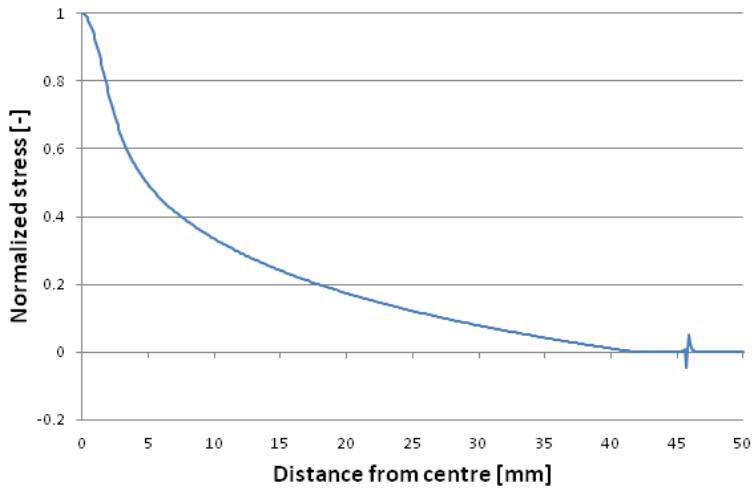

Figure 3-4 **Normalized maximum in-plane principal stress along a radial line on the bottom of the specimen.**

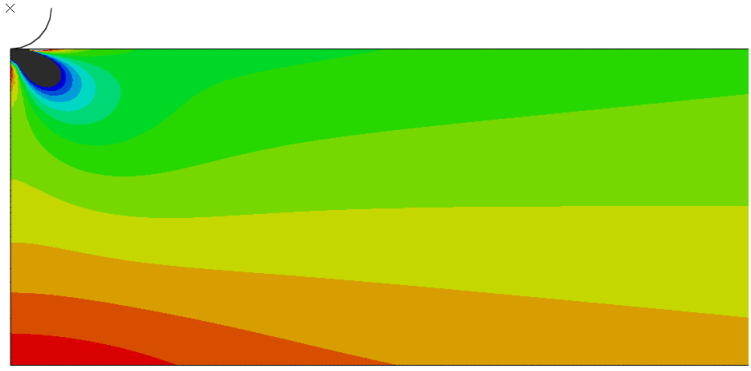

Figure 3-5 **Contour plot of maximal principal stress distribution.**

3.1.2.d Weibull analysis of De Pauw's results

In his PhD study, De Pauw [26] already performed many tests on small circular specimens using this set-up. He presented the results in the following manner:

Table 3-1 Axisymmetric bending test: Abaqus results (reproduced from [26]).

Sample	Flexural strength [MPa]		Max. displacement [mm]	Difference between calculated and measured max. displacement [%]
	mean	stdev	mean	
RC_AS_AS	221	64	0.38	17%
RC_AS_TS	232	46	0.40	19%
RC_TS_AS	111	32	0.19	12%
RC_TS_TS	153	72	0.27	26%
RG_NA_AS	210	80	0.36	11%
RG_NA_TS	172	53	0.30	17%

With RC = raw cut edge finish, RG = roughly ground edge, AS = air side, TS = tin side, NA = not applicable, and with the second letter combination being the cut side and the third the tensioned side.

He concluded that no significant overall influence from the tensioned surface (tin vs. air) could be found and that, by comparing the samples cut on the tin side with the other samples, it is clear that the cutting surface has a major influence. He attributed this to the fact that cutting on the tin side results in cuts which are much more irregular. The influence of the cutting surface position (in tension or compression) was deemed not consistent.

This does suggest that the set-up is not completely edge-independent. Note also the high differences between the measured and numerically calculated displacements. An attempt to improve upon this was made in section 3.1.2.c.

A further attempt by the author to better understand these results was made by presenting the results as Weibull plots. In Figure 3-6 a Weibull plot of all tests is shown. Since the points lie on a straight line, they follow a Weibull distribution.

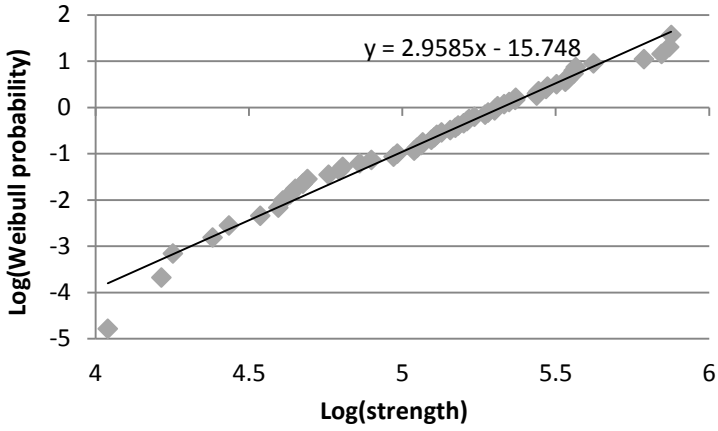

Figure 3-6 Weibull plot of results [26] from De Pauw.

The Weibull parameters are thus:

- m (shape): 2.96
- σ_0 (scale): 204.99

When separating the samples by tensioned side, a subsequent Weibull plot (Figure 3-7) does suggest no difference between the air and tin side. However, the cut side (Figure 3-8) does play an important role, as those Weibull plots differ greatly.

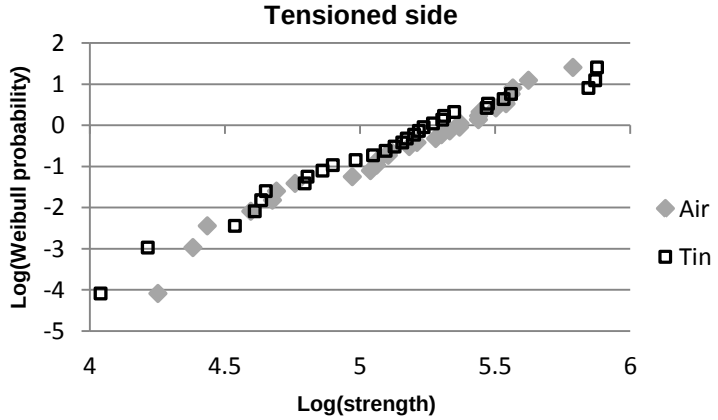

Figure 3-7 Weibull plot divided by tensioned side.

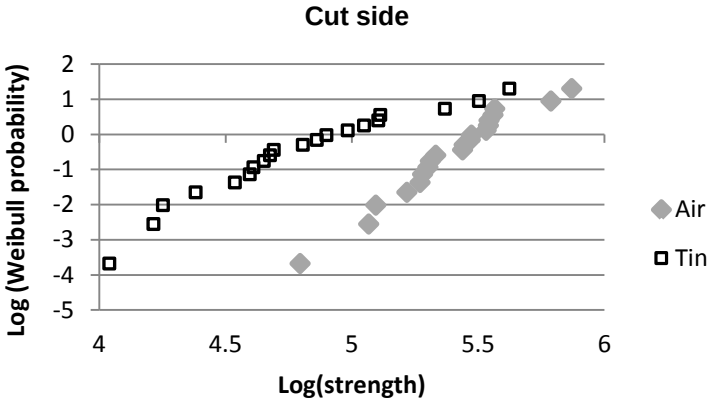

Figure 3-8 **Weibull plot divided by cut side.**

3.1.2.e Second test series

A second test series with four times twenty new specimens was decided upon and *all* tests were filmed with a high-speed camera to check the origin of fracture (centre or edge). It should be noted that, contrary to the samples of De Pauw, there was no visible difference in edge quality between samples cut on the air side and samples cut on the tin side, with both types having the same, *bad* edge quality (similar to the tin cut samples of De Pauw, with jagged edges all around, as in Figure 3-9 on the left below).

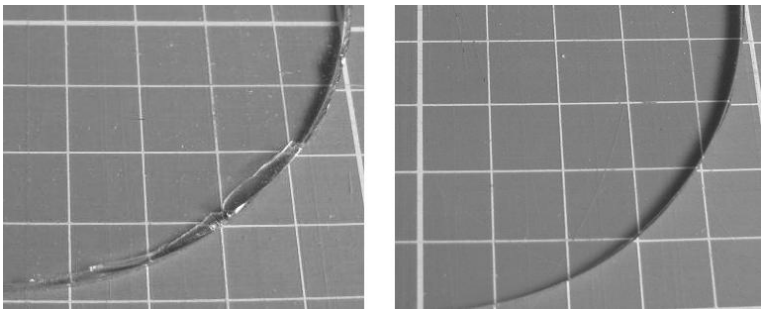

Figure 3-9 **Detail of specimen cut on the tin side (left) and air side (right) (edited from [26]).**

Here it became abundantly clear that there is a difference as apart from two, all tin cut & air side tensioned samples (3rd row Table 3-2) failed from the edge whereas the others all reached high stresses before fracture starting from the middle.

Table 3-2 **Number of specimens failed from the edge during axisymmetrical bending tests.**

Cut side	Tension side	Number of specimens failed from the edge
Air	Air	5/20
Air	Tin	1/20
Tin	Air	18/20
Tin	Tin	3/20

3.1.2.f Conclusions

The second test series, with a high number of failed tests (due to the fracture initiation at the edge of the specimens), seems to suggest that the test set-up is not so edge-independent after all. A Weibull analysis of De Pauw's results suggests the same. However, initial fracture does occur in the centre of the specimens if the edge finishing of the specimens is adequate to withstand the small stresses present there. Much higher fracture stress values (>200 MPa) are then found. This is important for the numerical simulations where glass fracture under impact will often be initiated from the centre of the specimen and the use of standard values will result in fracture happening way too early.

3.2 PVB

The objective of this part is to provide the necessary experimental data to determine the mechanical behaviour of a PVB interlayer and subsequently write a material law which can be used in FEM analysis (by Pelfrene [27]). This will prove to be a key step to enable prediction of forces, energies and ultimate failure of a broken laminated glass panel under a given impact or blast load.

A PVB interlayer, laminated between glass panels and subjected to a dynamic load, will experience a whole range of strain (rates). Along the cracks in the glass, strains and strain rates can be very high – depending on the adhesion level – whereas PVB near the undamaged corners or firmly attached to the middle of a large piece of glass may experience little strain. Ideally, the whole range of strains and strain rates are implemented in one material law.

The test campaign was divided in two parts, due to the constraints imposed by the speed limits of the different mechanical testing machines. The quasi-static and dynamic tests are thus discussed separately.

Samples for both test regimes were identical and are described hereafter. The specimens were cut from a sheet of PVB (type RB41) of thickness 0.76 mm using a metal die. The sample geometry of the PVB specimen is given in Figure 3-10. The checkered area was covered with small cardboard pieces, to ensure proper gripping in the clamping mechanism.

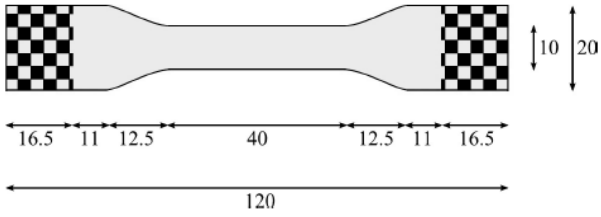

Figure 3-10 Dimensions (in mm) of the PVB samples.

The specimens were stored at room temperature in the laboratory where they were tested. The temperature was measured on the mounted specimen at the start of each test with a Fluke 561 infrared thermometer.

3.2.1 Quasi-static tests

The INSTRON 5800 R tensile testing machine (see also 3.1.2.b) was used for the low-speed tests. The crosshead speeds were predefined as 0.33 and 3.33 mm/s (the latter being the maximum value the machine could attain). In Figure 3-11 the average force-displacement measurements are shown.

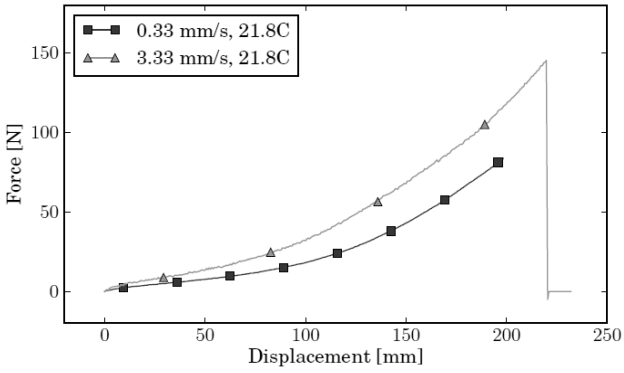

Figure 3-11 Quasi-static tensile test results.

3.2.2 Dynamic tests

A servo-hydraulic tensile testing machine (INSTRON IST Hydropuls) was used for the high-speed tests. Normally, a high-speed tensile test uses a lost-motion device (Figure 3-12 left). The device gives the actuator enough distance to accelerate to the desired test velocity before loading the sample. However, due to the fact that the test machine used here pulls down and not up it is impossible to use a lost-motion device in combination with PVB specimens as they started to stretch under the weight of the lost-motion device. Hence it was omitted. An alternative solution is found in positioning the machine clamps a mere 37 mm apart prior to the test, as opposed to the 87 mm distance between the chequered areas in Figure 3-10. In that position, the flexible interlayer specimen is curled up and experiences no force until it is straightened by a 50 mm downward motion of the crosshead.

All connecting components between the sample and load cells should be kept as light as possible to minimise inertia forces under acceleration. Therefore the PVB specimens are attached directly on one side to the actuator of the machine and on the other side to the load cell, using only small clamping mechanisms (Figure 3-12 right).

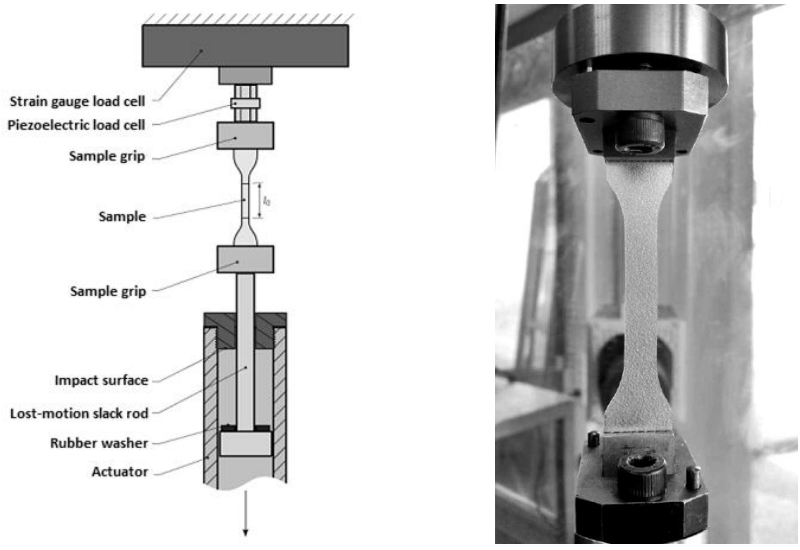

Figure 3-12 **PVB tensile test set-up with actuator cut away (left) & clamped PVB test specimen (right).**

For each speed (0.1, 0.333, 0.5, 3.0 & 10.0 m/s), five specimens were tested. Their force-displacement curves are shown in Figure 3-13, on which the high reproducibility is obvious. Time and displacement are reset to zero after the 50 mm

downward stroke of the lost-motion device to tension the pre-positioned PVB. The force-displacement curves for all high-speed tests approach a bilinear behaviour.

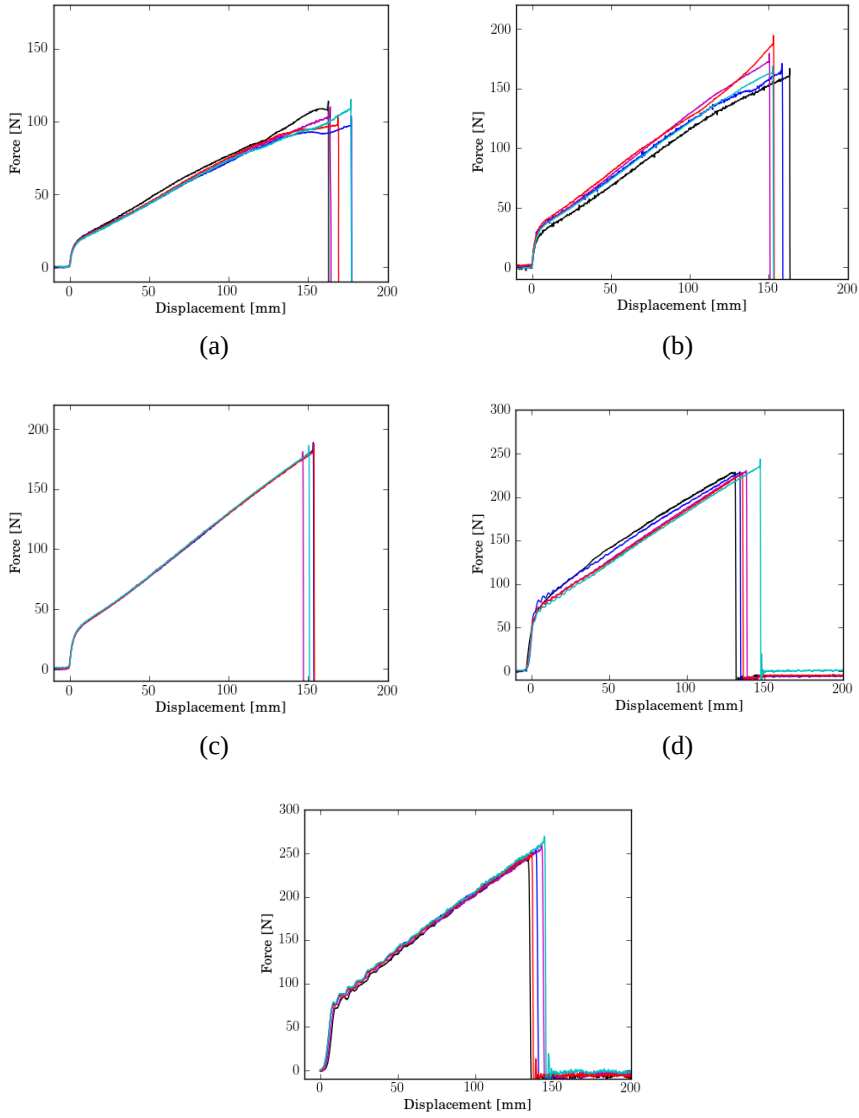

Figure 3-13 **Force displacement curves for (a) 0.1 m/s, (b) 0.333 m/s, (c) 0.5 m/s, (d) 3 m/s, (e) 10 m/s.**

At that point (the end of the 50 mm downward motion), for the testing speeds of 0.1, 0.333 and 0.5 m/s, the actuator has already reached its nominal speed, which

remains approximately constant thereafter (Figure 3-14 (left)). However, for 3.0 and 10.0 m/s, it is seen that the actuator has not accelerated to its nominal velocity yet when the specimen starts to extend. Neither does the actuator speed remain constant for the short duration in which the specimen is strained and tears (Figure 3-14(right)).

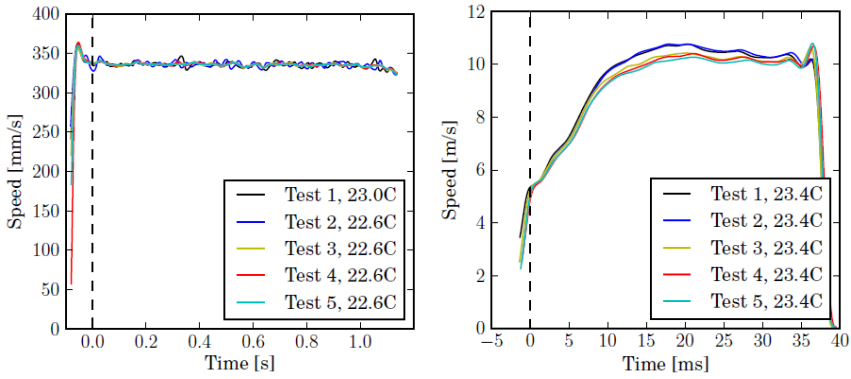

Figure 3-14 **Recorded speed for PVB tensile tests at (left) 0.333 m/s and (right) 10.0 m/s.**

The median of force-displacement responses at every testing speed is shown in Figure 3-15. The raw force data has been processed by a 2nd-order Butterworth filter with cutoff frequency of 2.3 kHz, 7.6 kHz, 11.5 kHz, 69 kHz and 93 kHz for lowest to highest speed respectively.

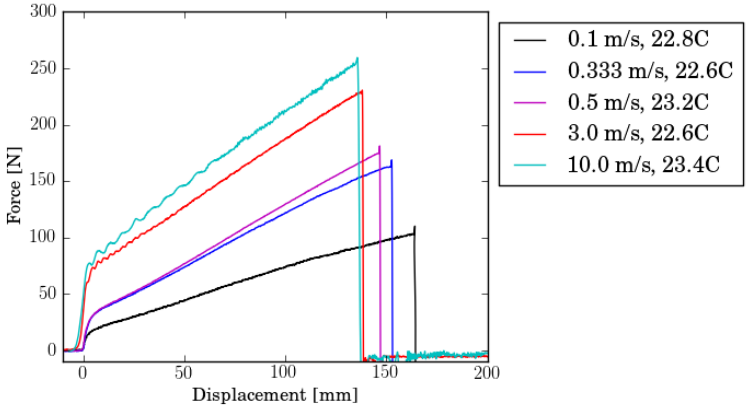

Figure 3-15 **Force-displacement curves for uniaxial tensile tests of PVB at various testing speeds.**

As expected, the material acts stiffer with higher rate of deformation. The extension at failure also decreases with increasing testing speeds.

3.2.3 PVB: Interaction with modelling (Pelfrene [27])

While showing rather complex mechanical behaviour, several simplifications can be made in constitutive modelling (Figure 3-16), depending on the considered load case. The small-strain behaviour of PVB is well captured by linear viscoelasticity, for which the time-temperature superposition principle applies. When the glass breaks under impact or blast, the PVB can locally reach large strains. In that case, the material can be modelled by rate-dependent hyperelasticity, a combination of hyper- and viscoelasticity or the more general viscoplasticity.

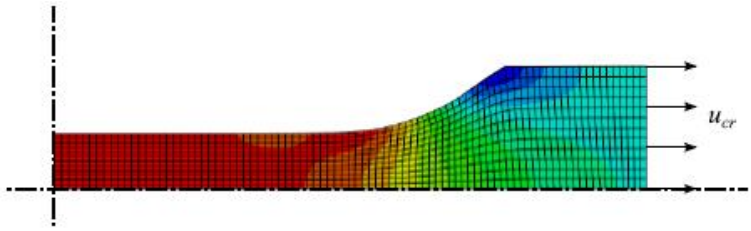

Figure 3-16 **Mesh and boundary conditions for uniaxial tensile test model of PVB specimen; contours of longitudinal stress at 10 mm elongation.**

The combination of a hyperelastic strain energy potential with Prony series for viscoelastic behaviour is used here, under the assumption that the stress-strain behaviour at finite strains can be scaled for different deformation rates by the same generalised Maxwell model as for the small strains.

An iterative simulation procedure has been developed to find the material constants for which a good fit with the experimental results (Figure 3-15) can be established. However, a proper match can only be found when the small-strain modulus of the 20th order polynomial function is allowed to deviate from the instantaneous modulus of D'haene's linear viscoelastic model [28], to which it is coupled. Also, it appears that the simulated behaviour at large strains only provides a good fit with the test data for a limited range of deformation rates. This indicates that it would be more correct to include rate-dependency of the viscous component in the material behaviour.

Finally, a PVB material model is proposed for use in numerical analysis of dynamic events with glass breakage. This material model is calibrated for a mid-range of strain rates, i.e. 0.1 to 10 s^{-1} (Figure 3-17 shows the force-displacement of both experiments and simulations of a tensile test using this model).

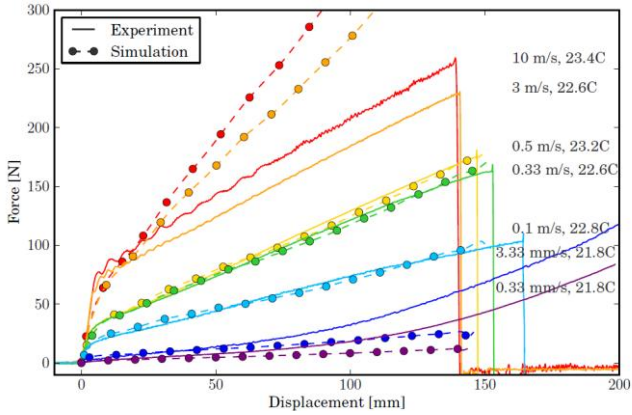

Figure 3-17 **Force vs. displacement for uniaxial tensile tests; simulated results for material model calibrated at 0.5 m/s and 23.2 °C.**

3.3 LAMINATES

This part is divided in three sections: i) an analytical approach to four-point bending, ii) an experimental campaign and iii) a mixed experimental-numerical approach using a resonalyser.

3.3.1 Four-point bending: Hooper's formula

An often appearing example of design for a structural glass unit is four-point bending loading. The general principle of a four-point bending test is shown in Figure 3-18; two equal loads are imposed at a certain equal distance from the bearing points. When the loading span is half the bearing span, the test is referred to as standard four-point loading.

In theory, a constant bending moment or stress is applied between the load introduction points and a linear stress course is applied between the supports and load introduction points. In general, the cantilevered sections left and right of the bearing points of the beams are not considered; the stresses there are assumed to be zero. Both the surface and the edges are subjected to the maximal stresses in the middle section of the beam. The tensile strength – or presence of critical flaws in the case of glass – of both surface and edges will influence the fracture behaviour.

Analytical solutions to the seemingly simple problem of bending of laminated glass are complicated due to the very large difference in stiffness between the outer glass layers and the polymer interlayer, which only transfers shear forces.

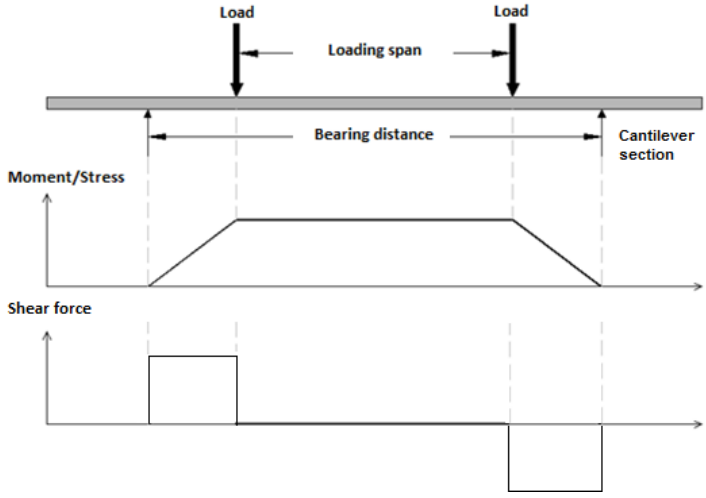

Figure 3-18 Principle four-point bending.

Attempts have been made since the 1970's when Hooper [29] first solved the differential equations for elastic standard four-point bending in a since then often cited article (e.g. [30-34] and in recent years [35, 36]). Indeed, for example Bati *et al.* [37] use the solution as proposed by Hooper to check their experiments and simulations.

Later attempts [38, 39] focused on simplifying the governing equations by ascribing an equivalent thickness to the laminated glass beam or plate, after which subsequent calculations could be performed as if it were for a monolithic beam or plate. Other research ventured in finite element analysis of simplified models to facilitate the solving of the equations.

Hooper only provided the solution for the displacement in the middle of a laminated beam. Because the tensile machine in our lab measures the displacement at the position of the 2 load introduction points, the solution along the full length of the beam is necessary. It was then that a discrepancy was found between our results and Hooper's results.

3.3.1.a Analytical expressions

The governing differential equation for the interfacial shear force, T(x), in a beam with two outer layers of the same material (though not necessarily the same thickness) and a much softer interlayer (see Figure 3-19) subjected to a bending moment M(x), with x = abscissa according to the beam axis, is [40]:

$$\frac{d^2T(x)}{dx^2} - \alpha^2 T(x) + \beta M(x) = 0 \tag{3.1}$$

With:

$$\alpha^2 = \beta\gamma\ell, \quad \beta = \frac{GB\ell}{E_g I t_3}, \quad \gamma = 1 + \frac{A_{tot} I}{A_1 A_2 l^2} \tag{3.2}$$

And:

G	=	Shear modulus of the interlayer [MPa]
E_g	=	Young's modulus of the glass layers [MPa]
B	=	width of the laminate [mm]
t_1,t_2,t_3	=	thickness [mm]
A_{tot}	=	$A_1 + A_2$ (A_1=Bt_1, A_2=Bt_2) [mm^2]
I	=	$I_1 + I_2$ (I_1=$Bt_1^3/12$, I_2=$Bt_2^3/12$) [mm^4]
ℓ	=	$(t_1 + t_2)/2 + t_3$ [mm]

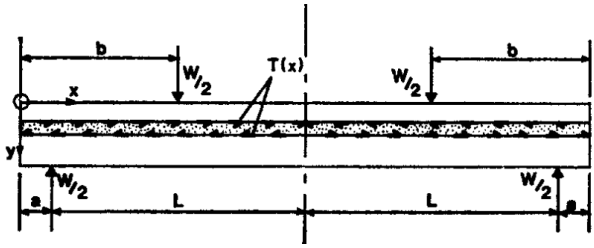

Figure 3-19 Beam parameters [29].

The cantilever ratio η is defined as the cantilever length 'a' divided by half of the bearing span L. A total force W is exerted on the load introduction points.
As the bending moment along the length of the beam is divided into three discrete sections, the solutions also have to be discretized, starting from the left free edge of the beam, with a first section between the free edge and the bearing point (where the moment is zero), a second section between the bearing and loading points (where the moment increases linearly) and a third section between the loading point and middle of the beam (where the moment is constant). Due to symmetry only half of the beam is considered in all following notions.

Hooper deduced an analytical elastic solution comprising the interlayer shear transfer for standard four-point loading. He calculates the deflection of the beam centre point by double integration of the equation:

$$E_g I \frac{d^2y}{dx^2} = -(M(x) - T(x) \cdot l) \tag{3.3}$$

With boundary conditions being y = 0 at the bearing points (x = a) and dy/dx = 0 at the middle of the beam (x = a+L). He then proceeds to give the solution, without any intermediate results:

$$y(L+a) = \frac{11}{96}\frac{WL^3}{E_g I} k_3 \tag{3.4}$$

With:

$$k_3 = 1 - \frac{1}{\gamma} - \frac{48}{11\gamma(\alpha L)^3}\left\{\frac{cosh(\alpha L) - 1}{cosh\big(\alpha L(1+\eta)\big)}\big[sinh(\alpha\eta L) - sinh\big(\alpha L(1+\eta)\big)\big] - \frac{cosh\left(\frac{\alpha L}{2}\right) - 1}{cosh\big(\alpha L(1+\eta)\big)}\left[sinh\left(\alpha L\left(\frac{1}{2}+\eta\right)\right) - sinh\big(\alpha L(1+\eta)\big) - \frac{\alpha L}{2}cosh\left(\alpha L\left(\frac{1}{2}+\eta\right)\right)\right] + sinh(\alpha L) - sinh\left(\frac{\alpha L}{2}\right) - \frac{\alpha L}{2}\right\}$$

However, to know the deflection along the entire length of the beam, intermediate results are necessary. Below, starting from equation (3.3), some intermediate results are given. The constant A is defined as $A = \frac{\cosh(\alpha L) - \cosh\left(\frac{\alpha L}{2}\right)}{\cosh(\alpha(a+L))}$.

First, the curvatures in each section are:

$$K_1 = \frac{W}{2E_g I}\frac{Asinh(\alpha x)}{\alpha\gamma} \tag{3.5}$$

$$K_2 = \frac{W}{2E_g I}\left(\frac{Asinh(\alpha x) + sinh\left(\alpha(a-x)\right)}{\alpha\gamma} + (a-x)\left(1 - \frac{1}{\gamma}\right)\right) \tag{3.6}$$

$$K_3 = \frac{W}{2E_g I}\left(\frac{Asinh(\alpha x) + sinh\big(\alpha(a-x)\big) - sinh\left(\alpha\left(a + \frac{L}{2} - x\right)\right)}{\alpha\gamma} + \frac{L}{2}\left(\frac{1}{\gamma} - 1\right)\right) \tag{3.7}$$

The rotation – the first integrate of equation (3.3) – along the length of the beam can be described by the following three equations (one for each section of the beam, as described above).

$$\theta_1 = \frac{W}{16E_gI}\left(\frac{8}{\alpha^2\gamma}\left\{A\left[cosh(\alpha x) - cosh\left(\alpha(a+L)\right)\right] + cosh(\alpha L) - cosh\left(\frac{\alpha L}{2}\right)\right\} + 3L^2(1 - \frac{1}{\gamma})\right) \tag{3.8}$$

$$\theta_2 = \frac{W}{16E_gI}\left(\frac{8}{\alpha^2\gamma}\left\{A\left[cosh(\alpha x) - cosh\left(\alpha(a+L)\right)\right] + cosh(\alpha L) - cosh\left(\frac{\alpha L}{2}\right) - cosh\left(\alpha(a-x)\right) + 1\right\} + (3L^2 - 4(x-a)^2)\left(1 - \frac{1}{\gamma}\right)\right) \tag{3.9}$$

$$\theta_{3=}\frac{W}{16E_gI}\left(\frac{8}{\alpha^2\gamma}\left\{A\left[cosh(\alpha x) - cosh\left(\alpha(a+L)\right)\right] + cosh(\alpha L) - cosh\left(\frac{\alpha L}{2}\right) - cosh\left(\alpha(a-x)\right) + cosh\left(\alpha\left(a + \frac{L}{2} - x\right)\right)\right\} + 4L(x - a - L)\left(\frac{1}{\gamma} - 1\right)\right) \tag{3.10}$$

The deflection along the length of the beam is:

$$y_1 = \frac{W}{16E_gI}\left(\frac{8}{\alpha^3\gamma}A[sinh(x\alpha) - sinh\,(a\alpha)] + 3L^2\left(\frac{1}{\gamma} - 1\right)(a-x)\right) \tag{3.11}$$

$$y_2 = \frac{W}{16E_gI}\left(\frac{8}{\alpha^3\gamma}\{A[sinh(x\alpha) - sinh\,(a\alpha)] + sinh\left(\alpha(a-x)\right) + \alpha(x-a)\} + \left(\frac{1}{\gamma} - 1\right)\left\{\frac{4}{3}(x-a)^3 + 3L^2(a-x)\right\}\right) \tag{3.12}$$

$$y_3 = \frac{W}{16E_gI}\left(\frac{8}{\alpha^3\gamma}\left\{A[sinh(x\alpha) - sinh\,(a\alpha)] + sinh\left(\alpha(a-x)\right) - sinh\left(\alpha\left(a + \frac{L}{2} - x\right)\right) + \frac{\alpha L}{2}\right\} + 4L\left(\frac{1}{\gamma} - 1\right)\left\{\frac{(x-a)^2}{2} + L(a-x) + \frac{L^2}{24}\right\}\right) \tag{3.13}$$

The deflection in the middle of the beam (x=a+L) is then given by the equation:

$$y^* = \frac{11}{96}\frac{WL^3}{E_g I}k_3 \tag{3.14}$$

With:

$$k_3 = 1 - \frac{1}{\gamma} - \frac{48}{11\gamma(\alpha L)^3}\left[\frac{cosh(\alpha L)}{cosh\big(\alpha L(1+\eta)\big)}\langle sinh(\alpha\eta L) - sinh\big(\alpha L(1+\eta)\big)\rangle - \frac{cosh\left(\frac{\alpha L}{2}\right)}{cosh\big(\alpha L(1+\eta)\big)}\langle sinh(\alpha\eta L) - sinh\big(\alpha L(1+\eta)\big)\rangle + sinh(\alpha L) - sinh\left(\frac{\alpha L}{2}\right) - \frac{\alpha L}{2}\right]$$

Although similar in appearance, some terms differ slightly from the one as derived by Hooper (equation (3.4)). Finite element analysis of the problem (see further) will prove that our results are correct, as opposed to those of Hooper.

The maximum bending stresses along the length of the beam can be calculated using

$$\sigma_{max} = \pm\frac{t_1}{2I}(M - Tl) + \frac{T}{Bt_1} \tag{3.15}$$

A similar expression is found for glass layer 2, by replacing t_1 with t_2.

3.3.1.b Finite Element Analysis

In order to validate the correct solution for the elastic standard four-point bending problem, a two-dimensional finite element model is built in ABAQUS because, in essence, it solves the same differential equations.

The geometry is based on the dimensions of the specimens from the experimental campaign (see further). Non-linear geometry is disabled, as the analytical expressions do not take these into account. A sufficiently small element size is chosen for convergence of the solution, in this case one tenth of the thickness of the individual layers. The load W/2 is placed in a single node at the top of the beam, in order to simulate the discrete load introduction as in the analytical expressions. The rolling support is administered in a likewise manner, at the bottom of the beam. Symmetry conditions in the middle of the beam are applied to reduce calculation time. Quadratic elements with reduced integration were used.

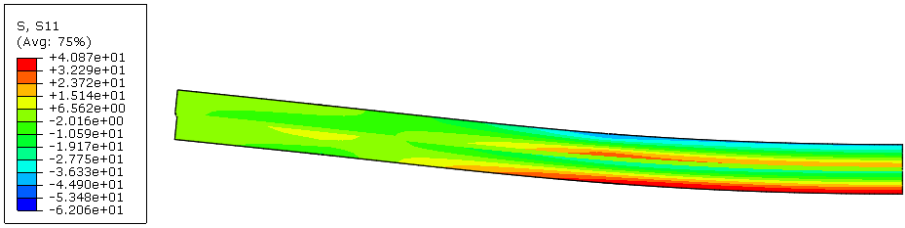

Figure 3-20 **Stress distribution of Abaqus simulation of laminated glass beam subjected to four-point bending (deformation factor = 5).**

For all results, the displacement and rotation along the length of the beam were extracted from the numerical simulations along the middle of the interlayer. When compared to the deflection at the top and bottom of the beam, only small discrepancies of maximum 0.4% were found, which occurred at the point of load introduction, with an average deviation of only 0.08% at a force of 500 N and displacement in the centre of the beam of 0.75 mm.

In Figure 3-21, the deflection, rotation and curvature along the length of the beam are shown, both analytically (using Equation (3.14) as deduced in this chapter) and numerically calculated, with a PVB shear modulus of 10 MPa and a load W of 500 N. The solution of Hooper for the deflection in the middle of the beam (equation (3.4)) is also indicated with a single red cross in the top figure. The numerical rotation and curvature are calculated with a central first order differentiation formula.

One can see there is a very good agreement between our analytical and numerical results, both for the rotation and deflection. Hooper's analytical expression underestimates the deflection in the middle of the beam.

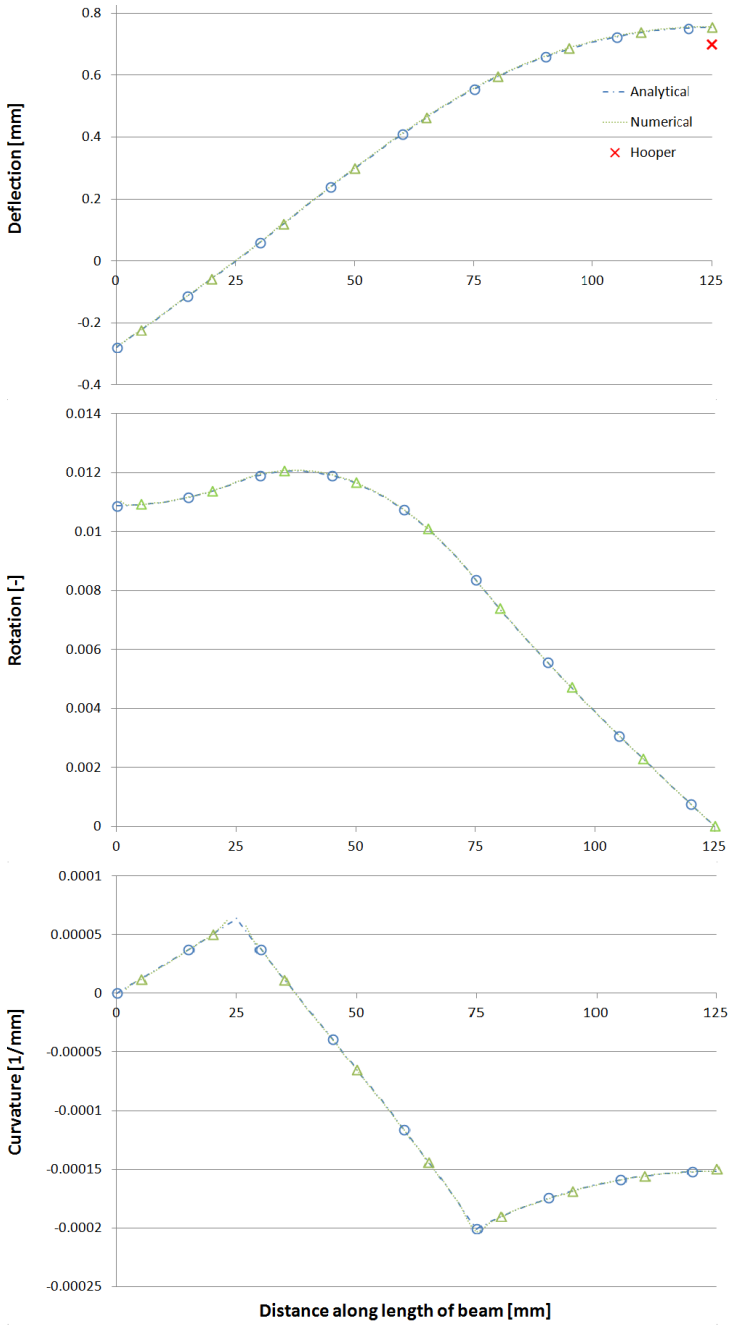

Figure 3-21 **Deflection, rotation and curvature of laminated glass beam subjected to four-point bending; analytical, numerical and Hooper's results.**

In Figure 3-22, the deflection in the middle of the beam is shown for a varying cantilever length, for the two used glass thicknesses, 2 mm (right axis) and 4 mm (left axis). Again, there is a very good agreement between our solution of the differential equations and the numerical simulations, whereas the solution as proposed by Hooper underestimates the deflection.

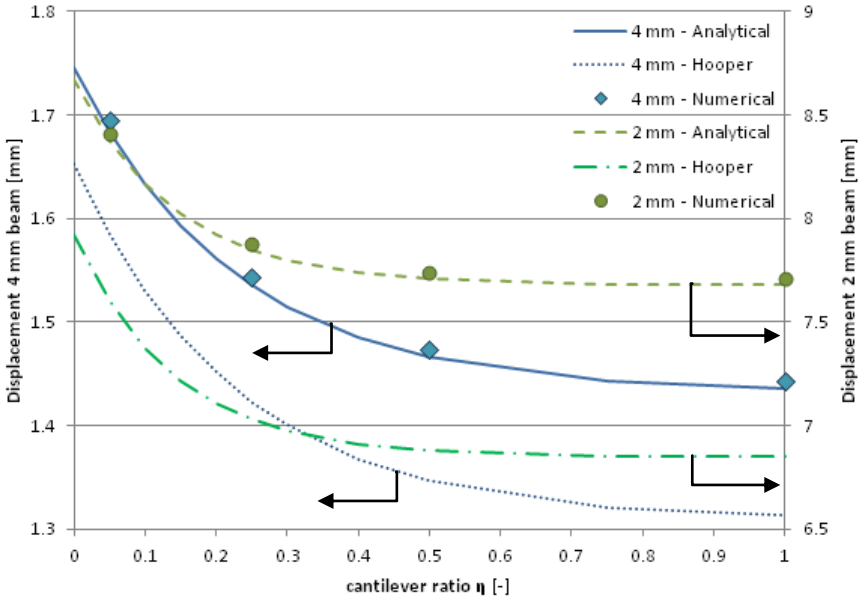

Figure 3-22 Comparison analytical, numerical and Hooper for 2 and 4 mm beam.

One can also clearly see that from a value of about 0.5 for the cantilever ratio η, the displacement reaches an asymptotic value. This happens more pronounced for the thinner samples.

When looking at the simulated stresses along the bottom of the beam, a deviation from the theoretical piecewise linear and constant stress distribution is found. Figure 3-23 shows the stress (maximum principal stress) distribution along the length of the beam for half a specimen with a force of 500 N. The results of elastic beam theory were calculated using the formula:

$$\sigma = \frac{Mz}{I'} \tag{3.16}$$

With z the vertical distance between the neutral axis and utmost edge of the glass beam, in this case equal to half the interlayer thickness plus the thickness of one glass ply; the moment follows from the moment distribution of a standard four-point

bending as depicted in Figure 3-23 (with M= WL/4 in the constant middle section). The analytical stresses are calculated using equation (3.15).

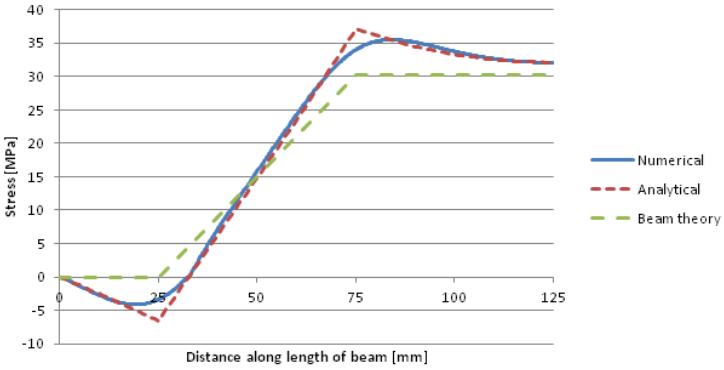

Figure 3-23 Calculated and modelled stresses along length of the beam.

In contrast with elastic beam theory, the stresses along the cantilever section of the beam are not zero, as is shown both by the analytical and numerical solutions. After reaching a minimum compressive stress at the bearing point, it only drops to zero, following a linear course, at the free end of the cantilevered beam.

Furthermore, the stress is not constant between the loading points. After reaching a maximum at the load introduction points, it decreases towards the middle of the beam. The decrease can be approximated by a parabola. This can explain why fractures are not uniformly distributed between the loading points, but have the tendency to be closer to one of the load introduction points.

However, for a monolithic beam, the simulated stress distribution does correspond to the theoretical bi-linear solution except for a smooth rather than abrupt transition between the three sections, although this transition zone is very limited in length.

To validate these observations concerning the stress distribution, several specimens with length 300 mm were equipped with strain gauges at 3 locations. These were positioned on the compressed glass ply (i) at the middle of the beam, (ii) opposite a bearing line and (iii) at the beginning of a cantilever section. The calculated strain in the cantilever section (using equation (3.15)) for a force of 350 N amounts to 83.16 με whereas the measured strain was on average 76.51 με, both in tension. According to the elastic beam theory, these strains should be zero, as is the case for a monolithic beam. The compressive strains in the middle of the span had an error of only 1.8% (417.3 με analytically vs. 424.7 με measured at a force of 350 N).

3.3.2 Four-point bending: Experimental campaign

3.3.2.a Test set-up

The tests follow the instructions as provided by the American standard ASTM C 158-02 (see also 3.1.1.a), concerning specimen and set-up geometry. Both the European and American standards prescribe a loading rate in function of applied stress, but since the stresses of laminated glass are highly dependent on the temperature-dependent properties of the polymer interlayer, the choice was made to perform all tests at the standard loading rate of 2 mm/min. Some tests are also performed at a higher 10 mm/min. All tests were performed on an Instron 5800R tensile testing machine with Fast Track controller and a 10 kN-range load cell. All data (force and displacement at load introduction points) was measured at the same time base of 20 Hz.

In Figure 3-24 a schematic for the set-up is shown. Note that the specimens are tested "upsidedown". The loading edges are cylindrical with a 5 mm radius and are below the specimen; the bearing edges have a tilted surface with a round contact point (radius 2 mm). A picture of the set-up is shown in Figure 3-25.

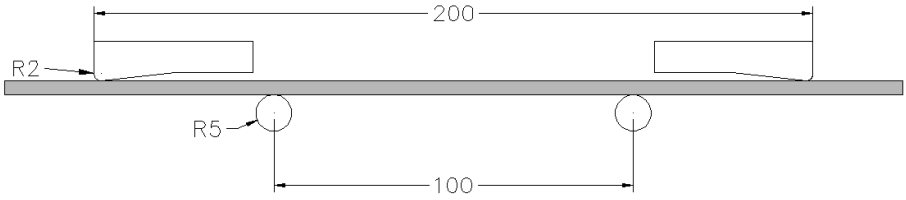

Figure 3-24 Test set-up four-point bending.

As all equations mentioned in the previous section deal with the elastic behaviour of laminated glass, the parameter of highest interest will be the bending stiffness of the laminate. It is calculated as the slope of the force-displacement curve between a low force threshold value (30 N) and the force at fracture (typically at around 500 N).

The value of the shear modulus of the PVB interlayer can be deduced in the following manner. When comparing the slopes of the force-displacement curves for different cantilever lengths, the value can be back calculated so that the averages of both theoretical and experimental slopes coincide. This can be done for both the samples with 2 and 4 mm glass thickness. With the value known, specimens equipped with strain gauges can be used to validate the stress formulations.

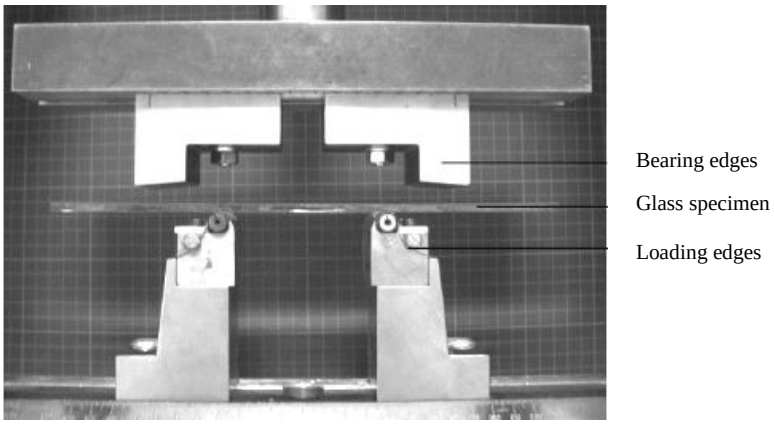

Figure 3-25 Four-point bending set-up.

3.3.2.b Materials

A total of 20 different sample series are tested, an overview is given in Table 3-3. The reference series is F4. All other series are different in one parameter compared to this series, to determine their influence:

- Cantilever length
- Glass thickness
- PVB thickness
- Adhesion level
- Loading rate

The glass with thickness of 2 and 4 mm was mechanically cut; the 6 mm glass pieces were cut by hand using a diamond wheel cutter. The series F11 to F22 were designed to investigate the influence of the cantilever length. However, due to a miscommunication to the supplier, the series F18 to F22 were erroneously made with 2 mm glass instead of 4 mm glass, impeding mutual comparison.

During testing the temperature varied between 20 and 23°C. The relative humidity was at 50-60% for series F0 to F13 and 30-40% for series F18 to F23.

Table 3-3 Overview test series four-point bending.

Series	Dimensions [mm]	Glass [mm]	PVB [mm]	Adhesion	Loading rate [mm/min]	Nr.
F0	250x38.1	4	-	-	2	5
F1	250x38.1	2	0.76	A	2	5
F2	250x38.1	2	1.52	A	2	5
F3	250x38.1	4	0.76	A	10	5
F4	**250x38.1**	**4**	**0.76**	**A**	**2**	**9**
F5	250x38.1	4	0.76	C	10	5
F6	250x38.1	4	0.76	C	2	5
F7	250x38.1	4	1.52	A	10	5
F8	250x38.1	4	1.52	A	2	5
F9	250x38.1	6	0.76	A	2	5
F10	250x38.1	6	1.52	A	2	5
F11	300x38.1	4	0.76	A	2	3
F12	350x38.1	4	0.76	A	2	3
F13	400x38.1	4	0.76	A	2	3
F18	210x43	2	0.76	A	2	5
F19	220x43	2	0.76	A	2	5
F20	230x43	2	0.76	A	2	5
F21	240x43	2	0.76	A	2	5
F22	250x43	2	0.76	A	2	10
F23	250x38.1	2	0.76	A	2	10

3.3.2.c Results & discussion

Monolithic glass

As mentioned in 3.1.1.b the results of the monolithic glass are incorporated here. The cut side was tested in compression. The force at fracture and subsequently calculated stress are given in Table 3-4.

These results once again prove how much scatter can occur on the failure stress of soda-lime-silica glass.

Table 3-4 Four-point bending failure stress (monolithic glass, series F0).

Specimen	Force [N]	Stress [Mpa]
1	161.53	42.67
2	220.95	57.90
3	137.82	36.58
4	388.11	102.00
5	312.75	82.80
Average	244.24	64.39
St. Dev.	105.00	27.57

Cantilever length

From Hooper's (corrected) formula, it can be deduced that the cantilever length of a laminated glass beam has an influence on the deflection in a four-point bending test. A higher cantilever length results in a smaller deflection for an identical force. A first test series (F4, F11-F13) was performed which had a nominal glass thickness of 4 mm. The length varied between 250 and 400 mm (which was the maximum due to the limited space between the columns of the tensile testing machine). The calculated slope for each series is presented in Figure 3-26.

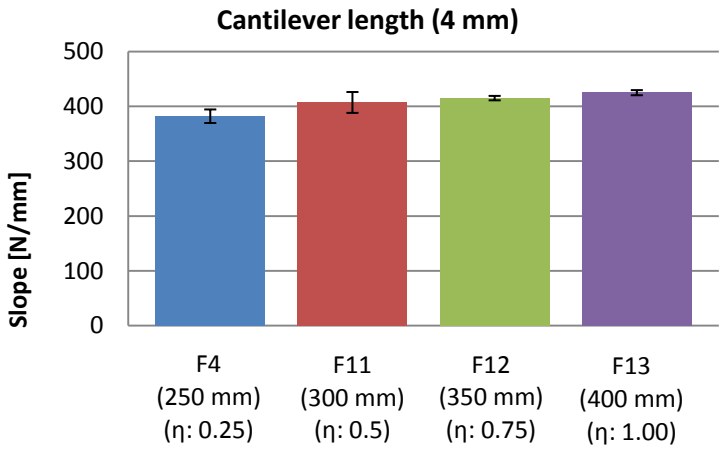

Figure 3-26 Slope for varying cantilever length beams (4 mm).

The slope clearly increases for an increased cantilever length. The effect, however, is quite small, due to the relatively high cantilever factor η. The lowest factor for the tests is 0.25, whereas the effects already diminish from about 0.3. Therefore a second test series (F18-F22) is performed where the factor varies between 0.05 and 0.25 (Figure 3-27). Their length varies between 210 and 250 mm.

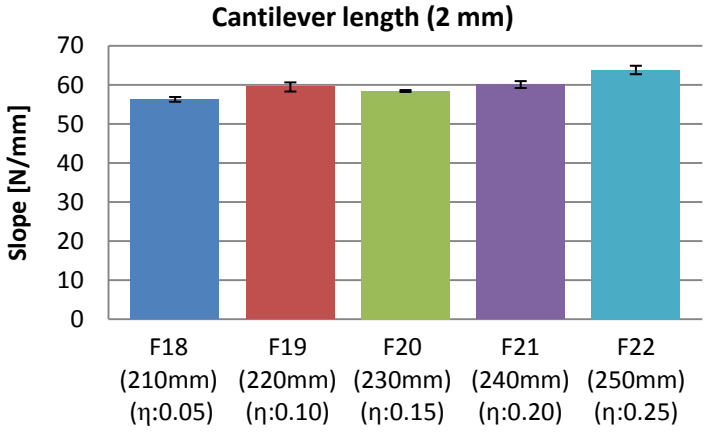

Figure 3-27 Slope for varying cantilever length beams (2 mm).

The difference between the samples with the lowest η factor and the highest is 13.4%. Thus, the cantilever length should always be specified when performing bending tests on laminated glass.

Glass thickness, PVB layers, Adhesion level, Loading rate

The results of the other parameters under investigation are only briefly summarized.

Increasing the glass thickness evidently increases the laminate's stiffness. Fracture stress, however, remains nearly the same. The exact values are difficult to calculate, as these depend on the interlayer stiffness. But since there is a large difference in duration of the loading (around 60 s for 2 mm glass, and only 20 s for 6 mm glass laminates), this also has an effect on the interlayer's shear modulus and thus load transfer.

Doubling the PVB thickness from 0.76 to 1.52 mm only results in a 7% decrease of laminate stiffness.

No difference whatsoever is noted between samples with a high adhesion level (F4) and a low level (F6), as is to be expected. The difference in adhesion only comes into play after breakage.

Increasing the loading rate from 2 to 10 mm/min results in a 9% increase in laminate stiffness, due to the higher interlayer modulus for shorter loads, and a 19% increase of glass fracture stress, which also corresponds with the theory.

3.3.2.d Conclusions

The cantilever length dependency on the deflection for a given force, as is shown by the analytical formulas, is clearly present. This should thus always be specified when testing laminated glass. Glass failure strength shows a very large scatter.

3.4 INTERFACE

Different methods are used in the industry to assess the adhesive bond between PVB and glass. Each method has its own advantages and shortcomings; these methods are the Pummel test [41], peel test [42], Compressive Shear Test (CST) [43, 44] and Through-Cracked Tension test (TCT test).

For a description of the Pummel and Compressive Shear Test the author refers to Chapter 2. The peel test and TCT test, as well as pull-off tests, are described hereafter.

3.4.1 Peel test

For completeness, a description of the peel test, although not performed in this study by the author himself, is given, as it was used so extensively for determining the adhesion levels of all test samples made in the Eastman laboratory in this research and in the numerical work of Pelfrene [45].

The experimental setup for the peel test is installed at the Eastman production plant where it is used daily for quality control of the produced Saflex® interlayers. The test specimens consist of PVB laminated on one side to the glass substrate. A thin layer of the soft aluminium alloy AL1145-O is glued to the free surface of the PVB. The aluminium acts as a stiff backing foil to avoid large longitudinal stretching and attain steady state. A crack is made along the width of the glass to clamp the peel arm between the grips of a Instron 5564 tensile test machine, as in Figure 3-28. The substrate is held fixed to a trolley on the testing device.

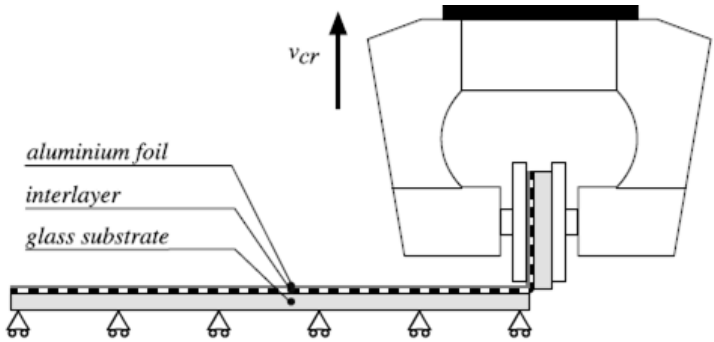

Figure 3-28 Concept drawing of the peel test set-up (reproduced from [27]).

Because PVB is highly sensitive to environmental conditions, the test room is kept at a temperature of 23 ± 2 °C and humidity in the room is controlled. During the test, the peel arm is moved upwards at constant crosshead speed v_{cr} = 127 mm/min while the trolley makes a horizontal movement accordingly as the adherend is peeled off. Meanwhile, the pulling force is measured.

The dimensions of the substrate are 40 x 115 mm. The thickness for each layer is: 2 mm for the glass, 0.76 mm (30 mil) for the PVB and 0.13 mm (5 mil) for the aluminium. A picture of the actual set-up is shown in Figure 3-29.

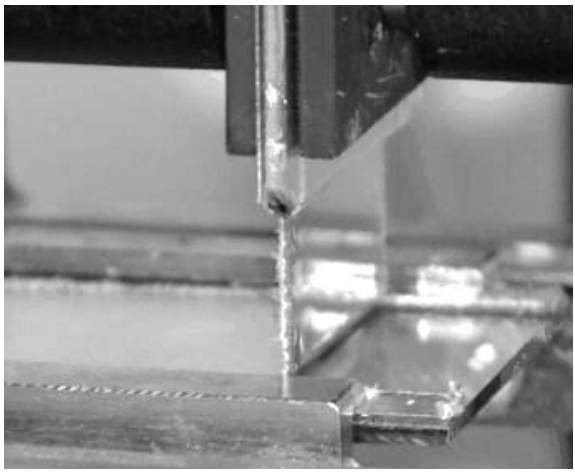

Figure 3-29 Close-up of peel test.

The measured peel forces for low and medium adhesion PVB foils are 2650 ± 50 N/m and 3575 ± 70 N/m in steady state peeling.

The aluminium backing foil, however, was tested in this study, using the Instron 5800 R tensile testing machine (see Figure 3-30). Its exact plastic behaviour proved very important for the FEA models. It is seen that the initial, elastic, stage is characterised by a Young's modulus of 69 GPa, common for all aluminium alloys. At a stress of 30 MPa, a clear yielding point is observed, initiating the plastic hardening phase.

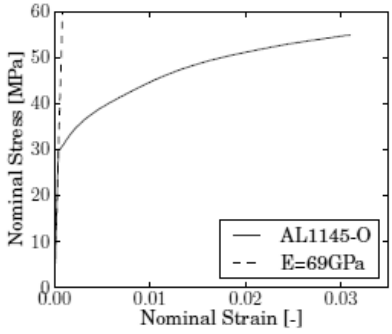

Figure 3-30 **Stress-strain curve of AL1145-O, obtained by tensile test on backing foil sample.**

3.4.2 Through-Cracked-Tension test

3.4.2.a Introduction

The TCT test was first coined by Sha et al. [46], who called it a tension adhesion test and proposed it as an alternative for the peel and pummel test. The TCT test has advantages over the other tests as it is not subjective, such as the Pummel test; it is not prone to cohesive failure, such as the Compressive Shear Test and it fails in mode II rather than mode I (as the peel test does) and thereby adheres closer to the reality of impact behaviour of laminated glass. Therefore, the through-cracked tension test is being more commonly used as a means to study the post-destructive behaviour of laminated glass [47-54].

However, due to their simplicity and convenience, the peel and pummel test are still the most common tests in industry, despite their inability to directly measure the debonding energy.

Figure 3-31 gives a schematic overview of the principle of a TCT test. Each specimen consists out of 2 glass panes with thickness h_g bonded together by an

interlayer with thickness 2h. The length of the specimen is 2L and its width is denoted b. Both dimensions are large in comparison to the interlayer thickness.

The glass panes are cracked in the middle of the specimen, perpendicular to the direction of the applied tensile force P, which coincides with the length direction of the specimen. Both halves are thus only bridged by the interlayer, which transfers all the energy. When both halves separate, an opening 2δ appears between both. Simultaneously the interlayer will start to delaminate from the glass. The length over which the interlayer delaminates, is denoted 'a'.

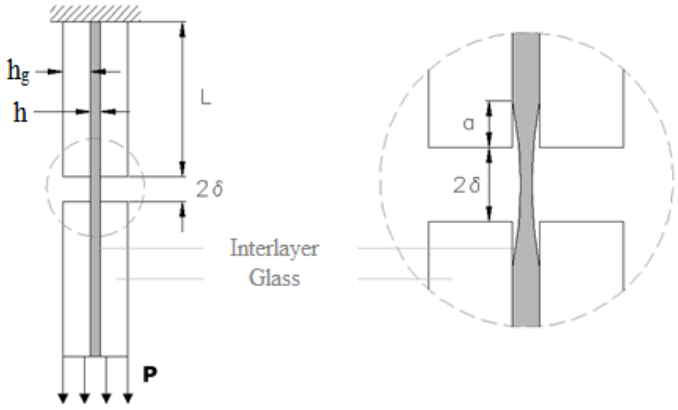

Figure 3-31 Schematic of a TCT test.

The nominal strain in the interlayer can be deduced as:

$$\varepsilon = \delta / a \tag{3.17}$$

Depending on specimen geometry, interlayer properties and loading conditions, a steady state may occur where the exerted force remains constant and the delamination and displacement are proportional to each other, resulting in a constant strain in the interlayer.

The macroscopic energy balance describes that the work done by the steady state force P_0 is used to deform and delaminate the interlayer. Suppose the interlayer delaminates a small distance 'da' when a small external displacement of dδ is applied to it. Assuming dW^e is the total elastic work stored in the interlayer and $b\Gamma_0 da$ is the energy released due to the formation of a new crack surface, with Γ_0 the fracture energy, the energy balance becomes:

$$P_0 d\delta = dW^e + b\Gamma_0 da \tag{3.18}$$

The strain energy stored in the interlayer can be rewritten as $dW^e = U(\varepsilon_0)bhda$, with $U(\varepsilon_0)$ the elastic strain energy density, and furthermore $d\delta = \varepsilon da$. Equation (3.18) then becomes:

$$P_0 = b(2\Gamma_0 E' h)^{1/2} \tag{3.19}$$

With the plain strain modulus $E' = E/(1-\nu^2)$. Thus, the fracture energy Γ_0 can be calculated by measuring the steady state force and strain during an experiment.

In the pioneering paper by Sha et al. [46], specimens with varying adhesion level, determined by the pummel test, were subjected to a very slow displacement rate ($8.47\ 10^{-6}$ m/s). However, no steady state occurred. In their research, they model the deformation and debonding of the interface using a cohesive zone model. The value of the fracture energy is estimated at 295, 154 and 104 Jm^{-2} for a high, medium and low level of adhesion respectively.

Muralidhar [47] report values for the interfacial adhesion between 280 – 930 Jm^{-2}. Nhamoinesu et al. [52] conducted experiments on samples with varying interlayer thickness at different extension rates. Comparing the curves, one finds that the steady state force is larger for a thicker interlayer and for a faster extension rate, although the influence of the latter on the steady state force is rather small. The initial stiffness that is reached before the steady state, is larger at a fast extension rate. Treating the data as one from a hyperelastic material and using a Compressive Shear Test, Jagota et al. [44] found values for the interface toughness in the range of 100 – 500 J/m^2.

3.4.2.b Experimental campaign

Specimens were clamped between screw side-action grips (Instron type 2710-116) and tested in an Instron 5800R tensile testing machine, which records the loading force and displacement of the crosshead. To avoid stress concentrations at the point of load introduction, aluminium plates are glued to the specimens.

The samples had a varying interlayer thickness and adhesion, raw cut edges and a length of 250 mm, to have a sufficient area for both the Digital Image Correlation (DIC, see Appendix A) speckle pattern and a view of the delamination front. Here, the technique is used to take into account possible slipping of the specimens in the grips, which would result in an overestimation of the displacement by the tensile testing machine. Thus, the test is filmed with a digital CCD camera (type Stingray from AlliedVision), placed perpendicular to the specimen. Two Dedocool spots, both 250 W, illuminate the specimen for optimal contrast between

the speckles. The complete set-up and a close-up of a specimen with speckle pattern are illustrated in Figure 3-32.

In order to perform a good TCT test, both glass plies have to be fractured without damaging the interlayer and both cracks have to be in the same plane. Applying the aluminium tabs, manually scoring the glass with a diamond wheel cutter and subsequently tapping the glass gently with a rubber hammer proved to be a good method (see Figure 3-33).

Figure 3-32 **TCT test set-up including CCD camera and lighting (left) and clamped TCT specimen (right).**

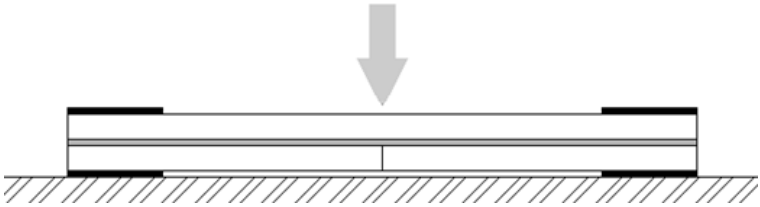

Figure 3-33 **Introducing the pre-crack by tapping the opposite glass ply after scoring it with a diamond wheel cutter.**

An overview of the samples is given in Table 3-5.

Table 3-5 Overview TCT samples.

Sample	PVB [mm]	Adhesion	Extension rate v_{cr} [mm/min]	Specimens
T1	0.76	High	5	4
T2	0.76	High	25	4
T3	0.76	High	125	4
T4	0.76	Low	5	4
T5	0.76	Low	25	4
T6	0.76	Low	125	4
T7	1.52	High	5	9
T8	1.52	High	25	9
T9	1.52	High	125	9
T10	1.52	Low	5	9
T11	1.52	Low	25	9
T12	1.52	Low	125	9

Recording and post-processing of the DIC images was done with the software platform MatchID [55]. For the highest loading rate, 125 mm/min, an image was taken every 200 ms; for all the other speeds an image was taken every 500 ms. Testing conditions varied between 20 – 22 ^{o}C and 29 – 33 % relative humidity.

The actual displacement is calculated by subtracting the displacement of the upper half of the laminate (which is fixed to the load cell) from the displacement of the lower half of the laminate, which is fixed to the moving crosshead of the tensile testing machine.

In order to calculate the strain in the interlayer and investigate the delamination behaviour in detail, the images of each test, used in first instance for the DIC measurements, undergo image post-processing to obtain the necessary data. A Matlab routine, based on one developed by Delincé *et al.* [53] automates this process using edge detection techniques (see Figure 3-34).

First, the vertical glass edges are detected. The opening 2δ between the two glass halves is detected next, although a more accurate value for this was already found with the DIC technique. It is, however, useful for calculating the degree of contraction of the interlayer. Finally, the delamination front is detected. The delamination length 2a is calculated using the median of the delamination front.

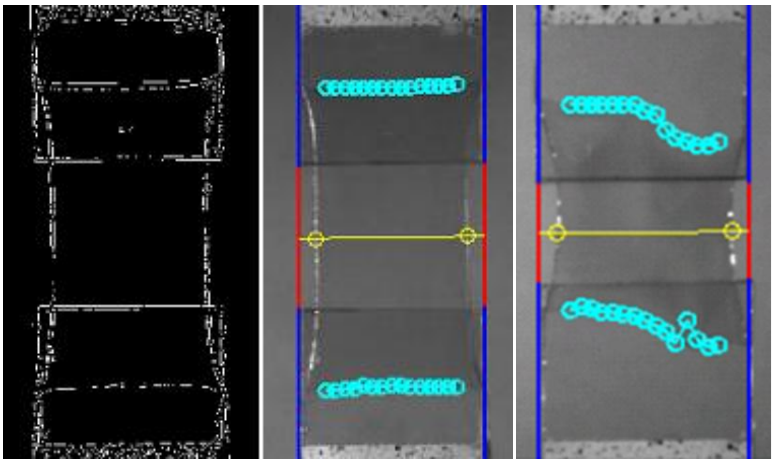

Figure 3-34 **Edge and delamination detection (left), processed image with straight delamination front (middle) and irregular delamination front (right).**

3.4.2.c Results & discussion

The displacement rate has a large influence on the shape of the force-displacement curve. Whereas the high and medium displacement rate result in a steady-state force, the tests conducted at the lowest rate (5 mm/min) do not attain such a steady-state. A comparison with representative specimens is given in Figure 3-35. At the lowest speed, oscillations of the force occur. The sudden increase in force at the end for the fast rate example is due to the delamination front reaching the grips.

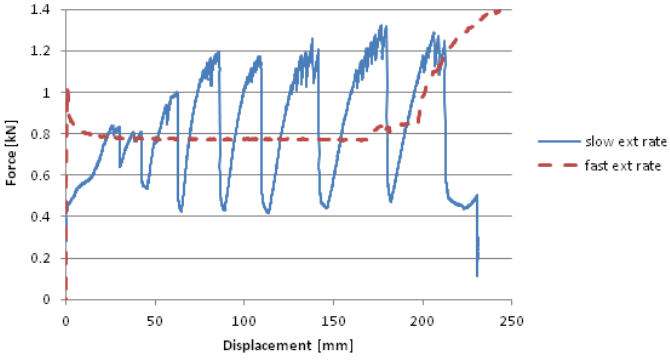

Figure 3-35 **Typical force-displacement curve for slowest and fastest extension rate (low adhesion, 1.52 mm interlayer).**

Figure 3-36 shows force measurements for specimens with a thick, low adhesion interlayer loaded at 25mm/min. All force vs. displacement curves in this figure reach a steady state at some point for which constant force is measured before ultimately tearing.

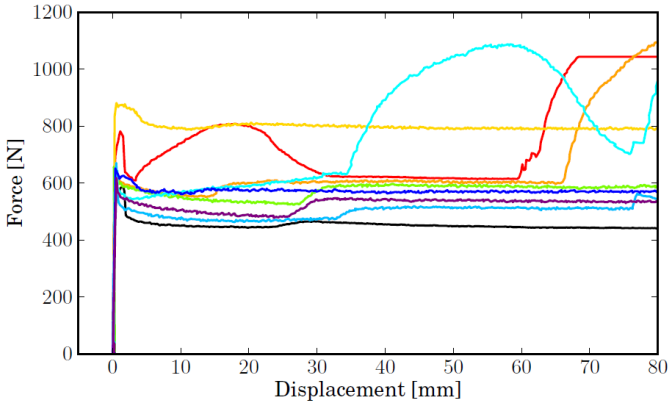

Figure 3-36 **Force vs. displacement for TCT test with 1.52 mm RC interlayer at extension rate of 25 mm/min.**

The steady-state force P_{ss} (if present), strain ε_{ss} and delamination rate $\frac{da}{dt}\Big|_{ss}$ are given in Table 3-6 for all tests conducted at 25 and 125 mm/min. When comparing the steady-state force, it is clear that the adhesion level has a rather small influence on it. Although in the peel test results, the force measured for Mode I debonding is 30% lower for the low level of adhesion, the difference between the steady state force for a high and low level of adhesion is on average only 3.1% in the TCT test. The interlayer thickness has a larger influence, increasing the steady state force with 54.2% when the thickness doubles.

The reader is reminded that RA and RC are the high and low adhesion grade PVB, respectively.

The difference in adhesion level is most visible when comparing the tearing behaviour (see Figure 3-37). The force at which tearing of the interlayer begins $P_{f,start}$, is on average 60% higher for specimens with a low level of adhesion. The difference is most pronounced at the medium displacement rate. No values are given at the fastest rate, because there the delamination front would reach the grips before tearing of the interlayer commenced.

Table 3-6 **Results for steady state in TCT tests on laminated glass with PVB interlayer. First column, between brackets: number of specimens showing steady state delamination.**

Adhesion	t_{PVB} [mm]	v_{cr} [mm/min]	P_{ss} [N]	ε_{ss} [-]	$\left.\frac{da}{dt}\right\|_{ss}$ [mm/min]
RA (2)	0.76	25	419±48	1.11±0.13	7.5±0.5
RA (2)	0.76	125	441±16	1.22±0.06	44±2
RA (3)	1.52	25	571±113	1.09±0.01	8.0±2.0
RA (6)	1.52	125	718±61	1.24±0.02	45±3
RC (1)	0.76	25	394	1.12	10.0
RC (4)	0.76	125	415±30	1.10±0.06	54±12
RC (9)	1.52	25	570±102	0.97±0.03	9.5±3.0
RC (8)	1.52	125	715±130	1.04±0.03	62±9

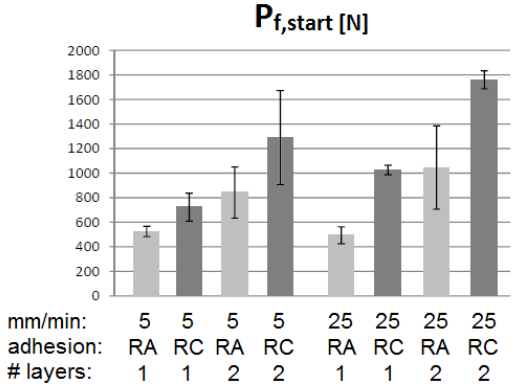

Figure 3-37 **Force at start of tearing.**

The difference between adhesion levels is also visible with the naked eye, as the low adhesion PVB turns to an opaque white colour instantly, whereas the high adhesion PVB only changes from transparent to opaque after a large displacement of about 200 mm. Moreover, at low displacement rate, the interlayer with high adhesion level will exhibit transparent and milky white patches (see Figure 3-38).

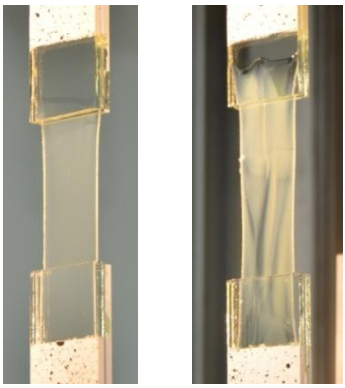

Figure 3-38 **Difference in behaviour for (left) low adhesion specimen and (right) high adhesion specimen.**

For the fastest extension rate, the delamination length in the steady state follows a linear course. Here, the adhesion level is discerned most clearly. Whereas for a low adhesion level the delamination rate, determined as the slope of the linear delamination history, is almost equal to the extension rate, for a high adhesion level it is about 30% lower. The difference between the two is more pronounced for a thicker interlayer (see Figure 3-39).

The strain in the steady state, as calculated with equation (3.17) based on the delamination and displacement found through the image post-processing, is higher for a higher adhesion level. Representative strain histories for four different samples at the fastest displacement rate are presented in Figure 3-40. When looking at equation (3.17), it is obvious that when the delamination length is shorter, as is the case for a higher adhesion level, the strain in the interlayer will be higher for the same opening between the glass halves. Despite the quasi-constant force, the strains do deviate a bit from a perfect constant value, rising until the end of the test.

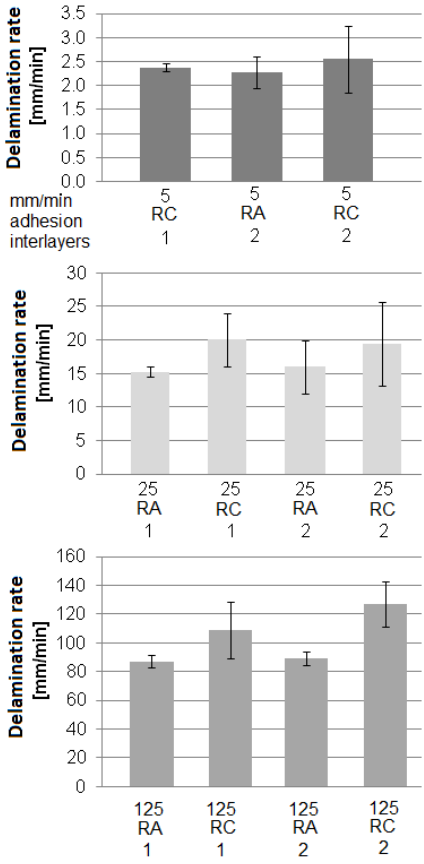

Figure 3-39 **Delamination rate as a function of displacement rate, adhesion level and number of interlayers.**

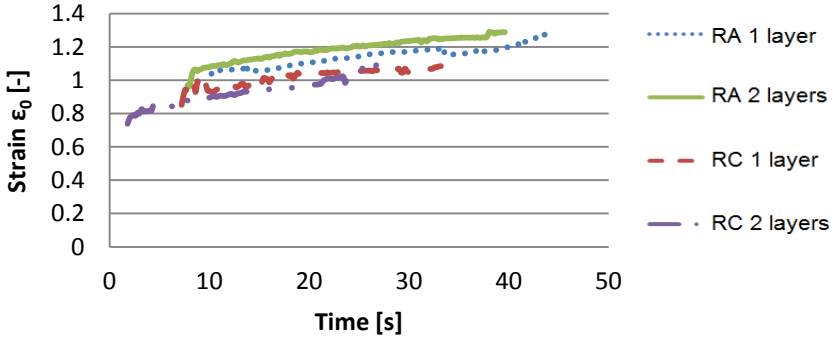

Figure 3-40 **Strain history.**

The intrinsic strain energy can be calculated using equation (3.19). The results are presented in Figure 3-41. Only samples where a steady state occurred are available for deducing the interfacial adhesion; these are the samples with medium and fast displacement rate.

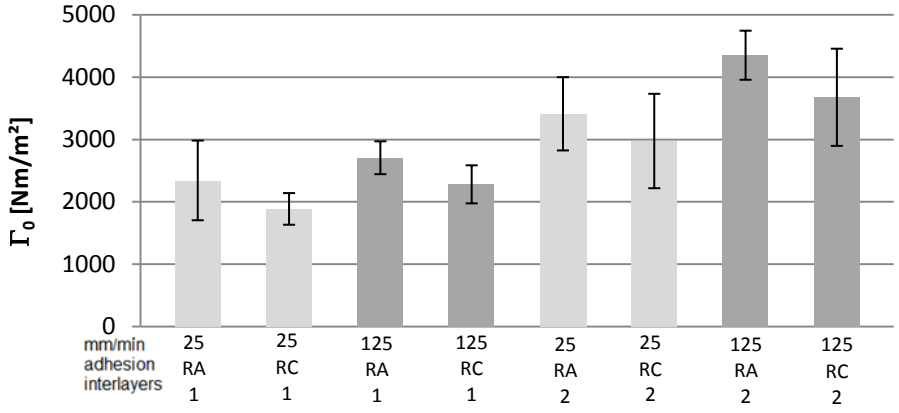

Figure 3-41 Fracture energies.

As was to be expected, a higher adhesion level leads to a higher interface energy value, although the difference is much less pronounced than in a mode I peel test. A thicker layer of PVB requires more energy to delaminate, even up to 50% more energy is required to delaminate over the same distance when the thickness doubles. A faster extension rate results in a higher interface energy; this behaviour shows that Γ incorporates the time-dependent behaviour of the interlayer, an assumption that was already made when deducting the governing equations.

3.4.2.d Conclusions

The through-cracked tension test is gaining in popularity, due to its ability to quantify the adhesion level in Mode II of the glass-interlayer interface in laminated glass, thereby adhering closer to the reality of impact behaviour as opposed to, for example, a peel test.

At the fastest extension rate (125 mm/min), a steady state always occurs. The forces needed to delaminate and extend the interlayer are highest for the fastest extension rate. The influence of the adhesion level – as measured in Mode I with a peel test – is rather small on the steady state force. Its influence can be discerned more clearly in the tearing behaviour of the interlayer, where a higher level of adhesion will induce tearing sooner due to the occurrence of higher strains. Furthermore, the delaminated interlayer with a low adhesion level will turn

instantaneously to a homogeneous opaque white colour, whereas an interlayer with a high adhesion level will still have patches of transparent PVB.

At a fast extension rate, the delamination will occur in both halves simultaneously and with a straight delamination front. At lower extension rates, the delamination front will usually advance in only one half of the specimen, with a crooked delamination front.

During the steady state, the occurring strains in the interlayer are quasi-constant, with values ranging from 0.7 to 1.3. For a higher adhesion level, the occurring strain is higher, due to a shorter delamination length. Based on the steady state force and strain, the interfacial adhesion can be determined. A higher adhesion level and displacement rate result in a higher interfacial adhesion level. Its value is also dependent on the interlayer thickness and can increase up to 50% when the thickness doubles.

3.4.3 Pull-off adhesion tests

To determine the Mode I bonding strength, tensile pull-off tests are performed. In a pull-off test, a laminated glass specimen is glued to metal stubs, named *dollies*, and pulled apart by which the glass-PVB interface should be separated.

3.4.3.a Materials & methods

The specimens are cilindrical with a nominal diameter of 30 mm and are composed of two plies of 4 mm thick glass and a 0.76 mm interlayer. To avoid debonding at the interface between the metal dollies and the glass, a strong adhesive has been selected: the 2-component epoxy glue 3M Scotch Weld 9323 B/A.

A first test series with specimens drilled from a larger plate (see Figure 3-42 (left)) showed high scatter in the results. Therefore, test specimens have been produced by waterjet cutting of a laminated glass plate, which does provide clean and smooth edges. The diameter of these specimens is slightly smaller than its nominal value: 29.25 ± 0.25 mm. For each specimen, the measured diameter is taken into account for calculation of the critical stress.

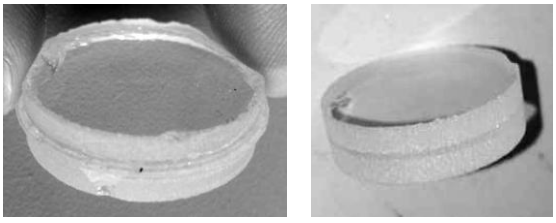

Figure 3-42 **Dolly specimens: drilled, bad quality (left), water jet, good quality (right).**

Experiments are performed with an Instron 8801 hydraulic tensile testing machine, equipped with a 50 kN load cell (Figure 3-43 (left)). The crosshead speed is 0.05 mm/min for all tests. The laboratory has a controlled temperature of 23 °C and the relative humidity varies between 29 and 33%. The stress state at the interface in a pull-off test is very sensitive to the alignment of the specimen and non-axiality of the loading [56]. Already, a small offset angle of 1° results in peeling behaviour rather than an even stress distribution. Thus, great care was taken in the positioning of each specimen and its axial alignment was checked with a laser level.

Five specimens were tested for each adhesion level.

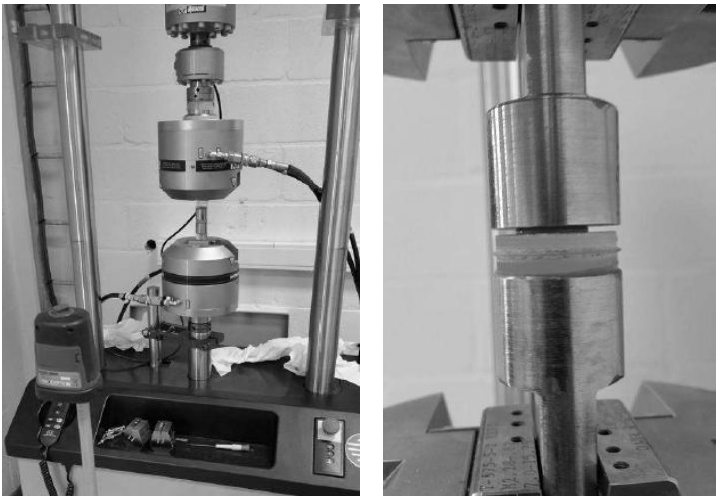

Figure 3-43 Pull-off adhesion test set-up, including laser level (left) and close-up of test specimen being glued in the clamps (right).

3.4.3.b Results & discussion

The failure loads and subsequently calculated failure stresses for all specimens are given in Table 3-7.

It is remarkable that the values of the failure stress of all the different adhesion levels are approximately equivalent. One would assume that the failure stress of PVB RC would be the lowest because a clear difference can be measured in the peel test.

Table 3-7 **Results for pull-off adhesion tests on specimens with high (RA), medium (RB) and low (RC) adhesion.**

Test number	RA Failure load [N]	Failure stress [N/mm^2]	RB Failure load [N]	Failure stress [N/mm^2]	RC Failure load [N]	Failure stress [N/mm^2]
1	3564.24	5.37	3343.69	4.97	3370.77	5.02
2	3907.06	5.83	4247.82	6.33	3050.13	4.52
3	3429.59	5.16	2997.51	4.45	4368.29	6.46
4	3106.11	4.59	3563.46	5.31	3956.59	5.87
5	3719.01	5.57	3368.19	5.00	4207.58	6.26
Average	3545.20	5.31	3504.13	5.21	3790.67	5.62
St.dev.	271.18	0.42	414.12	0.62	501.94	0.74

Typical force-displacement curves for all three adhesion levels are shown in Figure 3-44.

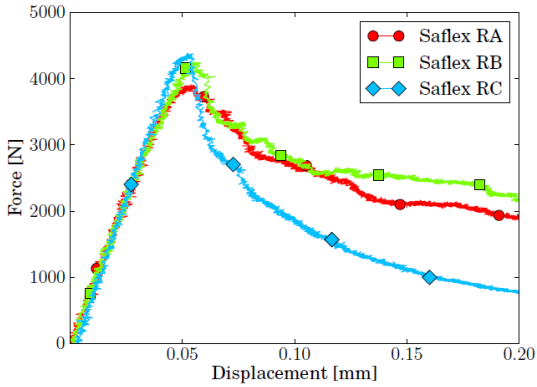

Figure 3-44 **Representative force measurements for three different PVB adhesion levels in a dolly pull-off test.**

Two failure mechanisms were observed. All specimens of type RA and RB failed by a loosening process between glass and PVB foil after reaching the ultimate load. All specimens with Saflex RC interlayer failed immediately at reaching the ultimate load and separated completely at one glass side, except for the one in test 2 that showed two-sided failure. In test 2, it looks like the interlayer gets peeled off the glass.

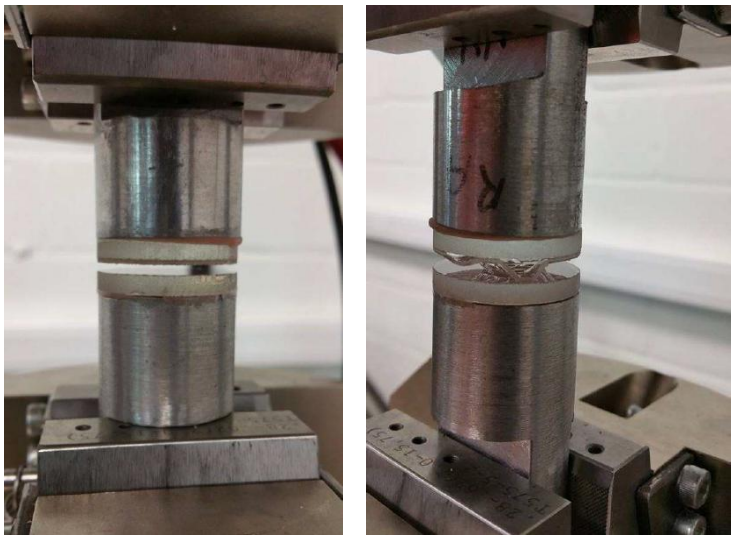

Figure 3-45 One sided (left) and two sided (right) failure.

At the end of the test, when the PVB is separated from the glass, a visual observation is made. Small circular dents or dimples are spotted in the interlayers with high and medium adhesion being the RA and RB series respectively. In the low adhesion interlayer RC, the dents are more like smudges.

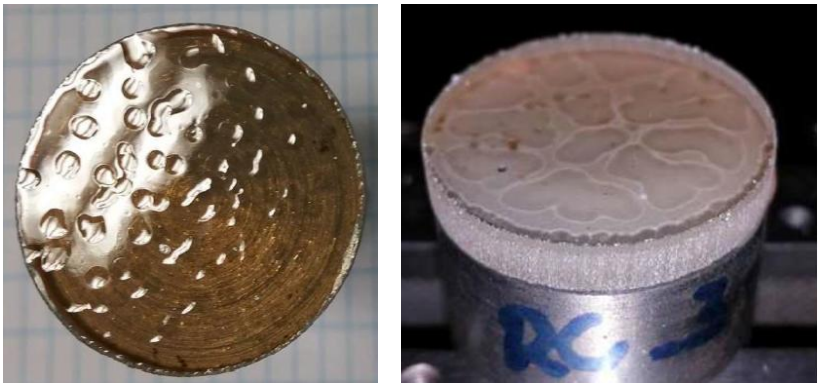

Figure 3-46 Occurrence of dents in post-test dolly specimens.

3.4.4 Interface: Interaction with numerical modelling (Pelfrene)

Several experimental test methods to determine the interface properties between glass and PVB interlayer have been used and analysed. Neither the 90° peel test, nor the through-cracked tensile test allow to quantify the interfacial strength and energy dissipated by delamination directly from the experiment. For the peel test, the complicating causes are the plastic deformation of the aluminium backing foil and the rapidly changing strain state of the viscoelastic interlayer around the crack tip (see Figure 3-47). In the case of the TCT test, high strains are reached in the delaminated PVB (Figure 3-48). The PVB material behaves highly nonlinear and rate-dependent, and a correct material model that captures this behaviour successfully is key to modelling the balance between elongation and delamination and therefore the force measured in steady state.

In numerical analysis of the peel and TCT test, it is seen that the interfacial adhesion, represented as a cohesive zone, is characterised by its strength and fracture energy. The actual shape of the traction-separation law has negligible influence. However, the strength and fracture energy should be determined for both fracture modes I and II, as delamination in the both tests is a mixed-mode process. It is seen that different combinations of these constants can yield the same steady state peel force.

The nonlinear viscoelastic material law for the interlayer can be calibrated to a uniaxial tensile test at a single speed and serves as an approximation for other speeds (or strain rates). It is seen that this approximation is less accurate at higher strains.

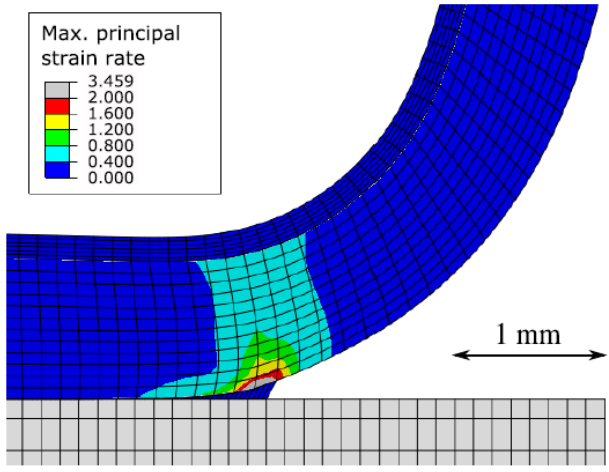

Figure 3-47 **Simulation result showing strain rates around crack process zone at steady state peeling.**

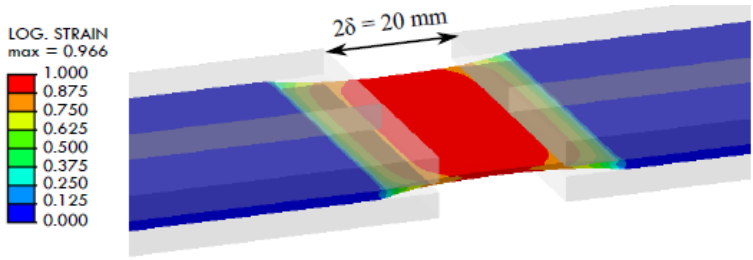

Figure 3-48 **Contours of logarithmic strain in length direction for TCT numerical model at crosshead speed of 25 mm/min.**

3.5 REFERENCES

[1] M. Haldimann, A. Luible, and M. Overend, *Structural Use of Glass* (Structural Engineering Documents, no. 10). Zürich: International Association for Bridge and Structural Engineering, 2008, p. 215.

[2] M. Vandebroek, J. Belis, C. Louter, and G. Van Tendeloo, "Experimental validation of edge strength model for glass with polished and cut edge finishing," (in English), *Engineering Fracture Mechanics*, vol. 96, pp. 480-489, Dec 2012.

[3] M. Vandebroek, J. Belis, C. Louter, and R. Caspeele, "Influence of the load history on the edge strength of glass with arrised and ground edge finishing," (in English), *Engineering Fracture Mechanics*, vol. 104, pp. 29-40, May 2013.

[4] *EN 1288-1:2000 Glass in building - Determination of the bending strength of glass - Part 1: Fundamentals of testing glass*.

[5] A. A. Griffith, "Phenomena of Rupture and Flow in Solids," (in English), *Asm Transactions Quarterly*, vol. 61, no. 4, pp. 871-&, 1968.

[6] T. Zarzycky, *Glasses and the vitrous state*. Cambridge: Cambridge University Press, 1991.

[7] *Glass in building, glass sides, concept, characteristics of side types and finishes*, 1986.

[8] X. Brajer, P. Forquin, R. Gy, and F. Hild, "The role of surface and volume defects in the fracture of glass under quasi-static and dynamic loadings," (in English), *Journal of Non-Crystalline Solids*, vol. 316, no. 1, pp. 42-53, Feb 2003.

[9] EN 1288-3:2000: Glass in building - Determination of the bending strength of glass - Part 3: Test specimen supported at two points (four point bending).

[10] ASTM C158-02 (2002): Standard Test Methods for Strength of Glass by Flexure (Determination of Modulus of Rupture).

[11] EN 1288-2:2000 Glass in building - Determination of the bending strength of glass - Part 2: Coaxial double ring test on flat specimens with large test surface areas.

[12] EN 1288-5:2000 Glass in building - Determination of the bending strength of glass - Part 5: Coaxial double ring test on flat specimens with small test surface areas.

[13] ASTM C1499 (2009): Standard Test Method for Monotonic Equibiaxial Flexural strength of Advanced Ceramics at Ambient Temperature.

[14] F. Bernard, "Sur le dimensionnement des structures en verre trempé: étude des zones de connexion," Ph.D., LMT Cachan, France, 2001.

[15] J. Güsgen, "Bemessung tragender Bauteile aus Glas," Ph.D. Thesis, RWTH Aachen / Shaker Verlag, 1998.

[16] W. Laufs, "Eind Bemessingskonzept zur Festigkeit thermisch vorgespannter Gläser," Ph.D. Thesis, RWTH Aachen / Shaker Verlag, 2000.

[17] J. Schneider, "Festigkeit und Bemessung punktgelagerter Gläser und stossbeanspruchter Gläser," Ph.D. Thesis, Institut für Statistik, TU Darmstadt, 2001.

[18] W. L. Beason and J. R. Morgan, "Glass Failure Prediction Model," (in English), *Journal of Structural Engineering-Asce*, vol. 110, no. 2, pp. 197-212, 1984.

[19] M. Overend, G. A. R. Parke, and D. Buhagiar, "Predicting failure in glass - A general crack growth model," (in English), *Journal of Structural Engineering-Asce*, vol. 133, no. 8, pp. 1146-1155, Aug 2007.

[20] DIN 1249-10:1990 Glass For Use In Building Construction - Part 10: Chemical And Physical Properties.

[21] W. G. Brown, "A practicable formulation for the strength of glass and its special application to large plates.," in "Technical Report Publication No. NRC 14372," National Research Council of Canada, Ottawa1974.

[22] A. Fink, "Ein Beitrag zum Einsatz von Floatglas als dauerhaft tragender Konstruktionswerkstoff im Bauwesen," Ph.D. thesis, Technische Hochschule Darmstadt, 2000.

[23] M. Haldimann, "Fracture Strength of Structural Glass Elements – Analytical and Numerical Modelling, Testing and Design," Ecole Polytechnique Fédérale de Lausanne (EPFL), Lausanne, 2006.

[24] S. M. Wiederhorn and L. H. Bolz, "Stress Corrosion and Static Fatigue of Glass," (in English), *Journal of the American Ceramic Society*, vol. 53, no. 10, pp. 543-&, 1970.

[25] F. A. Veer and J. Zuidema, "The strength of Glass, Effect of Edge Quality," presented at the Glass Processing Days, 2003.

[26] S. De Pauw, "Experimental and Numerical Study of Impact on Window Glass Fitted with Safety Window Film," Doctor in de Ingenieurswetenschappen: Werktuigkunde-Elektrotechniek PhD, Department of Material Science and Engineering, Mechanics of Materials and Structures, Ghent University, Ghent, 2010.

[27] J. Pelfrene, "Numerical analysis of the post-fracture response of laminated glass under impact and blast loading," Doctor in de Ingenieurswetenschappen: Werktuigkunde-Elektrotechniek PhD, Department of Material Science and Engineering, Mechanics of Materials and Structures, Ghent University, Ghent, 2016.

[28] P. D'Haene and G. Savineau, "Mechanical properties of laminated safety glass - FEM Study," presented at the Glass Processing Days 2007, Tampere, Finland, 15-18 june 2007, 2007.

[29] J. A. Hooper, "Bending of Architectural Laminated Glass," (in English), *International Journal of Mechanical Sciences,* vol. 15, no. 4, pp. 309-323, 1973.

[30] M. Z. Asik and S. Tezcan, "A mathematical model for the behavior of laminated glass beams," (in English), *Computers & Structures,* vol. 83, no. 21-22, pp. 1742-1753, Aug 2005.

[31] J. Belis, J. Depauw, D. Callewaert, D. Delince, and P. Van Impe, "Failure mechanisms and residual capacity of annealed glass/SGP laminated beams at room temperature," (in English), *Engineering Failure Analysis,* vol. 16, no. 6, pp. 1866-1875, Sep 2009.

[32] R. A. Behr, J. E. Minor, M. P. Linden, and C. V. G. Vallabhan, "Laminated Glass Units under Uniform Lateral Pressure," (in English), *Journal of Structural Engineering-Asce,* vol. 111, no. 5, pp. 1037-1050, 1985.

[33] H. S. Norville, K. W. King, and J. L. Swofford, "Behavior and strength of laminated glass," (in English), *Journal of Engineering Mechanics-Asce,* vol. 124, no. 1, pp. 46-53, Jan 1998.

[34] A. Van Duser, A. Jagota, and S. J. Bennison, "Analysis of glass/polyvinyl butyral laminates subjected to uniform pressure," (in English), *Journal of Engineering Mechanics-Asce,* vol. 125, no. 4, pp. 435-442, Apr 1999.

[35] M. Z. Asik, E. Dural, M. Yetmez, and T. Uzhan, "A mathematical model for the behavior of laminated uniformly curved glass beams," (in English), *Composites Part B-Engineering,* vol. 58, pp. 593-604, Mar 2014.

[36] L. Galuppi, G. Manara, and G. R. Carfagni, "Practical expressions for the design of laminated glass (vol 45, pg 1677, 2013)," (in English), *Composites Part B-Engineering,* vol. 56, pp. 599-601, Jan 2014.

[37] S. B. Bati, G. Ranocchiai, C. Reale, and L. Rovero, "Time-Dependent Behavior of Laminated Glass," (in English), *Journal of Materials in Civil Engineering,* vol. 22, no. 4, pp. 389-396, Apr 2010.

[38] L. Galuppi and G. F. Royer-Carfagni, "Effective thickness of laminated glass beams: New expression via a variational approach," (in English), *Engineering Structures,* vol. 38, pp. 53-67, May 2012.

[39] I. V. Ivanov, "Analysis, modelling, and optimization of laminated glasses as plane beam," (in English), *International Journal of Solids and Structures,* vol. 43, no. 22-23, pp. 6887-6907, Nov 2006.

[40] L. Chitty, "On the cantilever composed of a number of parallel beams interconnected by cross bars," *Philosophical Magazine,* vol. 38, no. 285, pp. 685-699, 1947.

[41] R. T. Nichols and R. M. Sowers, "Pummel," in *Encyclopedia of Chemical Technology* vol. 14, J. I. Krischwitz and M. Howe-Grant, Eds., 4th ed. New York: John Wiley, 1995, p. 1074.

[42] *ASTM D903-93, Standard Test Method for Peel or Stripping Strength of Adhesive Bonds*, 1995.

[43] K. Schneider, B. Lauke, and W. Beckert, "Compression shear test (CST) - A convenient apparatus for the estimation of apparent sheer strength of composite materials," (in English), *Applied Composite Materials*, vol. 8, no. 1, pp. 43-62, Jan 2001.

[44] A. Jagota, S. J. Bennison, and C. A. Smith, "Analysis of a compressive shear test for adhesion between elastomeric polymers and rigid substrates," (in English), *International Journal of Fracture*, vol. 104, no. 2, pp. 105-130, Jul 2000.

[45] S. Van Dam, J. Pelfrene, W. Van Paepegem, J. Degrieck, D. Lecompte, and J. Vantomme, "A new experimental test set-up for investigating impact resistance of laminated glass," presented at the Cost Action TU0905 Mid-term Conference on Structural Glass, Porec, Croatia, 2013.

[46] Y. Sha, C. Y. Hui, E. J. Kramer, P. D. Garrett, and J. W. Knapczyk, "Analysis of adhesion and interface debonding in laminated safety glass," (in English), *Journal of Adhesion Science and Technology*, vol. 11, no. 1, pp. 49-63, 1997.

[47] S. Muralidhar, A. Jagota, S. J. Bennison, and S. Saigal, "Mechanical behaviour in tension of cracked glass bridged by an elastomeric ligament," (in English), *Acta Materialia*, vol. 48, no. 18-19, pp. 4577-4588, Dec 1 2000.

[48] R. Iwasaki, C. Sato, J. L. Lataillade, and P. Viot, "Experimental study on the interface fracture toughness of PVB (polyvinyl butyral)/glass at high strain rates," (in English), *International Journal of Crashworthiness*, vol. 12, no. 3, pp. 293-298, 2007.

[49] C. Butchart and M. Overend, "Delamination in fractured laminated glass," presented at the International Conference Engineered Transparency, Düsseldorf, Germany, 25-26 October 2012, 2012.

[50] S. Bati, M. Fagone, and G. Ranocchiai, "Analysis of the post-crack behaviour of a laminated glass beam," 2009.

[51] M. Seshadri, S. J. Bennison, A. Jagota, and S. Saigal, "Mechanical response of cracked laminated plates," (in English), *Acta Materialia*, vol. 50, no. 18, pp. 4477-4490, Oct 28 2002.

[52] S. Nhamoinesu and M. Overend, "Simple Models for Predicting the Post-fracture Behaviour of Laminated Glass," presented at the XXV A.T.I.V. 2012 International Conference, Parma, Italy, 18-20 November 2010, 2010.

[53] D. Delincé, "Delincé D, Sonck D, Belis J, Callewaert D, Van Impe R. Experimental investigation of the local bridging behaviour of the interlayer in broken laminated glass. In: Siebert G, Hermann T, Haese A, editors. International Symposium on the Application of Architectural Glass ISAAG 2008 Conference Proceedings, Munich, October 27-28, 2008. p. 41–49.

[54] D. Ferretti, M. Rossi, and G. Royer-Carfagne, "Through-cracked-tensile delamination tests with photoelastic measurements," presented at the Challenging Glass 3, Delft, 2012.
[55] MatchID, "www.matchid.org."
[56] K. Allaer, I. De Baere, W. Van Paepegem, and J. Degrieck. Numerical study of the interfacial stress distribution in dolly pull-off adhesion tests for thin sheet materials. International Journal of Adhesion and Adhesives, 2015.

PART II – IMPACT

This part deals with the impact research performed in this study, namely those tests performed on the Small-scale drop weight and EN 12600 test set-up. This is preceded by a literature study.

Chapter 4 IMPACT: STANDARDS & LITERATURE

Overview

Before presenting the results of two distinct types of impact testing of laminated glass in chapters 5 and 6, an overview of the relevant standards as well as a description of the state-of-the-art is presented in this chapter.

4.1 STANDARDS

In this section, standards relevant to the impact behaviour of laminated glass are discussed. There are over 97 international Codes and Standards containing test methods relating to Safety Glazing. A further check of these documents revealed that there are 34 different test procedures. 22 of the 34 tests described are impact tests [1].

Glazing balustrades, glass doors or wall elements should be designed to resist dynamic human impact. As a first approach, human impact loads may be applied on the glass element as a static load, e.g. 1.5 kN at railing height. For non standard glass elements (e. g. point supported balustrades) and load bearing partitions (e. g. railings and balustrades) a dynamic analysis or impact tests are often required [2]. The tests specified in this case are either of the impact pendulum type (EN 12600, see 4.1.1) or of the ball drop type (EN 356, see 4.1.2).

4.1.1 EN 12600 [3]

The European Standard EN 12600 describes a safety standard test to classify various glass panes by performance under impact and by mode of breakage. There is reference to this standard in other normative works and regulations which specify the minimum safety performances of glass panes.

In the EN 12600 test an impactor, attached to a cable and lifted to a certain drop height, is released and hits a glass pane that is clamped in a frame (Figure 4-1).

Figure 4-1 EN 12600 set-up [4].

The classification by drop height corresponds to graded values of energy transmitted by the impact of a person. The aim of this classification is to increase the personal safety by:

- the reduction of cutting and piercing injuries to persons;
- the containment characteristics of the material, which implies the reduction of people or objects falling through the glass.

The standard defines three drop heights corresponding with a certain impact level, as summarized in Table 4-1. Class 3 corresponds with a load that is equivalent to a force exerted by an adult person that pushes hard against the glass or a child running into it. Class 2 is equivalent with a force that holds between an adult person walking into a glass door, and a determined attempt to force a way through by running at it. Class 1 is considered equivalent with critical conditions such as high velocity impact, caused by e.g. flying debris.

Table 4-1 Classification of the impact level based upon drop height.

Impact level	Drop height (mm)
3	190
2	450
1	1200

In other impact standards [5], a sand bag or a bag filled with small metal balls was used (see also 4.1.1.f). However, the energy transferred from the impactor to the glass pane was not high enough to represent the simulation of a human body impact. By using two tires around a steel cylinder with a total mass of 50 kg, the transferred energy is much higher, due to the greater stiffness and the smaller impact region.

4.1.1.a Procedure

The test shall be carried out at each drop height on four identical glass pieces. If the sequence of glass panes, glazing sheet material and interlayers is different from both outer surfaces, the test shall be executed on both sides. An exception can be made for situations where the risk of impact is coming from one side only.

Testing starts at the smallest drop height. The test is aborted if the test pieces are no longer in accordance with the requirements of the European Standard. If the test pieces remain intact or break according to the requirements, the testing will be continued for a higher drop height. This procedure is repeated until the final height, required for the intended purpose of the glass product, is reached.

4.1.1.b Modes of breakage and test requirements

The different types of glass panes can be characterized by the way fragmenting occurs. The three principal breakage modes (Figure 4-2) that are distinguished according to EN 12600 are:

- Type A: numerous cracks appear forming separate fragments with sharp edges, some of which are large. This mode of breakage is typical for annealed glass;
- Type B: numerous cracks appear, but the fragments are held together by the interlayer and do not separate. This mode of breakage is typical for laminated glass;
- Type C: disintegration occurs, leading to a large number of small particles that are relatively harmless. This mode of breakage is typical for toughened glass.

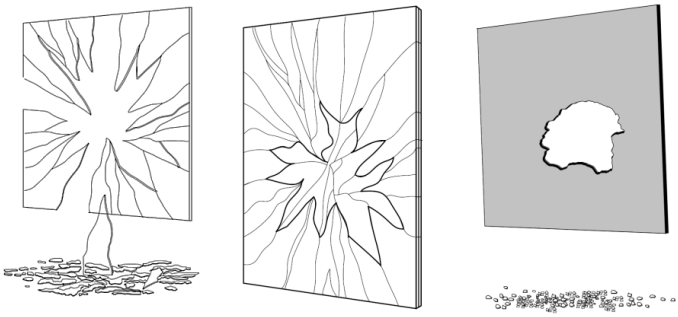

Figure 4-2 Modes of breakage: Type A (left), Type B (middle), Type C (right).

4.1.1.c Set-up

An overview of the different components of the test setup, as described in the European Standard, is given in Figure 4-3.

The main frame (1) is anchored into a concrete floor to create a rigid construction and an optional support member (4) can be provided to ensure the latter. The clamping frame (2) has internal dimensions of 847 ± 5 mm by 1 910 ± 5 mm. On the clamping frame, rubber strips are placed to protect the test specimen and to ensure uniform clamping. These strips are 20 ± 2 mm wide, have a thickness of 10 ± 1 mm and have a hardness of 60 ± 5 IRHD in accordance with the International Standard ISO 48 (BIN, 2003). When the glass pane is clamped, the strips are compressed so that the thickness of the strips is reduced by 5-10% of their

original thickness. For the impact test, the compression of the rubber strips has to be limited to 20%. A clamping device holds the main frame, clamping frame and glass pane together.

The impactor (3) consists of two tires of type 3.50-R8 4PR, an additional mass and a suspension system. The total mass is limited to (50 ± 0.1) kg and the tires have to be inflated to (3.5 ± 0.2) bar when the impact test is executed. The main function of the suspension cable is to ensure that the tires impact the middle of the test piece from the chosen drop height. When the impactor hits the test piece, energy will be transferred to the glass pane, resulting in micro strains in horizontal and vertical direction.

The distance between the impactor at rest and the test specimen should be between 5 mm and 15 mm. The horizontal centre line of the impactor has to be within 50 mm from the centre of the test piece.

The standard does not specify requirements for application, therefore various additional national requirements exist in European countries. In most countries (in contrast to Germany), impact resistance has to be verified for the glazing rather than the whole assembly. This means that the glass may be tested in a standardized frame instead of using the original components that will be used in the building [2].

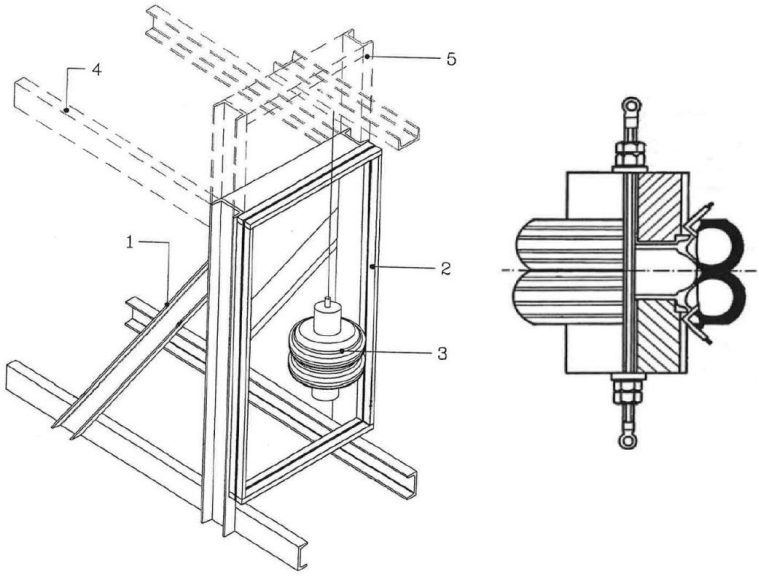

Figure 4-3 **Test set-up according to EN 12600 (left) and cross-section of the impactor (right) [3].**

4.1.1.d Calibration of the set-up

To test the validity of the experimental setup, the strains of a calibration plate have to be within margins that are linked with a certain drop height of the impactor. The calibration specimen is 10 mm thick and comprises a tempered glass pane with dimensions 876 ± 2 mm by 1938 ± 2 mm.

Strains are measured using a strain gauge rosette attached to the centre of the pane. Specifications are stated in the standard, with a Vishay Micro-Measurements CEA-06-125WT-350 strain gauge given as a qualified example.

The impactor is swung three times against the pane, for six drop heights. The mean peak strain value for the horizontal and vertical strain must fall within the limits given by the EN 12600 standard:

Table 4-2 Values for mean peak horizontal micro-strain.

Drop height [mm]	Mean peak value [micro-strain]	Mean peak value -10 % [micro-strain]	Mean peak value +10 % [micro-strain]
200	1275	1147	1402
250	1418	1276	1559
300	1542	1388	1696
450	1793	1613	1972
700	2063	1857	2269
1200	2503	2252	2753

Table 4-3 Values for mean peak vertical micro-strain.

Drop height [mm]	Mean peak value [micro-strain]	Mean peak value -10 % [micro-strain]	Mean peak value +10 % [micro-strain]
200	805	724	885
250	911	820	1002
300	1013	912	1114
450	1181	1063	1299
700	1389	1250	1528
1200	1742	1567	1916

These values are on the safe side as an impact of a person of 83 kg running from a distance of 2.5 m into a window only resulted in a strain level of about 1000 micro-strain in the horizontal direction [6].

4.1.1.e Numerical simulations [7]

Qualification of glazing by this test can become time-consuming and costly. Therefore, in Germany, the TRAV [8] prescribed the design method for defined glass sizes and only required experimental testing with the twin-tyre impactor for deviating glass components. The most recent German norm, DIN 18008-4 [9], now also allows the calculation by either a simplified method or by numerical transient analysis for the geometry and support conditions of the final design. Leading up to this norm, several researchers have drafted validated numerical models for simulation of the impact up to glass breakage.

In Schneider[10], and also Müller de Vries[11], the tyres are represented by volume-filling solid elements which are given a Young's modulus that corresponds to the observed stiffness of the tyre for a certain drop height. This approach receives the criticism that simulation results are matched rather than predicted and that they cannot be extrapolated to other glass setups than those for which the model has been validated. Brendler et al. [12] and later Schneider et al. [10] took account of the pressurized air volume in the tyres, but did not yet model the fibre reinforcement in the rubber tyre.

4.1.1.f ANSI Z97.1

An American counterpart to the European EN 12600 standard was long accepted worldwide as a safety standard for window glass. Indeed, the ANSI Z97.1 standard [5] shares many characteristics with the EN 12600 except for the impactor, which is here a leather punching bag filled with 45 kg of lead shots and covered in a loosely draped cloth towel (Figure 4-4).

However, Balkow et al. [13] showed that the tests have low reproducibility due to the changing characteristics of the shotbag over time. For this reason, it is now often replaced in the industry by the EN 12600.

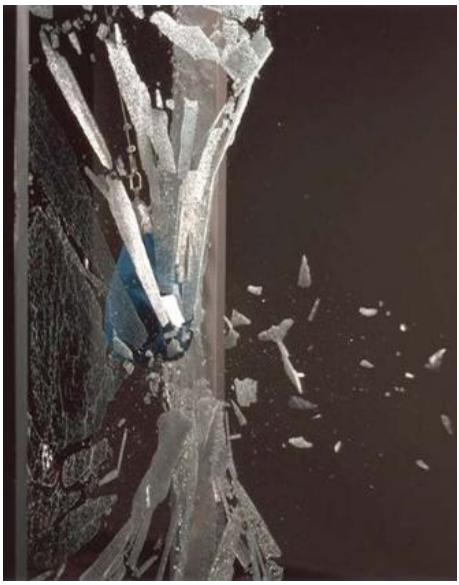

Figure 4-4 ANSI Z97.1 test with shotbag in blue (courtesy Eastman).

4.1.2 EN 356 [14]

Where the EN 12600 standard was conceived with human impact in mind, the EN 356 standard deals with a qualification for forced entry resistance. The terms used in the standard are anti-bandit or anti-vandal glazing. The aim of the security glazing is to resist such attacks by delaying access of objects and/or persons to the protected space for a short period of time.

4.1.2.a Procedure

Each sample submitted for testing will consist of three specimens. Specimens are 1100 ± 5 mm long and 900 ± 5 mm wide. Edges should be free from visible chips, cracks and flaws. The surface to be impacted (an asymmetrical configuration must be tested bearing in mind the final position of the glazing with respect to the protected space) must be marked on each specimen.

Table 4-4 Categories of resistance and corresponding drop heights.

Category of resistance	Drop height [mm]
P1A	1500 ± 50
P2A	3000 ± 50
P3A	6000 ± 50
P4A	9000 ± 50
P5A	9000 ± 50

For categories P1A, P2A, P3A and P4A the impactor shall be dropped onto each test specimen three times from the same height, in such a way that the impact positions form the pattern of an equilateral triangle with a side length of 130 ± 2 mm around the geometric centre of the specimen, with one side of the triangle parallel to the short side of the specimen. The impact position opposite to this side of the triangle shall be hit first.

For a P5A classification, the above procedure shall be repeated three times on each test piece, resulting in a total of 9 impacts, 3 on each point of the triangle.

Figure 4-5 EN 356 set-up with second steel ball in free fall before impact (courtesy SangBo).

After each impact, the test piece shall be checked for penetration by the impactor and loose fragments shall be removed from the test piece.

If the impactor went through the test piece within five seconds after impact, the test piece will be classified as penetrated. The test piece will also be examined for slippage. If more than 5 mm displacement from the clamping frame is found, the test is declared invalid.

The security glazing product is classified in a particular category of resistance if all three specimens prevent penetration by the impactor body when tested according to this method.

4.1.2.b Set-up

The impactor (hard body) shall be a steel sphere with a diameter of 100 ± 2 mm and a mass of 4.11 ± 0.06 kg. The sphere shall be manufactured from polished steel with a hardness of 60 to 65 HRC on the Rockwell C scale according to ISO 6508.

The equipment for holding the impactor shall enable adjustment of the drop height to the required tolerance. The holding equipment as well as the release mechanism should not induce any momentum of rotation in the impactor, so that the impactor is accelerated only by gravitational forces and falls vertically.

The test piece apparatus consists of a steel frame to clamp the edge of the specimen and a receiving box to collect fragments and the impactor. It should have a rigid connection to a solid base, ensure plane and parallel clamping of the specimen and be designed in such a way that the specimen only touches the clamping frame during the test. The clamping area of the four edges of the specimen is 30 ± 5 mm. This clamping area is covered with 30 mm wide rubber strips with a thickness of 4 mm and a hardness of 40 to 60 IHRD according to method N of ISO 48:1994. The edges should be clamped with a uniform pressure of 140 ± 20 kN/m^2. Furthermore, it should be ensured that the impactor is not damaged and does not rebound when hitting the bottom of the receiving box, and that air does not become trapped in the support apparatus so that it may cushion the effect of the impact. This can be prevented by supplying ventilation holes.

A second part of the standard describes an axe test (Figure 4-6) to simulate an even more brutal entry attempt. Depending on how many strikes a glass pane can resist, it is categorized in one of three safety classes.

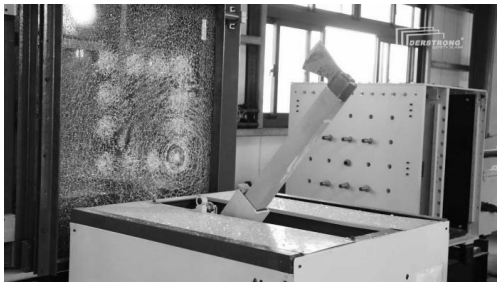

Figure 4-6 EN 356 axe set-up (courtesy Derstrong).

4.2 STATE-OF-THE-ART

In this section, some journal articles which deal with impact loading of laminated glass are discussed. These are grouped into two sections: i) automotive & architectural applications and ii) in-house designed test set-ups.

4.2.1 Automotive & architectural applications

Most research of impact on laminated glass is oriented towards applications in the automotive industry, and consequently uses laminate configurations specifically designed for windshields i.e. with relatively thin glass.

Grant *et al.* [15] study the effect of varying the thickness of one or both glass plies on the overall impact resistance to road chippings and the failure processes are investigated. Impact velocities in the range 4-20 m/s were achieved using a catapult system. The glass thicknesses varied between 0.7 and 2.5 mm. Each 200 by 200 mm plate was clamped in a square frame and hit in 5 different spots.

Damage was classified into four categories. The critical impact speed was defined as the lowest impact speed for which one of these categories of damage occurred. It strongly depends on the thickness of the outermost layer of glass whereas the inner thickness has a secondary effect on this damage threshold. A study of the impacted laminates highlighted a change in failure mode from flexure-induced star cracking in systems with thin outer layers to top surface cone cracking in constructions with a thick outer layer.

The European Enhanced Vehicle-safety Committee described in a report [16] a test method to simulate the impact of a human head on a windshield. An impactor, designed to behave as a human head and fitted with an internal accelerometer, impacts perpendicularly a windshield at a speed of 40 km/h. The imposed accelerations must remain under a certain limit to prevent damage in real-life. Thus, a thick laminate of which the glass does not break, will fail the test. The Euro NCAP safety rating system uses this test.

This test has been the subject of study by Zhao *et al.* [17], Timmel [18] , Liu *et al.* [19] and Peng *et al.* [20] (Figure 4-7), who all used detailed finite element models of test dummies and pedestrian headform impactors for crashworthiness simulations [7].

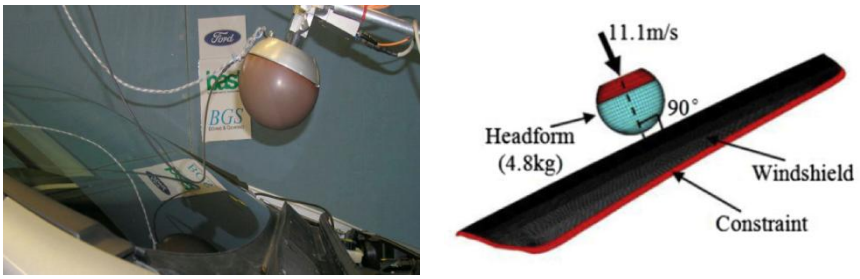

Figure 4-7 **Test for pedestrian headform on windshield: EEVC crash test (left) and finite element simulation (right) [20].**

Pyttel *et al.* [21] present a failure criterion for laminated glass in case of impact. The main idea of this criterion is that a critical energy threshold must be reached over a finite region before failure can occur. Afterwards, crack initiation and growth is based on a local Rankine (maximum stress) criterion. To calibrate the criterion and evaluate its accuracy, a wide range of experiments with plane (Figure 4-8) and curved specimens of laminated glass were done. For all experiments finite element simulations were performed.

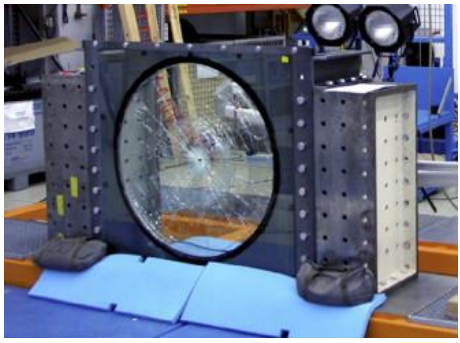

Figure 4-8 **Experimental set-up used by Pyttel et al. in [21].**

Results from those experiments and simulations were used to simulate pedestrian impact on a car windscreen. Displacement of the plane specimens was measured using 10 laser extensometers and could be simulated to a reasonable extent, which also holds for the deceleration of the impactor.

4.2.1.a SJ Mepla

SJ MEPLA is a finite element program specially developed to perform (simplified) static and dynamic calculations of architectural glass structures. With it, one can calculate any shape of system including laminated glass, point fixings, balustrade clips... It can also be applied for calculations involving insulated glass. A variety of bearing and loading situations can be attributed to the glass panels. Both static load cases and dynamically calculated impacts for the use of glass as fall protection are incorporated on the program. An example is shown in Figure 4-9.

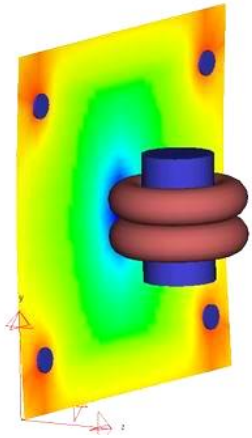

Figure 4-9 **Dynamic simulation of the twin-tyre pendulum impact tests according to EN 12600 (courtesy SJ Mepla).**

4.2.2 In-house designed test set-ups

Nourry and Nugue [22] use an energy incremental approach to describe laminated glass perforation under hard-body impact. They discretize the global energy balance of the impact and quantify the mechanical phenomena responsible for the input energy dissipation of the projectile.

For this, they built an ‘interrupted impact’ device, which allows halting the impactor at any given time during the impact event (Figure 4-10). By changing this time of interruption, the damage to a laminated glass sample can be controlled.

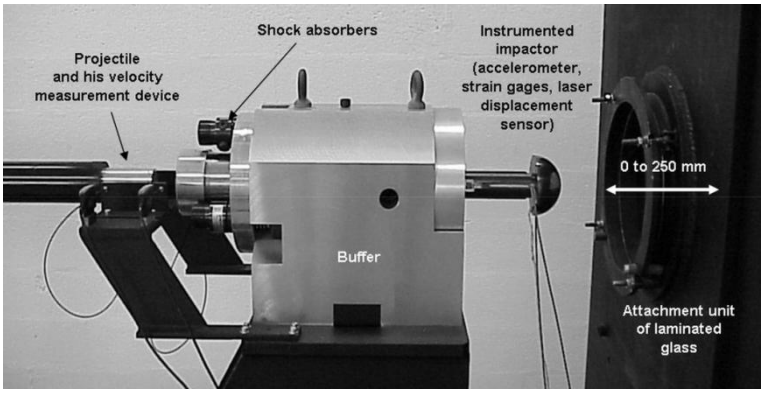

Figure 4-10 Interrupted impact test set-up as designed by Nourry [22].

The analysis of the energy balance of the hard body impact on laminated glass confirms the small part of energy dissipated by fragmentation and projection of glass fragments. The interlayer deformation, governed by the properties of adhesion, dissipates the major part of the kinetic energy of the impactor.

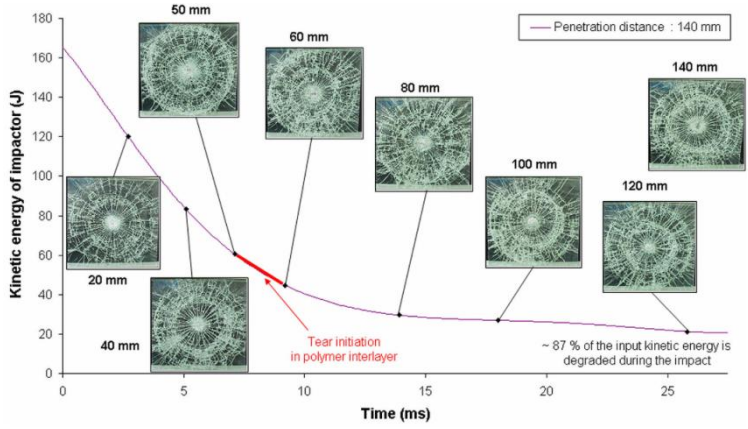

Figure 4-11 Evolution of impactor kinetic energy after contact with the laminated glass and fragmentation patterns [22].

Using high-speed photography, Xu *et al.* [23] investigated crack propagation behaviour of PVB laminated glass, when it is subjected to impact using a set-up which contains a 'force direction convertor' (see Figure 4-12). This was done to facilitate filming the specimen during impact.

The time histories of the averaged radial crack tip position, propagation velocity and acceleration were obtained. It was found that the steady-state cracking speed of PVB laminated glass is lower than that of pure glass, and it also increases with higher impactor speed and mass.

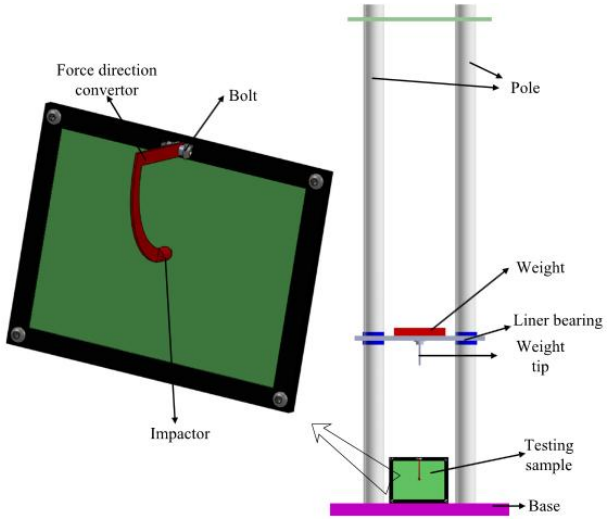

Figure 4-12 **Test set-up of drop weight set-up including detailed view of sample and force direction convertor [23].**

Zhang *et al.* [24] conducted airbag pendulum impacts on laminated glass of various thicknesses. The 670 x 670 mm specimens were subjected to a uniform pressure, which was applied by having a 300 kg pendulum weight slamming into an inflated airbag, making contact with the 600 x 600 mm free area of the glass. A 35 mm thick strike plate was positioned in front of the airbag so as to fully confine the airbag and to distribute the impact force on the airbag. A pressure transducer was inserted inside the airbag to record air pressure applied on the glass specimen. A laser Linear Variable Displacement Transducer was elevated to the centre of the glass pane to measure the deflection history at the centre of the specimen.

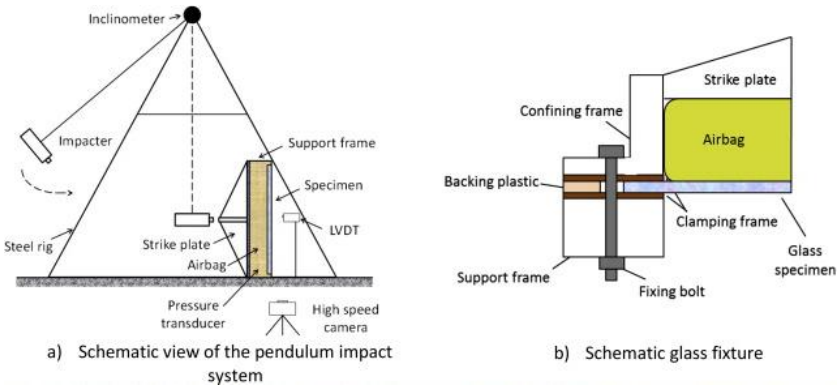

Figure 4-13 Pendulum test set-up.

The recorded pane's central deflection and the pressure histories were used to evaluate the accuracy of design standards and equivalent SDOF analysis. It was found that the ASTM F2248 standard underestimates the laminated glass responses. UFC 3-340-02 and the other SDOF-based approaches [25, 26] give reliable predictions of glass window responses when the deflection level is relatively small.

Only four laminated panes, each one with different properties, were tested. The applied pressures fluctuated quite a bit, which the authors attribute to the differing panel response.

Although the experiments were conceived as a simulation of a blast event, the duration of the applied pressure (more than 100 ms for all tests) suggests a comparison with impact tests is more appropriate.

In an earlier article by Zhang *et al.* [27] results are presented from laminated glass with very thick interlayers (1.52 – 2.66 mm) being impacted with wooden blocks (Figure 4-14) at a speed of 15 m/s. The interlayer thickness was found to play a dominating role in determining penetration resistance.

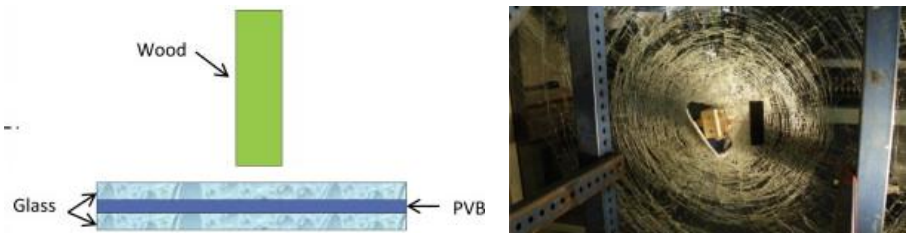

Figure 4-14 Schematic (left) and post-test picture (right) of the wooden block impact test (edited from [27]).

Again, only four specimens were tested but the results of these four different tests were used to 'calibrate' a numerical model, which was subsequentely used to make predictions about the behaviour for impact with heavier objects at higher speeds.

4.3 CONCLUSIONS

This chapter started with a description of both the EN 12600 and EN 356 standards – set-ups which will be further discussed in future chapters. Classification of tested specimens is done with discrete categories.

Several articles were then summarized, in a variety of fields of study. Most of the research is oriented towards automotive applications. A mixed experimental/numerical approach is often employed.

Given the fact that laminated specimens, especially larger ones, are quite expensive, and the tests require a lot of preparation, many researchers often limit the amount of specimens in one 'sample'. This results in conlusions which have to be used with caution. Further extrapolating of the results should be avoided, especially for design problems.

4.4 REFERENCES

[1] L. Jacob, "Impact Standards for Safety Glass and Relevance to the Community," presented at the Glass Processing Days, Tampere, Finland, 1999.

[2] M. Haldimann, A. Luible, and M. Overend, *Structural Use of Glass* (Structural Engineering Documents, no. 10). Zürich: International Association for Bridge and Structural Engineering, 2008, p. 215.

[3] EN:12600:2002. Glass in building - Pendulum test - Impact test method and classification for flat glass, 2002.

[4] Fröling, M. (2013). Strength Design Methods for Glass Structures Department of Construction Sciences, Lund University.

[5] ANSI Z97.1 - Safety Glazing Materials Used in Buildings Safety.

[6] J.-D. Wörner, J. Schneider, and A. Fink, *Glasbau - Grundlagen, Berechnung, Konstruktion*. Springer, 2001, p. 275.

[7] J. Pelfrene, "Numerical analysis of the post-fracture response of laminated glass under impact and blast loading," Doctor in de Ingenieurswetenschappen: Werktuigkunde-Elektrotechniek PhD, Department of Material Science and Engineering, Mechanics of Materials and Structures, Ghent University, Ghent, 2016.

[8] Deutsches Institut für Bautechnik (DIBt), Berlin. Technische Regeln für die Verwendung von absturzsichernden Verglasungen (TRAV), 2003.

[9] DIN 18008-4. Glass in building - Design and Construction Rules - Part 4: Additional Requirements for Barrier Glazing. Beuth Verlag, Berlin, 2013.

[10] J. Schneider, "Festigkeit und Bemessung punktgelagerter Gläser und stossbeanspruchter Gläser," Ph.D. Thesis, Institut für Statistik, TU Darmstadt, 2001.

[11] C. Müller de Vries. Numerical simulation of façade / window fracture under impact loading. In Bos, Louter, Nijsse, Veer, editor, Challenging Glass 3, pages 489-500, 2012.

[12] S.A. Brendler. Rechnerisches Bemessungskonzept für absturzsichernden Glastafeln. PhD thesis, Technische Universität Carolo-Wilhelmina, Braunschweig, 2007.

[13] K. Balkow, H. von Bock, H. Krewinkel, and R. Rinkens. Glas am Bau - Technischer Leitfaden. Deutsche Verlags-Anstalt, Stuttgart, 1980.

[14] EN:356:1999. Glass in building - Security glazing - Testing and clissification of resistance against manual attack., 2000.

[15] P. V. Grant, W. J. Cantwell, H. McKenzie, and P. Corkhill, "The damage threshold of laminated glass structures," (in English), *International Journal of Impact Engineering*, vol. 21, no. 9, pp. 737-746, Oct 1998.

[16] European Enhanced Vehicle-safety Committee. Working Group 17 Report: Improved Test Methods to Evaluate Pedestrian Protection Afforded by Passenger Cars, 1998.

[17] S. Zhao, L.R. Dharani, L. Chai, and S. Barbat. Analysis of damage in automotive glazing subjected to simulated head impact. Engineering Failure Analysis, 13:582-597, 2006.

[18] M. Timmel, S. Kolling, P. Osterrieder, and P. A. Du Bois, "A finite element model for impact simulation with laminated glass," (in English), *International Journal of Impact Engineering*, vol. 34, no. 8, pp. 1465-1478, Aug 2007.

[19] Q. Liu, J. Liu, Q. Miao, D. Wang, and X. Tang. Simulation and test validation of windscreen subject to pedestrian head impact. In 12th International LS-DYNA Users Conference, 2012.

[20] Y. Peng, J. Yang, C. Deck, and R. Willinger. Finite element modeling of crash test behavior for windshield laminated glass. International Journal of Impact Engineering, 57:27-35, 2013.

[21] T. Pyttel, H. Liebertz, and J. Cai, "Failure criterion for laminated glass under impact loading and its application in finite element simulation," (in English), *International Journal of Impact Engineering*, vol. 38, no. 4, pp. 252-263, Apr 2011.

[22] E. Nourry and J.-C. Nugue, "Impact on Laminated Glass: Post-breakage Behaviour Assessment," presented at the Glass Processing Days 2005, Tampere, Finland, 2005.

[23] J. Xu *et al.*, "Experimental and macroscopic investigation of dynamic crack patterns in PVB laminated glass sheets subject to light-weight impact," (in English), *Engineering Failure Analysis*, vol. 18, no. 6, pp. 1605-1612, Sep 2011.

[24] Zhang, X., Hao, H., & Wang, Z. (2015). Experimental study of laminated glass window responses under impulsive and blast loading. International Journal of Impact Engineering, 78, 1-19.

[25] J. M. Biggs, *Introduction to structural dynamics*. McGraw-Hill, 1964.

[26] C. Morison, The resistance of laminated glass to blast pressure loading and the coefficients for single degree of freedom analysis of laminated glass, [PhD thesis] Cranfield University (2010).

[27] X. H. Zhang, H. Hao, and G. W. Ma, "Laboratory test and numerical simulation of laminated glass window vulnerability to debris impact," (in English), *International Journal of Impact Engineering*, vol. 55, pp. 49-62, May 2013.

Chapter 5 IMPACT: SMALL-SCALE DROP-WEIGHT

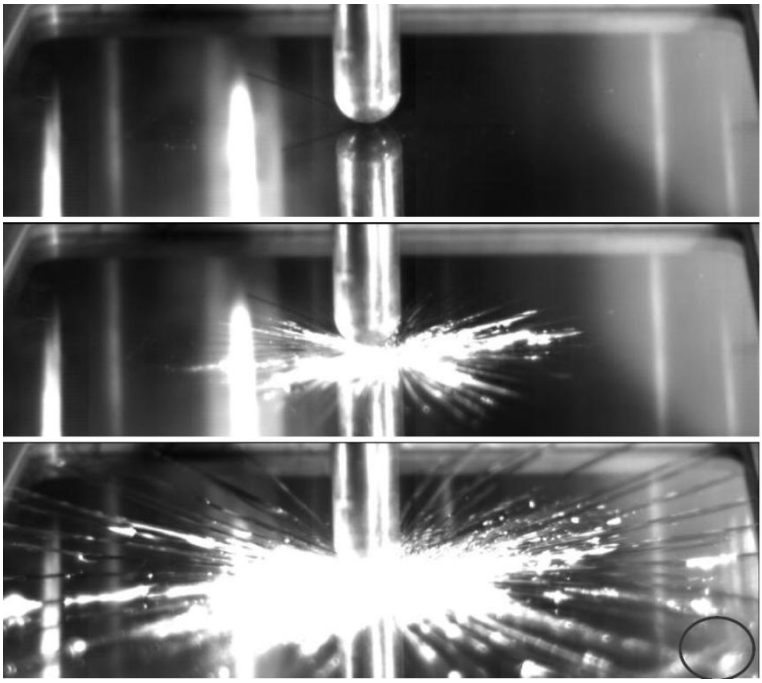

Overview

In this chapter the first venture into impact testing of laminated glass is described. Square and circular samples are subjected to a respectively hard and soft impact with a small-scale drop-weight (SSDW) set-up to try and evaluate the influence of several parameters on the dynamic behaviour of said specimens. First, the instrumented test set-up is introduced. Several scripts have been written in order to automatically process the obtained test data. A high-speed camera was used for analyzing the event of impact and for distinguishing several fracture stadia. Furthermore, a method was developed to mathematically evaluate the inflicted damage. A large part of the discussion of the results has been moved to Annex B, as the goal of obtaining different responses for different adhesion levels could not be achieved. In a final part, results from a simpler, larger set-up without much instrumentation are presented and compared with the results from the SSDW test campaign.

In his PhD study [1] De Pauw improved an existing drop tower set-up to investigate the impact behaviour of glass fitted with safety window film. The same set-up will be used in this research, albeit with some small modifications, especially concerning the automation of the test process. The basics of the set-up (5.1) and instrumentation (5.2) needed for a good understanding of the tests are repeated here. For an even more detailed description the author refers to Annex B, where also some of the experimental results are discussed in more detail.

5.1 TEST SET-UP

The test set-up consists out of three separate parts: i) a steel rigid base support in which the specimens are clamped, ii) an impactor striking the specimen and iii) guiding rails to guide the impactor. Special attention was given to the interception of shattered glass fragments and the deceleration of the impactor after hitting the specimen, as well as to the instrumentation, which is described in the next section. The realized setup is shown in Figure 5-1. The three parts that make up the test set-up are described in the following paragraphs.

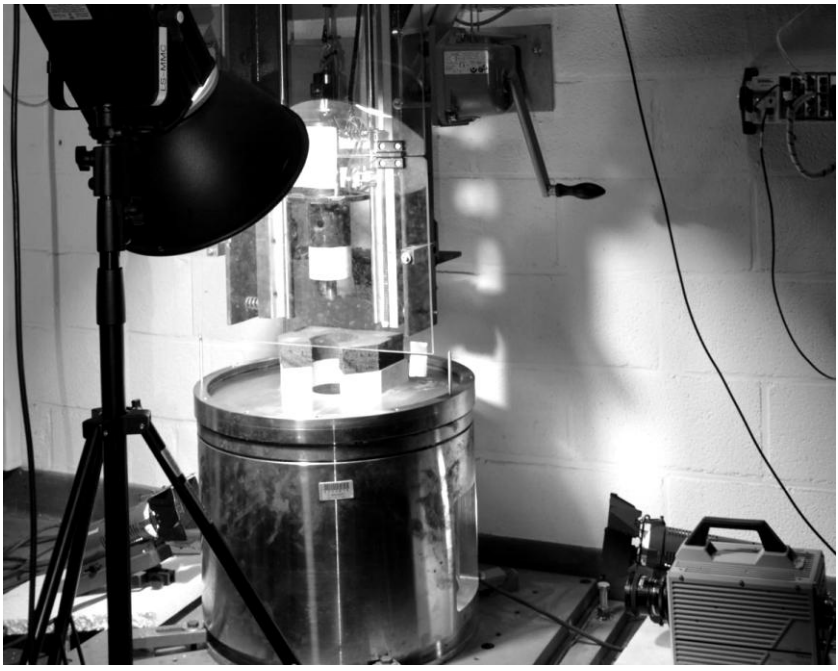

Figure 5-1 Complete set-up including high-speed camera and lighting.

5.1.1 Base support

The main function of the base support is to support the test specimens and impose the desired boundary conditions without influencing the test results. Additional functions are protection from flying impact fragments and stopping the impactor after it has penetrated the test specimen.

The parts of the base support are displayed in Figure 5-2, here the composition for circular test specimens with a diameter of 470 mm is given. In order to view the specimen from underneath via a 45° tilted mirror, two rectangular holes were cut in it. Steel spacer rings were inserted to provide the possibility of testing specimens with different thicknesses. Polypropylene rings avoided direct contact between the glass specimen and steel support.

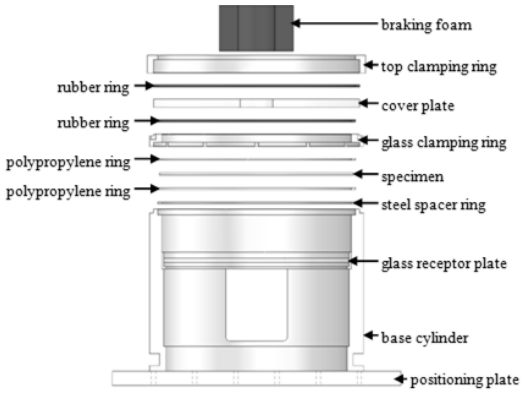

Figure 5-2 Base support parts [1].

For the square plates the composition of the base is slightly altered. The principle stays the same but the glass clamping ring is now used to clamp an intermediate steel circular fixture in which the square test specimens can be mounted in a similar manner as the circular pieces.

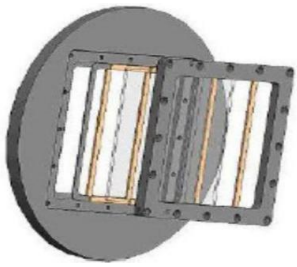

Figure 5-3 Intermediate steel circular fixture for square test specimens.

5.1.2 Guiding frame

Basically, the framework exists out of two vertical profiles attached to the wall by four supporting structures. Two guiding rails are attached to the vertical profiles by a total of eight adjustable support blocks to ensure optimal vertical alignment. The railing system allows the impactor to move in the vertical direction in a controlled way. To release the impactor, an electromagnet is powered that counteracts the magnetic forces of the permanent magnet, replacing the rudimentary release mechanism with a rope.

5.1.3 Impactor

The impactor itself is the moving part of the test setup (Figure 5-4). It also provides housing for diverse instrumentation cells. The force sensor is sandwiched between the indentor and the main body of the impactor.

The indentor is a crucial part of the impactor because it makes contact with the test specimen. The shape and elastic properties of the indentor material are its most important parameters. As mentioned earlier, there are two main types of impact. The first is impact by small and hard objects like debris, stones, crowbars, etc… They deliver a very high and localized pressure upon the glass. The second type is impact by soft and large objects like human impact, footballs, large birds, etc… the latter type delivers a lower but a more spread out pressure. Therefore two kinds of indentors were developed that embody both impact types.

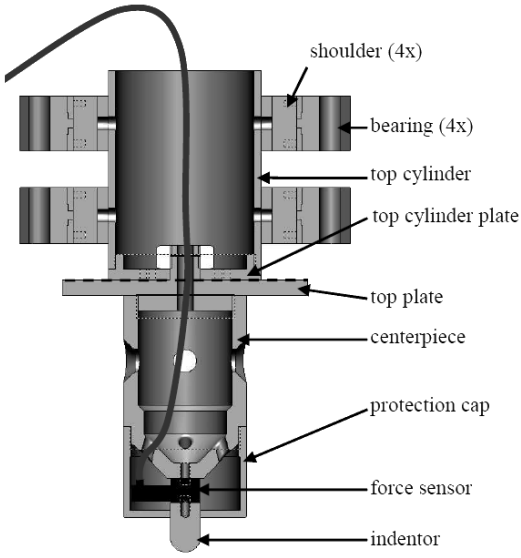

Figure 5-4 Impactor parts.

5.1.3.a Hard indentor

The hard indentor is a steel cylinder with a 10 mm radius, ending in a spherical tip. To increase the resistance against the wear resulting from repeated glass impacts the tip was hardened. The total height of the indentor is 55 mm and its mass is 0.12 kg.

Figure 5-5 Hard indentor.

5.1.3.b Soft indentor

The material used to manufacture a soft indentor was a bi-component silicone rubber. The Shore hardness (type A) of the cured compound is situated around 22.

The silicon shape was mechanically connected to an aluminium base by three equidistant screws situated at the circumference. To prevent lateral deformation at the base of the silicon shape, a relatively large plastic ring was fitted over the upper part as seen in Figure 5-6. It has a diameter of 136 mm, a height of 42 mm and the spherical bottom has a curvature radius of 334 mm. The mass of the silicone part is 0.89 kg. The total mass of the soft indentor is 1.47kg.

Figure 5-6 Soft indentor.

5.2 INSTRUMENTATION

The instrumentation on the test setup consists of three sensors (force, acceleration and displacement) mounted on the impactor which measure i) the force applied by the indentor, ii) the acceleration and iii) the displacement of the impactor. Some test specimens were equipped with a number of strain gauges to visualize their deformation and a high-speed camera was used to capture the actual breaking process. The details of all sensors and of the data acquisition system can be found in Annex B.

5.2.1 High-speed imaging

Because glass fracture is a very fast and visual phenomenon a high-speed camera was used. The different phenomena that occur during impact (time of first crack, radial crack formation, time of failure, etc…) can thus be visualized and correlated to diverse sensor measurements.

The high-speed camera (Photron Fastcam SA4) was positioned on the right side of the test setup (Figure 5-7). A bottom view of the test specimen was obtained by placing a mirror in the base support underneath the glass receptor plate at an angle of 45 degrees. A Nikkor AF-S 50mm f/1.4D lens was used for al tests.

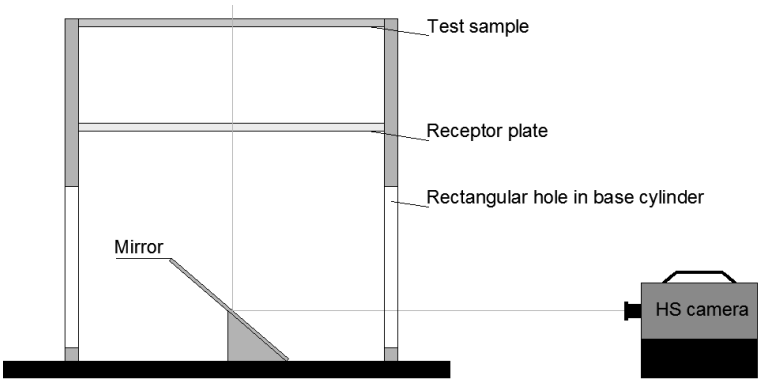

Figure 5-7 Camera set-up and mirror construction.

The lamps used for this test setup were one Hedler Daylux D 04 400W spot and two Dedolight COOLT3 250W spots. A Dedolight spot was placed at each side of the base cylinder, shining upwards through the rectangular holes. The Hedler spot was placed on a tripod shining from above the base cylinder towards the test specimen (see Figure 5-1).

5.3 EXPERIMENTS: SQUARE SAMPLES

5.3.1 Materials

The specimens had dimensions of 255 by 255 mm and were manufactured with glass with a nominal thickness of either 4 or 2 mm and three kinds of interlayers. A total of eight different test sample series were manufactured (Table 5-1), each containing twelve test specimens which makes a total of ninety-six test specimens.
All the test samples were stored in the impact lab of the department. The relative humidity of the lab varied between 25% and 55%. The square test samples were stored in cardboard boxes, horizontally placed in stacks of six with no spacers provided. All of the square test samples were tested within two months after production. The DG-series used for samples I7 and I8 is one with an increased stiffness compared to the RA and RC series.

Table 5-1 Sample series.

Sample series	Composition	Interlayer material	Interlayer adhesion
I1	44.2	RA	High
I2	44.2	RC	Low
I3	44.4	RA	High
I4	44.4	RC	Low
I5	22.4	RA	High
I6	22.4	RC	Low
I7	22.2	DG	Very high
I8	44.2	DG	Very high

Test series I1 was used to find several ‘standard’ drop heights, resulting in different amounts of damage; it was a process of trial and error but eventually led to the following presets listed in Table 5-2.

Table 5-2 Drop heights.

Drop height	Damage	Description
10 cm	Very low	Only used for I5 and I6 samples.
25 cm	Low	Fracture of the bottom plate and possible upper plate.
40 cm	Medium	Intermediate damage.
55 cm	High	Complete failure of specimen with possible indentor penetration.

5.3.1.a Boundary conditions

The boundary condition of the specimen determines the stress distribution in the specimen. For safety purposes and to avoid vibrations of the specimen it was preferred to have the edges fixed. Thus it is assumed that rotation and displacement at the edges of the test specimen is hampered (but not completely) in every direction.

The glass specimen is clamped by tightening the bolts around the square clamping ring. The 255 mm x 255 mm specimen is visually positioned so that the edges are ideally 7.5 mm supported. This means the free area of the specimen is 240 mm x 240 mm. One has to make sure that the steel clamping components are not in direct contact with each other; this would compromise the required distribution of the clamping pressure.

In Figure 5-8 it is seen that there is a tolerance of 1.66 mm for a 44.2 specimen (I1, I2, I8), so there is definitely enough tolerance for a 44.4 specimen (I3, I4). One has to keep in mind that the tightening of the bolts will also compress the polypropylene rings and the PVB, so an extra reserve must be taken into account.

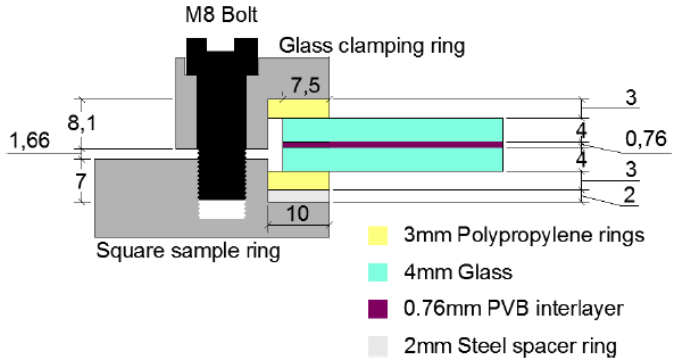

Figure 5-8 Clamping of test specimens I1 to I4 and I8.

The bolts were first screwed hand tight and then tightened by means of a torque wrench. The ultimate torque was set to 15 Nm for each bolt. This torque was applied in three steps: first to 5 Nm, then to 10 Nm and finally to 15 Nm.

The first test specimen (I1_1) cracked at the corners while fastening the bolts and also the second specimen (I1_2) suffered from this phenomenon displayed in Figure 5-9. Delamination of the glass-interlayer surface was observed.

A solution was found in lowering the torque tension to 5 Nm, applied in a single run. After all the bolts were tightened another control tightening round was performed to compensate the drop in bolt tension created by the fastening of the other bolts. A single control tightening round proved to be sufficient.

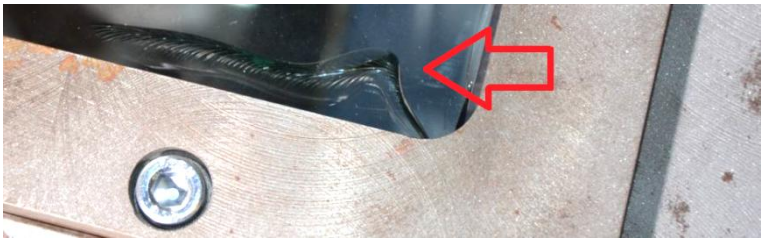

Figure 5-9 Delamination due to too severe tightening of the bolts.

For specimens with thinner glass (I5, I6, I7) an additional 3 mm PP ring was placed under the lower PP ring and a 2 mm steel ring above the upper PP ring.

Another boundary condition applied was a felt fixing, as illustrated by Figure 5-10.

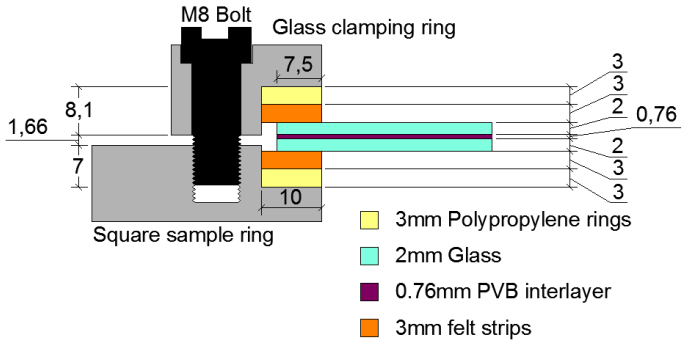

Figure 5-10 Felt clamping of 22.2 specimens.

Eight felt strips with a thickness of 3 mm were used for this setup; the felt is fairly compressible but supposedly thick enough to distribute the clamping forces to the entire specimen edge. Furthermore, it should allow some rotation of the specimen's edges. The torque applied to the bolts was also lowered to 2 Nm to better allow the edge rotation of the specimen.

5.3.2 Test program

The tables listing the different test specimens and their test conditions (impactor drop height, temperature and bolt torque) can be found in Annex B. The second half of the test samples (I5 to I8) were partly tested with different boundary conditions; the boundary conditions as described in 5.3.1.a are added to their tables.

5.3.3 Specimen behaviour during impact

The data processing scripts are capable of extracting the most valuable information. In Figure 5-11 a typical force history plot of a test is shown. The bumps are multiple impactor hits because the impactor does not necessarily penetrate the specimen but can also rebound from it and hit it multiple times until it comes to a stop.

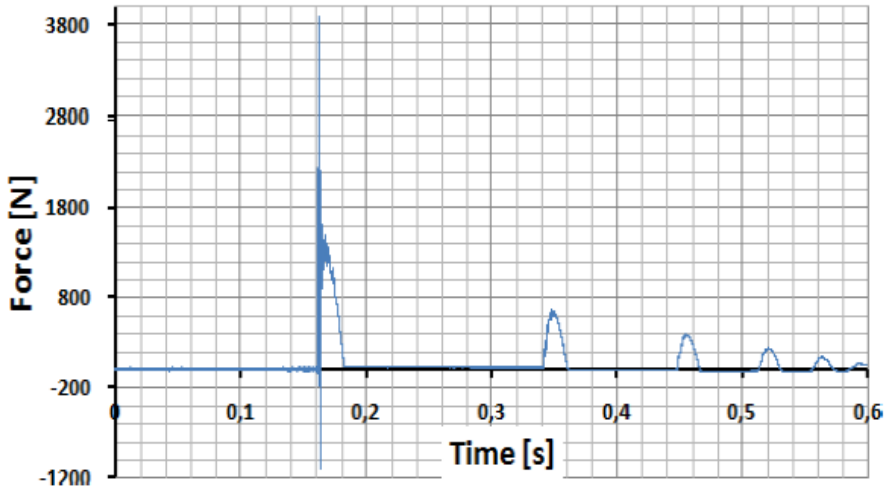

Figure 5-11 General force history plot including rebounds of impactor.

The focus of this study will only be on the first impact, so data needs to be extracted to generate a smaller data matrix which facilitates fast data processing. Figure 5-12 displays a detailed view of the first impact.

This specimen has experienced fracture of both the bottom as well as the upper plate. This is seen in the graph because of the two sudden force drops. Other indications are the oscillations in the force signal after fracture of the upper plate and the long stretched tail of the force signal that follows after it.

This last behaviour is caused by deformation of the interlayer. In this part there are fewer oscillations noticeable and the force signal has a quasi constant value until it smoothly returns to zero, as the impactor is fully rebounded from the specimen. On the high-speed footage it is seen that concentric cracking occurs in this region, thus it can be stated that the formation of these cracks does not significantly influence the force diagram.

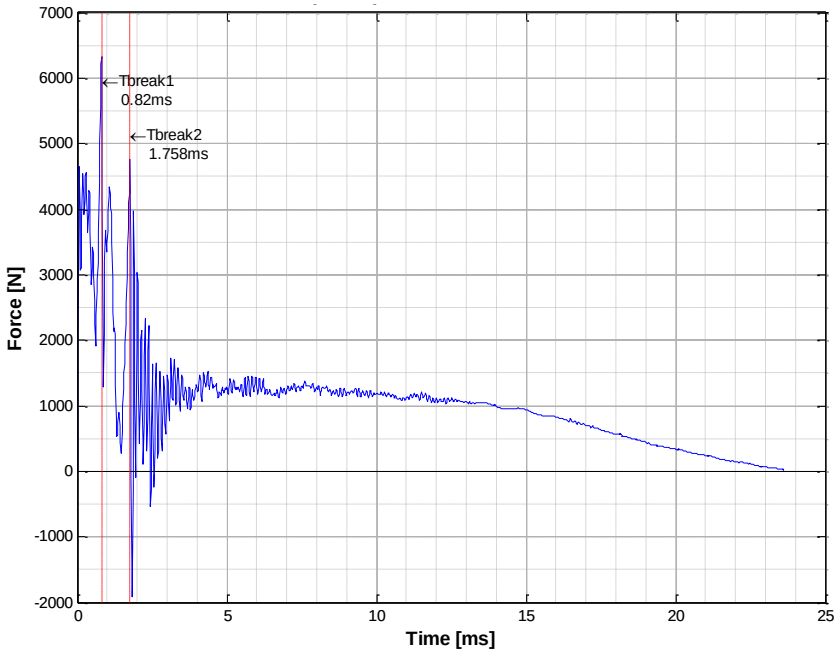

Figure 5-12 Force history plot (drop height 40 cm).

At the start of the impact, the force can often be seen to oscillate while increasing (Figure 5-13). The theory behind these oscillations is that upon impact the centre of the specimen gets propelled forward due to a transfer of momentum. This causes the contact pressure to drop for a certain time until the velocity of the specimen is decreasing again because the low contact pressure does not deliver enough propulsion to maintain the built up speed. Next, the contact pressure increases again and so does the velocity of the specimen. This repetitive interaction is assumed to cause these oscillations.

The above reason explains the force dropping after approximately 0.5 ms and taking back up shortly after. This way the glass specimen is actually submitted to multiple impact hits. The force of each impact gets bigger and bigger due to the fact that the deformation of the specimen is continuously increasing, until a certain point where the bottom glass plate will fracture.

This behaviour is present for all specimens but best discernible for specimens with a delayed fracture of the bottom plate, such as the specimen in Figure 5-14. Presumably, the bottom plate contained very few surface flaws and was therefore exceptionally strong.

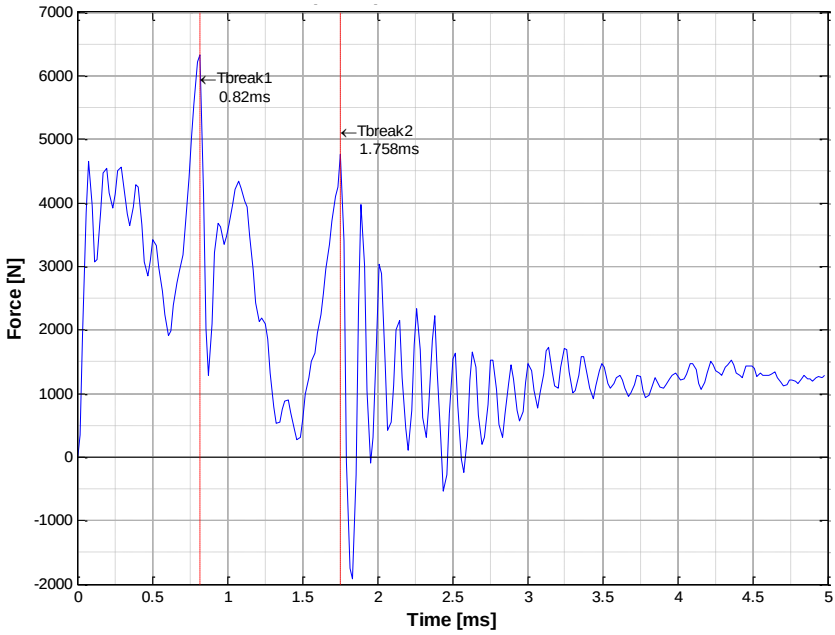

Figure 5-13 Zoomed force history plot, double plate fracture (drop height 40 cm).

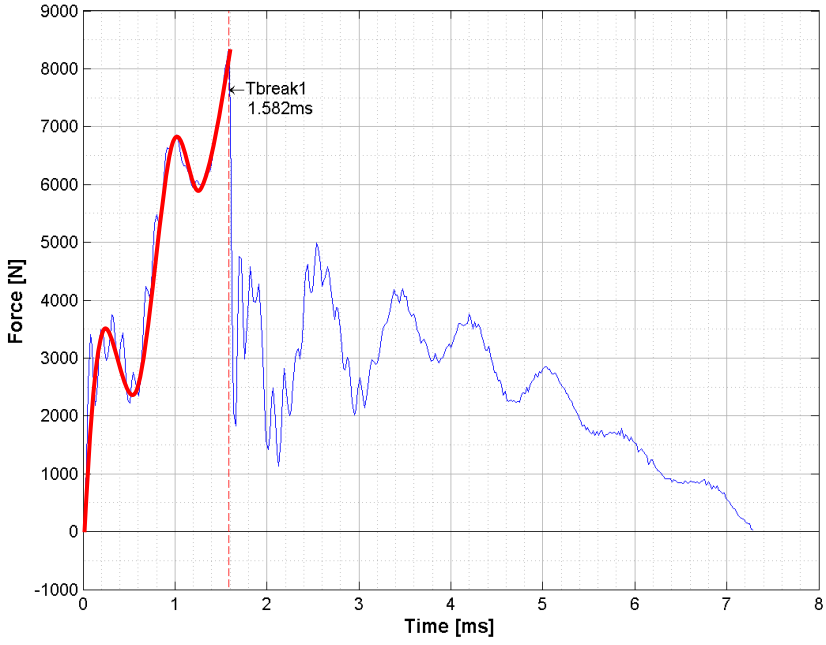

Figure 5-14 Fracture of bottom plate occurring at 3rd impact (drop height 25 cm).

5.3.4 Processing

The performed tests are accompanied by large quantities of data which have to be processed before data interpretation can occur. Therefore, diverse scripts were written and developed in the numerical computing environment "Matlab" by MathWorks.

In the following paragraphs all information that was extracted from the experimental data (and, if applicable, how) is presented. The actual results are discussed in the next sections.

Based on the first force peak the time of impact (t_{impact}) is determined; it is defined as the time of the force data point before the sudden force increase. The end time of the impact (t_{end}) is addressed as the moment where the force is lower than a specific value (30 N) for a long enough time. The data extracted is not the data between those two time stamps but slightly extended for visualization means.

5.3.4.a Impact velocity

The impact velocity is an important parameter as it relates directly to the kinetic energy. Derivation of the discrete displacement signal is not an option because it magnifies the noise present in the signal. The velocity course obtained from a 4th degree curve fitting method is used. Due to bearing friction (and some air friction) the actual impactor velocity is lower than the theoretical.

In Table 5-3 the average impact velocities for the different drop heights are determined and compared to the theoretical (no friction) value calculated as:

$$v_{theory} = \sqrt{2 \cdot g \cdot h_{drop}} \tag{5.1}$$

Table 5-3 Average impact velocities at different drop heights.

Height [cm]	V_{impact} [m/s]	V_{theory} [m/s]	Difference [%]
10	1.20	1.40	-14.3
25	1.92	2.21	-13.1
40	2.52	2.80	-10.0
55	2.99	3.28	-8.8

The values are slightly smaller than the theoretical values, mainly due to friction of the impactor with the guiding rails. This becomes less pronounced for higher drop heights.

When looking at the derivative of the curve fit, the acceleration is seen to decrease in function of time and thus with decreasing impactor height. This suggests an increased friction coefficient on the lower parts of the guiding rails, explaining the lower difference between theoretical and experimental velocity for increasing drop heights.

5.3.4.b Post-impact velocity

The post-impact velocity can be obtained by integrating the acceleration curve or integrating the acceleration curve obtained from the force curve. The integration constant is the velocity at impact. Another way to know the velocity is by derivation of the displacement signal, although this will inevitably lead to noise (Figure 5-15).

The velocity curves obtained from integration are very smooth and alike. However, a choice has to be made between these curves in order to have a velocity reference curve.

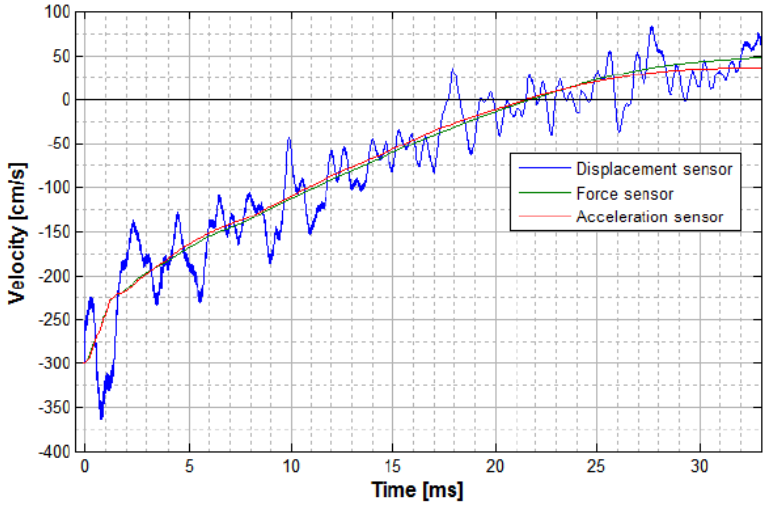

Figure 5-15 **Comparison of the velocity curves obtained from different sensors (drop height 55 cm).**

Further investigation leads to calculation of the displacement signals by integrating the above velocity curves (Figure 5-16). The integration constant is known because at t_{impact} the displacement is zero.

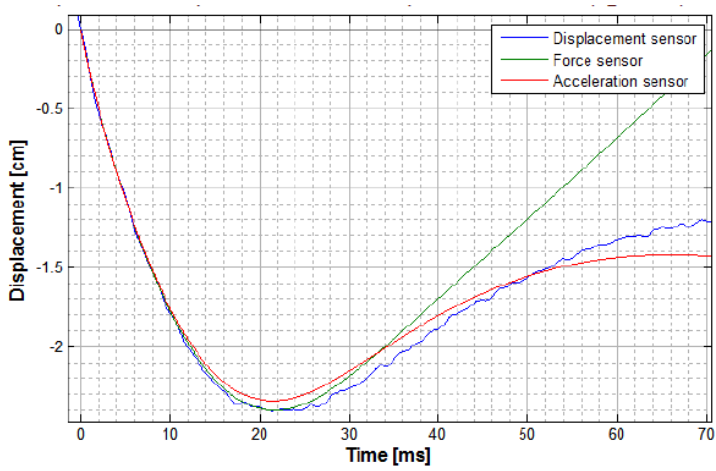

Figure 5-16 Displacement history plot for different sensors (drop height 55 cm).

For most of the specimens it is observed that the acceleration based integrated displacement curve has a better overall fit to the measured displacement and the force based integrated displacement curve has a better initial fit. All of the obtained velocity and displacement curves are stored in the data matrix that results from executing the processing script.

The drift of the force sensor data is due to it no longer being subjected to any force, whereas the accelerometer on the other hand is still experiencing a certain acceleration (of the rebound).

5.3.4.c Determining glass fracture using high-speed images

Each experiment was recorded with at least one high-speed camera. Not only were these pictures interesting from a qualitative point of view, but we tried to extract a maximum amount of quantitative data from them.

For each experiment, the high-speed footage folder contains thousands of ".tif" image files per second recorded, depending on the frame rate of the camera. Most specimens were filmed with a frame rate of 18.000 frames per second. The image and thus time of fracture can be retrieved by detecting a difference between two consecutive frames.

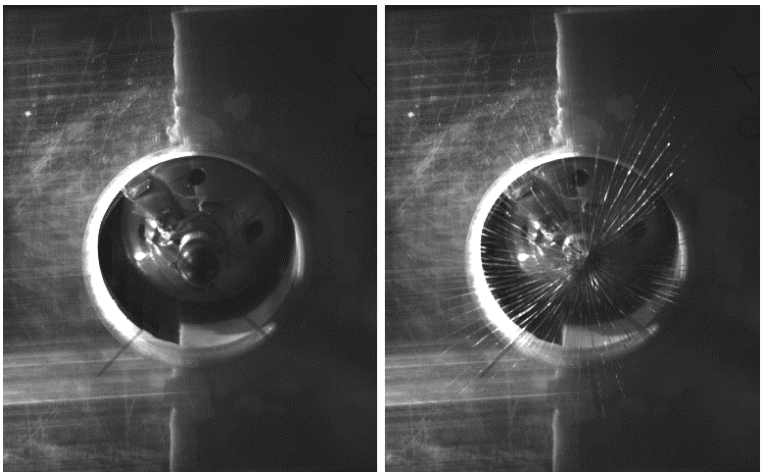

Figure 5-17 **Image before fracture (left) and consecutive image with crack formation (right).**

To compare two consecutive images they can be subtracted from one another. Then the resulting image is converted to black and white, creating a binary image. The operation is displayed in Figure 5-18. The binary conversion is done with high sensitivity for white pixels for tracing means.

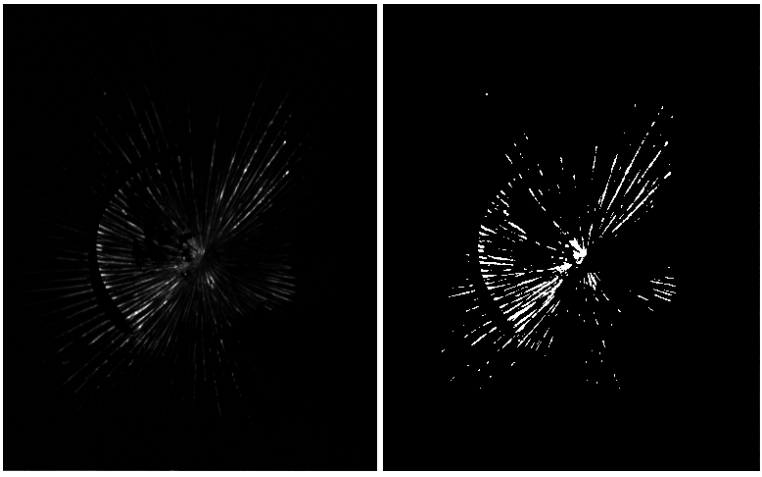

Figure 5-18 **Subtracted image in greyscale (left) and same image converted to binary (right).**

Now the white pixels are counted and if the white pixel to total pixel ratio is greater than a preset value, it is concluded that fracture of the bottom plate takes place.

Fracture of the upper plate is detected in the same way, but it proved to be more difficult because of the fact that crack propagation continuously takes place after fracture of the bottom plate. For specimen I8_4 upper plate fracture is hardly detectable with the naked eye, as can be seen on Figure 5-19. However, the method can easily determine such small differences as illustrated by Figure 5-20.

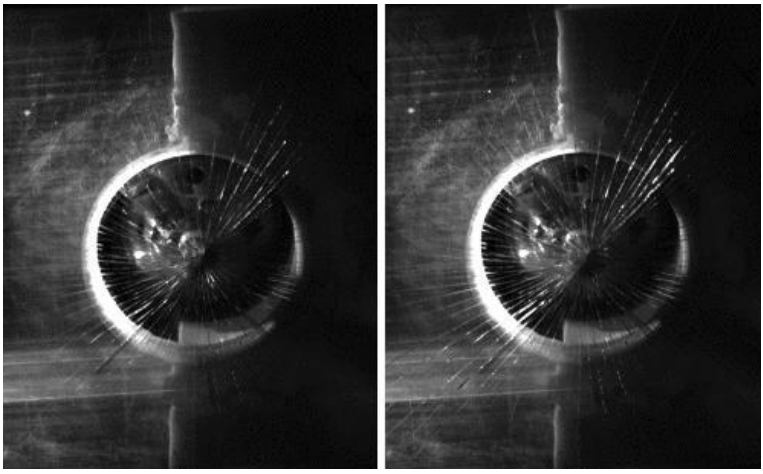

Figure 5-19 **Image before upper plate fracture (left) and consecutive image with upper plate crack formation (right).**

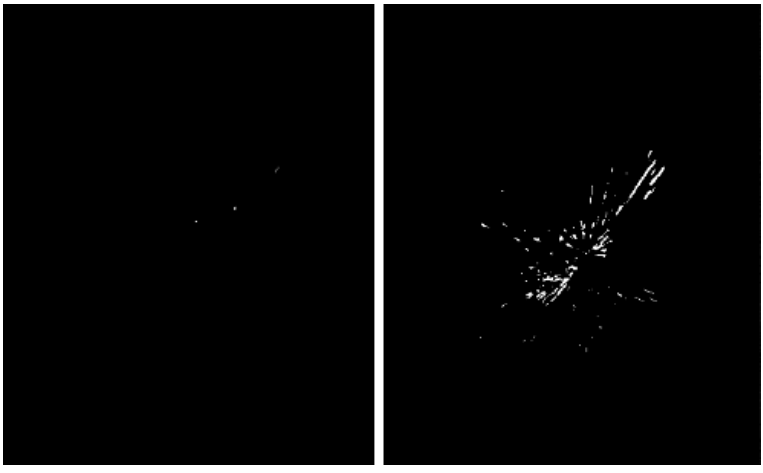

Figure 5-20 **Binary subtracted image before upper plate fracture (left) and consecutive image with upper plate crack detection (right).**

The time passed between bottom and upper plate fracture is 0.28 ms. This is indeed correct: this was verified by observing the force history graph of the specimen.

The program proved to be effective in 85% of the cases. In 12% of the cases detection of fracture was detected a single frame too late. For the other 3% fracture of the upper plate could not be detected, but even visual detection proved to be impossible. The latter only occurred if the fracture of both glass plates occurs quasi simultaneous.

5.3.4.d Fracture number

The problem with visual observation of the fracture pattern and the amount of damage is that it is subjective, one cannot always say with 100% certainty which specimen is damaged 'the most'. For that reason it would be very useful to have a numerically determined fracture number. The idea is to apply high contrast to the sample by means of specific lighting. In this way the fracture lines should be enlightened and the clear unharmed glass fragments should come out darker.

The taking of the photographs occurred on two different times. Test series I1, I2, I3 and I4 were positioned on a specially developed blue coloured stand with adjustable positioning screws. However, this frame was accidentally destroyed, so another one had to be made for test series I5, I6, I7 and I8. This adjusted stand is black coloured and slightly more light reflective. Both setups are compared in Figure 5-21.

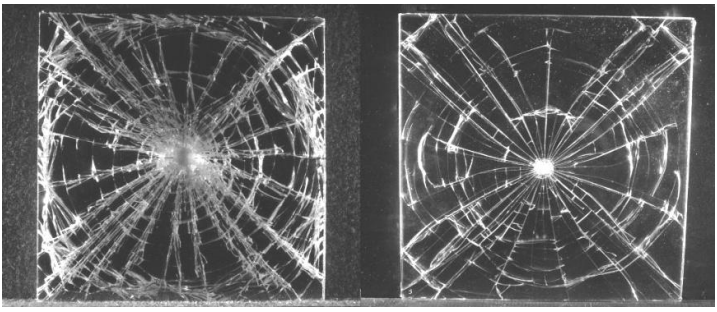

Figure 5-21 Photograph (of different specimens) with first stand (left) and second stand (right).

The edges of the specimen can be detected because they are lighter than the standard background. To detect the edges the image is converted to black and white colouring and a line filter is applied. The total amount of pixels is determined, as well as the

amount of white pixels, which indicate the cracks and thus the damage. The fracture number is now determined as the following ratio:

$$fracture\ number = \frac{white\ pixels}{total\ pixels} \tag{5.2}$$

The fracture number is situated in the interval [0,1], the higher the number the more the specimen is damaged. So a fracture number equal to unity means that 100% of the pixels are white and the entire surface is cracked or – more likely – crushed.

Another interesting number is the centre fracture. It is calculated in the same way as the fracture number, but now only the centre region of the specimen is considered. The centre region is defined as a circle; its diameter is half the length of the side and its centre collides with the centre of the specimen. This region is displayed in Figure 5-22 by a red circle.

Figure 5-22 Processed picture with central region indicated by red circle.

5.3.4.e Collection of all data

The script starts with analyzing the force sensor signal starting from the point of impact. In the end, for each specimen the following values (Table 5-4) were extracted automatically from the data files.

Table 5-4 Extracted values for each specimen.

Name	Description
t_{impact}	Time of impact
t_{end}	End of impact
$t_{duration}$	Time in milliseconds between t_{impact} and t_{end}
v_{impact}	Velocity of the impactor at time of impact
$E_{kin,impact}$	Kinetic energy of impactor at time of impact, $E = mv^2/2$
t_1	Time of fracture bottom plate
t_2	Time of fracture upper plate
Intertime	Time span between both glass plate fractures
F_{max}	Maximal force at beginning of impact
F_1	Force value at fracture of bottom plate (t_1)
F_2	Force value at fracture of upper plate (t_2)
v_1	Velocity at fracture bottom plate (t_1)
v_2	Velocity at fracture upper plate (t_2)
v_{end}	Rebound velocity at t_{end}
δ_{max}	The maximal displacement of the impactor caused by the deflection of the specimen
$t_{max.\ disp.}$	Time of maximal displacement
$Workt_1$	Work performed until t_1
$Workt_2$	Work performed until t_2
WorkR	Work performed by the rebound
Frame rate	Frame rate of the high-speed footage
Framebreak	Frame number when bottom plate fractured
Double break	Check if both plates are broken, based on a positive value of the intertime
Fracture number	The total fracture number of the post-fracture specimen
Centre fracture	The centre fracture number of the post-fracture specimen
Fracture ratio	The ratio of the fracture number to the centre fracture

When strain gauges were used, their data was not taken into account in the script. Due to the low occurrence of these measurements, they were manually processed.

5.3.5 Results & discussion

The reader is referred to Annex B for a detailed discussion of the results, which, unfortunately, did not yield a single parameter for which a noticeable difference between adhesion levels could be discerned. However, the most important aspects of the results are summarized here.

Within a single test series and for fixed testing conditions, the test specimens exhibit quasi identical pre-fracture behaviour, meaning the test set-up is capable of producing repeatable results. Fracture occurs first for the bottom plate, the occurrence of this event is characterized by a significant drop in the force signal.

Bottom plate fracture will occur during the first, second or third impactor hit, for which the maximal developed contact force increases respectively. However, bottom plate fracture does not necessarily occur when the contact force is greatest. In some cases the specimen failed between two consecutive impact hits. Probably the previous impactor hit did not fully develop a fully grown cracking nucleus in the glass and fracture was postponed.

After bottom plate fracture the contact force may even be higher than before failure, depending on the residual impactor energy. Only radial cracking of the bottom plate is observed until this moment. It was derived from strain gauges that even though fracture of the bottom plate had occurred, still 80% of the strain value of the upper plate is also present in the bottom glass fragments. Therefore the integrity of the specimen is not severely affected by the occurrence of this event.

Failure of the upper plate is comparable with that of the bottom plate. However, now the residual flexural strength of the specimen is almost completely destroyed. A very big dip in the force signal is noticeable, followed by severe oscillations. These oscillations damp out by the presence of the interlayer, which absorbs the residual impactor energy. The latter is noticeable by the belly shape of the force signal after the moment of upper plate fracture. During this process the deformation of the specimen increases; forming concentric cracks in both glass plates. Neither the forming of these cracks nor the delamination of the glass has an influence on the force signal.
If no piercing of the interlayer occurs, then the impactor is rebound by the release of the residual elastic energy stored in the test specimen.

For increasing drop heights, the forces are greater and the occurrence of events is faster. The maximal displacement also increases for greater drop heights. Increasing drop heights also inflict more damage to the glass plates, thus creating a denser crack pattern.

There was no significant or consequent influence regarding the sensor data and their derived quantities for the applied boundary conditions. However, fracture patterns can determine the preset boundary condition.

Thicker glass increases the moment of inertia and thus the flexural stiffness of the specimen. This creates higher impact forces and accelerates the occurrence of events. The maximal displacement naturally decreases for greater glass thickness and more energy is dissipated before total specimen failure. Thus less energy needs to be absorbed by the interlayer. Furthermore, the residual post-destructive integrity of the thicker glass samples is greater.

Doubling the number of interlayers does not significantly affect the pre-fracture behaviour. However, for the post-fracture behaviour the impact duration and the maximal displacement are smaller due to the increased resistance of the interlayer. The energy absorption capacity is also increased for greater thicknesses, resulting in a reduced risk of object penetration.

No significant and consistent influence was observed for a change in interlayer adhesive bonding strength**.**

The use of the structural interlayer increased the stiffness of the test specimens. Therefore the forces and the work performed before fracture are greater. The maximal displacement and the duration are smaller and the occurrence of events is accelerated. Piercing of the interlayer and delamination of glass fragments is more likely to occur if the structural interlayer is used.

5.4 EXPERIMENTS: CIRCULAR SAMPLES

5.4.1 Material and test program

Circular test specimens have the advantage to be axisymmetric. When applying a circular load with its centre on the axis of symmetry of the specimen the stress distribution before fracture will also be axisymmetric. This can vastly improve numerical modelling of the problem. Another advantage of using circular specimens is the absence of torsion stresses, which are present in the corners of the square test specimens

For the circular test samples the tin side of the glass plates makes contact with the interlayer, which, theoretically, weakens the interlayer bonding. All of the eighteen circular specimens had the same composition as displayed in Table 5-5.

Table 5-5 Properties circular test specimens.

Property	Value
Diameter	470 mm
Composition	44.2
Interlayer	PVB: Saflex RB41
Edge finishing	Chamfered and ground

The circular test specimens were made available by AGC Glass Europe. Each specimen was marked with a product label which displayed the product information. This will prove important later on. The circular samples were positioned quasi vertically, tilted at a small angle to stabilize their position and separated with soft glass spacers. The circular samples were tested within seven months after production.

Shortly after testing began, concerns arose about the very large scatter on results with some specimens breaking at heights as low as 50 cm while others did not break at the highest possible drop height of the SSDW (200 cm) for these tests.

Since all specimens had the exact same composition this was not to be expected and we felt this could not be attributed to differences in glass strength solely. In the end, the product label sticker – which was removed prior to each test – proved to be a clue to the answer.

Many tests had already been performed before this different behaviour in glass plate strength was discovered. Test sample 4 was the first that was oriented with its sticker side downwards and did not experience fracture. Specimen 6 was tested at a drop height of 175 cm, 190 cm and 200 cm without breaking. The triggering of the sensors did however not occur properly because of the problems with the displacement sensor. No data is available for these tests and therefore they are not included in the test program tables (see below). After the testing of sample 7 the underlying cause of the observed phenomenon was discovered and validated: the sticker side glass plate is significantly stronger than the non sticker side glass plate.

AGC, the supplier, was contacted but they could not provide an answer as to why this behaviour manifested itself. They could not think of steps in the manufacturing process that might cause this dependency on the ‘sticker side’.

The complete list of performed tests can be found in Annex B.

5.4.2 Processing

The overall course of a typical force history curve is much smoother than compared to one of a square specimen. This is to be expected because of the deformable indentor. The first moment after impact there is a little force shock followed by small oscillations. For approximately 1.5 ms after impact the force is relatively low and quasi constant, after which it increases.

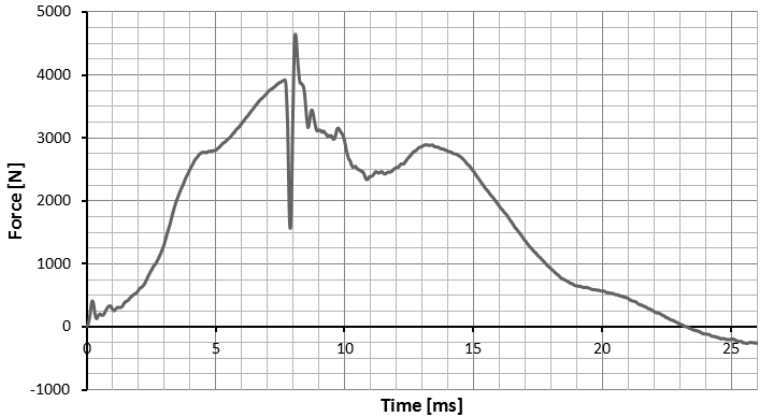

Figure 5-23 Force history plot for circular specimen.

The deformation of the indentor causes the contact area to enlarge until a certain point. Due to the occurrence of this deformation, the impact point can be determined on the high-speed footage in contrast to the test with the hard indentor. If the corresponding high-speed footage is observed one can see that it takes 1.5 ms for the indentor to deform in such a way that the spherical cap has become flat and is in full contact with the test specimen. This explains the relatively low force plateau for the first 1.5 ms.
Until the point of bottom plate fracture the body of the impactor expands laterally without enlarging the contact area. On Figure 5-24 the evolution of the impactor during an impact is illustrated.

Because the deformation of the indentor is important for modelling purposes, it was filmed in side view. This was done for specimen 4 with a drop height of 150 cm, Figure 5-25 illustrates the shape of the indentor at rest and at maximal compression. Additionally, the movie allows observing the shock wave of the impact travelling through the silicone indentor and back.

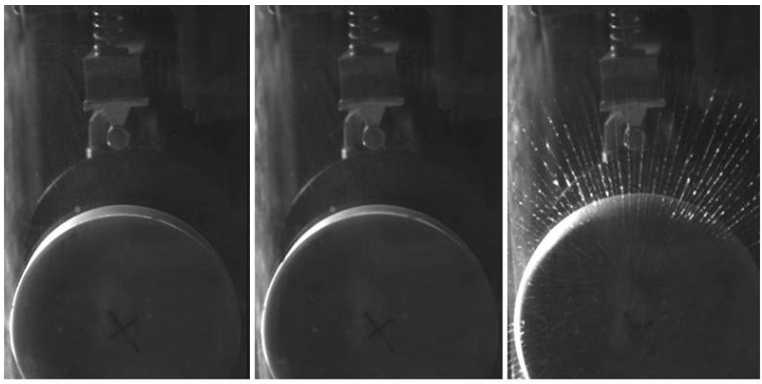

Figure 5-24 **High-speed footage: impact of the soft indentor on upper plate (left), moment of full contact (middle) and glass fracture (right).**

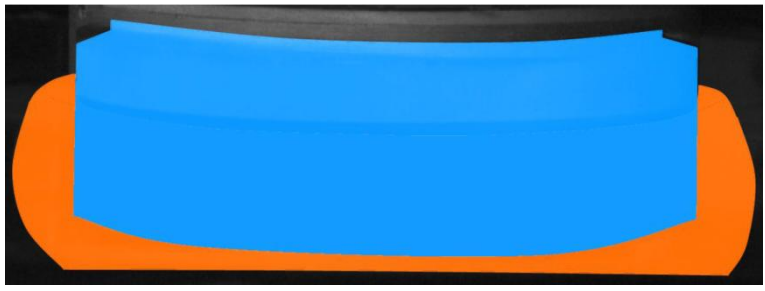

Figure 5-25 **Shape of the soft indentor at rest (blue) and at maximal compression (orange).**

5.4.3 Experiments & discussion

Because all specimens have the same composition only differences in test setup parameters are discussed.

5.4.3.a Drop height

Elastic tests were performed on specimen 16 with its sticker side downwards. The impactor drop height was increased from 20 to 160 cm in steps of 10 cm. The obtained force sensor data is plotted in function of time on Figure 5-26.

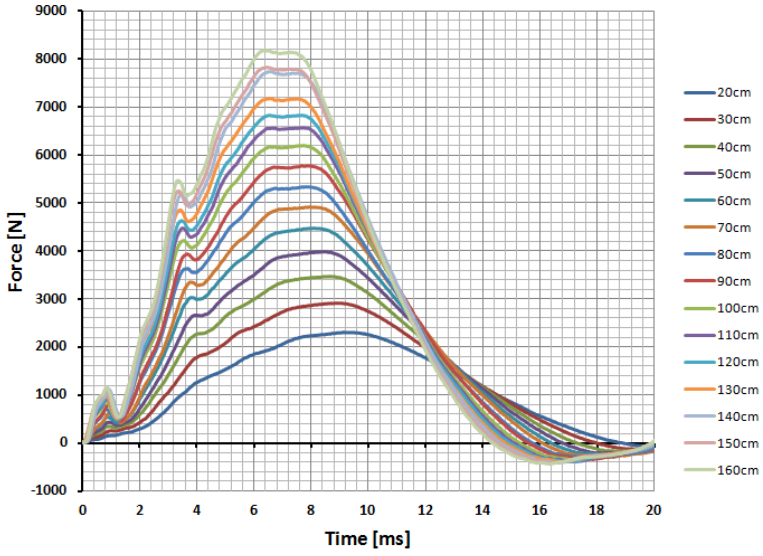

Figure 5-26 Force history plot for increasing drop height.

Higher drop heights result in higher forces. If no failure occurs, higher drop heights result in shorter contact times. Figure 5-27 visualizes the exponential relation between the impactor drop height and the impact duration.

Elastic energy builds up more quickly by the deformation of the specimen and the indentor at high contact forces. Therefore the rebound also takes place earlier. For specimens which exhibit fracture, the impact duration is larger for higher drop heights, as seen for the square test samples.

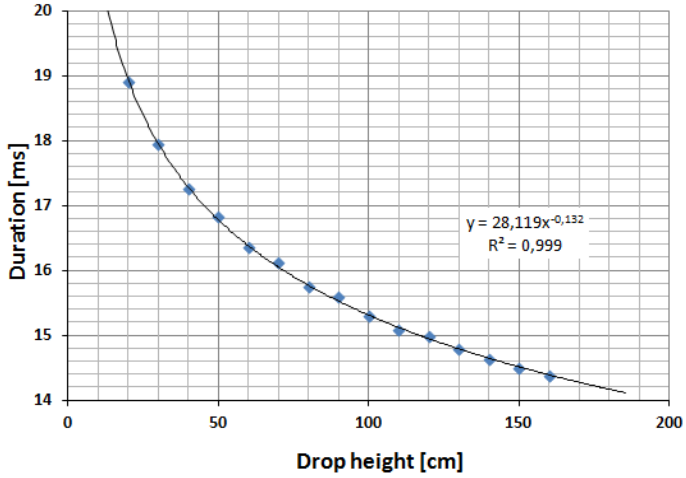

Figure 5-27 Duration of impact.

Figure 5-28 compares the force history curve of specimen 16 for a drop height of 20 cm, for both sticker orientations. The pre-fracture behaviour is quasi identical. Note that the specimen had been tested to a height of 160 cm before without failure.

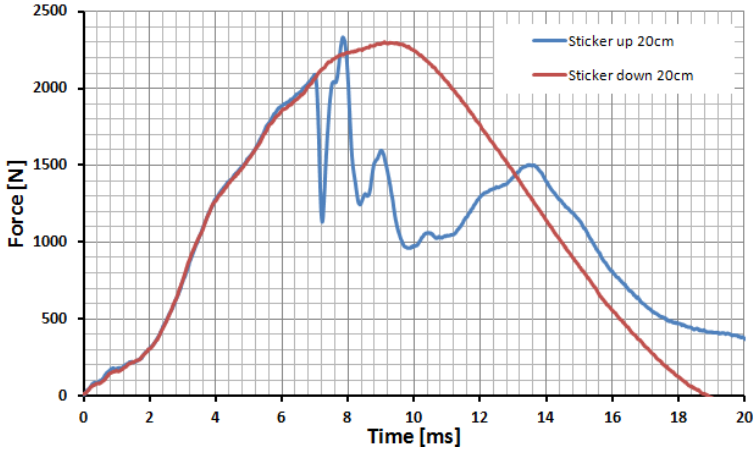

Figure 5-28 Comparison of the force history for specimen tested at drop height of 20 cm with its stickers side oriented upwards and downwards.

A single test specimen 4 was also equipped with two strain gauges and was tested for increasing drop heights. The strain gauges were placed on the upper plate (non sticker side) at radius/2 from the edge and measured strains in the radial and tangential direction. The specimen failed for a drop height of 80 cm with its sticker

side oriented downwards. However, it had been tested multiple times before at drop heights of up to 160 cm without failing. The tangential strain is represented in Figure 5-29. The great peaks at around 16 ms are due to electrical disturbances caused by the release mechanism.

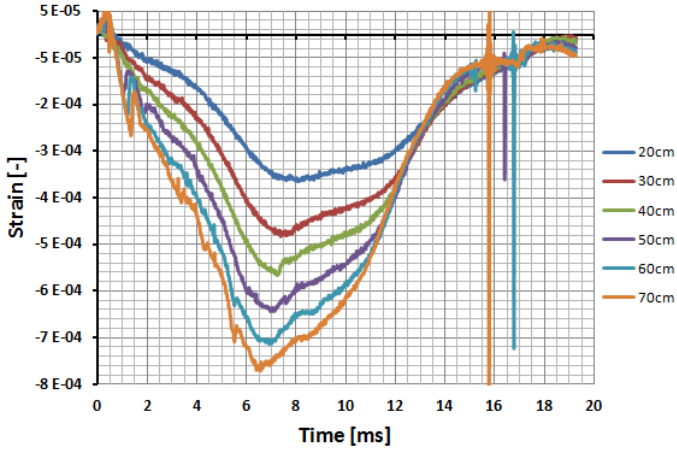

Figure 5-29 Tangential strain upper plate history plot.

5.4.3.b Torque of clamping bolts

The degree of edge fixing was verified by testing one specimen at different fixing pressures by adjusting the bolt torque. This was done for test specimen 9 with its sticker side downwards for a testing height of 120 cm. The different force history plots obtained from these tests are compared in Figure 5-30.

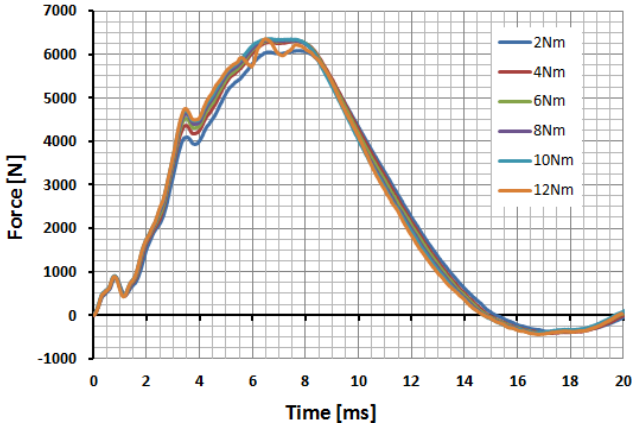

Figure 5-30 Force history plot for different bolt torques.

It is observed that the acting forces are only slightly greater for greater clamping pressures. This is explained by the increasing resistance against edge rotation; which results in a stiffer behaviour of the specimen.

The specimen failed at a bolt torque of 12 Nm. Remarkably it failed only at the edges of the upper plate as can be seen on Figure 5-31. This explains the fluctuating behaviour of the corresponding force curve (orange line) on the graph.

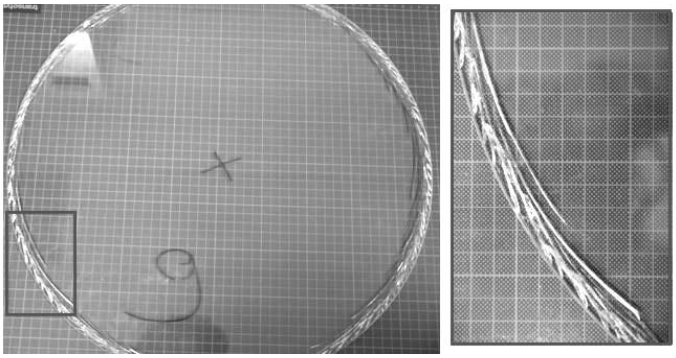

Figure 5-31 Edge fracture specimen 9.

When plotting the force in function of displacement for these tests (Figure 5-32), another interesting phenomenon can be observed: hysteresis. This behaviour is typical for visco-elastic materials (PVB and the indentor), but is also caused by the friction of the bearings along the guidance rails, experienced by the impactor during the impact. The area that these curves describe is a measure for the energy dissipated by both mechanisms during the impact: on average this is 5.7 J. This is 5.9% of the total kinetic energy of the impactor upon impact (97.0 J).

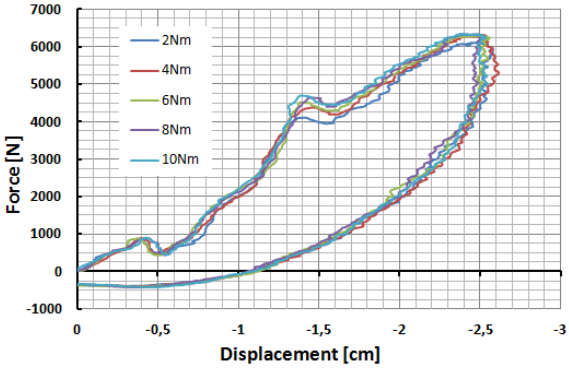

Figure 5-32 Force in function of displacement for different applied bolt torques (specimen 16).

5.4.4 Conclusions circular specimens

Multiple specimens were tested elastically for a number of times. The testing history of the specimen did not influence the elastic behaviour of future tests. However, in several cases the specimen did eventually fail after numerous tests had been performed.

Due to the great deformation capacity of the soft indentor the force history curves are much smoother than for the hard indentor used with the square samples. The silicone indentor imposes an area load on the specimen which results in a crackled fracture pattern and non-concentric crack initiation nuclei of the bottom and upper glass plate.

For increasing drop heights, the forces are greater and the occurrence of events is faster. For elastic impact testing the load duration is shorter and the maximal displacement is greater for greater drop heights.

Increasing the bolt torque had a minimal effect on results.

5.5 EXPERIMENTS: SOLUTIA DROP TOWER

At their Quality Control lab, Solutia also has a drop tower facility, albeit with a steel ball being released instead of an instrumented guided impactor. With it, the Mean Break Height (MBH) of a laminate can be determined. The Mean Break Height is defined as the ball drop height at which 50% of the samples would hold the ball and 50% would allow penetration. This provides a more quantitative measure of laminate impact strength instead of a mere pass/fail criterion.

A 1 kg steel ball is used to impact 30 by 30 cm specimens. The specimens should be in the 20°C room for an hour before testing. For a successful test, it is necessary that the ball goes through the laminate, as 2 magnetic field detector coils are placed beneath it, separated by a known distance, which can detect the passing ball and subsequently calculate the residual velocity after impact.

Knowing the energy of the ball before impact (which can be calculated based on the drop height) and measuring the residual energy after impact, the energy absorbed by the interlayer can be calculated as the difference between both. The schematic of the set-up is given in Figure 5-33.

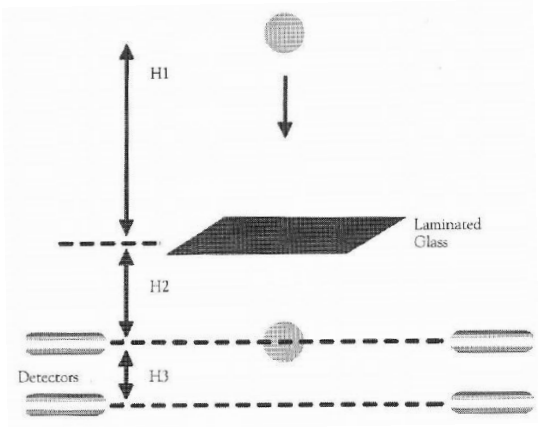

Figure 5-33 Schematic of Mean Break Height test set-up.

Based on this, the Mean Break Height can be calculated as:

$$V_{in} = \sqrt{2g(H_1 + H_2)} \tag{5.3}$$

$$V_{out} = (H_3/t) \tag{5.4}$$

$$MPV = \sqrt{V_{in}^2 - V_{out}^2} \tag{5.5}$$

$$MBH = \frac{MPV^2}{4g^2} \tag{5.6}$$

With V_{in} the velocity of the ball at the top coil with no test laminate, V_{out} the velocity at the top coil after the ball penetrates the laminate, H_1 the drop height, H_2 the distance between the laminate and first coil, H_3 the distance between the two coils and t the time it takes to travel the distance between both coils.

To check whether or not there was a difference in impact behaviour due to a difference in adhesion level and interlayer thickness (as it could not be discerned during the SSDW tests described in paragraph 5.3), several specimens were produced and tested using the Mean Break Height set-up at Solutia.

Four types of specimens were made, each with a different interlayer configuration: (i) one (0.38 mm) interlayer with high adhesion A1, (ii) one low adhesion interlayer C1, (iii) 2 high adhesion interlayers (0.76 mm) A2 and (iv) 2 low adhesion interlayers C2. All specimens were made with 2 mm glass plies.

Of each type four specimens were made and tested at the maximal drop height of 9 metres. The results are listed in Table 5-6.

Table 5-6 Test matrix and Mean Break Height.

Specimen	V_{in} [m/s]	V_{out} [m/s]	MPV [m/s]	MBH [m]
A1_1	13.1	8.3	10.2	5.28
A1_2	13.1	9.3	9.3	4.40
A1_3	13.1	8.6	9.9	5.03
A1_4	13.1	9.7	8.8	3.98
AVG.	13.1	9.0	9.6	**4.67**
ST.DEV.	0.0	0.6	0.6	**0.59**
C1_1	13.1	5.3	12.0	7.33
C1_2	13.1	5.2	12.1	7.42
C1_3	13.1	7.7	10.6	5.78
C1_4	13.1	3.1	12.8	8.30
AVG.	13.1	5.3	11.9	**7.21**
ST.DEV.	0.0	1.9	0.9	**1.05**
A2_1	NF			
A2_2	NF			
A2_3	NF			
A2_4	NF			
C2_1	NF			
C2_2	NF			
C2_3	NF			
C2_4	NF			

While the scatter on the results is relatively high, a clear trend is visible between both types of adhesion. The low adhesion specimens had the highest impact resistance (i.e. the highest Mean Break Height) with an average of 7.21 m needed to – theoretically – penetrate half of the specimens. For the high adhesion laminates this was only 4.67 m.

The ball did not pierce the specimens (No Fail, NF) with a double (0.76 mm) interlayer A2 and C2. Consequently no Mean Break Height could be calculated. It would exceed the maximal drop height of 9 metres.

5.6 CONCLUSIONS

All of the test samples contained two outer annealed glass panes combined with one or two 0.76 mm PVB interlayers. The investigated sample parameters were: interlayer adhesive bonding strength, interlayer stiffness, interlayer thickness and glass thickness. The main test parameters are the impactor drop height and the boundary conditions of the specimen. Below the most important observations for the different parameters are summarized.

The interlayer adhesive bonding strength did not significantly influence any of the test results despite a relative large difference in adhesive strength, as evidenced from the ball drop tests at Solutia.

An increased interlayer stiffness enhances the structural integrity of the specimen. However, it also imposes a greater risk of small object penetration and detachment of possibly dangerous glass fragments.

Doubling the interlayer thickness reduces the risk of small object penetration, but did not yield significantly different results compared to a single thickness laminate.

Doubling the glass thickness substantially enhances the structural integrity and the impact resistance of the specimen. Additionally, the post destructive integrity of these specimens is greater

An increased impactor drop height creates a denser fracture pattern, increases the risk of object penetration and reduces the post destructive integrity of the specimens.

The applied boundary conditions did not significantly influence the pre- and post-destructive behaviour of the specimen. However, the acquired fracture pattern is very distinctive.

Despite many attempts to find other indicators for laminate adhesion strength of interlayer thickness based on experimental results, none were found.

From the experiments conducted at the drop tower facility of Solutia, it was made clear that in order to be able to differentiate between a high and low level of adhesion the laminates must be loaded very severely resulting in complete failure. Only then do the distinctive traits of the different interlayers become apparent. This was not possible with the small-scale drop-weight set-up at our department.

5.7 INTERACTION WITH MODELLING (PELFRENE [2])

Pelfrene studied the fracture of glass extensively, based on the drop weight impact tests on a small, circular specimen of De Pauw (tests not described in this chapter); in this case, the elastic response only agreed with the experiment when the deformable clamping rings were modelled as such. Subsequent fracture simulations showed that fragmentation of the modelled glass part requires the stress field due to bolt clamping to be taken into account as well.

The most encountered simulation technique for the cracking of structural and automotive glass panels is that of element deletion. This technique is relatively easy to implement, but far from perfect; it shows tremendous mesh sensitivity, leaves cracks as wide as an element's length and is unable to capture gradients near

the crack tip. But the element deletion method can be used for thin-walled structures under dynamic loading and does allow crack branching and coalescence. Three different approaches for the formulation of the fracture criterion and damage evolution are evaluated for unit elements and for the drop weight impact tests on glass disks:

- Immediate deletion with no damage evolution (implemented as VUMAT).
- Hillerborg model (built-in material model in ABAQUS).
- Crack delay model (implemented as VUMAT): this material model is designed to overcome issues experienced with other approaches and is intended specifically for glass cracking. It is based on the fact that the evolution of damage is not instantaneous. The limiting damage rate is derived from the maximum crack propagation velocity, and aids in preventing overly high stress oscillations in the simulated glass fragments. Furthermore, crack directionality is taken into account and only physical constants are used as input for the material model.

Also the use of cohesive zone elements has been considered for dynamic fracture. This approach requires the insertion of interface elements at all interelement boundaries, for which an efficient program has been developed. However, the cohesive zone, initially with zero thickness, has an additional stiffness that distorts the elastic response to an impact loading. This can be solved by assigning the interface elements a small, finite thickness. Upon fracture, cracks initiate at many locations, rather than a few propagating cracks. Subsequently, the damage in the cohesive zone does not reach its ultimate separation at most of the cohesive elements, which further act with reduced stiffness and fragmentation no longer occurs.

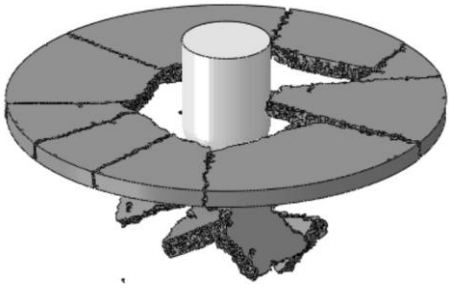

Figure 5-34 **Fracture of simulated 4xØ100 mm glass plate with *Brittle Cracking at t = 10 ms for refined tetrahedral elements mesh with compressive clamping conditions.**

For the simulation of laminated specimens tested in §5.4, a mesh was made for a plate of 470 mm in diameter, with two glass plies, each 4 mm in thickness, and a PVB interlayer of 0.76 mm. Since this configuration no longer allows to construct a tetrahedral mesh in a consistent manner, it was opted to use 6-node elements as a compromise. In this way elements layers can be stacked in thickness direction. The PVB and each of the glass plies consist of 4 element layers, and the cohesive zones use 1 (zero-thickness) element layer. With a characteristic element length of 1 mm, the laminated glassplate consists of a total of 1 436 792 elements.

It was quickly seen that the hard contact with the rigid impactor tip can not be handled by the element deletion method in a laminated configuration, with elements failing only locally at the impactor tip, causing a punch-through rather than cracking. An alternative impactor tip, made of rubber for a distributed contact zone, is better handled. In the model, the modified impactor (now 7.6 kg) is dropped from a height of 1.5 m. Again, clamping is simulated between outer, steel rings and inner, polypropylene rings.

As would be expected, the simulation results show that, after an initial elastic response, radial cracking at the bottom glass ply quickly leads to fragmentation, shortly followed by the top glass ply. Then, concentric cracks appear in both glass plies. At a later stage, also some local delamination at the interfaces between glass and PVB becomes visible.

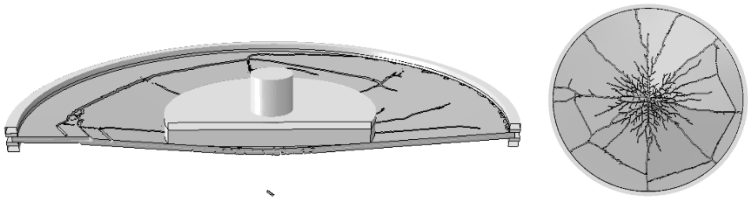

Figure 5-35 **Snapshot of the simulation of drop weight impact on laminated glass, at 15 ms after impact: 3D cut view (left) and bottom view (right).**

In analogy with Nourry and Nugue [3] an energy balance can be made for the simulation, containing the contribution of the mechanical energies to the dissipation of the input kinetic energy. This includes: glass fragmentation, viscoelastic deformation of the interlayer and delamination. In accordance with the results of Nourry, it is seen that dissipation by glass fracture is very small (less than 1%) with respect to the initial kinetic energy. The major part of energy dissipation is accounted for by interlayer deformation and delamination, which are, of course, dependent on fragmentation of the glass.

5.8 REFERENCES

[1] S. De Pauw, "Experimental and Numerical Study of Impact on Window Glass Fitted with Safety Window Film," Doctor in de Ingenieurswetenschappen: Werktuigkunde-Elektrotechniek PhD, Department of Material Science and Engineering, Mechanics of Materials and Structures, Ghent University, Ghent, 2010.

[2] J. Pelfrene, "Numerical analysis of the post-fracture response of laminated glass under impact and blast loading," Doctor in de Ingenieurswetenschappen: Werktuigkunde-Elektrotechniek PhD, Department of Material Science and Engineering, Mechanics of Materials and Structures, Ghent University, Ghent, 2016.

[3] E. Nourry and J.-C. Nugue, "Impact on Laminated Glass: Post-breakage Behaviour Assessment," presented at the Glass Processing Days 2005, Tampere, Finland, 2005.

Chapter 6 IMPACT: EN 12600

Overview

In this chapter a test campaign with a standardised EN 12600 set-up is discussed. First, the set-up, as modified and improved by Stijn De Pauw, is described, followed by an in-depth study on the twin tyre impactor, including measuring the pressure applied by the tyres to the glass plates and the impact velocity. Next, the results from impact tests on laminated glass panels with different interlayers are discussed. All numerical work in this chapter, which is added for a good understanding, was done by Pelfrene [1].

Similar to the Small-Scale Drop Weight (SSDW) set-up from the previous chapter, an existing but inadequate set-up was available for the EN 12600 tests in the PhD of Stijn De Pauw [2]. Again the set-up was improved so experiments could take place. This retrofit included measures such as the instalment of necessary safety precautions (e.g. fencing around the set-up, a glass collecting box to catch falling particles, an ergonomic lift-and-release mechanism, a breaking system to prevent second impact), a new clamping system using pneumatic cylinders (Figure 6-1) and a re-designed impactor. For a detailed description of these adjustments, the author refers to the work of De Pauw [2].

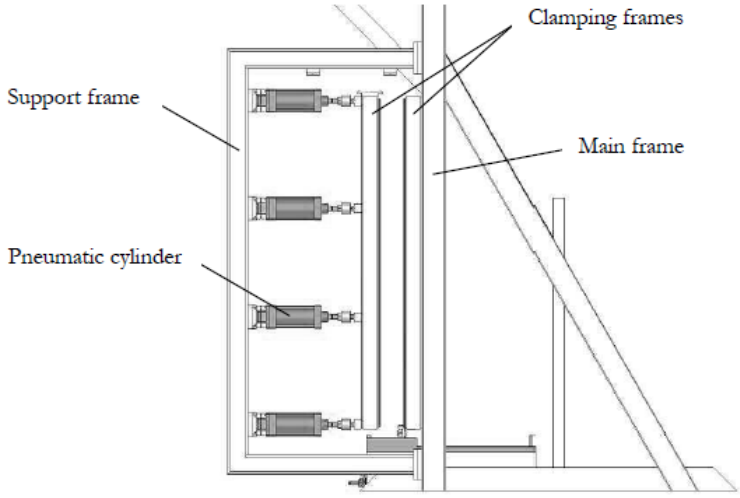

Figure 6-1 CAD design side view of modified set-up with pneumatic cylinders [2].

The most important, specific (i.e. not standard related) characteristics of the set-up, needed for a good understanding, will be summarized in the next section. For a general introduction to the set-up, the author refers to Chapter 5.

6.1 TEST SET-UP

A photograph of the current set-up can be seen in Figure 6-2 (and a detail of the twin-tyre impactor in Figure 6-3). One part that is not mentioned in the EN standard but was added for an increased usability is a swing arm to lift the pendulum impactor.

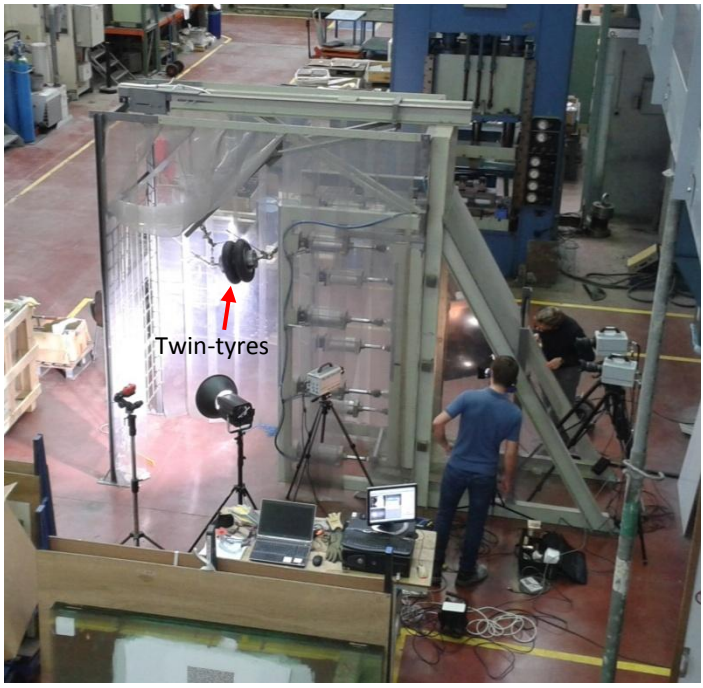

Figure 6-2 **EN 12600 set-up with twin-tyre impactor suspended, high-speed cameras, lighting and computers.**

Figure 6-3 **Detail of the EN 12600 set-up.**

The set-up itself does not encompass any instrumentation, although some has been added in this research (see further).

6.1.1 Calibration

Every EN 12600 set-up needs to be calibrated, in order to compare results between different set-ups (or be allowed to deliver certification proofs for the industry). A tempered glass panel is used for this process. The strain values in the middle of the panel for a number of given drop heights must lie within a small range of acceptable results. Once the set-up fulfils these requirements, it is considered calibrated and other glass specimens can be tested.

The horizontal and vertical strains were measured at the centre of the glass plate by use of strain gauges. Figure 6-4 shows the maximum strains in the experiment and in the simulation, along with the boundaries prescribed by the standard, for different drop heights.

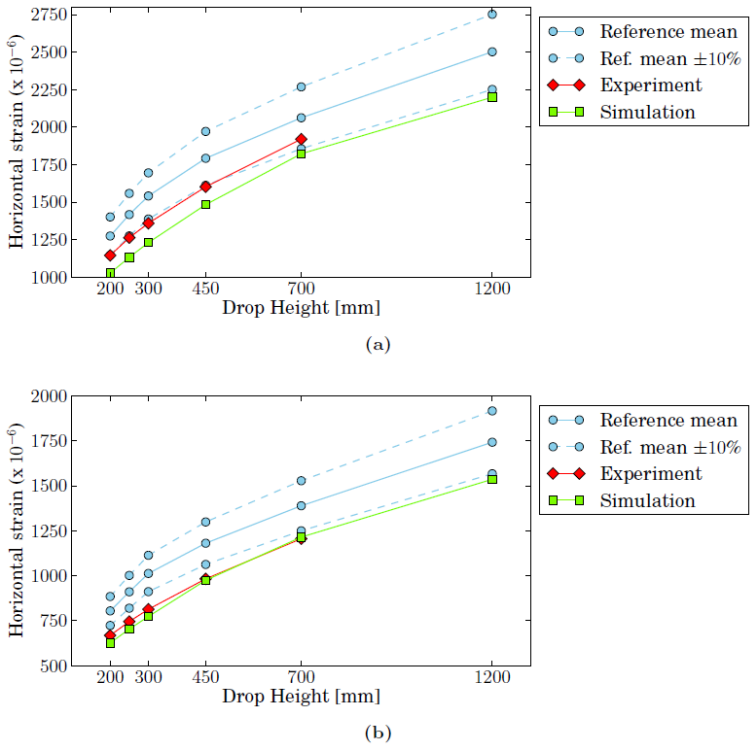

Figure 6-4 **Maximum strain at the middle of the backside of the calibration plate for different drop heights: (a) horizontal strain and (b) vertical strain.**

The measured strains are slightly lower than required by the standard. This might be ascribed to a slight deviation from the standard in the design of the impactor, in the sense that a part of the deadweight is located between the two rims to avoid bending of the central axle. In the standard, the deadweight is divided in parts above and below the rims, but not in between. This makes no difference for the centre of gravity of the impactor, but the rotational inertia is slightly lower than in the configuration of the standard. The central deadweight also causes the spacing between the two STARCO tyres, because they appear to be thinner than the tyres that were previously mounted on the test rig in the work of De Pauw [5]. In the glass industry, it is common knowledge that different tyres may produce very different results for the EN 12600 test setup. However, the strains measured with the STARCO tyres are roughly the same as those recorded by De Pauw.

No strains were measured at the drop height of 1200 mm as the calibration plate fractured (see also the cover picture of this chapter), which should not have happened. The cause of this failure is unknown. The impactor was filmed from the side during other tests but no metal parts (centre deadweight or cable connection pieces) came into contact with the glass plates at any point during impact, despite the rotation of the centre deadweight.

6.1.2 High-speed cameras set-up

For the test campaign in this study, 3 high-speed cameras were available which, combined with the Digital Image Correlation technique, were used as instrumentation.

Two Photron Fastcam SA4 cameras were positioned behind the glass specimens to measure out-of-plane deformations (Figure 6-5 & Figure 6-6). The third camera (an APX-RS) was used to film the actual impact of the twin-tyres from the side. All cameras were synchronised and manually triggered upon impact.

Figure 6-5 **EN12600 set-up including high-speed cameras and additional lighting.**

Figure 6-6 **Detail of back of specimen, including DIC speckle pattern and high-speed cameras.**

6.2 TYRE IMPACTOR

A very important part in the numerical models of the tests will be the twin tyre impactor. However, the tyres of the pendulum body are usually modeled as simple

homogeneous solids or shell elements with linear elastic material properties in literature [3]. Experimental tests are executed to obtain the material parameters in the FE model. At first sight, these simplified models seem accurate, since good correlation between experimental and numerical results is present. Nevertheless, these assumptions are only valid under well-defined conditions because the material (and geometrical) properties are obtained iteratively for a specific set of variables.

For example, Müller de Vries [4] created a tyre model with an internal pressure of 4 bar. An impact test against a rigid wall was executed and for each drop height, the modulus of elasticity of the FE model was adjusted until good agreement was found with the test data.

In order to be able to use the same model for different glazing configurations, a detailed and accurate FE model of the tyre is necessary. Such a model takes into account the real geometry, different materials, material laws, … and represents the physical behavior of the tyre. Impact tests and compression tests can then be used for validation purposes.

6.2.1 Tyre geometry and properties

The test tyre (type STARCO TR13 ST11 3.50-8 4PR) is a diagonal (bias) tyre, used in wheel barrows. Bias tyres consist of body ply cords, a side wall and a tyre bead, i.e. the area that makes contact with the rim after inflation. The body ply is a layer, composed of nylon, which supports the vehicle and keeps the deformations within bounds. These plies are layered diagonally and extend from bead to bead as shown in Figure 6-7. The side wall consists of a rubber compound and body plies. The bead zone includes the bead wire (steel cords) and ensures that the tyre does not slide off the rim when inflation of the tyre is initiated.

The rubber compound cannot be tested solely because the nylon wires are intertwined with the rubber. Therefore a hardness test according to ISO 48 is executed in which a vertical plunger (durometer) with a rigid ball or spherical surface on the lower end is pushed into the rubber sample (BIN, 2003). Based upon the indentation of the plunger and the indenting force, an IRHD value of 59.5 is obtained. In (Altidis et al., 2004), a shore hardness of 59.5 corresponds to an elastic shear modulus of 1.16 Mpa. The hardness test cannot be seen as an accurate test method. It is used here due to lack of information of the tire manufacturer.

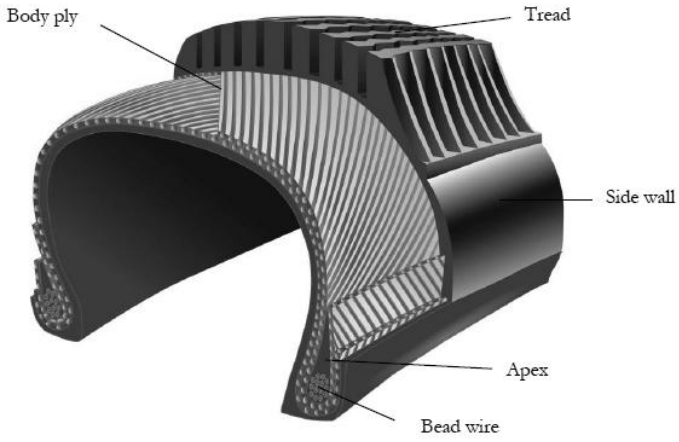

Figure 6-7 **Overview of the different components of the diagonal tyre (courtesy ClassicTrucks.com).**

The reinforcement materials, consisting of the tyre cords and the bead wire, are the load carrying members of the cord-rubber composite. These materials provide strength to contain the air pressure and give sufficient sidewall impact resistance to ensure the stability of the tyre (Gent, 2005). For the body ply, Nylon Type 6 tyre cords are used. The diameter of the nylon cords, the spacing between these cords and the angle between the body plies can be obtained from a CT-scan which visualizes the different components of the tyre. An illustration is given in Figure 3-6. This figure shows the orientation and position of the different cord layers. The angle between two nylon cord layers is 60 degrees and their diameter is 0.45 mm. The spacing between the individual nylon wires is 1.60 mm.

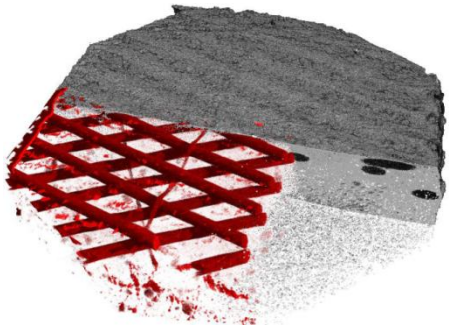

Figure 6-8 **µCT-scan of a section of a tyre with visualisation of the rubber compound (grey) and nylon cords (red).**

For determining the Young's modulus of the nylon cords, a tensile test is executed on a single nylon wire to obtain a stress-strain curve. In a tensile test, one end of the wire is clamped in a loading frame while the other end is subjected to a controlled displacement δ and by means of a transducer the corresponding load $P(\delta)$ is determined. The engineering stress-strain curves of the four different samples are shown in Figure 6-9.

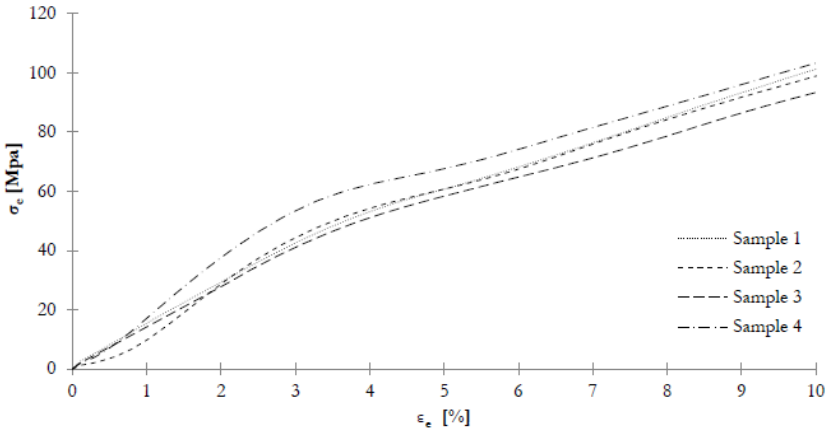

Figure 6-9 Engineering stress-strain curve for the nylon cords.

Since only small deformations (strains) will occur in the impact tests, Hooke's law holds so that the modulus of elasticity can be obtained based upon the engineering stress-strain curve. The final value for the modulus of elasticity is determined as the mean value, resulting in a value of 1.39 GPa.

The bead wire consists of nine steel cords with a diameter of 1 mm each. Table 6-1 gives the material properties of the reinforcement materials.

Table 6-1 Material parameters of bias-ply tyre.

Component	Mass density [kg/m^3]	Young's modulus [GPa]	Poisson's ratio [-]
Bead wire (steel)	7850	210	0.3
Body plies (nylon)	1440	1.39	0.3
Rubber compound	1100	3.48e^{-3}	0.5

Since no detailed information is given with regard to the dimensions of the tire, a sectional strip of the tire is cut out and the dimensions are measured. As can be seen

in Figure 6-10, eight longitudinal grooves are present and the thickness of the rubber compound varies along the meridional direction.

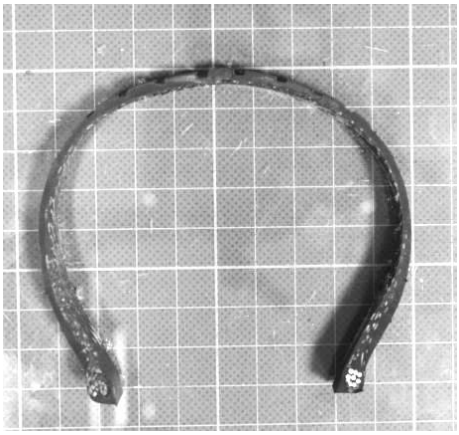

Figure 6-10 Illustration of the cross-section of the tyre.

6.2.1.a Numerical model of the tyre [1]

For a detailed report about the development of the numerical model of the tyre, the author refers to Pelfrene [1]. However, since its creation was intertwined with tests in this study, it is briefly summarized here:

The geometry of a symmetric tyre section is drawn in its unstressed state, as shown in Figure 6-11. This model is discretised by a finite element mesh of 931 axisymmetric elements, using continuum elements for both the rubber compound and the steel bead wires. The nylon cord plies can be modelled in Abaqus by use of a rebar layer, embedded in the elements of the rubber compound. In the case of the bias-ply tyre, two equal nylon cord plies are assigned with orientations -30° and +30° with respect to the meridional direction. Contact surfaces are defined between the tyre and the rigid rim to allow for frictional sliding during the mounting and inflation stages.

A detailed solid model is conceived through Symmetric Model Generation (SMG) in Abaqus. In essence, the SMG revolves the nodes of the axisymmetric model at regular offsets and connects them to form a 3D continuum elements mesh.

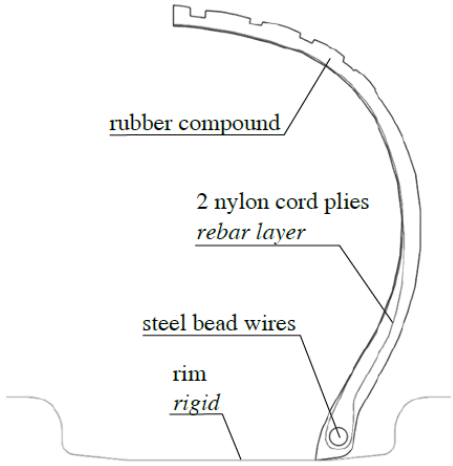

Figure 6-11 Axisymmetric model of bias-ply tyre, initial unstressed state [1].

For simulation of the impact event using an explicit solving scheme, a more efficient 3D model is preferred. This model is constructed using shell elements with rebar layers defined for the nylon cord plies and the steel bead wires. The shell element thickness is taken to be constant and equal to the sidewall thickness measured on the tyre, i.e. 3.0 mm. Two rebar layers are defined for the nylon cord plies, each at a constant offset from the shell middle surface. An extra rebar layer for the steel bead wires is placed near the inner diameter of the tyre.

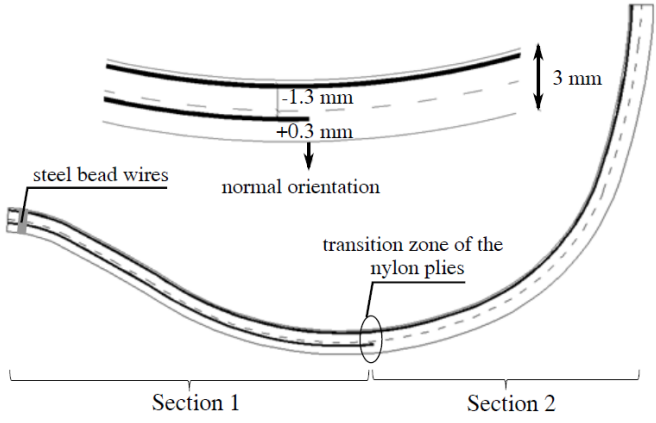

Figure 6-12 Definition of rebar layers and steel bead wire in the efficient shell model of the tyre [1].

6.2.2 Uniaxial tensile tests

The rubber compound is intertwined with the nylon cords. Therefore, results of a tensile test are only valid for a numerical model that consists of both rubber compound and nylon cords. Furthermore, the FE model should also match the shape of the real sample and its boundary conditions. In the laboratory, transverse and longitudinal samples, as shown in Figure 6-13, were subjected to uniaxial tension. The transverse sample has dimensions 113 mm x 50 mm and the longitudinal sample has dimensions 100 mm x 48 mm. The load values during elongation were measured. Despite clamping of the specimen in the jaws at the top and bottom, slippage occurred (Figure 6-14).

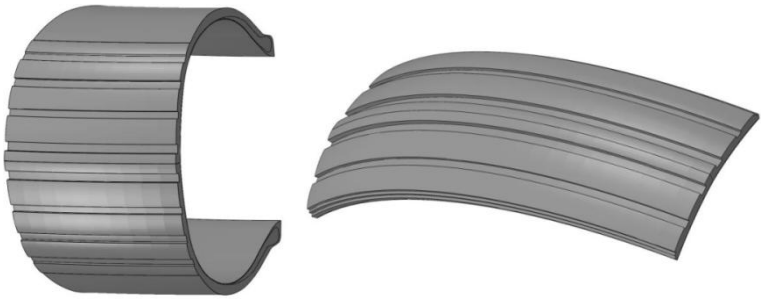

Figure 6-13 **Transverse sample (left) and longitudinal sample (right) [1].**

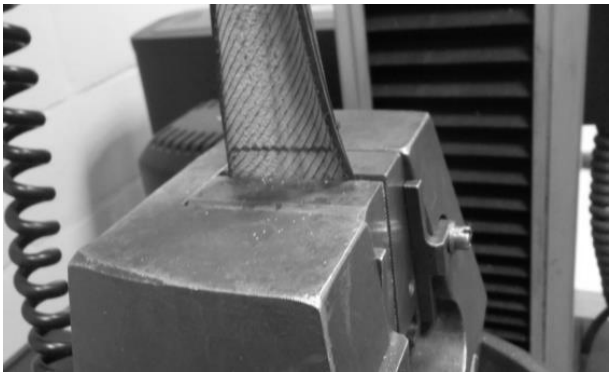

Figure 6-14 **Slippage of the test specimen. The horizontal line was initially positioned at the end of the jaw.**

For tensile tests in transverse and longitudinal direction, five samples were tested to obtain reliable results. The samples show no significant dependency on the displacement rate. In Figure 6-15 and certainly Figure 6-16, large differences

between the different test results can be observed. Variations in the results could rather be attributed to poor clamping.

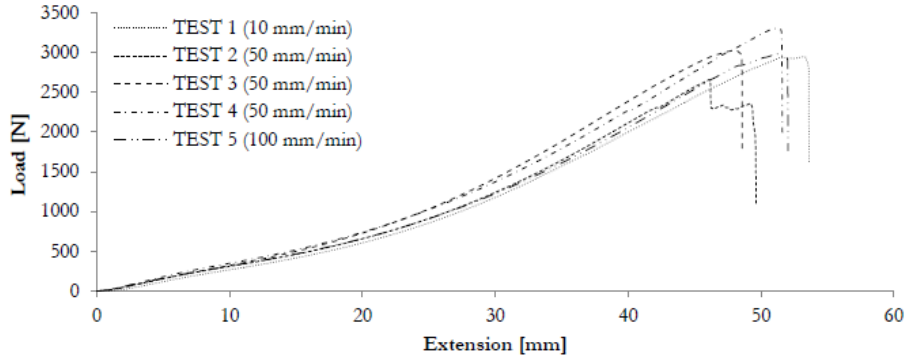

Figure 6-15 Load-extension curves for the transverse tensile tests.

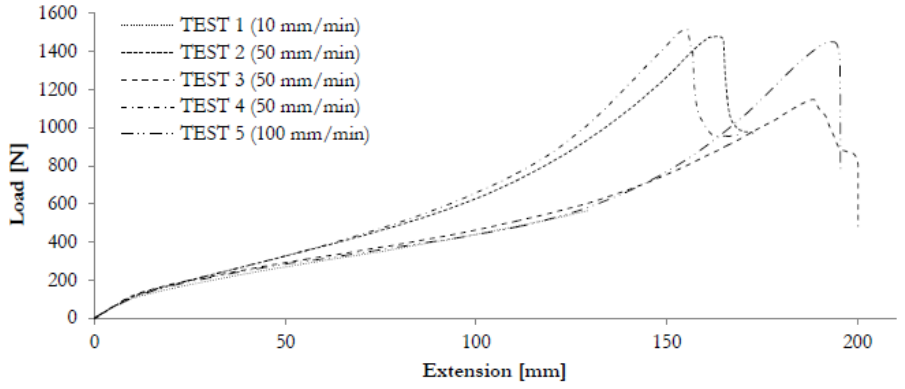

Figure 6-16 Load-extension curves for the longitudinal tensile tests.

These tests are then modeled, the result of which is shown in Figure 6-17. The experimental data is compared with the results of the FE model. For small strains the numerical results correspond well to the measured values. For higher strains, larger differences are observed and the numerical model seems stiffer than the experimental model. These discrepancies can be explained by inadequate clamping of the samples in the laboratory, as seen in Figure 6-14. The elongation of the test specimen is therefore larger for the same load and this effect is more distinct with increasing load. In general, good correspondence is observed between the experimental and numerical load values for small strains.

Figure 6-17 **Initial and deformed state of the numerical model of the transverse sample [1].**

6.2.3 Quasi-static loading of the tyre

The second validation test is a compression test. The tyre is placed between two rigid plates in the INSTRON 5800 R testing machine (Figure 6-18). The upper plate is fixed and the bottom plate moves upward at a constant rate of 1 mm/min, compressing the tyre. Positioning of the tyre is important since any skewness can affect the results. The tyre is inflated at a pressure of 3 bar and the force-displacement relation can be obtained.

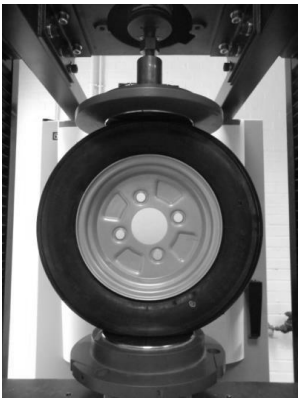

Figure 6-18 **Compression test of bias-ply tyre.**

Three experiments were performed at this testing speed, for which the average force curve is shown in Figure 6-19. The maximum standard deviation is 10.2 N. There is a very good correspondence between the experiments and simulations.

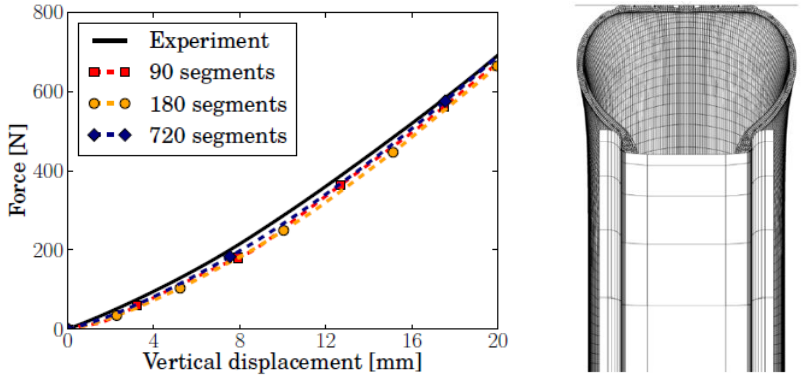

Figure 6-19 **Force vs. displacement for compression test of the bias-ply tyre: mean experimental curve and simulated results for solid models (left) and cut view of simulation (right) [1].**

6.3 PRESSURE PLATE

A third test for validation of the numerical model is impact testing against a rigid wall [3, 4]. This test can be executed by placing the impactor in front of a vertical rigid wall (e.g. a masonry or concrete wall) and by attaching a steel rod, which ensures the pendulum movement, to the ceiling.

Such tests, however, are often not very instrumented. To mitigate this, the addition of a pressure-sensitive plate, most often used to measure the pressure an athlete puts on his feet during jogging, is chosen. Together with a force plate, the pressure applied by the tyres during an impact event can thus be known.

To achieve this, a massive steel plate with a thickness of 9.5 mm is placed as a support at the backside of the rear clamping frame. On top of this plate, the force plate is attached together with a pressure plate, as can be seen in Figure 6-20. The force plate is fixed on to the steel plate with eight bolts to ensure that no relative movement occurs between the steel and force plate. The pressure plate is tied to the force plate with an adhesive tape.

Figure 6-20 Force measurement set-up: front (left) and back (right).

The KISTLER® Type 9281 B11 force plate has dimensions 600 mm x 400 mm x 100 mm and weighs 42 kg. It is characterized by a high rigidity, implying minimal deflections, and is used in combination with an 8-channel charge amplifier Type 9865E. The force plate is connected to an electronic unit which converts the electrical charges yielded by the force transducers into electrical voltages. Eight transducers allow calculation of the in- and out-of-plane forces. The calibrated range of the vertical force F_z lies between 0 and 20 kN.

The pressure plate is a RSscan International 0.5 m Hi-End footscan® system with dimensions 578 mm x 418 mm x 12 mm and a mass of 4.2 kg. It consists of 4096 sensors, arranged in a 64 x 64 matrix, and sensor dimensions 7.62 mm x 5.08 mm. The pressure range lies between 1 and 127 N/cm² and the maximum data acquisition frequency is 500 Hz, corresponding to an output every 2 ms.

The data of the footscan® pressure plate is transferred to digital input by means of a footscan® 3D interface box. This interface box synchronizes the pressure plate and force plate, so that every 2 ms a visualization of the impact zone of the tire and the corresponding force can be retrieved.

In contrast to a perfectly immovable impact zone, the steel plate on which the force plate is attached, is not completely rigid. During impact testing a certain horizontal deflection was observed. This can be observed when looking at the bottom right corner of Figure 6-21 c (dashed circle). A displacement of the plate in the direction of the impact force leads to a reduction of the measured forces, and thus an underestimation of the accelerations, compared to a rigid wall impact. This

does not pose a problem as long as the deformability of the plate is taken into account in the FE model. Another important issue is the horizontal distance between the impactor at rest and the pressure plate. Due to practical reasons, the pressure plate is placed 14.7 cm from the equilibrium position of the pendulum. Because of this, the impactor swings past its equilibrium position and hits the pressure plate under a small angle, with the lower tire making first contact. The velocity of the impactor slightly decreases because the pendulum swings past its resting equilibrium position, and the restoring gravity force decelerates the pendulum.

In Figure 6-21 the rotation of the pendulum is clearly visible.

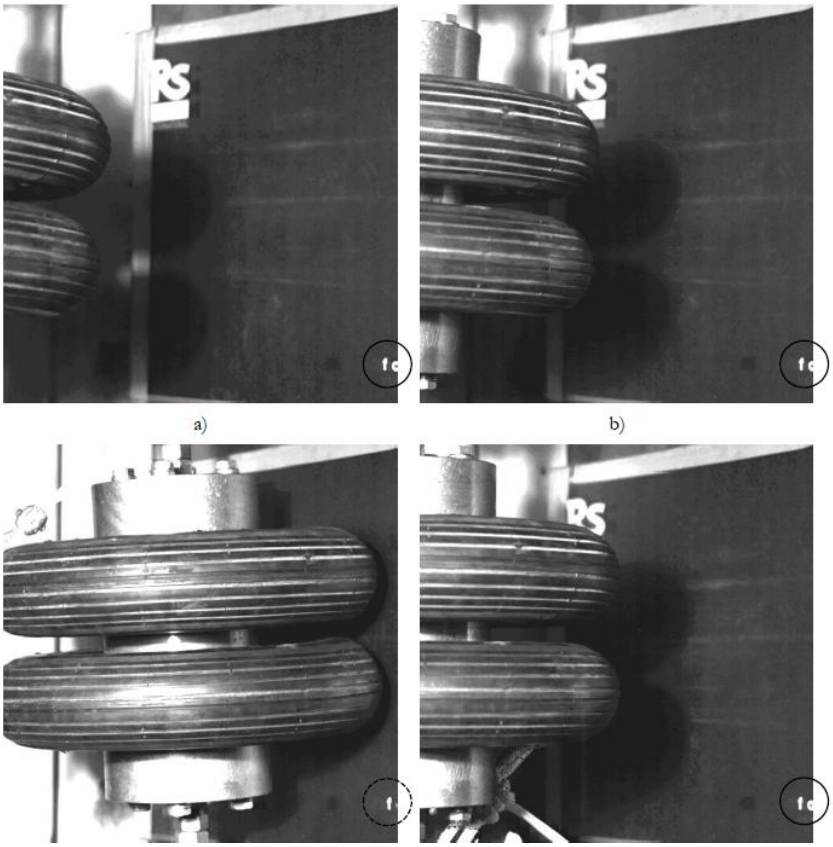

Figure 6-21 High-speed images of impact against the pressure plate.

6.3.1 Pressure plots

The pressure distribution of the two tires at maximum impact is obtained with the footscan® plate. Here, only the results for a drop height of 700 mm are examined

and compared with the numerical data. A graphical comparison at an impact time of 24 ms can be found in Figure 6-22. The legend is representative for both the experimental and numerical pressure data. It can be seen that in reality, the pressure distribution shows the presence of the tire tread. This tread is not modeled in the numerical shell model to reduce the complexity. The obtained pressure values are slightly higher for the numerical model, although this could be explained by the relatively low measurement frequency (2 ms) of the footscan® plate.

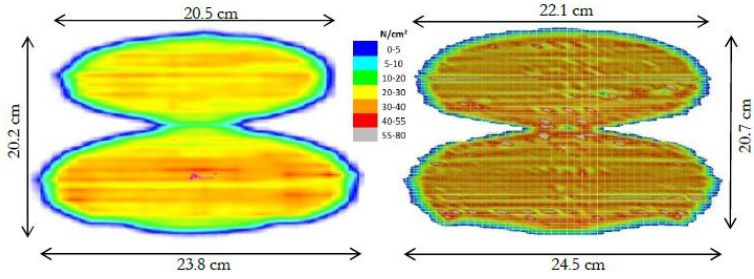

Figure 6-22 **Comparison of tyre footprints for a drop height of 700 mm at t = 24.0 ms after impact: experimental measurement (left) and simulated result (right [1]).**

In Figure 6-23, the experimental force curves are compared with the numerical data. Fairly good correspondance is achieved, except for the higest and lowest drop height. In the case of the lowest drop height, 20 mm, this anomaly most likely has its origin in the experimental testing procedure. The positioning of the impactor to its correct drop height can only be realized with an accuracy of a few millimeters. For small drop heights, the error margin will therefore be larger. No explanation was found for the discrepancy at the highest drop height.

Even though the actual tests on laminated glass will be performed at heights up to 1200 mm, forces corresponding to a drop height of 900 mm and more are not measured. A drop height of 900 mm might result in a force higher than 20 kN, exceeding the calibrated limit value of the KISTLER® force plate.

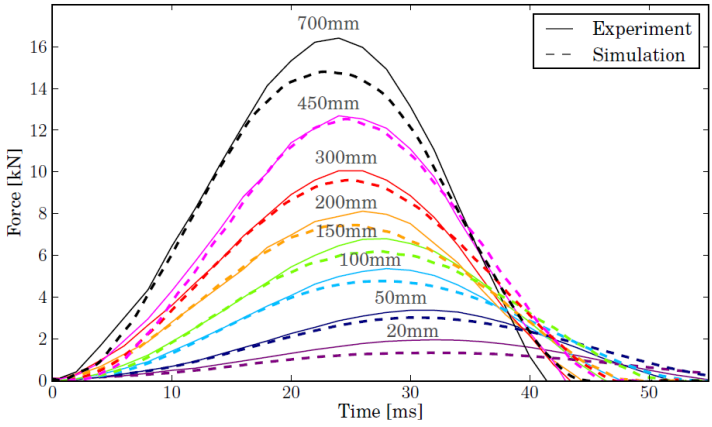

Figure 6-23 **Comparison of experimentally measured and simulated impact forces for different drop heights of the twin-tyre pendulum impactor (numerical results from [1]).**

6.3.2 Impactor acceleration during impact

To verify the finite element model with the performed tests, the acceleration of the impactor against the calibration plate was determined. A steel plate with speckle pattern was attached to the impactor. The movement of the impactor and speckle pattern was filmed by two high speed cameras to determine the acceleration of the centre of the pattern.

Figure 6-24 **Steel plate with speckle pattern for DIC.**

Based on the displacements of that point, the velocity was determined by the correlation software. The acceleration was then determined in the X and Y direction, by deriving the velocities. The amplitude of the resultant acceleration vector is shown in Figure 6-25. To filter the data noise, the resultant signal is filtered with a Butterworth filter at a cut-off frequency of 100 Hz.

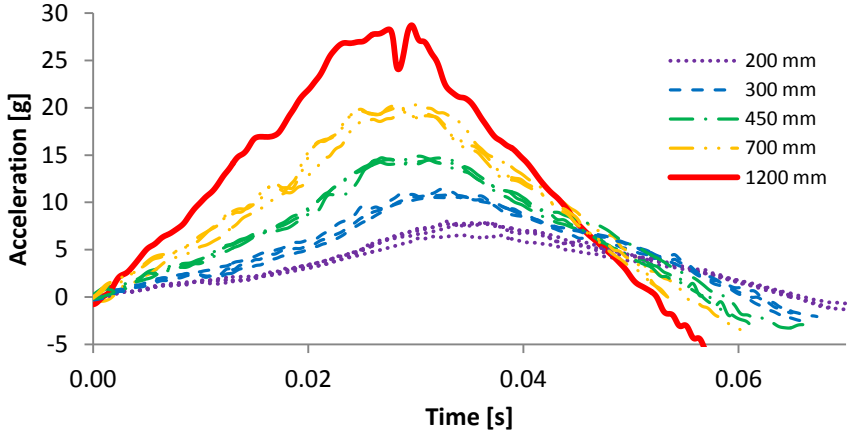

Figure 6-25 Acceleration of impactor during impact.

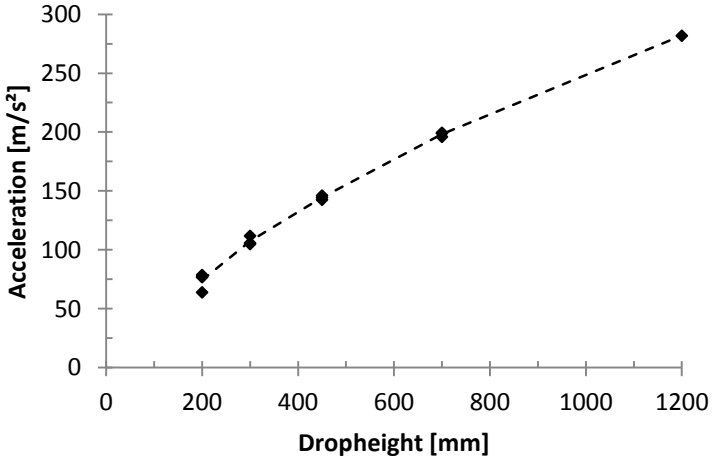

Figure 6-26 Maximum acceleration for each drop height.

In Figure 6-27 the recorded accelerations and strains for a drop height of 450 mm are compared to simulations using SJ Mepla and the detailed ABAQUS model [1].

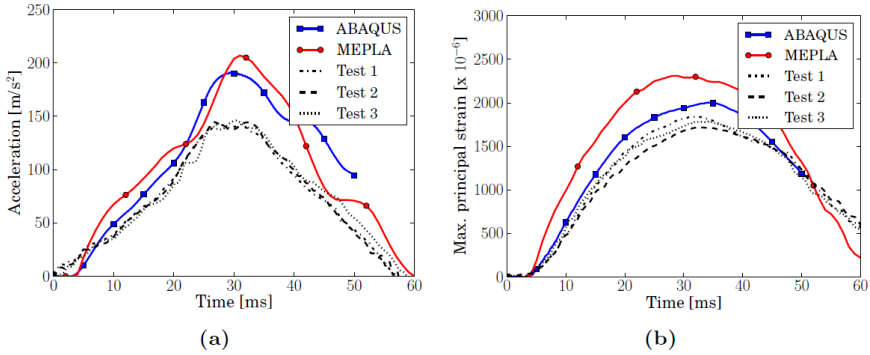

Figure 6-27 **Response of laminated glass upon pendulum impact at drop height of 450 mm: (a) accelerations and (b) strains (numerical results from [1]).**

While conservative, the results of SJ Mepla are remarkably close to the detailed ABAQUS simulation results.

6.4 EXPERIMENTS

A total of 60 specimens were tested. These had different compositions (meaning both glass and PVB thicknesses) and adhesion levels.

6.4.1 Preparations of the specimens

The central area of all specimens was coated with three layers of white paint (Figure 6-28), to provide a high-contrast background for the DIC speckle pattern, which was applied using laser transfer paper (Figure 6-29).

Figure 6-28 **Three layers of white paint were applied to the central area.**

Figure 6-29 Applying the DIC speckle pattern transfer paper.

6.4.2 List of performed tests

During the tests four parameters have been investigated (see Table 6-2). First of all, the glass thickness varied between 3 and 6 mm, secondly the thickness of the PVB-interlayer varied between 0.38 mm (1 layer), 0.76 mm (2 layers) and 1.52 mm (4 layers). A third parameter is the adhesion of the interlayer, high (RA), medium (RB) and low (RC) adhesion is tested. The last parameter is the influence of the lamination side. During the tests it was noticed that some specimens had different lamination sequences (air or tin side laminated against the PVB).

For all tests the pixel resolution was 1 024 x 736 pixels and the frame rate varied between 3 000 fps and 5 000 fps, depending on the drop height.

The presentation of the results is done in two steps; first, a qualitative discussion with many pictures, and secondly a quantitative discussion based on graphs obtained with the DIC technique.

Table 6-2 List of performed tests.

Composition	PVB	Drop height [mm]	Number of tests
33.1	RB11	700	6
33.2	RA41	700	2
		1200	3
	RB41	450	3
		700	5
		1200	3
	RC41	700	3
		1200	3
33.4	RB41	450	5
		700	3
		1200	2
66.2	RB41	450	8
		700	7
		1200	7

6.4.3 Qualitative analysis

In Figure 6-30 a typical post-test specimen is shown. Both glass panels have fractured, with radial cracks starting in a single point and extending to the edges, and with concentric cracking distributed over the entire plate. The area which came into contact with the tyres shows a very dense network of cracks.

The radial cracks all seem to originate from one centre (Figure 6-31). Sometimes more than one such centre can be discerned; all are located in the impact area (the area making contact with the tyres). The centres for both glass plies do not necessarily coincide. This suggests that in the impact area, where the glass is subjected to an elevated level of stress, the critical defect (see also 4.1.2) comes once again into play. Similar behaviour was also observed during the small-scale blast tests (see Chapter 8).

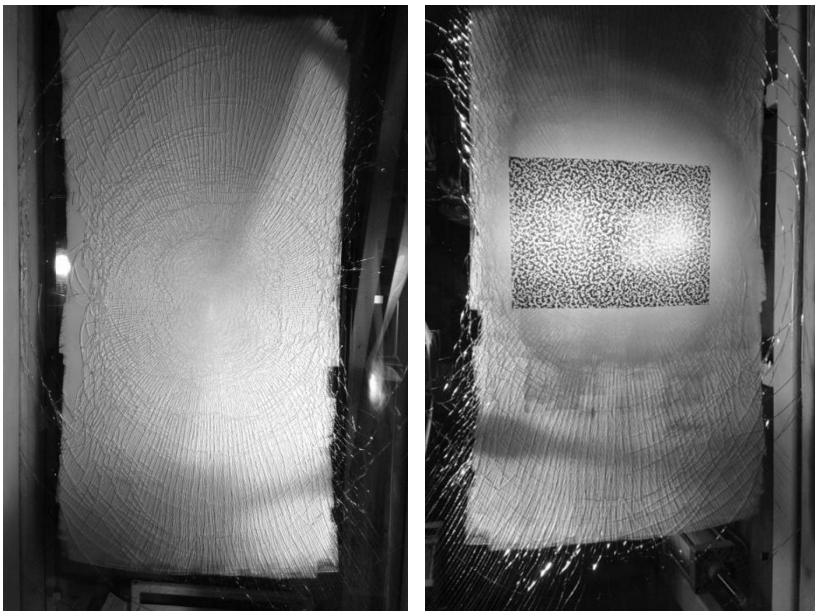

Figure 6-30 **Typical post-test specimen with fractured panels but without tearing of the interlayer (front and back).**

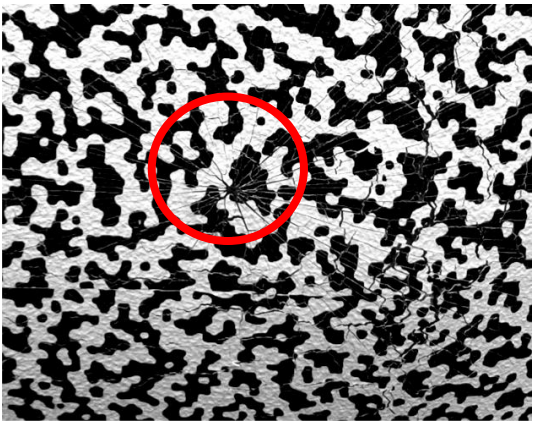

Figure 6-31 **Fracture origin of radial cracks.**

After removing the specimen from the set-up, a permanent deformation can be observed (Figure 6-32). When looked at from the side, two 'bumps' corresponding to the two tyres are clearly visible.

Figure 6-32 Visible imprint of twin tyre impactor in post-test specimen.

Some of the samples tested at higher drop heights experienced tearing of the PVB interlayer (Figure 6-33 and Figure 6-34).

Figure 6-33 Tearing behaviour of PVB interlayer.

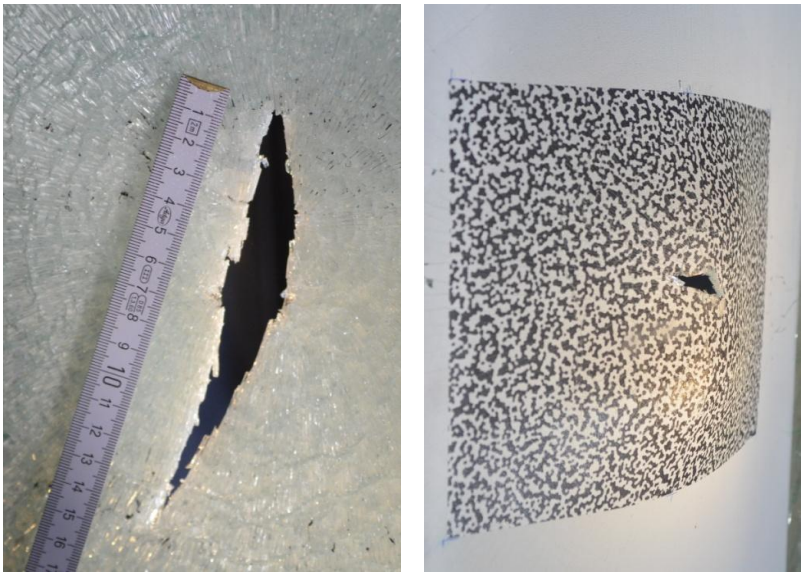

Figure 6-34 Tearing behaviour of PVB interlayer.

Some specimens showed many short fracture lines branching every 2 cm from a longer, more typical fracture (Figure 6-35). One could deduce that the total length of glass fractures remains about the same, but, since in this specific case they are bundled together, for this type of fracture relatively larger pieces of glass remain unfractured.

This was also the case for a handful of samples in the small-scale drop weight (SSDW) tests, described in the previous chapter. What exactly triggers this kind of fracture behaviour remains unknown.

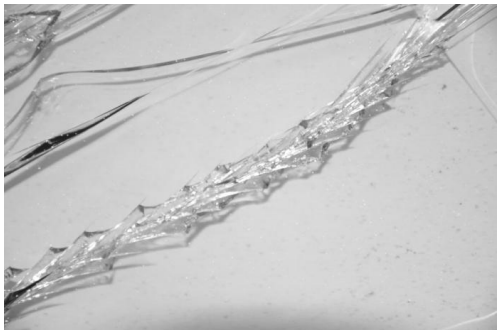

Figure 6-35 'Lightning bolt' cracks.

As evidenced by Figure 6-36, crack density near the edges can be quite low.

Figure 6-36 Post-test specimen: near the edges crack density can be very low.

6.4.4 Quantitative analysis

The mid-point deflection history for a specimen (composition 33.2) experiencing fracture of both glass plies is shown in Figure 6-37.

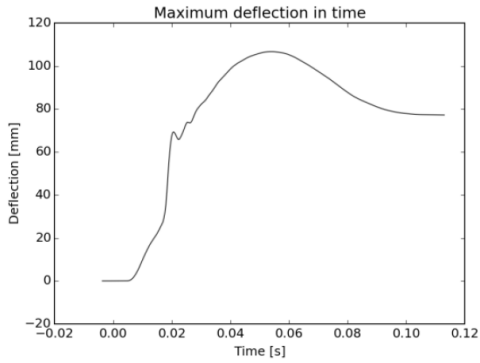

Figure 6-37 **Typical mid-point deflection history for a 33.2 specimen where both glass plies failed (drop height 1200 mm).**

The response of the plate starts with a bilinear course. There's a first part in which the bottom tyre impacts the plate, and a second, steeper part, when also the top tyre makes contact. The pressure in the tyres increases and a little later the full weight of the 50 kg impactor is pushing against the plate. The permanent post-test deflection is visible as well. Interlocking fractured glass fragments impede a full return.

The typical mid-point deflection of a specimen that did not break is shown in Figure 6-38. After impact, the plate continues to vibrate with a small amplitude.

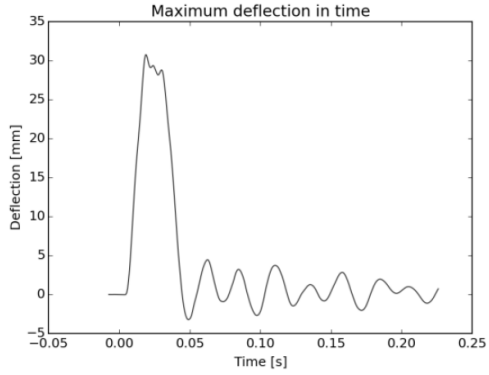

Figure 6-38 **Typical mid-point deflection history for a specimen without glass fracture (drop height 700 mm).**

When only one of the two glass plies fractures, the response is similar apart from two differences: a slightly higher maximum deflection and a more dampened response – the oscillations after the first peak have a higher amplitude and a lower frequency (Figure 6-39).

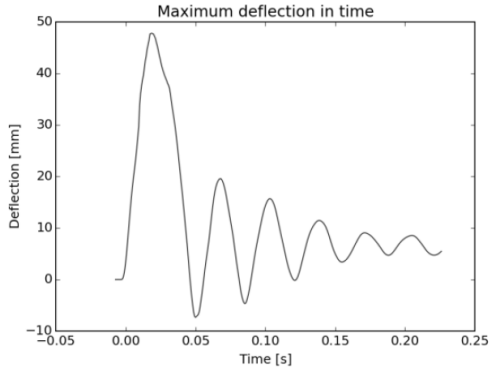

Figure 6-39 **Typical mid-point deflection history for a specimen where only one glass ply fractured (drop height 700 mm).**

The deflection along a horizontal line through the middle can be plotted for several time steps (see Figure 6-40). The rebound of the specimen happens at a slower rate than the initial outward deflection, as evidenced by the smaller distance between the blue lines.

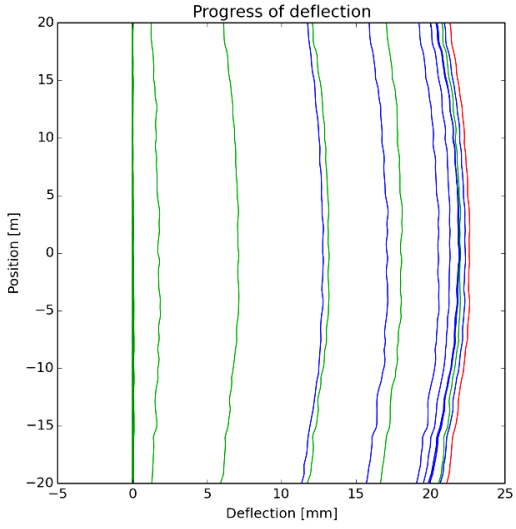

Figure 6-40 **Typical mid-line deflection in steps of 10 ms (green: up to maximum; red: maximum; blue: rebound after maximum).**

Typical principal strains in the middle of a specimen of which both glass plies broke, are shown in Figure 6-41.

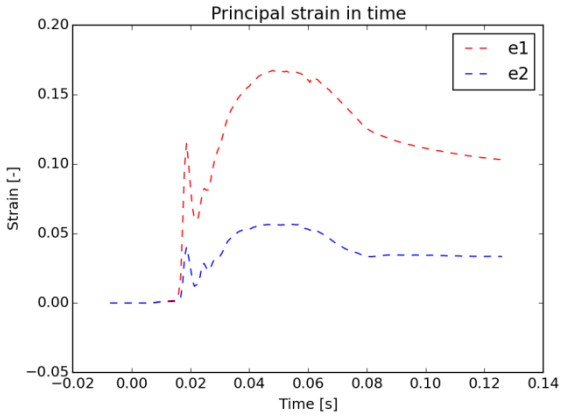

Figure 6-41 Typical principal strains.

In the next paragraphs the four parameters under investigation (glass thickness, interlayer thickness, adhesion level and lamination sequence) are discussed.

6.4.4.a Glass thickness

To compare the influence of the glass thickness, all specimens with an interlayer of 0.76 mm and medium adhesion are used. Table 6-3 gives the total number of tests for each drop height, as well as the amount of broken glass panes and the percentage of broken glass panes for both glass thicknesses.

Table 6-3 Influence glass thickness - number of broken specimens.

Drop height	**450**		**700**		**1200**	
$\mathbf{t_{glass}}$	Total	Broken	Total	Broken	Total	Broken
3 mm	3	3	5	5	3	3
6 mm	2	0	5	1	8	6

It is clear that the glass thickness has an influence on the strength of the laminated glass panel. For each drop height, all of the glass panels with glass thickness of 3 mm break, while the glass panels of 6 mm only start to break at 700 mm drop height. Even at 1200 mm, 25% of the laminated glass panels remain intact.

In Figure 6-42 the mean of the maximum deflections of the non-broken specimens is given for each drop height. Two such tests were executed at 450 mm,

four at 700 and two at 1200 mm. Since all specimens with a glass thickness of 3 mm are broken, it is not possible to study the influence on the glass thickness on non-broken specimens.

The deflection increases proportional with the drop height. For these non-broken specimens this can be expected since this shows the elastic behaviour.

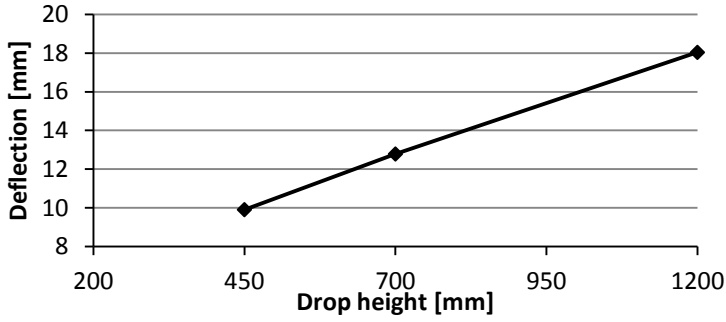

Figure 6-42 Deflection for non-broken 6 mm specimens for different drop heights.

In Figure 6-43 the mean of the maximum deflections of the broken specimens is given for each drop height. The laminated glass made by panes of 6 mm deflects less than the laminated glass made by panes of 3 mm. This is because the thick shards of a 6 mm ply stick to the PVB interlayer which makes it more difficult to deflect the glass pane.

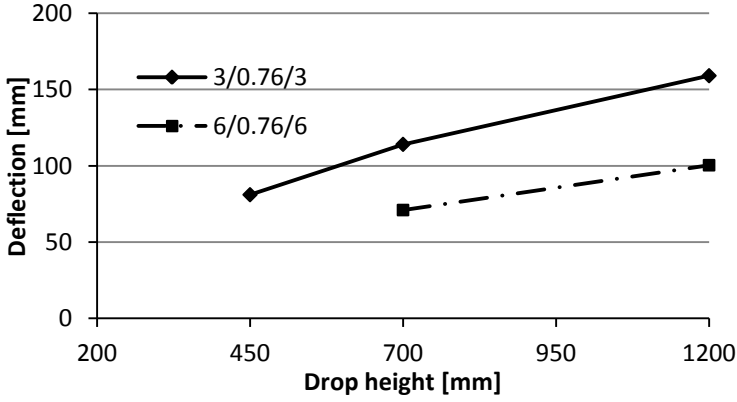

Figure 6-43 Deflection for broken 3 and 6 mm specimens.

6.4.4.b PVB thickness

To compare the influence of the PVB thickness, all specimens with 3 mm glass and medium adhesion are used.

In Figure 6-44 the mean of the maximum deflections of the broken specimens is given for each drop height. A distinction is made between completely broken specimens (both glass plies) and specimens from which only the glass ply in tension is broken. Two specimens with 0.38 mm interlayer broke completely at 700 mm drop height, three broke only half. The specimens of which only one glass ply broke are not considered in this graph. Three specimens with 0.76 mm interlayer broke completely at 450 mm, six at 700 mm and 3 at 1200 mm. One specimen with 1.52 mm interlayer broke at 450 mm, three at 700 mm and two at 1200 mm.

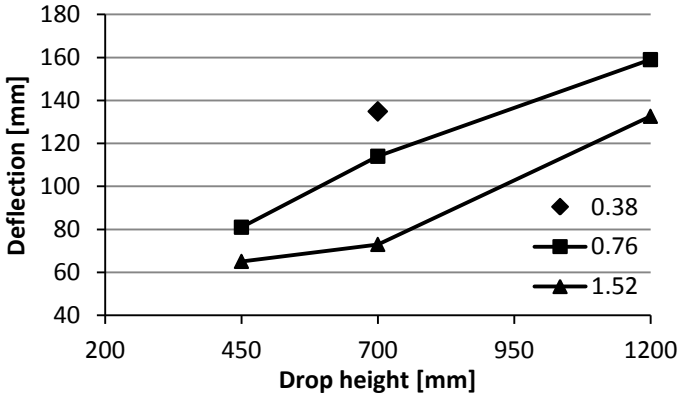

Figure 6-44 Deflection for broken 3 mm specimens with different interlayer thicknesses.

At 700 mm drop height a comparison can be made of the deflection for the different configurations. As expected, the deflection decreases when the thickness of the interlayer increases. The deflection of the half broken specimens is much lower than the deflection of completely broken specimens.

6.4.4.c Adhesion

To compare the influence of the adhesion of the PVB, the specimens with 3 mm glass and a PVB interlayer of 0.76 mm are used.

Three specimens of high RA adhesion are broken at 1200 mm drop height. From one of the three specimens the interlayer was torn. At medium RB adhesion three specimens are broken without tearing the interlayer at 450 mm, five tests are

broken at 700 mm from which two were torn and three specimens are broken with tearing of the interlayer at 1200 mm drop height. One specimen is broken of low RC adhesion at 700 mm and two at 1200 mm drop height, none of these were torn.

Due to the low adhesion, the RC interlayer delaminates more around the cracks in the glass. Because of that, a larger area of PVB can deform under tension. For higher adhesion the area that can deform under tension is significantly smaller causing the interlayer to tear.

6.4.4.d Lamination side

In this part the effect on the lamination side on the glass strength and on the post-fracture behaviour is checked. The nomenclature of the indication of the lamination side is given in Figure 6-45.

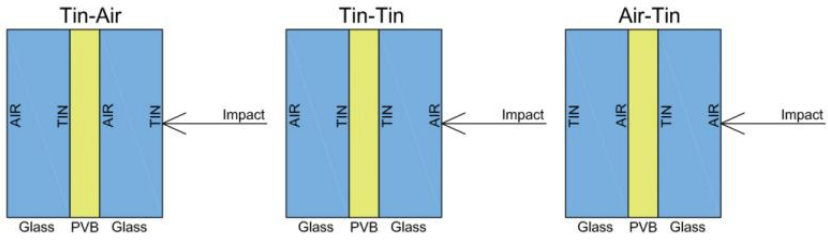

Figure 6-45 Nomenclature lamination side.

In Figure 6-46 and Figure 6-47 the deflection over time is given for specimens with an interlayer of 0.38 mm and 0.76 mm respectively. The following colours and line type codes are used in these graphs:

Colours:
- Blue: tin-air
- Green: air-tin
- Red: tin-tin

Line styles:
- Solid: non-broken
- Dotted: half broken
- Dashed: completely broken

In Chapter 2 it was already stated that the cutting of glass, which in the industry always happens on the air side, results in different degrees of damage for both new edges (see also 2.2.5.a). When simplifying these impact tests as just bending tests, it is clear from the above nomenclature that for a tin-air configuration both sides in tension will be air edges, which have a higher degree of damage. For tin-tin the outer edge, experiencing the highest strains, is also an air edge. Air-tin, however, has tin edges in tension.

The influence of this is clearly visible in these graphs. Tin-air specimens (in blue) will fracture very early, whereas the other configurations most likely will not fracture at all, for the same drop height.

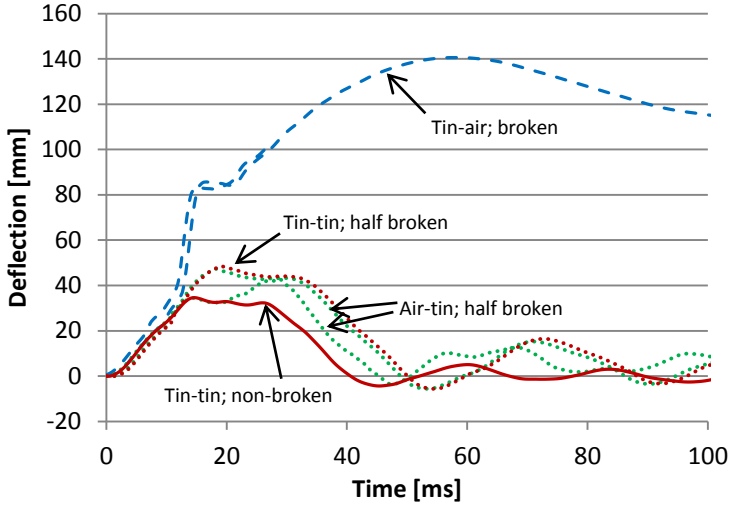

Figure 6-46 **Influence of lamination configuration – Deflection over time for a 0.38 mm interlayer.**

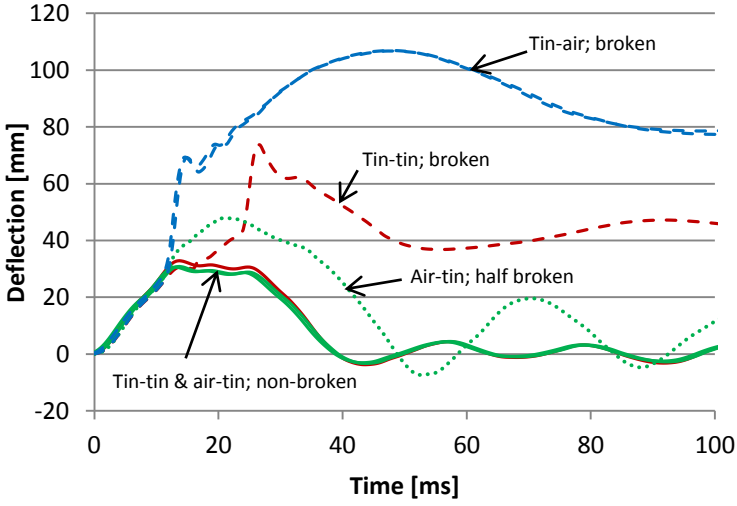

Figure 6-47 **Influence of lamination configuration – Deflection over time for a 0.76 mm interlayer.**

When performing standardised tests, the exact configuration can thus have an enormous influence on whether or not the specimens pass or fail. A configuration where the cut (usually air) sides are in compression – and not in tension – will result in better results.

6.4.4.e Comparison different laminate configurations

The mean values of the maximum deflections for each drop height are plotted for different broken glass compositions in Figure 6-48. Only the specimens where both glass plates fractured are considered.

The highest deflections can be found for the thinnest configuration, 33.2. The difference between 33.4 and 66.2 is rather small.

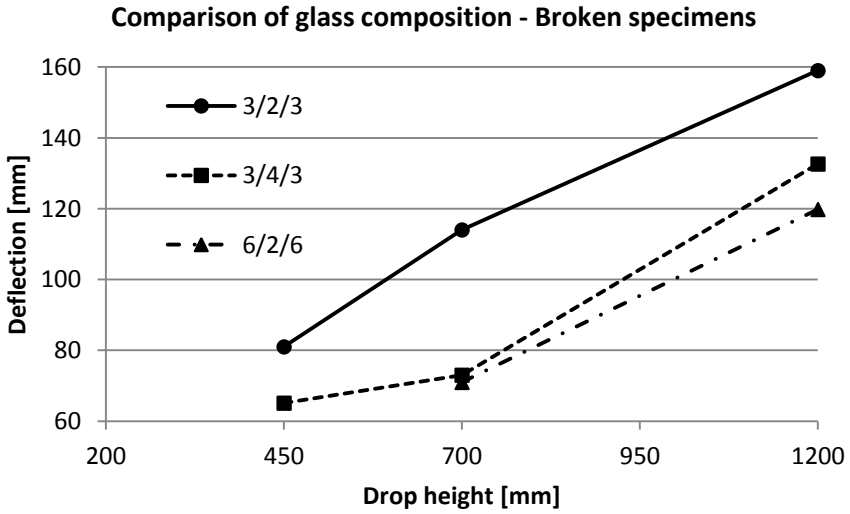

Figure 6-48 Deflection for different laminate configurations.

6.5 CONCLUSIONS

From the EN 12600 impact tests it can be concluded that the strength of the glass is influenced by the thickness of the glass. The lamination side also has an influence on the strength of the laminated glass panel. The tin side is stronger than the air side, as a consequence of the cutting procedure.

The post fracture behaviour is influenced by the thickness of the glass and the thickness of the PVB interlayer as well as by the adhesion. The laminated glass

made by panes of 6 mm deflects less than the laminated glass made by panes of 3 mm. This is because the thick shards of a 6 mm ply stick to the PVB interlayer which makes it more difficult to deflect the glass pane. As expected, the deflection decreases when the thickness of the interlayer increases. Apart from the thickness, the adhesion of the PVB also has an influence on the post-breakage behaviour. Due to the low adhesion, the RC interlayer delaminates more around the cracks in the glass. Because of that, a larger area of PVB can deform under tension. For higher adhesion the area that can deform under tension is significantly smaller causing the interlayer to tear. No distinction could be made in post-breakage behaviour of PVB laminated on the tin or air sides. Therefore it is recommended to laminate the glass based on which side will be in tension. For EN 12600 impact tests the strongest configuration is air-tin.

6.6 INTERACTION WITH MODELLING (PELFRENE [1])

The impactor model accounts for the compressibility of the pressurised air volume within the tyres, and takes account of the reinforcement wires in the rubber material. Fairly good correspondence is obtained when comparing the simulated response with experimental test data for a compression test, impact on a quasi-rigid force plate and impact on a tempered glass plate. However, the numerical simulations tend to underpredict the impact loads up to 11%.

Contrary to simplified approaches, the detailed model does allow to simulate the impact response of laminated glass with and beyond fracture of the glass (Figure 6-49). Thick and thin panels are analysed for two drop heights at which many of the specimens broke in experimental testing. Delamination is not accounted for in the numerical models as no discernible difference in impact response could be seen for test plates with different adhesion grades. Because of the need to import results from the implicit simulation of the inflation of the tyres, it is not possible to use the crack delay model (cf. 4.1.3) for shell elements, where an element is deleted as soon as the first material point reaches failure. Instead, the requirement for failure at all material points in the element is used.

Partly due to this limitation, cracks propagate slower and appear fewer in number than expected for the simulations. Furthermore, the post-fracture deformation of the panels does not consistently show good correspondence with experimental results, which leads to conclude that the reliability of the investigated method is still lacking. Nonetheless, the post-fracture simulations do show that fairly high strains are

reached at the interlayer material bridging the cracks. Eventually, this may allow to assess the ultimate failure of the panel by tearing of the interlayer.

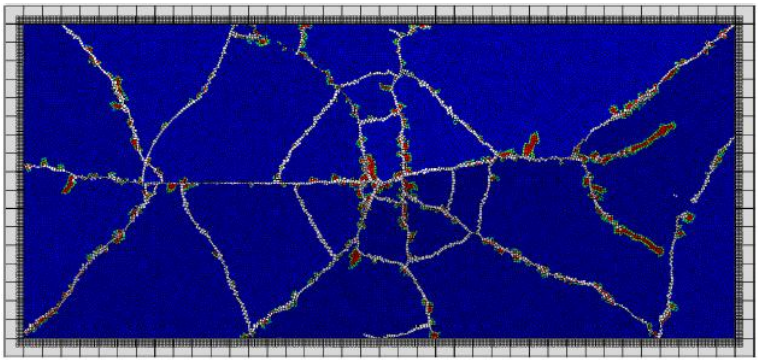

Figure 6-49 **Cracking of simulated glass panel with 3 + 0.76 + 3 mm thickness in EN 12600 pendulum test, at t = 100 ms. Contours of damage at integration point on outward-facing surface: elements in white are deleted, elements in red have failed at outer integration point.**

6.7 REFERENCES

[1] J. Pelfrene, "Numerical analysis of the post-fracture response of laminated glass under impact and blast loading," Doctor in de Ingenieurswetenschappen: Werktuigkunde-Elektrotechniek PhD, Department of Material Science and Engineering, Mechanics of Materials and Structures, Ghent University, Ghent, 2016.

[2] S. De Pauw, "Experimental and Numerical Study of Impact on Window Glass Fitted with Safety Window Film," Doctor in de Ingenieurswetenschappen: Werktuigkunde-Elektrotechniek PhD, Department of Material Science and Engineering, Mechanics of Materials and Structures, Ghent University, Ghent, 2010.

[3] J. Schneider, "Festigkeit und Bemessung punktgelagerter Gläser und stossbeanspruchter Gläser," Ph.D. Thesis, Institut für Statistik, TU Darmstadt, 2001.

[4] C. Müller de Vries. Numerical simulation of façade / window fracture under impact loading. In Bos, Louter, Nijsse, Veer, editor, Challenging Glass 3, pages 489-500, 2012.

PART III – BLAST

This part deals with the blast research performed in this study, namely the small-scale open air and shock tube tests, and the large-scale tests. A literature study precedes this.

Chapter 7 BLAST: INTRODUCTION, STANDARDS & LITERATURE

Overview

Before presenting the results of small-scale and large-scale blast test series of laminated glass in chapters 8 and 9 respectively, an overview of the relevant standards as well as a description of the state-of-the-art is presented in this chapter. It starts, however, with an introduction to explosions and terms related to that.

7.1 INTRODUCTION TO EXPLOSIVES

An explosion or blast phenomenon is a rapid release of stored potential energy characterized by a bright flash and an audible blast which expands a shock wave in radial direction. There are three distinct types of explosions [1]:

- **Physical explosions**: a sudden release of a highly pressurised fluidum without the existence of any chemical reaction. An everyday example is an exploding balloon.
- **Nuclear explosions**: a nuclear interaction between different atomic nuclei. During these interactions, a large amount of energy is released in a very short period of time. Examples are the splitting of heavy elements such as uranium or the contrary, fusion of light elements such as heavy water.
- **Chemical explosions**: a chemical reaction between oxygen and another component takes place. Once triggered, the reaction causes a rapid expansion of gases which results in a shock wave.

Next to a shock wave, the last two types also cause (extreme) heating of the surrounding medium. In this research only chemical explosions will be considered.

Explosive materials can be classified based on their physical state as solid, liquid or gaseous. Out of these, the effects of solid explosives are well characterized and best known. Due to this fact, solid explosives are used for many different purposes.

They can also be classified on the basis of their sensitivity to ignition as primary and secondary explosive. Primary explosives can be easily detonated by simple ignition from a spark, flame or impact. Secondary explosives can be detonated less easily than primary explosives. When a secondary explosive is detonated, it creates shock waves which can result in widespread damage to the surroundings. Examples of such materials are tri-nitrotoluene (TNT), nitroglycerine, RDX (cyclonite) etc [2].

7.1.1 Blast wave

The detonation of an explosive causes a chemical reaction which converts the solid explosive charge into a highly pressurised gas at very high temperatures. This concentrated pressure causes a blast wave, which is essentially a high pressure disturbance moving radially away from the source through a certain medium at a propagation velocity U. A sound wave loses energy while propagating further away from the source. This is also the case for a shock wave that travels away from the detonation point.

An explosion releases a certain amount of energy. This energy is distributed over the total volume of the medium that is already affected by the blast wave. The volume increases with increasing distance that the blast wave has travelled. This increasing volume requires a forth-going distribution of energy across the volume, which causes the energy to lower along the propagation direction of the shock wave. Next to this decreasing energy, which induces a decreasing overpressure, the shock wave also loses energy due to a rarefaction wave [3, 4] (see further).

A typical pressure-time diagram at a certain distance from the source is presented in Figure 7-1. The explosive detonates at t = 0. First, the shock wave has to travel through the medium from the source to the considered position. To do so, it needs an arrival time t_a. This is when the pressure front reaches the considered position. The time needed for the detonation wave to travel through the entire charge is incorporated in the time of arrival [5]. At this time, a high rise in pressure occurs in a very short period of time. Theoretically, this can be considered to be instantaneous. This is called an ideal shock front [6].

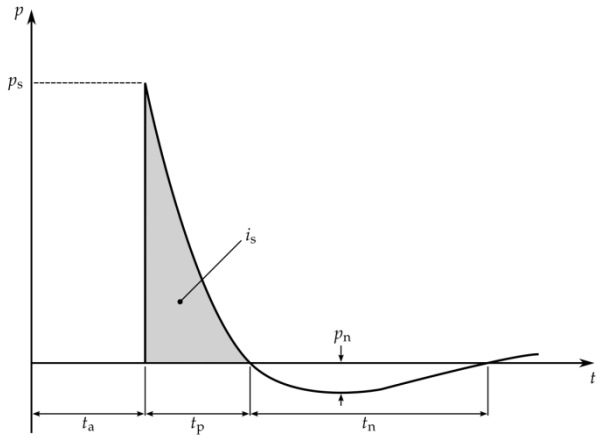

Figure 7-1 Typical pressure history plot of a blast wave in free air [7].

From hereon, the pressure follows an exponential decay. After a period t_p, the pressure reaches the ambient pressure. This period t_p is called the positive phase duration. The further away from the source, the longer the positive phase duration. The area enclosed by the pressure-time curve and the horizontal axis in the time-interval $[t_a, t_a + t_p]$ is called the specific impulse i_s. This is given by:

$$i_s = \int_{t_a}^{t_a+t_p} p(t)dt \tag{7.1}$$

The scaled distance is given by $Z = \frac{R}{W^{1/3}}$ where R is the distance in meter between the centre of the charge and the considered position and W is the TNT equivalent weight of the charge in kg. This equation is based on the Hopkinson-Cranz scaling law (Figure 7-2) which can be described as follows (quoted Baker *et al.*) [8]:

Self-similar blast waves are produced at identical scaled distances when two explosive charges of similar geometry and of the same explosive but of different sizes are detonated in the same atmosphere.

This means that the ratio of the charge diameters is equal to the ratio of the scaled distances at which the same peak overpressure occurs. The same ratio holds for the time of arrival t_i of the blast wave and the impulse I_i:

$$\frac{t_1}{t_2} = \frac{I_1}{I_2} = \frac{R_1}{R_2} = \left(\frac{W_1}{W_2}\right)^{1/3} \tag{7.2}$$

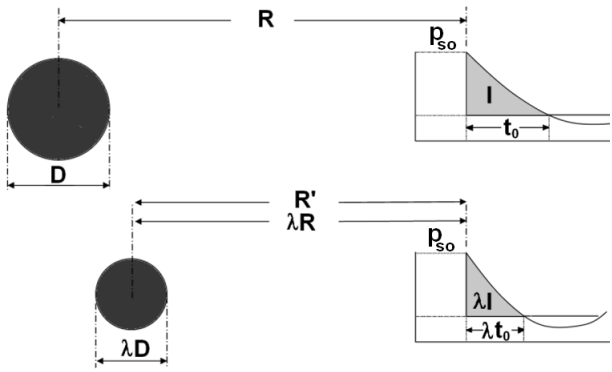

Figure 7-2 Basis of the Hopkinson-Cranz scaling law [2].

Due to this law, it is theoretically possible to perform scale tests. Assume that a certain charge and distance is given and the pressure acting on a structure needs to be experimentally determined, there is no need to perform a full scale test. The researcher can choose a charge mass, e.g. depending on the maximum allowed

charge mass for the testing site at his disposal, and then calculates the stand-off distance such that an equal scaled distance is obtained.

However, after reaching the ambient pressure for a first time, the pressure continues to drop, reaching negative values. This can be explained as follows: the molecules of the considered medium have a certain velocity at which they travel away from the source. These molecules have a mass and this, together with the velocity, results in a momentum. The momentum causes an over-expansion, which results in a negative phase with duration t_n and lasts longer than the positive phase duration t_p. The maximum negative phase pressure is denoted by p_n. This pressure is usually only a fraction of the positive peak pressure. After reaching p_n, the propagation direction of the molecules switches and the molecules travel back towards the source. Hereafter, the pressure returns to the normal atmospheric conditions. The process described above can be approximated using the modified Friedlander equation given by:

$$p(t) = p_s \left(1 - \frac{t}{t_p}\right) e^{-b_p \frac{t}{t_p}} \tag{7.3}$$

where t is the time measured after the arrival of the wavefront and b_p is the waveform parameter. The latter is also called the decay parameter and is a function of the scaled distance Z.

7.1.2 TNT equivalent weight

It is impossible to present a complete list of possible explosive compounds since there are dozens of weapon-grade explosives used by the army, such as C4 – of which the explosive component is actually RDX. Next to these, there are home-made explosives used by terrorists and anarchist movements. All of these explosives have different properties.

However, research has shown that the effects of explosions are related to the energy that is set free [5]. Each type of explosive has a mass specific energy Q_x. It is known that one kilogram of TNT releases approximately 4.680 kJ when detonated [9, 10]. Each explosive has a TNT equivalent, which is the ratio of the mass specific energy of the considered explosive with the mass specific energy of TNT. Using this ratio, an equivalent mass can be calculated. This is a mass of TNT which releases the same amount of energy as the used charge weight of the considered explosive. This mass of TNT is presented by W (in kg). Many models, such as ConWep (see Table 7-1), use TNT as the reference explosive. So, in order to use these models, the real mass of an explosive charge needs to be converted to a TNT equivalent mass. Some TNT equivalences are presented in Table 7-1. The equivalent is dependent on

what parameter will be calculated, so the value for the calculation of the pressure is not the same as the one used to validate the impulse [11].

Table 7-1 TNT equivalent for different explosives [11].

Type of explosive	Factor eq. pressure	Factor eq. impulse
TNT	1.00	1.00
ANFO	0.82	0.82
Composition A-3	1.09	1.07
Composition B	1.11	0.98
Composition C-4	1.37	1.19

Most calculation methods assume the TNT equivalent as a constant, well-determined value. This assumption is unfortunately too simplistic. Errors of up to 50% have been determined. Research has shown that the value not only depends on the pressure level, but also on many other parameters such as the scaled distance Z [3, 12-14].

7.1.3 Blast wave interactions

7.1.3.a Reflection

As is known from basic physics, when a wave travelling through a certain medium encounters another, denser medium, the incident wave will be reflected. This is also the case for a blast wave [1]. The interaction of the incident with the reflected wave causes a higher pressure than the incident wave alone. Next to this interaction, also the momentum of the air behind the wave front causes higher pressures on the structure. The amplitude of the reflected pressure in comparison with the incident pressure can be described with the following ratio:

$$C_r = \frac{p_r}{p_s} \tag{7.4}$$

where C_r is called the reflection coefficient. From the two extremes mentioned above, it could be concluded that $2 \leq C_r \leq 8$. However, experiments have shown that values for C_r above 20 can occur at very small stand-off distances [15]. The reason for this is that the air does not behave like an ideal gas at short distances due to the turbulent explosion processes, leaving the formula inaccurate for these situations.

The incident wave angle does not have to be equal to zero. Different angles cause other, more complex, interactions between the incident and the reflected wave. The reflected pressure is not monotonically dependent of the angle of incidence α_I [16]. Regular reflection occurs when the angle lies between 0° and $\alpha_{I,lim}$. If regular reflection occurs at an angle different from 0°, the reflected pressure will be smaller than the reflected pressure occurring at a perpendicular incident wave.

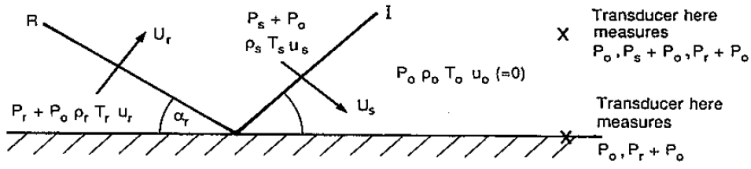

Figure 7-3 Regular reflection [1].

If this angle $\alpha_{I,lim}$ is reached, the reflected pressure will be bigger than the reflected pressure generated in reflection at perpendicular incidence. In the case of air, $\alpha_{I,lim}$ is approximately 40°. During this so-called Mach reflection, the reflected wave catches up and fuses with the still incident wave at a certain height above the reflecting surface. This results in a third wavefront termed the Mach stem. The point of coalescence of the three waves is called the triple point. In corner geometries where multiple reflected waves interact, larger pressures can occur than first expected [17]. Such behaviour will be encountered during the shock tube tests.

7.1.3.b Diffraction

In the preceding discussion, only infinitely large structures are considered. When the structure is of finite dimensions, the blast wave will diffract around it [1]. The most important part of the diffraction process is called the clearing effect.

Before the blast wave encounters the front face of the considered structure, the pressure is equal to the ambient pressure. At the moment the blast wave front encounters the front face, the pressure instantly changes to the reflected overpressure. This causes a large difference between the pressure at the edges of the structure, being equal to the reflected overpressure, and the incident pressure occurring in the part of the wave that passes over the top and around the sides of the considered structure. Due to this difference, a rarefaction wave is created propagating from the circumference to the centre of the front face. This rarefaction wave reduces the pressure and consequently the impulse loading the front face.

7.1.4 Blast loading

With the basic interactions known, more complex interactions between structures and blast waves can be considered. There are three possible situations to be distinguished, as illustrated in Figure 7-4 [1]:

- A large explosion loading a large structure: the structure is engulfed by the blast wave and will be crushed due to the static overpressure. The dynamic pressure wants to blow away the structure but because of the size of it, it will not move.
- A large explosion loading a small structure: in this case, the small structure or object - e.g. a car - will also be engulfed and crushed by the blast wave. However, because of the small size, the dynamic loading will be able to cause a displacement of the object, causing more damage.
- A small explosion loading a large structure: the blast wave does not last long enough to engulf the structure entirely. For this reason, not the entire structure will be loaded simultaneously. Because of this, any calculation concerning blast loading of the considered structure has to be done in steps since the structure will only be loaded partially.

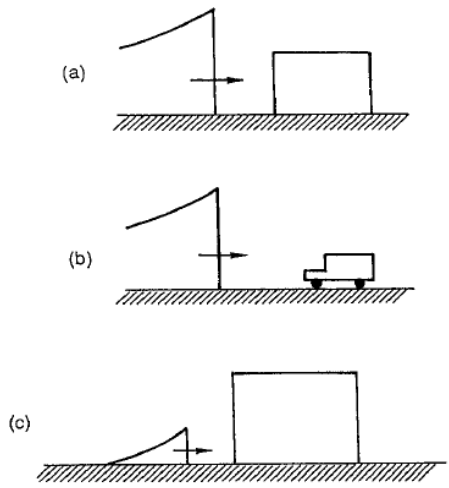

Figure 7-4 **Different blast loading targets: (a) large-scale blast and large target, (b) large-scale blast and small target, (c) small-scale blast and large target [1].**

The magnitude of the blast load also depends on whether the explosion is confined or unconfined. An unconfined explosion happens in open air and acts on a structure

from the outside while a confined explosion takes place inside the considered construction, loading it from the inside.

Of course, a structure can initially be considered as confined but if the structural elements are not strong enough to withstand the accumulated pressures, they will fail. Due to this failure, an open surface can develop which allows faster venting. Also due to this new open surface, a concentration of leaking pressures develops, which can load surrounding structures quite heavily.

An important example is failure of windows since glass is usually one of the weakest spots when it comes to blast loading. Common float glass will fail quickly, leaving an open gap through which the blast wave can propagate without much energy loss. However, when laminated safety glass (LSG) is used, the interlayer will not fail as fast as the glass itself. This offers a longer resistance against the blast load. When the interlayer finally fails, a lot of the explosive energy is dissipated, causing less damage in the space behind the LSG.

7.2 BLAST LOADING AND LAMINATED GLASS

The increasing occurrence and severity of crime and terrorist activities in recent years have significantly increased the need for protective glazing design, i. e. glass façades with enhanced blast performance. The primary purpose of glazing protection is to minimize the number of injuries caused by sharp edged fragments that are propelled from glazed openings when glass is subjected to blast (Figure 7-5). The two other aims of glazing protection are to minimize damage to equipment within the building (minimize loss of property) and to allow re-occupation of the building within the shortest period of time (minimize loss of business) [18].

Figure 7-5 **Burst of a single window after an explosion (courtesy: US Army Corps of Engineers).**

7.2.1 Standards

Several standards have been put forward by government agencies, to help architects and construction companies to achieve a minimum level of safety, depending on the level of risk the buildings or constructions are expected to be at.

7.2.1.a EN 13541

Several current standards address the qualification of glazing under blast loads. In Europe, the standard EN 13541 [19] describes the performance of the (laminated) glass as a building product, while the standards EN 13123 [20, 21] and EN 13124 [22, 23] specify requirements for windows, doors and shutters, complete with their frames and infills. EN 13541 defines the procedure for shock tube testing of a 0.9x1.1m glass test specimen, clamped at all sides in a rigid frame. Several load levels are defined as combinations of the positive, reflected peak pressure p_r, positive load duration t_p and positive specific impulse i_p, as given in Table 7-2. A glass product qualifies for a certain load level when there are no penetrable holes in the panel and no openings to the frame. The EN 13123 and EN 13124 use the same qualification, but without specification of the size or clamping of the glazing.

Table 7-2 Blast load levels as defined in EN 13541 [19].

Load level	P_s [kPa]	t_p [ms]	i_p [kPa.ms]
ER1	50	20	370
ER2	100	20	900
ER3	150	20	1500
ER4	200	20	2200

7.2.1.b ASTM F 1642

The US standard ASTM F 1642 [24], which serves as a global reference, treats both the product and the specific design. This standard defines no qualification requirements, but describes the procedure to test glazing and façade systems using a test container and a witness panel to assess the size and reach of the debris (Figure 7-6). World-wide security requirements are specified in the GSA Security Criteria [25]. In this document, protection levels are defined for structural components under several threats, among which blast loading. For the testing of window glazing, referral is made to ASTM F 1642, and to Wingard [26] for calculation.

A repeatable means of generating the airblast loading is required which can be either compressed air or explosively driven shock tubes or an open-air arena. The

window is mounted to a frame in a manner consistent with the installation in the field. A witness panel is placed at a distance of 3 meters from the window under test. The witness panel consists of a 2.5 cm thick layer of aluminum faced extruded Styrofoam insulation. The witness panel serves to record the presence of fragments that impinge upon its surface. Instrumentation to record the blast wave pressure time loading is required to assure the desired loading is achieved.

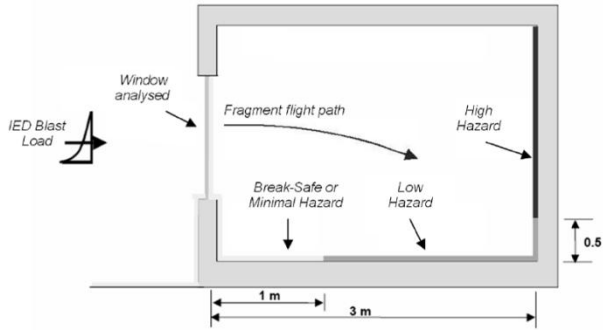

Figure 7-6 Hazard classification according to the UK Glazing Hazard Guide.

7.2.1.c ISO 16933

The international standards ISO 16933 [27] and ISO 16934 [28] specify testing procedures for glass as a building product under open air blast and in a shock tube respectively. The test method of ISO 16934 is identical to that described in EN 13541, except that two additional load levels are defined in the lower range. However, both ISO standards are only rarely used in the building industry.

7.2.2 State-of-the-art

Laminated glass panels are designed and supposed to fail by tearing of the interlayer rather than pulling them out of their frames. In the case of being entirely pulled out, the glass units would be blown into the building or on the street causing a hazard and probably some major injuries. A membrane action occurs if the glass panels are correctly fitted and they remain in position during the blast. The shear stress between the glass panels and the frame is transferred by the structural sealant. This allows the laminated glass to develop its full membrane capacity [29]. Figure 7-7 illustrates this membrane action.

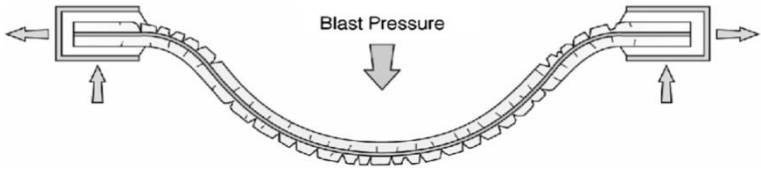

Figure 7-7 Membrane action of laminated glass under blast loading [29].

A distinction can be made into five different phases to describe the failure of laminated glass. These phases are presented in Figure 7-8 [30]:

- Elastic deformation of both glass plies;
- Failure of the glass ply on the convex side of the panel during bending, no failure of the interlayer, shards stick to the interlayer
- Failure of the second glass ply, interlayer still behaving elastically, shards stick to the interlayer;
- Interlayer deforms plastically, still retaining the glass splinters to the interlayer;
- Failure of the interlayer due to cutting of the splinter edges or by reaching its failure strength

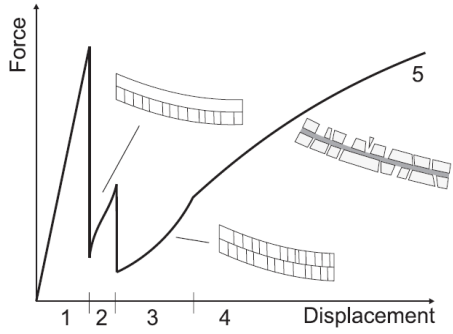

Figure 7-8 Five phases of laminated glass failure [30].

Based on a test series using different explosive charges, Hooper [7] observed a fracture pattern with two clearly distinguishable zones after failure: a central zone and a zone between this centre and the edges of the glass pane. For low reflected pressures, the central zone has an elliptical shape where for high pressures this zone is rather rectangular as can be seen in Figure 7-9. The glass fragments in the central area are significantly (up to ten times) larger than the fragments in the outer area.

Depending on the blast load, the glass can even be degraded to dust in the outer area, losing its adhesion with the PVB.

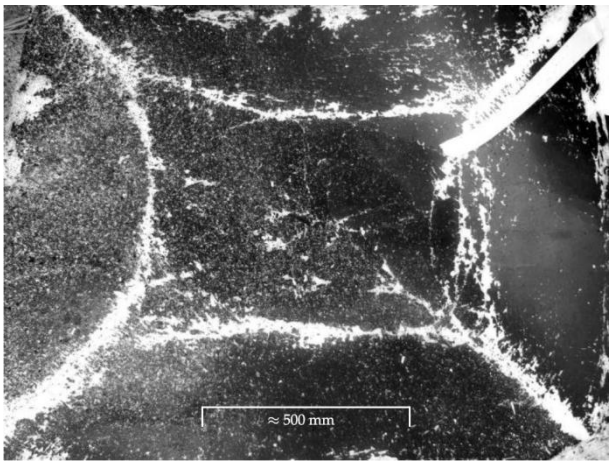

Figure 7-9 Fracture pattern of laminated glass subjected to a blast load [7].

The development of the pressures during blast loading according to the Friedlander formulation has been discussed earlier. It was mentioned that a sudden high positive pressure occurs, decays to zero and reaches a negative pressure of a smaller magnitude but with a longer duration. According to Krauthammer and Altenberg [31], this negative phase has an important influence on glass failure due to the longer lasting negative pressure, potentially causing larger stresses in the glass.

However, the importance of this negative phase increases with the scaled distance: the greater the scaled distance, the greater the negative pressure which can eventually become as large as the positive pressure. The negative phase becomes important for scaled distances larger than 20 $m/kg^{1/3}$, especially if they become larger than 50 $m/kg^{1/3}$.

The importance of the negative phase can be explained as follows. Assume a shock wave loading a glass panel such that the stresses in the glass stay below its elastic limit. This load causes the glass to deflect in the direction of propagation of the wave. Due to its elastic properties, the glass will rebound and even deflect in the direction of the source of the explosion. If the negative phase hits the glass panel on the same time of the outward deflection due to the rebound, the glass will deflect even more in the outward direction, causing a larger bending and thus larger stresses. The latter can be so large that it causes the glass to fail [32].

A blast load is a highly dynamic event, which means that the load acts very quickly. During blast events, it is preferable that the interlayer has a high failure strain. The larger this strain, the more energy can be dissipated before tearing of the interlayer. Once the interlayer fails, only the remaining energy of the blast wave propagates into the room. Of course, not only the behaviour of the laminated glass pane itself is important, also the fixing of this pane to the rest of the building structure is important. The fixing needs to be strong enough to resist the reaction forces of the glass pane and keep the pane in its place. This can be done by e.g. adhesive bonding. If this bonding is not strong enough, the glass pane will be propelled into the room in its entirety, possibly causing severe injuries.

7.2.2.a State-of-the-art

Hooper [7] performed full-scale open-air blast tests to study the behaviour of LSG with a PVB interlayer. Samples for these tests were rectangular (1.5 m x 1.2 m) and explosive charges with a TNT-equivalent of 15 kg and 30 kg at a distance of 10 m to 16 m were used. The results of these tests were compared to a finite element model to evaluate its accuracy.

Looking at the out-of-plane displacement, one notices that the contour lines have a nearly rectangular shape and are closely adjacent to each other at the sides of the plate. From this it can be inferred that out-of-plane deformation is concentrated at the edge of the LSG with the centre of the plate remaining fairly plane and undistorted.

Deflection of the glass is a result of the momentum gained by the pane since the duration of the blast wave is considerably shorter than the natural period of the glass pane. A transverse deceleration wave is initiated into the plate because the edges of the glass are fixed to a stiff frame. This deceleration wave removes the momentum that the glass pane acquired and brings the frame to a stand-still. The existence of this deceleration wavefront can be observed in the out-of-plane deformation, the flat central area reduces through time until the entire plate is bent. The same observation is made for the principal strain evolution. Strain is concentrated at the edges and remains relatively limited in the central area. The zones with a high strain value are those typically showing a large amount of fracture lines.

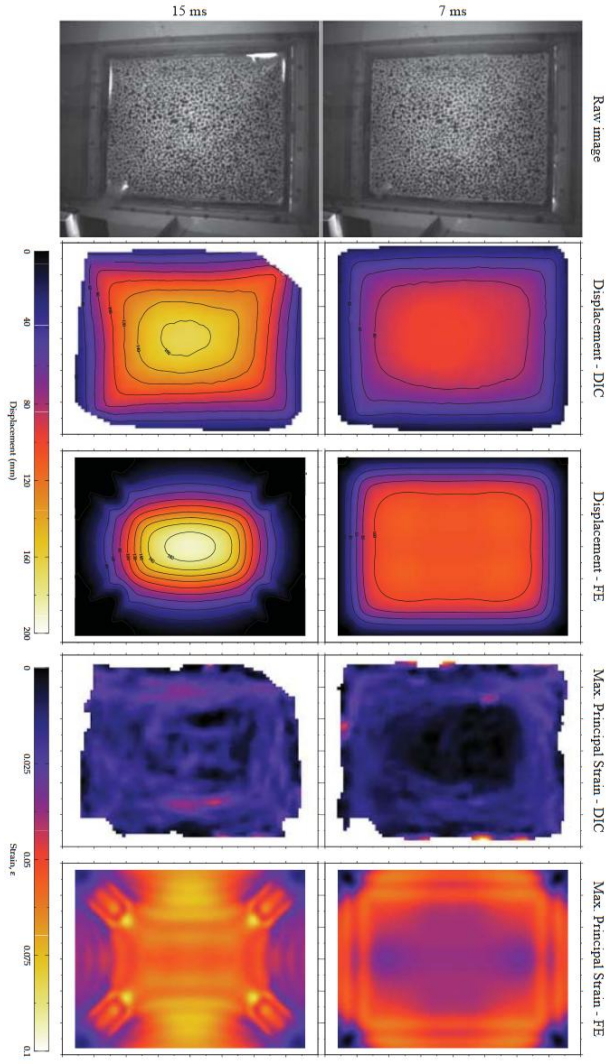

Figure 7-10 **Deflection and max. principal strain, DIC and numerical results (adjusted from [7]).**

Cross-sections of the out-of-plane displacement through time reveal the same information as stated above. The deceleration wavefront is easy to notice. A remarkable difference between the finite element model and the real tests is observed at the edges. The FEA shows zero deflection at the edges while the experimental curves deviate from this with increasing time. An explanation for this

lies in the fact that the edge in the FEA was modelled as a rigid support, while in reality the clamping frame will be moved by the blast wave.

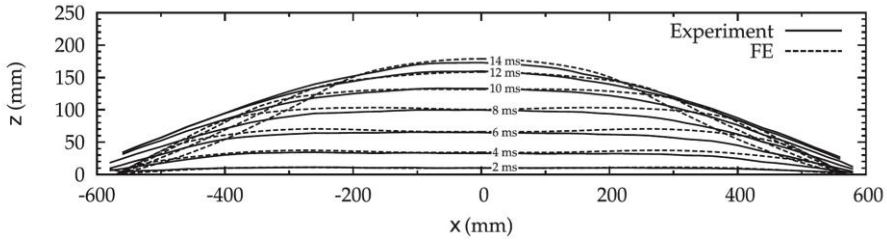

Figure 7-11 Hooper: cross-section deflection (experimental results vs. FEA) [7].

Some large scale open air blast tests have been performed on laminated glass in literature. An overview is given in Table 7-3. All tests had a 33.4 laminate composition.

Table 7-3 Available experiments in literature [30].

	Panel size [m]	**Blast wave source**	**Charge**	**Distance**	**Measurements**
Morrison	1.25 x 1.55	Solid explosive	60 kg TNT	12 m	Pressure, displacement
Kranzer	1.1 x 0.9	Solid explosive & Shock tube	0.5 kg PETN 0.25 kg PETN 0.125 kg PETN	5.75 m 3.7 m 2 m	Pressure, displacement
Hooper	1.5 x 1.2	Solid explosive	15 kg C4	10 - 13 m	Pressure, displacement and angle at border
Morison	1.25 x 1.55	Shock tube	100 kg TNT 500 kg TNT	31 m 65 m	Pressure, displacement

The experiments by Kranzer [33] are very similar to the large-scale experiments which will be performed in this study (Chapter 10). Therefore these experiments are explained in more detail.

A concrete test wall (3 m x 3 m) with a steel frame (0.9 m x 1.1 m) was used for both the shock tube tests and the open air tests. A sketch of the test arrangement is shown in Figure 7-12.

Laminated 7.5 mm glass panes (3 mm float glass – 1.52 mm PVB – 3 mm float glass) of 1.1 m wide and 0.9 m high were used for all tests. The panes were clamped to the rigid frame all around by 50 mm restraint. The area loaded by the blast was 1.0 m by 0.8 m. For the high explosive tests PETN (Seismoplast) charges were prepared with charge masses 0.5 kg, 0.25 kg and 0.125 kg.

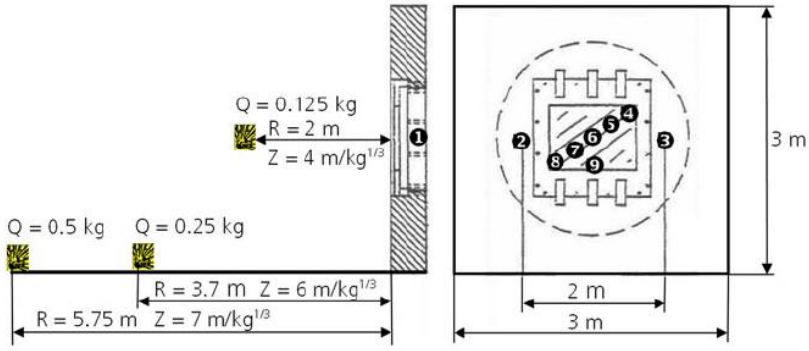

Figure 7-12 Schematic of large-scale tests by Kranzer [33].

For each test the pressure-time histories were recorded at both sides (measuring point 2 and 3 in Figure 7-12) of the test pane by pressure transducers. Extra experiments were done with a rigid plate and transducers (measuring points 4 to 9) to correctly assign the blast pressure and blast impulse at different positions. This makes it possible to measure the pressure-time histories along the pane.

Non-contact displacement gauging was done at the centre of the glass pane by a laser optical displacement transducer.

The Break Safely B/S / No Hazard level of damage was caused by explosive blast, if a blast impulse of approximately 70 Pa.s to 80 Pa.s was applied to the 7.5 mm laminated glass panes within one-quarter of the natural period of oscillation 3.9 ms.

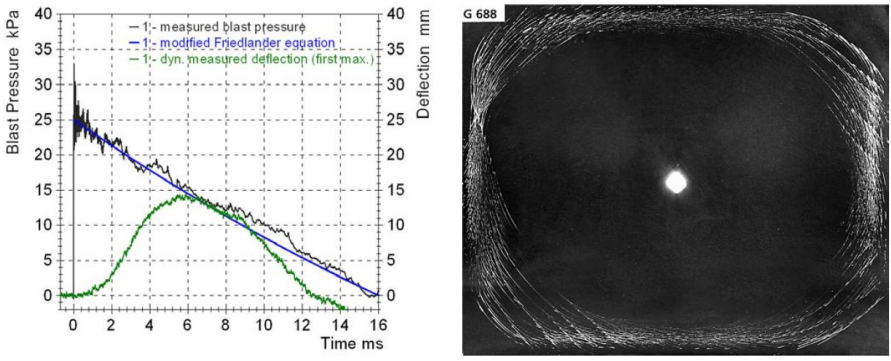

Figure 7-13 Pressure time history and mid-point deflection for a shock tube test (left) and fracture pattern of tested panel [33].

Figure 7-13 (left) shows the measured pressure-time history and the deflection-time history of the shock tube test. The maximum deflection of 14 mm was reached at 5.7 ms. The blast overpressure affected the pane for 16 ms. The positive duration of the blast is much longer than the reaction time.

From their experiments they concluded that "the complete iso-damage curve for laminated glass that indicates the Break Safely level of damage in a P-I diagram can be obtained from a small number of experiments. One-quarter of the natural period of oscillation determines the critical time. The critical impulse can be determined experimentally with small high explosive charges or with shock tube tests."

Kuntsche *et al.* used the shock tube at the Fraunhofer Ernst-Mach-Institut in Germany to conduct large-scale blast tests on laminated glass [34-37]. The test panels were composed of two 6 mm annealed glass panels and a 1.52 mm PVB interlayer. Different PVB products were tested, Kuraray's Trosifol® ES and BG. Due to a higher glass transition temperature, the ES-variant is a stiffer type of PVB, similar to the Saflex® DG interlayer, used in this research. The Trosifol® BG products have elastic properties that are similar to Saflex® R-series and also come in different adhesion grades.

After filling the compression section of the shock tube with highly pressurised air, a steel diaphragm is punctured to release the air into the expansion section. In addition to the measurement of the free incident pressure and the reflected pressure, the strains at the middle of the outward-facing glass ply were measured by strain gauges to detect glass breakage. The displacement at the centre of the back-facing glass has been measured by a laser sensor in tests where no total failure was expected, in order to protect the laser (Figure 7-14). A high-speed camera was used to record the initial breakage of the glass, the breaking pattern and the evolution of the panel deformation.

A first assessment of the post-breakage behaviour was done by a classification into four performance levels as illustrated by Fig. 7.32. A lower adhesion leads to a superior performance under blast loading in terms of ultimate failure by interlayer tearing.

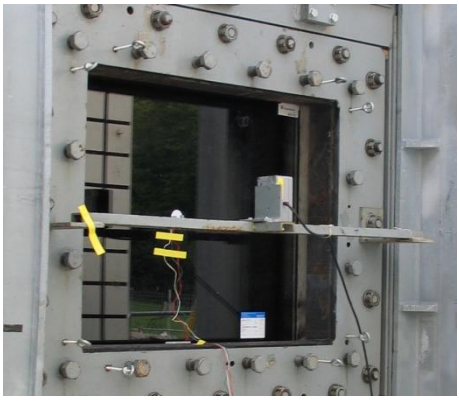

Figure 7-14 **Specimen ready for testing with laser measuring centre displacement mounted on backside.**

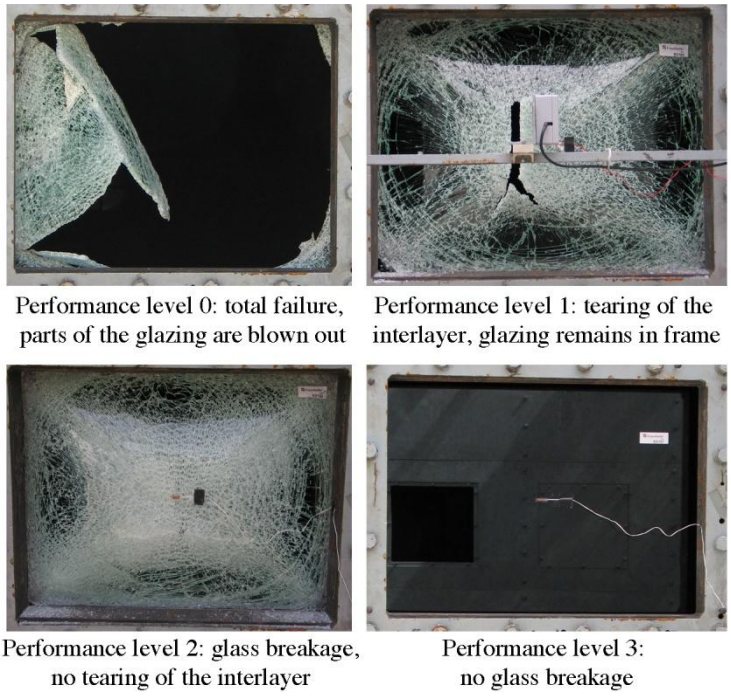

Figure 7-15 **Different performance levels as defined by Kuntsche et al. [37].**

The stiff ES interlayer performed rather poorly in the shock tube tests. These laminates either remained fully intact with no glass fracture, or failed completely. A

stiff PVB interlayer does not allow for much deformation to absorb the shock wave energy, and acts more brittle than a soft PVB interlayer. Consequently, a low adhesion level combined with low stiffness of the interlayer enables higher energy absorption of the shock wave by the laminate before its ultimate failure.

7.3 CONCLUSIONS

An introduction to explosions and their effects was given in this chapter. The equations governing explosions and blast loading of structures have been presented in some detail. Many of them have been empirically determined, but numerical modelling has shown to provide more accurate results. Scaled distance and TNT equivalent weight have been introduced as important parameters.

Several international standards can be consulted for performing (large-scale) blast tests on laminated glass, but most of them classify results in simple categories and none employ instrumentation.

Failure of laminated glass subjected to blast loading exhibits complex behaviour with brittle cracking of the glass plies and highly elastic behaviour and ultimate tearing of the PVB interlayer. Several researchers have conducted large-scale tests.

7.4 REFERENCES

[1] P. D. Smith and J. G. Hetherington. Blast and ballistic loading of structures. Butterworth-Heinemann, Oxford, 1994.

[2] S. Palanivelu, "Energy Absorption of chrusable Tubes for Protective Structures under Static, Impact and Blast Loading," Doctor in de Ingenieurswetenschappen: Werktuigkunde-elektrotechniek PhD, Department of Material Science and Engineering, Mechanics of Materials and Structures, Ghent University, Ghent, 2011.

[3] P. W. Cooper and S. R. Kurowski. Introduction to the technology of explosives. Wiley-VCH, New York, 1996.

[4] Ufc 3-340-02: Structures to resist the effects of accidental explosions.

[5] C. N. Kingery and G. Bulmash. Airblast parameters from tnt spherical air burst and hemispherical surface burst. Technical report, Defence Technical Information Center, Ballistic Research Laboratory, Aberdeen Proving Ground, Maryland, 1984.

[6] S. Glasstone and P. J. Dolan, "The effects of nuclear weapons," *United states of Defence, Washington. D.C,* 1977.

[7] P. A. Hooper, R. A. M. Sukhram, B. R. K. Blackman, and J. P. Dear, "On the blast resistance of laminated glass," (in English), *International Journal of Solids and Structures,* vol. 49, no. 6, pp. 899-918, Mar 15 2012.

[8] W. E. Baker, P. S. Westine, and F. T. Dodge. Similarity methods in engineering dynamics: theory and practice of scale modeling. Spartan Books, New Jersey, 1973.

[9] A.M. Shariff, R. Rusli, C.T. Leong, V.R. Radhakrishnan, and A. Buang. Inherent safety tool for explosion consequences study. Journal of Loss Prevention in the Process Industries, 19:409–418, 2006.

[10] J. Casal. Evaluation of the effects and consequences of major accidents in industrial plants. Elsevier, 2008.

[11] Tm5-855-1: Fundamentals of protective design for conventional weapons.

[12] P.M. Locking. The trouble with tnt equivalence. In 26th International Ballistics Symposium, 2012.

[13] P. W. Cooper. Comments on tnt equivalence. Technical report, Sandia National Laboratories, Albuquerque, July 1994.

[14] U.S. Army Materiel Command. Engineering design handbook: Explosive series, properties of explosives of military interest. Technical report, U.S. Army, 1971.

[15] G. C. Mays and P. D. Smith, *Blast effects on buildings*. London: Thomas Telford Publications, 1995, p. 132.

[16] C. E. Needham. Shock wave and high pressure phenomena. Springer-Verlag, Berlin, 2010.

[17] C. Mougeotte, P. Carlucci, S. Recchia, and H. Ji. Novel approach to conducting blast load analyses using abaqus/explicit - cel. In 2010 SIMULIA Customer Conference. U.S. Army - ARDEC, Dassault Systèmes Simulia Corp., 2010.

[18] M. Haldimann, A. Luible, and M. Overend, *Structural Use of Glass* (Structural Engineering Documents, no. 10). Zürich: International Association for Bridge and Structural Engineering, 2008, p. 215.

[19] DIN EN 13541. Glas im Bauwesen - Sicherheitssonderverglasung - Prüfverfahren. CEN, 2012.

[20] DIN EN 13123-1. Fenster, Türen, Abschlüsse - Sprengwirkungshemmung - Anforderungen und Klassifizierung - Teil 1: Stossrohr. CEN, 2001.

[21] DIN EN 13123-2. Fenster, Türen, Abschlüsse - Sprengwirkungshemmung - Anforderungen und Klassifizierung - Teil 2: Freilandversuch. CEN, 2004.

[22] DIN EN 13124-1. Fenster, Türen, Abschlüsse - Sprengwirkungshemmung - Prüfverfahren - Teil 1: Stossrohr. CEN, 2001.

[23] DIN EN 13124-2. Fenster, Türen, Abschlüsse - Sprengwirkungshemmung - Prüfverfahren - Teil 2: Freilandversuch. CEN, 2004.

[24] ASTM F 1624. Standard Test Method for Glazing and Glazing Systems Subject to Airblast Loadings, 2004.

[25] GSA. Security Criteria, 2003.

[26] ARA. Applied Research Associates: Window Glazing Analysis Response & Design WINGARD: Technical Manual, 2005.

[27] ISO 16933. Glass in builduing - Explosion-resistant security in glazing - Test and classification for arena air-blast loading, 2007.

[28] ISO 16934. Glass in builduing - Explosion-resistant security in glazing - Test and classification for shock-tube loading, 2007.

[29] H.D. Hidallana-Gamage, D.P. Thambiratnam, and N.J. Perera. Failure analysis of laminated glass panels subjected to blast loads. Engineering Failure Analysis, 36:14–29, 2014.

[30] M. Larcher, G. Solomos, F. Casadei, and N. Gebbeken, "Experimental and numerical investigations of laminated glass subjected to blast loading," (in English), *International Journal of Impact Engineering*, vol. 39, no. 1, pp. 42-50, Jan 2012.

[31] T. Krauthammer and A. Altenberg, "Negative phase blast effects on glass panels," (in English), *International Journal of Impact Engineering*, vol. 24, no. 1, pp. 1-17, Jan 2000.

[32] Smith, D. Glazing for injury alleviation under blast loading – UK Practice. In Proceedings of Glass Processing Days 2001, 18-21 June, Tampere, Finland. 2001.

[33] C. Kranzer, G. Gürcke, and C. Mayrhofer, "Testing of Bomb Resistant Glazing Systems Experimental Investigation of the Time Depemdent Deflection of Blast Loaded 7.5 mm Laminated Glass," presented at the Glass Processing Days 2005, Tampere, Finland, 2005.

[34] J. Kuntsche and J. Schneider. Experimental and numerical investigation of the mechanical behavior of explosion resistant glazing. In Proceedings of engineered transparency, pages 175-184, Düsseldorf, Germany, 2014.

[35] J. Kuntsche and J. Schneider. Explosion resistant glazing - experimental tests and numerical simulation. In Glass Performance Days, pages 173-177, 2013.

[36] J. Kuntsche and J. Schneider. Mechanical behavior of polymer interlayers in explosion resistant glazing. In C. Louter, J. Belis, F. Bos, and J.P. Lebet, editors, Challenging Glass 4 and COST Action TU0905 Final Conference, pages 447{454. Taylor and Francis Group, 2014.

[37] J. Kuntsche. Mechanisches Verhalten von Verbundglas unter zeitabhängiger Belastung und Explosionsbeanspruchung. PhD thesis, Technische Universität Darmstadt, 2015.

Chapter 8 BLAST: SMALL-SCALE TESTS

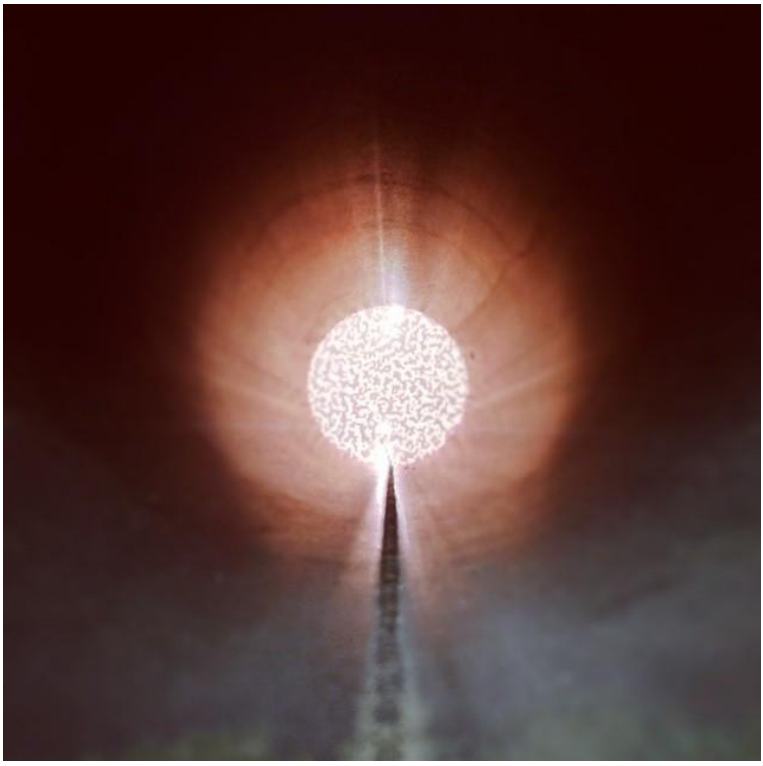

Overview

This chapter deals with the small-scale explosion tests, conducted in an underground bunker. The first few test series, which did not achieve the set goals, are briefly summarized. The results obtained with the finalized set-up, with a shock tube, are described in detail. Pressure measurements for both open air and shock tube tests are discussed as well. In the end, a clear distinction could be discerned for laminates with different adhesion levels of the interlayer, with higher adhesion leading to a lower blast resistance.

The tests are described in two parts. The objective was to obtain different responses for different types of adhesion of the glass laminates. In the first three test series, this goal could not be achieved, due to a variety of reasons which will be explained. Their results are thus grouped – and only briefly summarized – in a first part of so-called preliminary tests (9.2). The final test series with a shock tube, where the goal could be achieved, is described in detail (9.3). Both parts start with an investigation on the shock wave pressure. The parts of the test set-ups which remained the same for all tests, such as the high-speed camera set-up, the steel frame and the used explosives, are presented first.

8.1 TEST SET-UP

All experiments were performed in the test bunker of the Laboratory for the Analysis of Explosion Effects (LAEE) at the Royal Military Academy in Brussels under the supervision of ing. Bruno Reymen.

A steel plate of 1 by 1 metre with a thickness of 15 mm was designed and constructed. Threaded holes (as opposed to the old system with threaded bolts and nuts) ensured a swift replacement of one tested glass panel for the next one. A clamping ring, similar to that of the small-scale drop weight (SSDW) set-up of Chapter 6, was constructed as well. The polypropylene spacer rings were, however, replaced with felt strips, a material commonly used in the glass industry. Steel U-profiles were welded to one side of the steel plate to improve bending stiffness. The steel plate is attached to the floor with a construction profile along the bottom edge, and with two hinged profiles, essentially creating a mini truss work. A picture is shown in Figure 8-1.

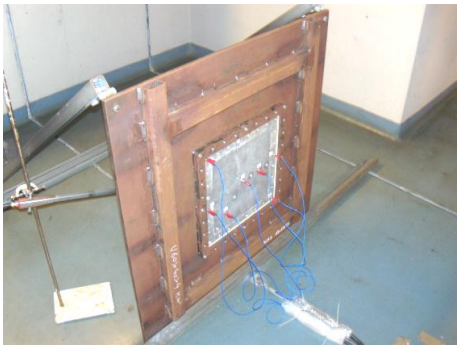

Figure 8-1 **Steel plate for mounting test specimens, including welded U-profiles, clamping ring and aluminium test plate with pressure sensors.**

The technical drawing of both steel plate and clamping ring (with all dimensions in mm) are shown in Figure 8-2.

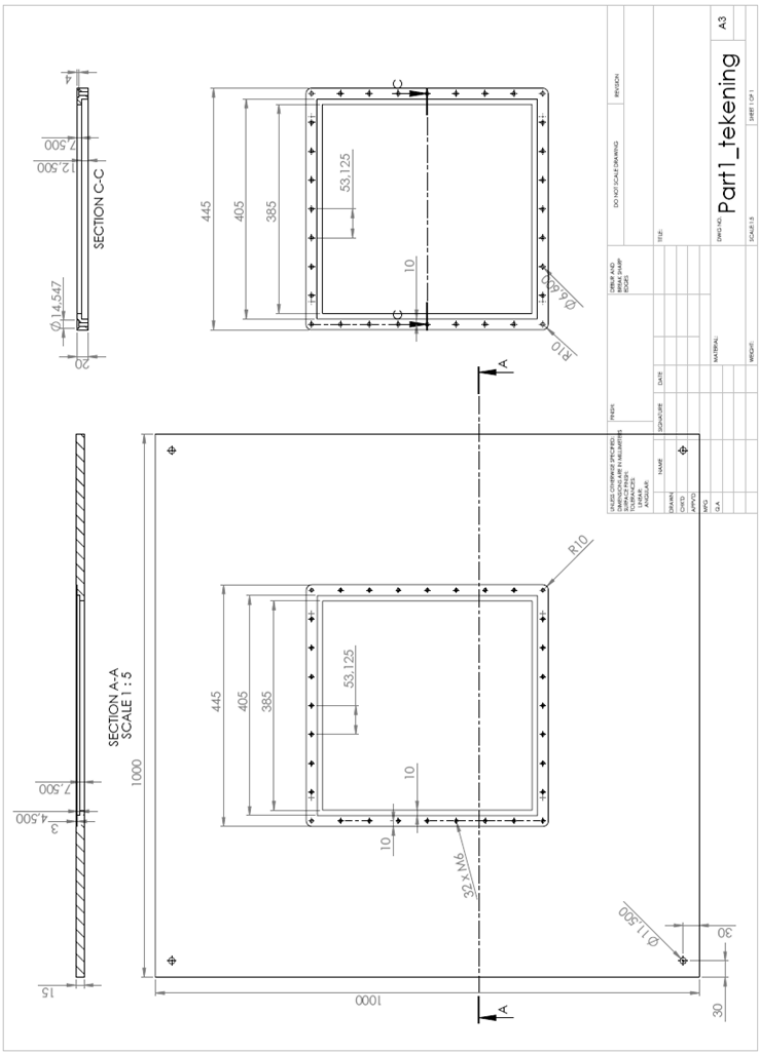

Figure 8-2 Technical drawing for steel plate and clamping ring.

8.1.1 Explosive material

The used explosive is Composition 4, better known as C-4. This explosive is a member of the Composition C family, which are all plastic explosives with a relative high concentration of RDX. RDX stands for Research Department Explosive and is

an explosive nitroamine, generally used in military and industrial applications. The word 'Composition' illustrates that the explosive is compounded from several ingredients. According to the United Nations Database, C-4 nowadays usually contains the following components:

- 91% explosive material: RDX
- 5.3% plasticiser: di(2-ethylhexyl) sebacate
- 2.1% binder: polyisobutylene
- 1.6% motor oil

Because C-4 is a plastic explosive, it is kneadable by hand and mouldable in the desired shape. The relatively stable nature of C-4 results in several advantages with regqrd to the safe application of the explosive. It is insensitive to most physical shocks and lighting the C-4 with a match will just make it burn slowly, like a piece of wood. Detonation by means of a gunshot or dropping it onto a hard surface is not possible. Because of the stabiliser elements in the RDX, it takes a considerable shock to set off the explosive reaction. The only way of detonating C-4 is by initiating a combination of extreme heat and a shockwave. This can typically be done by firing a detonator inserted into the C-4.

Proper alignment was ensured using laser levels attached to the symmetry planes of the large steel plate. An example of a charge aligned in the centre is shown in Figure 8-3.

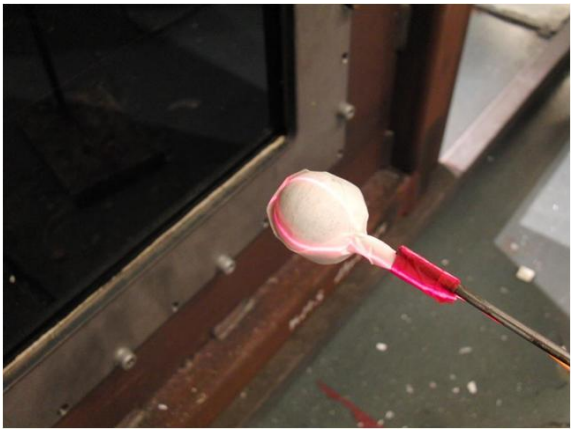

Figure 8-3 Alignment of the charge using laser levels.

8.1.2 High-speed camera set-up

Apart from pressure and strain gauge measurements (see further), the main instrumentation for the tests were two high-speed cameras combined with the DIC technique (Figure 8-4). Two Photron Fastcam SA5 cameras were available.

Figure 8-4 **High-speed camera set-up including 4 additional lighting sources and Laser Doppler Vibrometer (LDV) in the middle.**

For all tests, the frame rate was set to 25.000 fps with a resolution of 512 by 512 pixels and a shutter speed of 1/40.000 s. Four additional light sources (2 x 1000 W and 2 x 400 W) illuminated the specimen sufficiently. A schematic of the test set-up is shown in Figure 8-5.

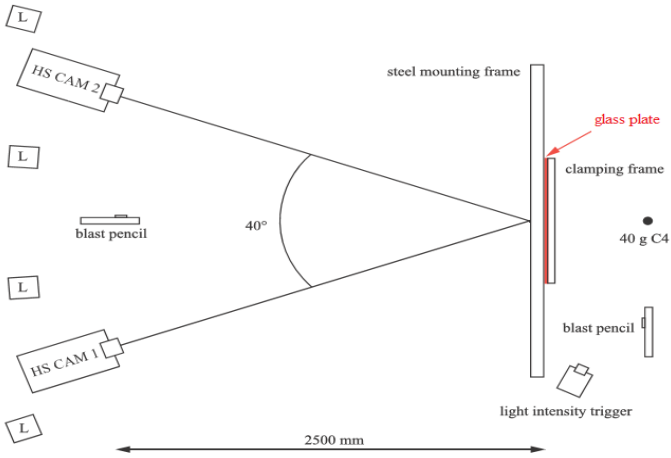

Figure 8-5 **Schematic of test set-up (adapted from [2]).**

8.2 PRELIMINARY TESTING

In this section the preliminary blast tests will be discussed. However, before presenting the actual results, pressure measurements of open air blast tests on the set-up are discussed. Those results will be very useful for the numerical simulations and to know the forces acting on the glass panels.

8.2.1 Pressure measurements

The test setup consists of a rigid aluminium square plate with dimensions 0.40 x 0.40 x 0.02 m. This plate is clamped in the larger steel frame using the same camping ring used for tests with laminated glass. The plate is provided with several predrilled holes in which pressure sensors can be installed. The explosives are positioned on the other side of the plate by means of an adjustable stand so that the required distance to the plate can be obtained. Furthermore, also a blast pencil is installed on the same side as the explosive. The set-up is presented in Figure 8-6.

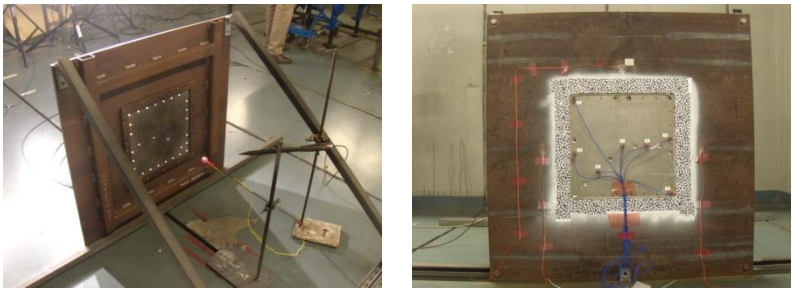

Figure 8-6 **Pressure measurement set-up: explosive and blast pencil (left) and aluminium plate with mounted pressure sensors (right).**

Two types of sensors are used according to the type of pressure to measure the pressure to which the plate is exposed:

- Dynamic pressure: High frequency ICP® pressure sensor, Model 102B04
- Static pressure: Free Field Blast ICP® pressure probe, Series 137A20

Figure 8-7 **Pressure sensors: dynamic pressure (left) and static pressure (right).**

The sensors for the dynamic pressure are all installed into the aluminium plate. The exact location of all 7 sensors is illustrated in Figure 8-8.

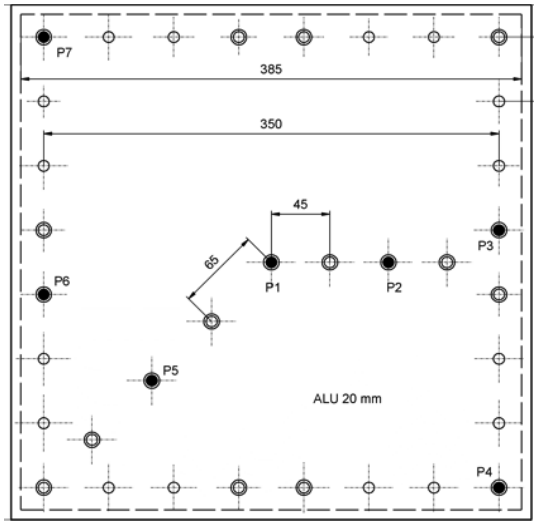

Figure 8-8 Location of the dynamic pressure sensors.

The weight of the charges (20 g) is simply controlled by using a balance with an accuracy of 0.01 g. The distance charge-frame (30 cm) and the height of the charge (50 cm) are maintained by measuring them with a standardised ruler. A mould is used to form the charges to be sure that the charge has every time the same spherical shape. A 3D printer is used to construct such precise mould (see Figure 8-9). In the mould there is a small opening provided through which a small pin can be pressed so that a tubular opening is made in the charge. The detonator can be inserted in this tubular opening.

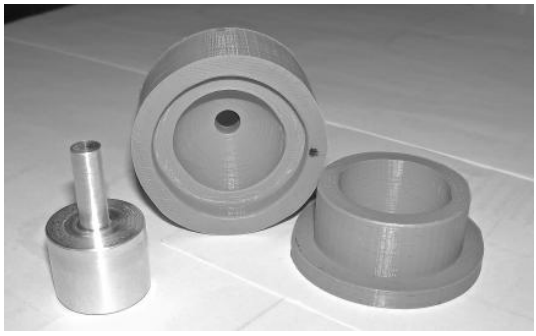

Figure 8-9 3D-printed mould for forming a spherical charge.

Blast tests have the tendency to show a spread on the test data. Two individual tests can therefore result in very different pressure-time curves. This results in the need to combine the 10 individual tests in 1 averaged curve. Furthermore, every individual curve shows many different succeeding peaks and lows. This can be seen in the curves of test 1 to 5 in Figure 8-10. These peaks and lows also result in the need for a more average and smoother curve.

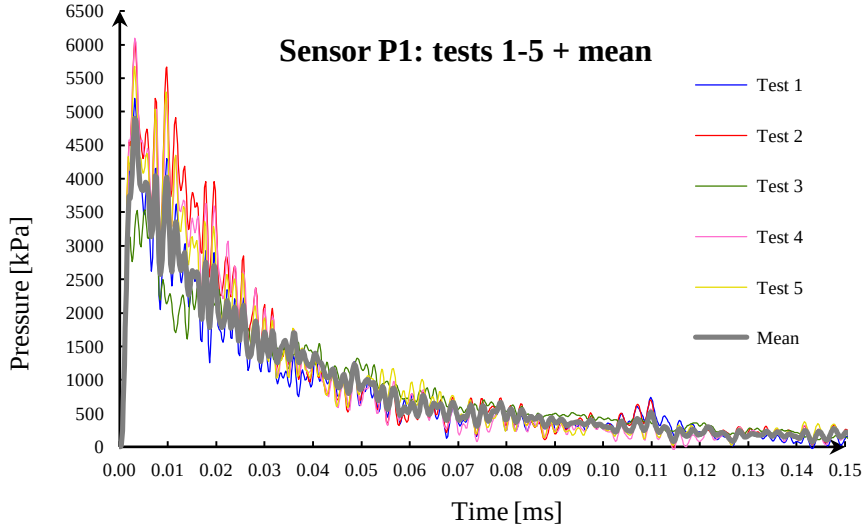

Figure 8-10 Individual pressure-time curves and the mean curve.

The next step in obtaining a mean curve is taking the average of the 10 reference tests for each time step. By doing this, unexpected excessive peaks can be averaged out. The resulting curve after averaging each time step still shows some peaks and lows. Therefore a moving average will be applied. Every pressure value up to five values after the peak is kept. The moving average of the 10 previous values is taken from the sixth value on. Figure 8-11 shows the mean curve before and after taking the moving average.

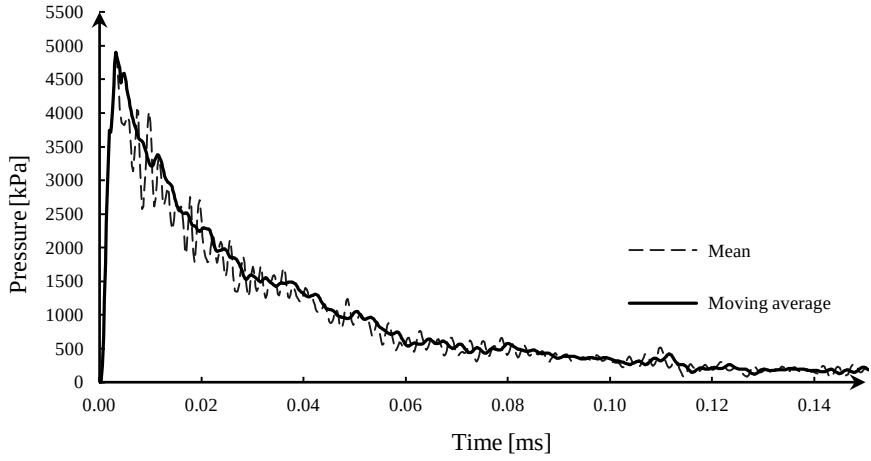

Figure 8-11 Mean vs. moving average for reference tests of sensors P1.

Figure 8-12 shows pressure-time curves for all sensors, averaged over the 10 tests.

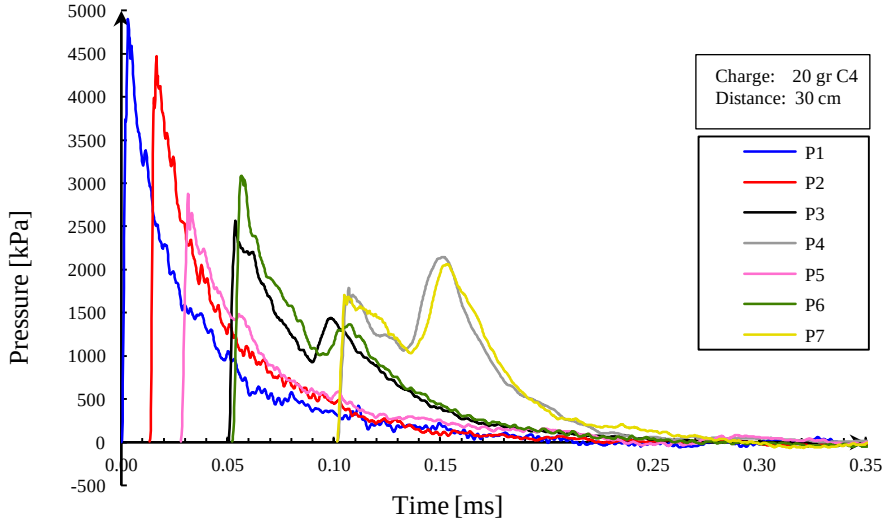

Figure 8-12 Pressure-time curves reference tests.

First of all it is clearly visible that the time needed for the wave front to reach a sensor, increases when a sensor is located further from the centre of the plate. The wave front reaches sensor P1 first, since this is the sensor located in the centre of the plate. The sequence of sensors, in increasing distance from sensor P1, is: P2 (90

mm), P5 (130 mm), P3 & P6 (177 mm), P4 & P7 (247 mm). Furthermore, it is stated that the further a blast wave travels, the more the peak pressure at the wave front decreases. This statement is valid according to the results since the sensors more distant of P1 register a smaller peak pressure.

Concerning the symmetric sensors, it is confirmed that the wave front reaches these sensors almost perfectly at the same time. Sensors P4 & P7 register nearly exactly the same peak pressure and their curves have the same trend. The trend of the curves of sensors P3 & P6 is similar but not perfectly the same. Also their peak pressures are different (17% deviation).

The curves of the sensors P3, P4, P6 and P7 show a second peak some time after the first. These are the sensors located near the edge of the plate, so near the clamping ring. Reflections of this clamping ring could be the reason of this second peak.

8.2.2 First test series: Open air, narrow clamping ring

The first blast test series was straightforward, with the boundary conditions determined by the initial design of the clamping frame and with an 'open air' charge positioned at some distance of the test sample.

The test series was conducted in two sessions; a total of 30 tests were performed. For session 1, all samples had adhesion level A (high). For session 2 also samples with a low adhesion level were tested.

Session 1 was executed mainly to get a feel of the set-up, see which charge weights and distances resulted in which amount of damage, and assess how reproducible the tests were.

Behind the frame, on the side of the charge, a blast pencil was placed. To avoid damage to the pencil, it was placed at a distance of minimal 30 cm of the C-4 charge. Placing this pencil will allow us to monitor the pressure variation through time and thus detect the moment when the blast wave hits the glass panel. A second blast pencil is located next to the high speed cameras. The idea behind this is to determine the time at which the blast wave reaches the cameras. The blast wave will cause the cameras to vibrate and the data obtained by digital image correlation after this will not be accurate anymore.

All the instrumentation is synchronised by a flash detector. The detector makes sure that all data is recorded as soon as the flash of the explosion is observed. A test specimen ready for testing is shown from the back (explosion) side in Figure 8-13 and from the front side in Figure 8-14.

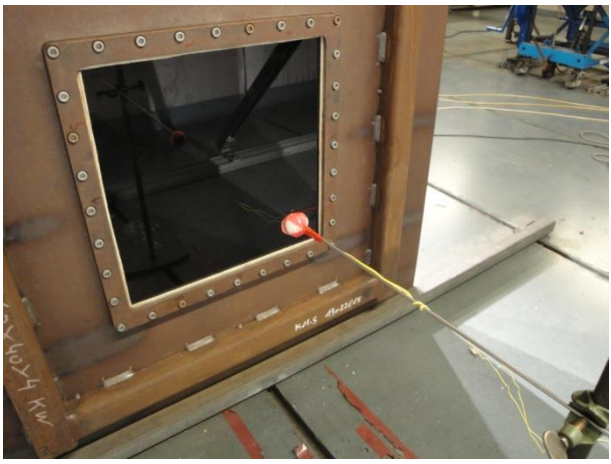

Figure 8-13 Laminate ready for testing with charge attached to rod.

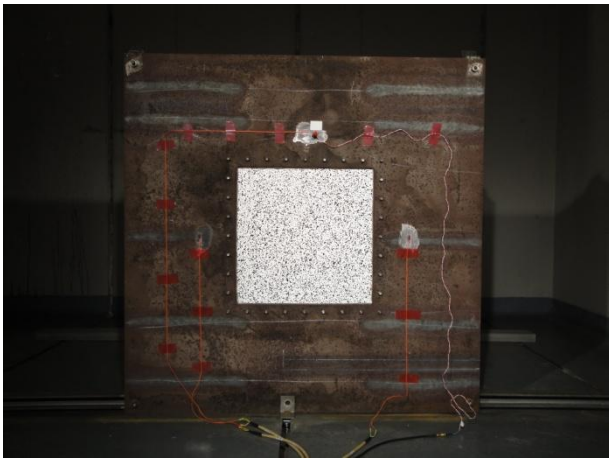

Figure 8-14 Laminate ready for testing (front view).

8.2.2.a Elastic response

In the first test session, two tests with a C4-charge of 20 grams located at 40 centimetres of the laminated glass panel resulted in unbroken glass panels. Looking at the average out-of-plane deformation of the central area of the glass, a comparable oscillating behaviour for both tests can be observed.

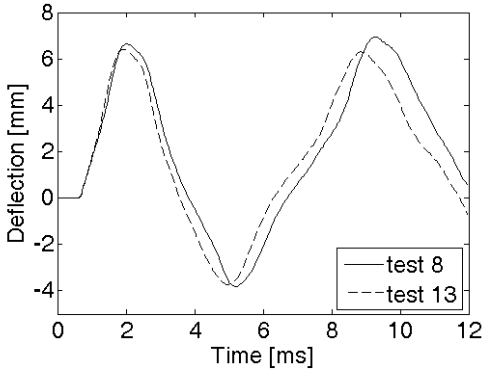

Figure 8-15 Out-of-plane deformation for two elastic tests.

This information can prove useful for the numerical simulations to assess the boundary conditions, as the felt clamping is difficult to characterize.

8.2.2.b Breakage pattern

After the execution of every test, a photo was taken of the breaking pattern on the glass at the charge side. In Figure 8-16 the breaking pattern of test 1 can be seen.

One notices that nearly all patterns are similar to each other; the cracks are concentrated at the corners of the frame and directed diagonally to the middle of the glass plate where their direction changes to eventually form a square rupture pattern in the central area. Figure 8-17 illustrates the typical rupture pattern in a simplified way with the lines showing the concentration of fracture lines.

Figure 8-16 Typical breakage pattern after test.

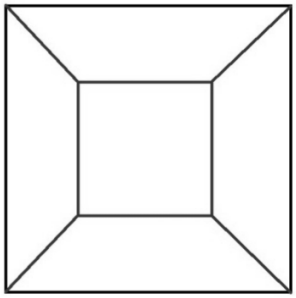

Figure 8-17 Simplified typical fracture pattern.

The relatively undamaged square area has an approximate size of 100 mm x 100 mm. In the corners of the central square area the glass is broken in a large number of small, rectangularly shaped pieces. Along the edges of the central square area the glass broke into long strips lying parallel to one another.

8.2.2.c Severe loading

For some tests it was observed that one or more edges of the specimen were pushed out of the clamping area. An example is shown in Figure 8-18.

Figure 8-18 Partially detached test plate after test.

The most ‘aggressive’ test, with a charge of 40 g at 20 cm from the specimen, caused the glass panel to be blown out of the frame completely (Figure 8-19). The plate ended up 2 meters in front of the frame (Figure 8-20). The PVB interlayer

remained intact but the glass broke. In fact for no single test the PVB interlayer was ruptured, nor did visible delamination of the glass plate occur.

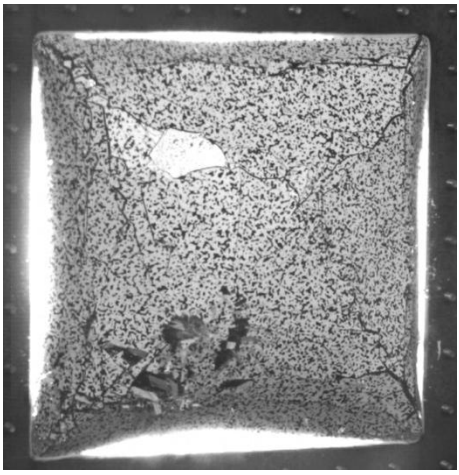

Figure 8-19 **Laminate edges being pulled out of clamping frame.**

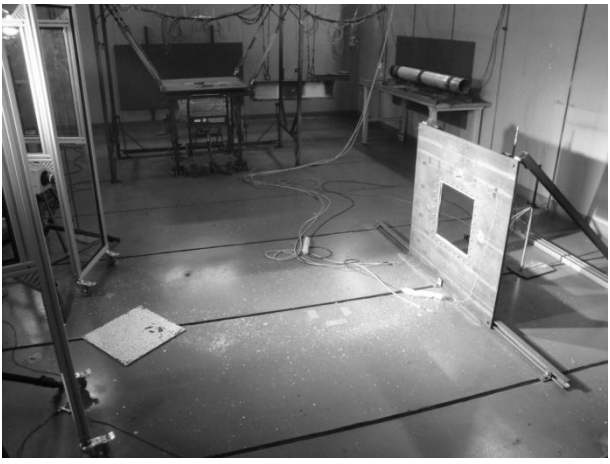

Figure 8-20 **Laminate blown out of frame. Polycarbonate shields in front of high-speed cameras are also visible.**

The impact tests from Chapter 5 made clear that severe loading of the specimen was needed to notice differences between different adhesion levels. An attempt to solve this problem was made in the second test series.

8.2.3 Second test series: Open air, wide clamping ring

To mitigate the above problem, a wider clamping ring was designed (Figure 8-21). These provided a clamping of 50 mm around the entire plate, as opposed to only 7.5 mm provided by the narrow clamping frame. The visible area, not inside the clamping rings, was thus reduced to 300 by 300 mm.

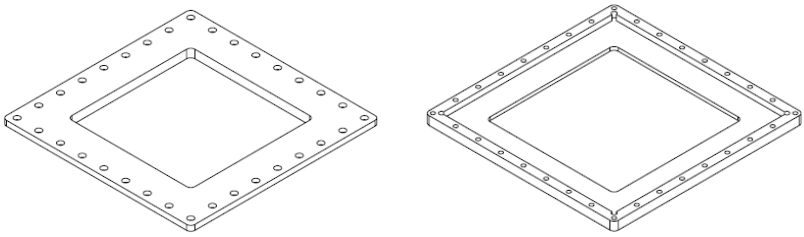

Figure 8-21 Two parts of wider clamping ring set-up.

Whereas the plates no longer were pushed out of the frame for severe loading, still no tearing of the PVB interlayer could be achieved. A charge of 40 grams placed at a mere 10 cm from the plate, caused heavy damage, but no rupture of the interlayer and thus no difference in result between different adhesion levels.

A charge placed so close to the laminate meant that local effects came into play and predicting the actual loading became difficult, if not impossible, without detailed numerical models of the explosion event. An attempt to overcome this problem was made in a third, and final, preliminary test series.

8.2.4 Third test series: Small shock tube, wide clamping ring

A small shock tube, available from a different research project at the LAEE, was employed for the third test series. This meant that a severe loading could be applied to the centre of the laminate. Furthermore, a shock tube – of sufficient length – results in a plane shock wave, with the same pressure for equal charges (as opposed to the unreliable local effects due to the very small distance in the previous test series).

A picture of the set-up is shown in Figure 8-22. The shock tube had an inner diameter of 16.7 cm.

For the first test immediately a high charge weight of 40 grams was used; if this did not result in tearing of the PVB further testing would be pointless.

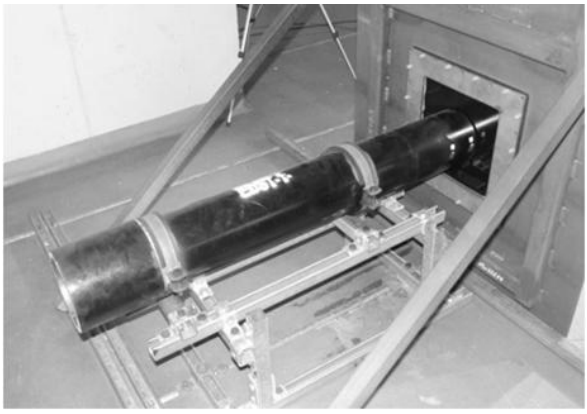

Figure 8-22 Small shock tube used during preliminary testing.

The result is shown in Figure 8-23 and Figure 8-24. The shock wave caused immediate tearing of the PVB along a circle with a diameter slightly larger than that of the shock tube itself. The circular piece was blown several meters away, with almost no more glass particles attached to it. The black PVB foil, used to block the light from the explosion (which would temporarily saturate the high-speed cameras' CCD chips), is clearly visible.

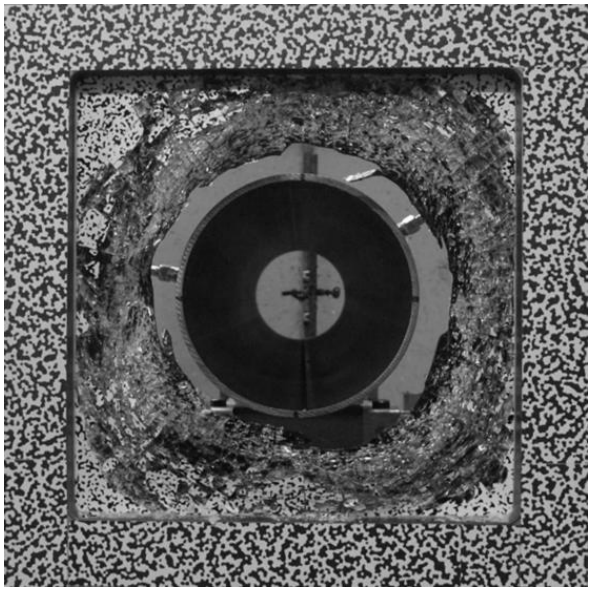

Figure 8-23 Destroyed panel after small shock tube test.

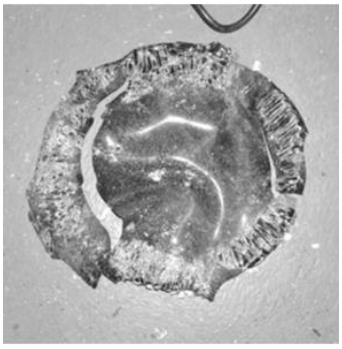

Figure 8-24 Piece blown out of laminate.

When using lower charges, finally a difference between the adhesion levels became apparent (Figure 8-25).

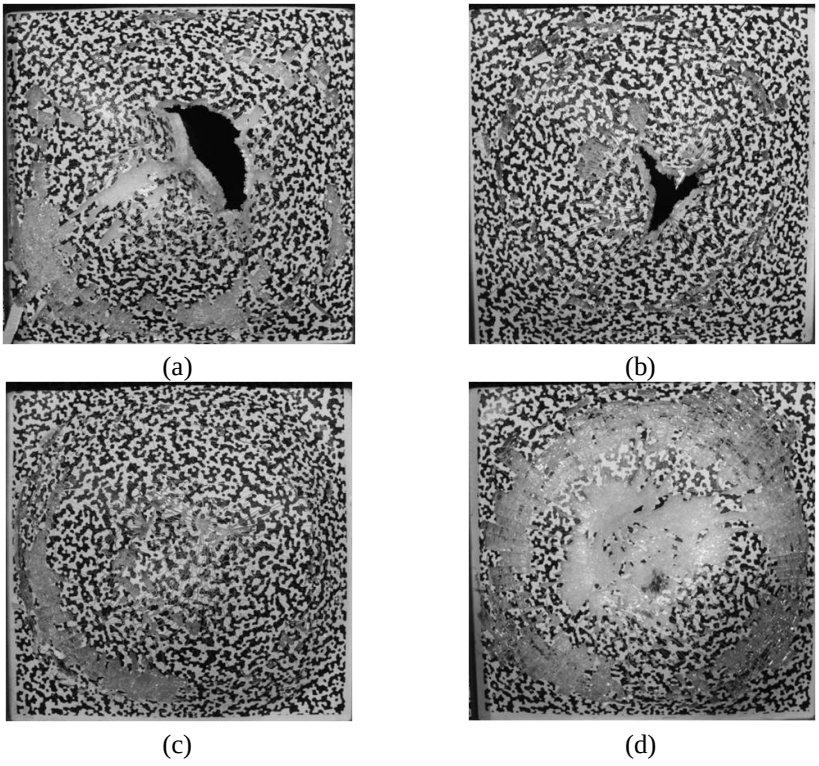

Figure 8-25 Difference in laminate behaviour: (a) & (b) high adhesion with tearing of the PVB and (c) & (d) low adhesion without tearing.

However, the correlation of the images was hindered due to the massive amount of tiny glass fragments which propelled forward as soon as the shock wave hit the specimen (Figure 8-26). This made extracting quantitative data out of the images impossible.

The glass fragments often cracked about halfway through their thickness, meaning that thin flakes remained attached to the foil as well as flew forward. These are called lateral cracks (see Figure 8-27).This is clearly visible in Figure 8-25 (d) where large areas of the speckle pattern have disappeared and instead now show glass.

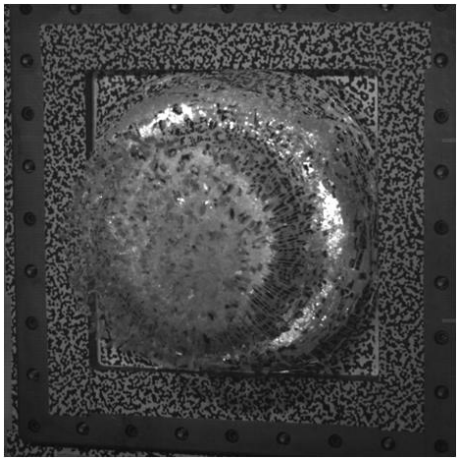

Figure 8-26 Glass fragments preventing correlation of the images.

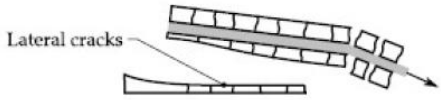

Figure 8-27 Cross-section of laminated glass with lateral cracks.

Further proof that the loading was concentrated on the centre of the laminate became visible when removing the specimens from the clamping frame. Often, large portions of the laminate were still completely intact (Figure 8-28). These areas were found in the corners of the clamping area.

Figure 8-28 **Back of specimen tested with small shock tube; corner completely undamaged.**

This final preliminary test series was designed to overcome the last problem of a concentrated high load, which resulted in glass fragments hindering correlation.

8.3 SHOCK TUBE

The preliminary tests, their problems, and subsequent steps to solve them can be summarized as follows. With the initial design of the set-up (open air blast and limited clamping), severe loading, needed to tear the PVB interlayer, resulted in the specimens being blown out of the frame. This was remediated in the second set-up with wider clamping rings. However, even with high charges very close to the specimen, no difference in behaviour, depending on adhesion level, could be discerned. Furthermore, this resulted in unpredictable pressures. The third set-up thus used a small-shock tube which could deliver a high load with reasonable precision. This concentrated force, however, resulted in immediate lateral cracking and problems with the correlation of the high-speed images.

In this final test series, it will be shown that using the new, larger shock tube overcomes all these problems. As with the preliminary open air blast tests, first the pressures will be investigated using the same aluminium test plate with pressure sensors.

8.3.1 Test set-up

The shock tube has an inner diameter of 425 mm and a length of 1.5 m. A base with wheels was attached with bolts to ensure that the centre of the tube corresponded to

the centre of the laminated specimens, at a height of 50 cm. This also made moving the shock tube easier. A picture of the shock tube is shown in Figure 8-29. The rest of the set-up remained the same, with the wider clamping rings still in use.

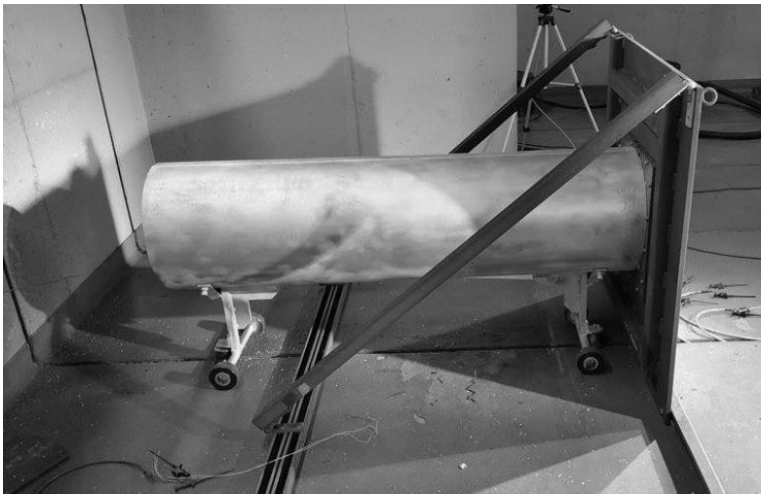

Figure 8-29 Newly constructed, large shock tube for final test series.

8.3.2 Pressure measurements

Apart from the addition of the shock tube, the pressure measurements use exactly the same test set-up as in 8.2.1 (including the same sensors and aluminium plate). The explosives are positioned at the centre of the end of the shock tube using the same stand as shown in Figure 8-6 and Figure 8-13. The position of the sensors, however, was changed a bit, as the outer rows of possible locations were now inside the clamping ring (see Figure 8-30).

A total of 9 tests were performed, 3 for each charge weight of 10, 12.5 and 15 g. The results of 15 g are presented in more detail.

Figure 8-31 shows that the shock front arriving at the test plate is indeed planar and quasi-uniform over the loaded surface. Moreover, the blast loading can be repeated excellently. The average peak pressure is 11.03 bar and the average pressure impulse is 558 kPa ms.

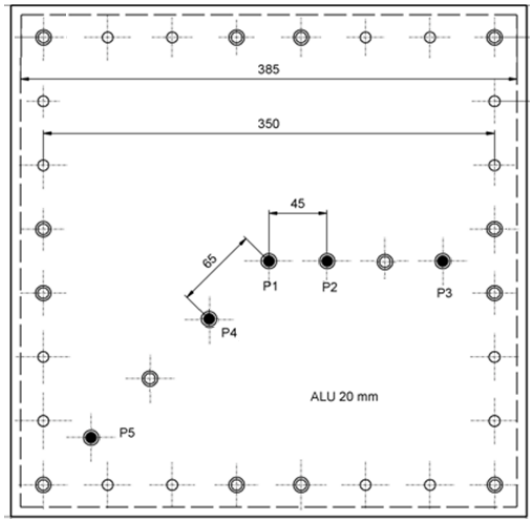

Figure 8-30 **Position pressure sensors shock tube tests.**

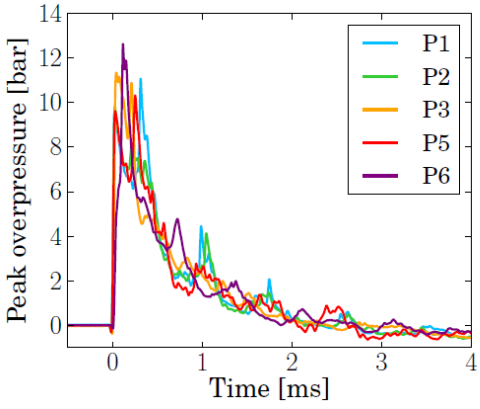

Figure 8-31 **Blast pressures on test plate with 15 g charge of C-4 and shock tube at all probes for a single test.**

Also when looking at the same sensor for three different tests with a 15 g charge, the reproducibility is evident (Figure 8-32).

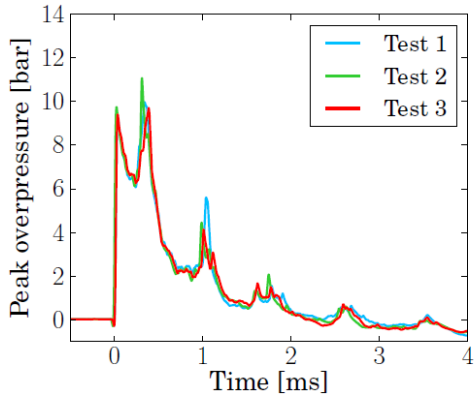

Figure 8-32 **Blast pressures on test plate with 15 g charge of C-4 and shock tube at centre probe P1 for repeated tests.**

8.3.3 Large shock tube tests on laminated glass

8.3.3.a Introduction

With the planarity and reproducibility of the shock wave proven, the actual testing of laminated glass could commence. The set-up is shown in Figure 8-33 and the high-speed camera set-up in Figure 8-34, where also the screens used to protect them are visible.

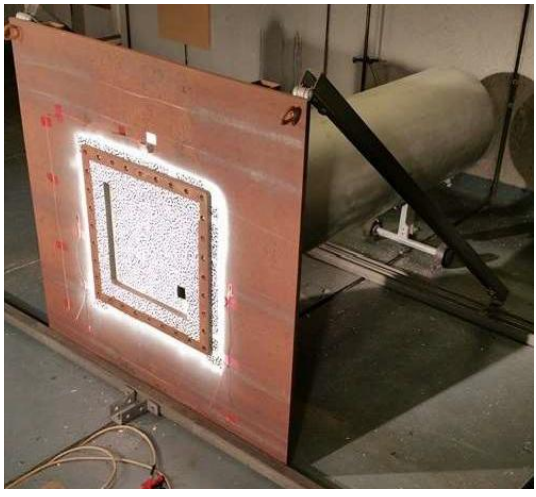

Figure 8-33 **Test set-up of final configuration with large shock tube.**

Figure 8-34 **High-speed camera set-up including shielding screens; a wide, square ring of felt is visible in the clamping area.**

A strain gauge rosette was applied in the bottom right corner of all specimens (Figure 8-35).

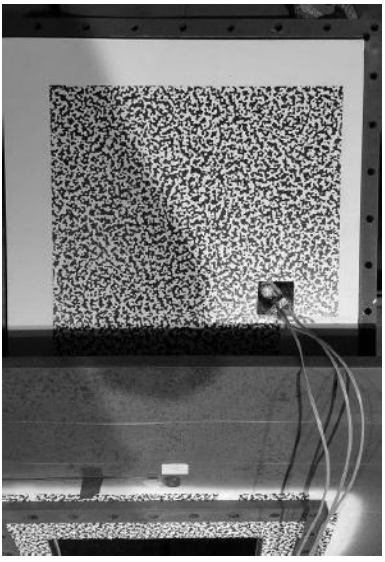

Figure 8-35 **Test specimen with speckle pattern and strain gauge rosette, ready for mounting in the clamping rings.**

8.3.3.b Description of executed tests

An overview of all executed tests is presented in Table 8-1. Three different adhesion levels were tested, with varying charge weights placed at the end of the shock tube.

All interlayers had a thickness of 0.76 mm. A short failure description is also already given in this table. The test sequence has been re-ordered to show increasing charge weights grouped per adhesion level.

Table 8-1 Test sample overview.

PVB type	C4 [gram]	Test nr	Failure description
RA	7.5	8	PVB interlayer intact, plane rebounded
RA	10	7	central area blown out
RA	10	10	PVB interlayer intact, plane rebounded
RA	10	11	PVB interlayer torn, plane rebounded
RA	12.5	15	lateral cracks , plane rebounded
RA	12.5	24	PVB interlayer torn, plane rebounded
RA	12.5	25	PVB interlayer intact, plane rebounded
RA	12.5	26	PVB interlayer torn
RA	15	16	PVB interlayer torn + failure at the edges (later)
RB	7.5	2	PVB interlayer intact, plane rebounded
RB	10	1	PVB interlayer torn, plane rebounded
RB	10	3	PVB interlayer intact, plane rebounded
RB	10	4	PVB interlayer intact, plane rebounded
RB	12.5	5	PVB interlayer intact, plane rebounded
RB	12.5	17	PVB interlayer intact, plane rebounded
RB	12.5	20	PVB interlayer torn
RB	15	6	delamination/lateral cracks + small PVB tear
RB	15	21	PVB interlayer torn
RB	15	23	everything is blown out except the upper edge
RC	10	12	PVB interlayer intact, plane rebounded
RC	10	13	lateral cracks , plane rebounded
RC	10	14	little delamination at the edge
RC	12.5	22	PVB interlayer intact, plane rebounded
RC	15	9	delamination
RC	15	18	PVB interlayer torn + failure at the edges (later)
RC	15	19	central area blown out

Images for different time frames of a test on an RB laminate with a charge of 10 g are shown in Figure 8-36. After a short light pulse (not shown) at the time of the explosion (0.0 ms), the shock wave needs approximately 2 ms to reach the laminate. The specimen starts to deflect with a central, square area remaining quite flat. A high degree of curvature is found on the diagonal lines (up to this central area). Reflection of the additional lighting for the cameras is visible around these (upper) lines. This is very similar to the first preliminary tests described in the previous section.

The maximum deflection is attained around 6.8 ms, after which the laminate starts to rebound. This is made clear by the switching of the reflection from the top part to the bottom part of the images. Again, a central, square area remains relatively flat, until the maximum rebound deflection (image at 18.8 ms).

Afterwards, the laminate will oscillate with decreasing amplitude, until a final deformation is reached. As evidenced in the last image at 48 ms, the laminate experiences a permanent, small deflection towards the shock tube.

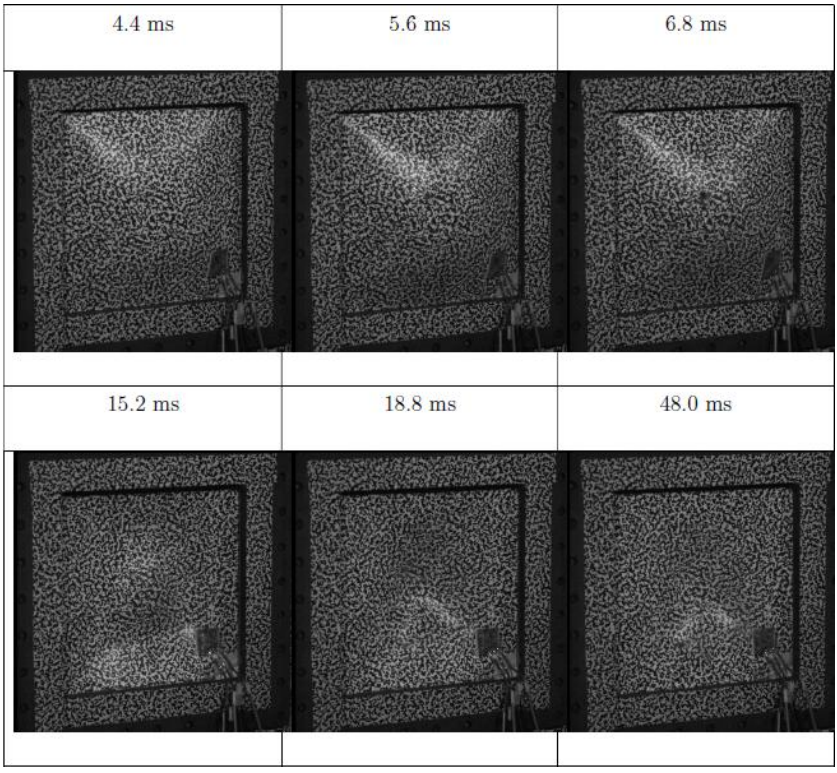

Figure 8-36 High-speed images for test 4 (RB, 10g) without tearing of interlayer.

Although not clearly visible in these images, glass fracture takes place almost immediately after the shock wave reaches the laminate. This also tears apart the strain gauge, impeding further processing of their results.

In Figure 8-37 a similar test (RB, 10 g) is shown, but this time the interlayer tears. The beginning of the deflection remains the same. However, at around 5 ms a Y-shaped tear appears in the middle of the laminate. Each of the 3 ‘lines’ extends only a few centimetres. The three resulting flaps curl outward, and after some time, inwards (view from second camera).

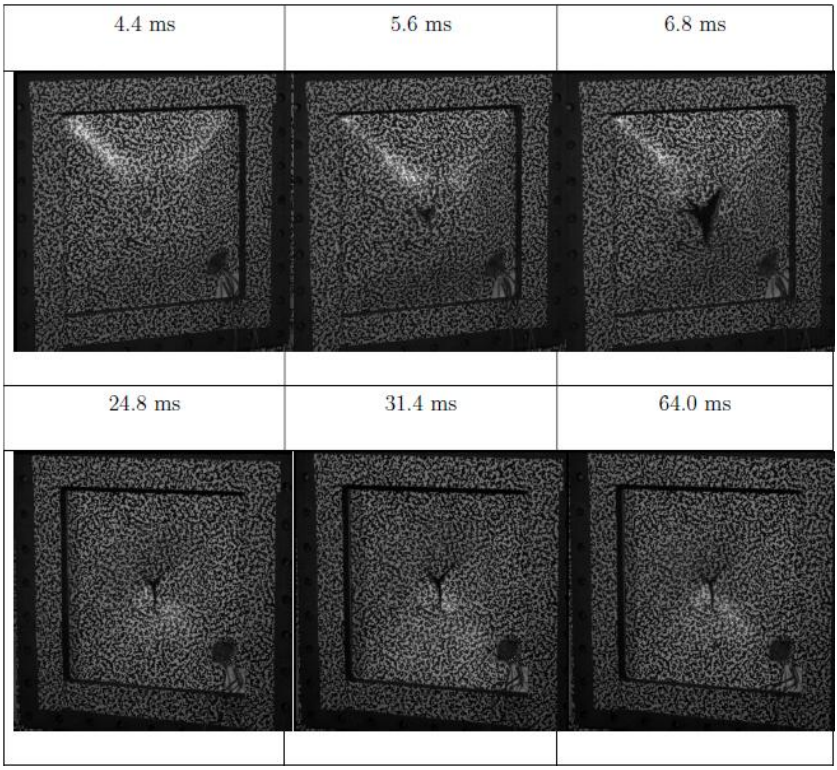

Figure 8-37 High-speed images for test 1 (RB, 10 g) with tearing of interlayer.

More severe tearing of the interlayer is shown in Figure 8-38 (test with 10 g and high (RA) adhesion level). Again, the initial deformation behaviour is the same as for the previous examples.

Next, the interlayer starts to tear along 3 edges of the central area, resulting in a flap of material which excessively bends upwards.

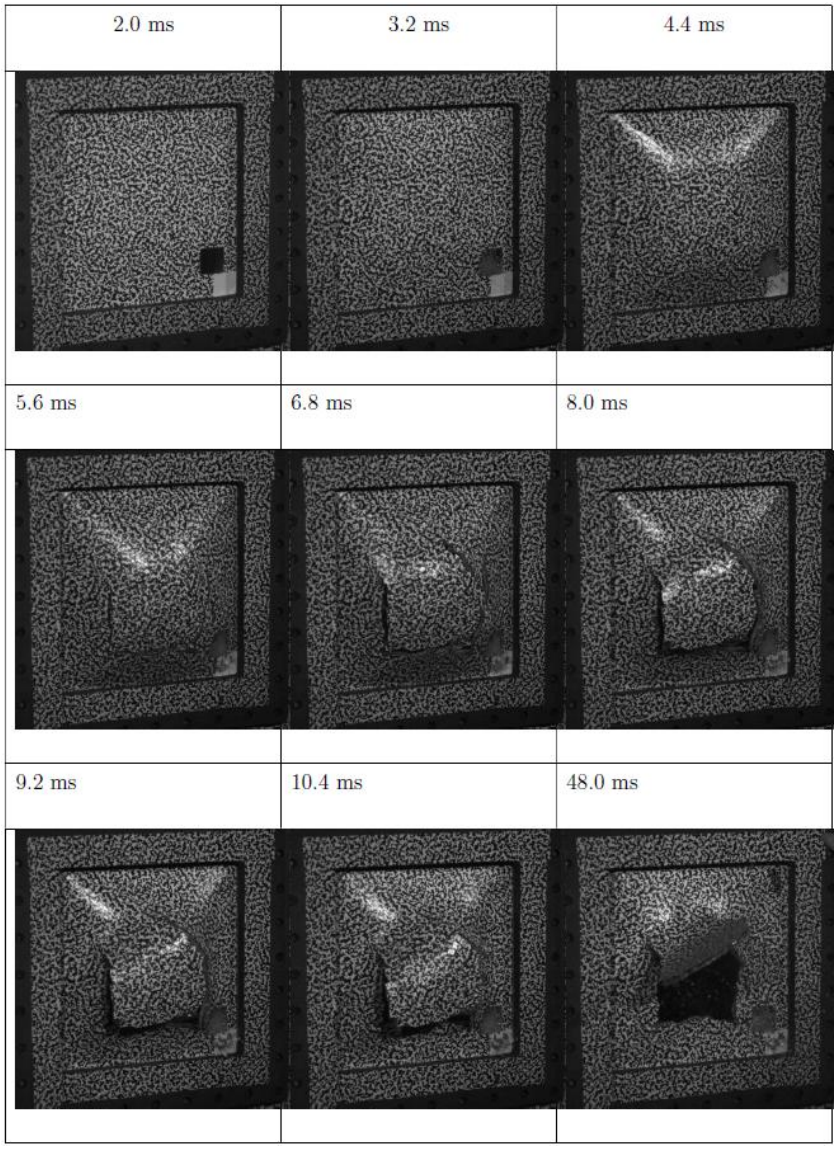

Figure 8-38 High-speed images for test 7 (RA, 10 g) with tearing of interlayer.

The post-test result is shown in Figure 8-39. The upward deflection of the central area is permanent.

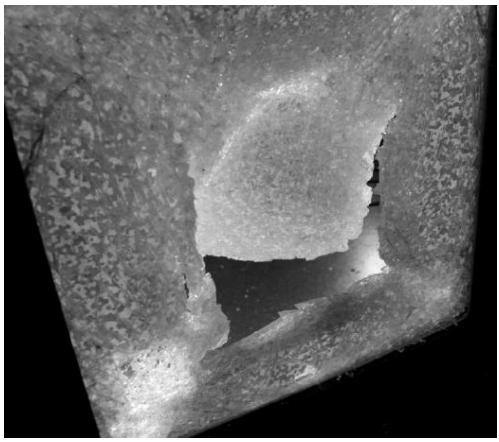

Figure 8-39 **Post-test specimen showing permanent deflection of separated area (view from blast side).**

A clear difference in fracture behaviour of the glass could be observed between the two glass plates of a single laminate. The plate oriented towards the shock tube appeared completely crushed, whereas the other plate fractured in a manner similar to the impact (Chapters 5 & 6) and preliminary blast tests, in relatively large pieces with simple fracture lines going through the entire thickness. This behaviour is made visible in Figure 8-40, which shows the cross-section of a small piece that was removed from a specimen after testing. A large amount of glass dust was also found inside the shock tube after every test.

This also made photographing the fracture patterns difficult, as on the front side the speckle pattern was applied and the backside appeared completely shattered.

Figure 8-40 **Difference in glass fracture: bottom part, appearing crushed, was oriented towards shock tube.**

However, it could be discerned that the overall fracture pattern adhered to the type mentioned earlier, with diagonal lines starting in the corners, branching to each other halfway, and a central area with less damage (see also Figure 8-17).

When looking at the total number of tests where the PVB tore, the difference between adhesion levels becomes clear (charge weights between brackets):

- High adhesion RA: 5 (10, 10, 12.5, 12.5, 15)
- Medium RB: 4 (10, 12.5, 15, 15)
- Low RC: 2 (15, 15)

Only at high loads do some of the low adhesion specimens fail. Given the minor difference in peel strength between RA and RB (respectively 42 and 37 N/cm) as opposed to RC (27 N/cm), the similar behaviour of RA and RB laminates is no surprise.

8.3.3.c DIC analysis

All plates were equipped with a speckle pattern so a DIC analysis could be performed on them. The mid-point displacement and the deflection along a horizontal line through the middle (Figure 8-41) are discussed in the next section.

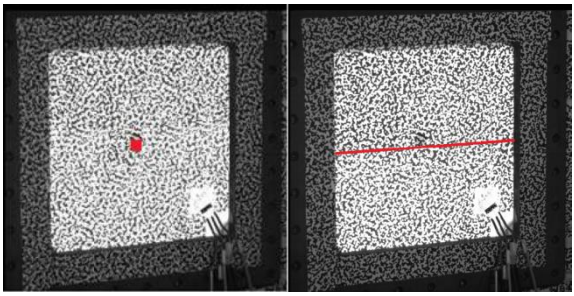

Figure 8-41 Centre point and horizontal line for data extraction.

The maximal and minimal deflection (where applicable), as well as the maximal principal strain for all tests with a 10 g charge are presented in Table 8-2. The mid-point deflection history is presented in Figure 8-42.

The maximum deflection for test 10 and 11 occurs around 6.4 ms. For test 7 the PVB in the central area starts to tear around 5.6 ms and gets pushed out (see also Figure 8-44), at which point the DIC algorithms can't track it anymore. From the overpressure measurements described earlier, it is known that the negative phase for an explosion of 10 grams of C4 starts at approximately 5 ms. Thus, the negative phase starts before the plate starts to rebound and it can counteract the deflection.

Table 8-2 **Deflection and max. principal strain at specimen centre for 10 g tests. (* denotes the maximal strain recorded before tearing of the interlayer)**

PVB	Test nr.	W_{max} [mm]	W_{min} [mm]	Max. principal strain [-]
	7	84.2	N/A	0.088*
RA	10	66.0	-37.8	0.135
	11	65.5	-37.8	0.098
	1	76.3	-51.38	0.303*
RB	3	60.6	-29.6	0.133
	4	62.8	-52.6	0.187
	12	65.8	-36.9	0.136
RC	13	67.2	-52.1	0.098
	14	59.2	-7.2	0.149

Overall, hardly any difference can be noticed in the deflection behaviour between different adhesion levels, at low loads. Both maximum deflection and rebound behaviour appear very similar. One test with a high adhesion level (RA), however, already experienced tearing of the interlayer.

In the horizontal cross section (Figure 8-43 & Figure 8-44) it can be seen that the centre of the laminated safety glass remains quasi-planar up to 5.6 ms. The largest deformation can be observed at the edges of the central zone.

When looking at the rebound (dotted lines in Figure 8-43), one can see that, again, the central area lags behind, and only in the end will the middle point reach the highest (negative) deflection.

When looking at a test where the interlayer tore (Figure 8-44), this tearing is clearly visible in the DIC results. Although difficult to pinpoint the exact moment of tearing due to loss of correlation along the tear line, after 5.6 ms a discrepancy between the deflection from the left and from the right is visible.

The principal strain along the mid-line deflections pictured in Figure 8-44, are shown in Figure 8-45. A lower strain in the centre is evident, as the panel stays relatively flat in that area.

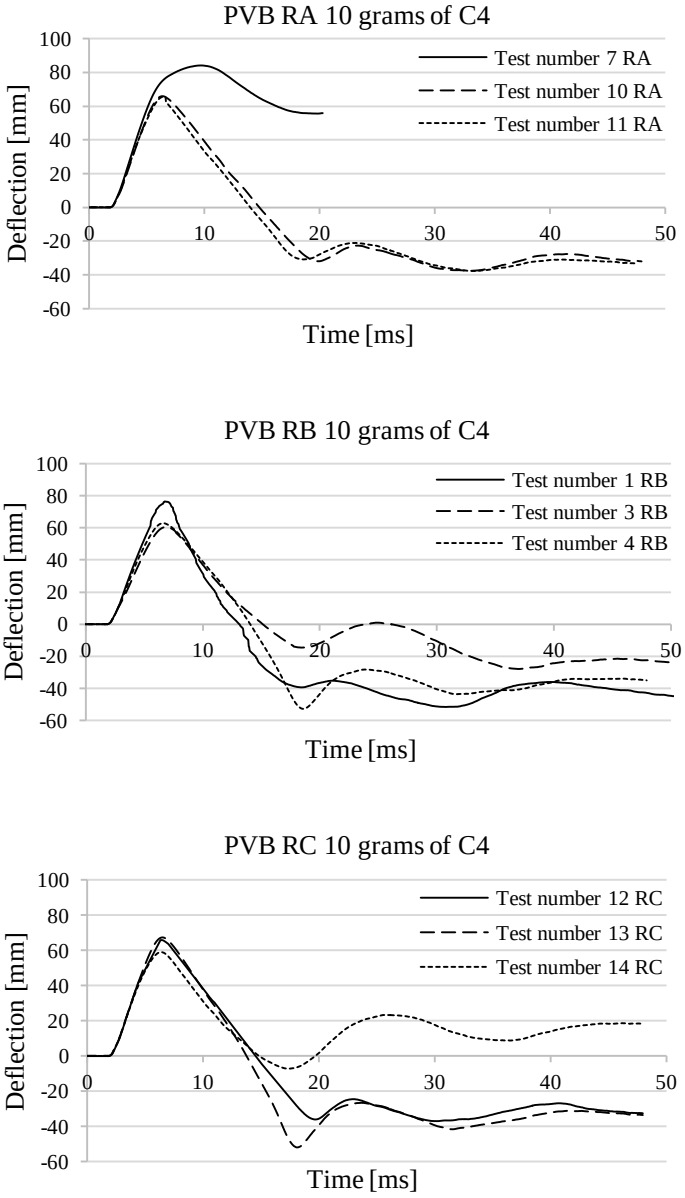

Figure 8-42 **Deflection - time curve of centre point for tests with a 10 g charge and a high (RA), medium (RB) and low (RC) adhesion level.**

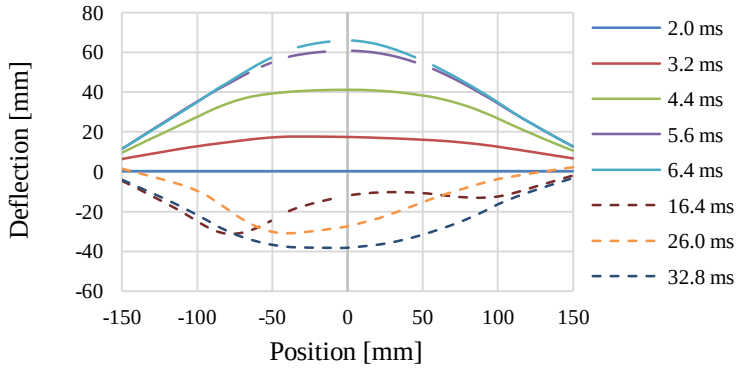

Figure 8-43 **Mid-line deflection (test 10, RA, 10 g).**

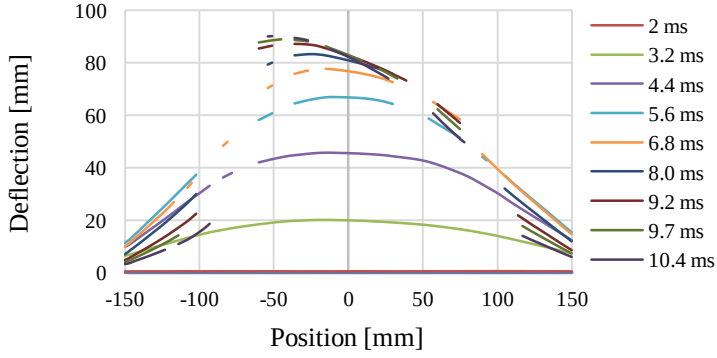

Figure 8-44 **Mid-line deflection, torn PVB (test 7, RA, 10 g).**

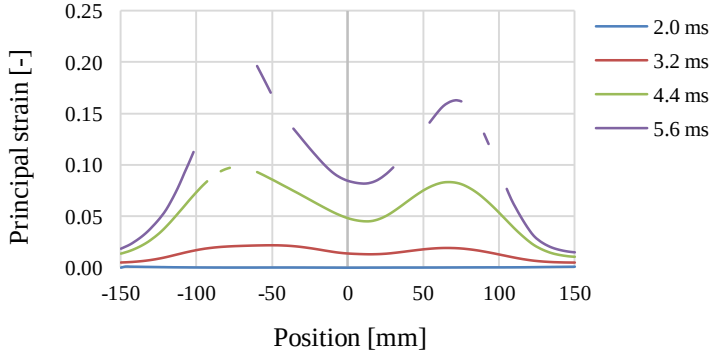

Figure 8-45 **Mid-line principal strain (test 7, RA, 10 g).**

Whereas the tearing of test 7 (see also Figure 8-38) covered a large area, the tearing occurring in test 1 (see also Figure 8-37) is much more localized. This is also visible in the DIC results, where the mid-line deflection (Figure 8-46) can be approximated as two linear pieces with the centre of the torn PVB acting as a 'hinge'. Also during the rebound this behaviour can be observed, with again the central area lagging behind.

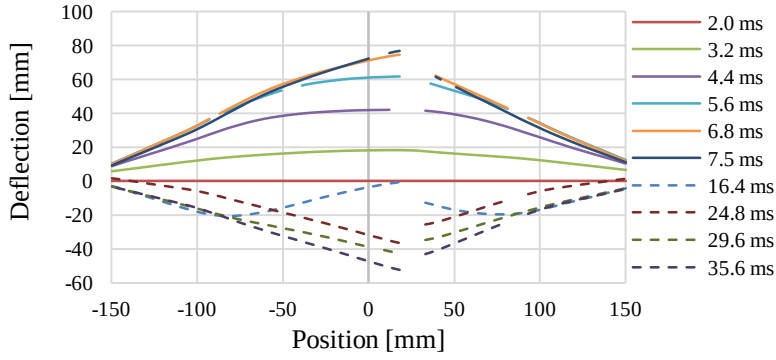

Figure 8-46 Mid-line deflection, torn PVB (test 1, RB, 10g).

The single tear near the centre of the specimen also results in a different strain curve with a single high peak (Figure 8-47).

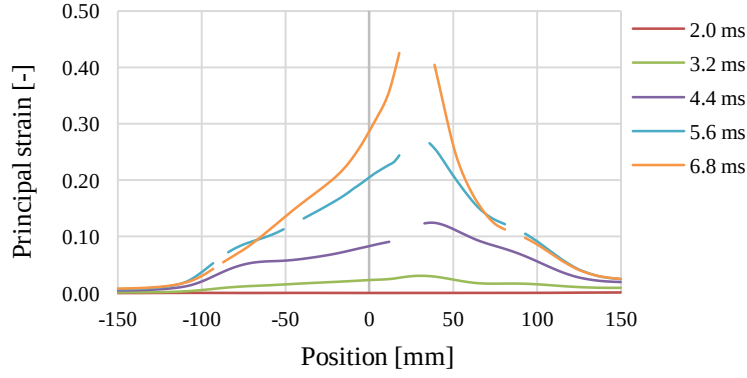

Figure 8-47 Mid-line principal strain (test 1, RB, 10g).

8.4 CONCLUSIONS

Several test series where laminated glass panels were subjected to blast loads were performed in the underground facilities of the RMA.

In a first test series the laminates could not be subjected to a severe enough blast loading, due to the limited clamping area. Too high a charge weight and the panels would blow out of the frame as a whole.

A wider clamping ring was designed but even then no difference between samples with different adhesion could be discerned. Using high charge weights at a small distance also resulted in unpredictable pressures, due to local effects.

A small shock tube which was readily available was used to mitigate these problems, but this proved too localized a force, and flying glass particles impeded correlation of the high-speed images. However, tearing of the interlayer could finally be achieved and it seemed dependent on adhesion level.

A final set-up with a larger shock tube was designed which finally yielded good results. A clear difference in behaviour was observed between specimens with a higher adhesion (RA and RB) and with lower adhesion (RC), where the RA and RB specimens were more prone to tearing of the interlayer. This was to be expected because the low delamination results in higher strains in the interlayer to bridge the cracks in the glass.

Pressure tests were performed both for the initial (open air) and final (shock tube) set-up. They proved the shock waves were reproducible, and planar in case of the shock tube. A study was performed to investigate the influence of parameters such as charge shape, degree of alignment and use of a mould on the shock wave characteristics.

8.5 INTERACTION WITH MODELLING (PELFRENE [1])

8.5.1 Open air tests (see 8.2.2)

The crack patterns for the unstructured and structured meshes are given in Figure 8-48. Similar to the experiments, the first and major cracks appear as an inner square and along the diagonals. Later in the simulation, more cracks appear in the central area of the panel, which is seen for the tested glass panes as well, although not to such extent. An unstructured mesh allows for a more `natural' formation of cracks along the direction of the maximum principal stress at fracture, as defined in the crack delay material model.

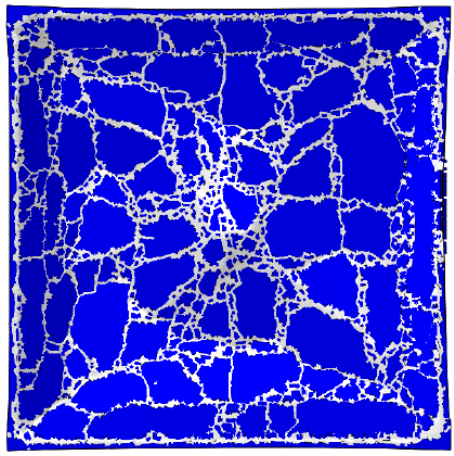

Figure 8-48 **Crack formation for unstructured mesh of laminated glass plate in small scale open air blast tests at t = 4 ms.**

Figure 8-49 shows the deflection at the middle of the laminated glass panel for the simulations in comparison with two of the experiments.

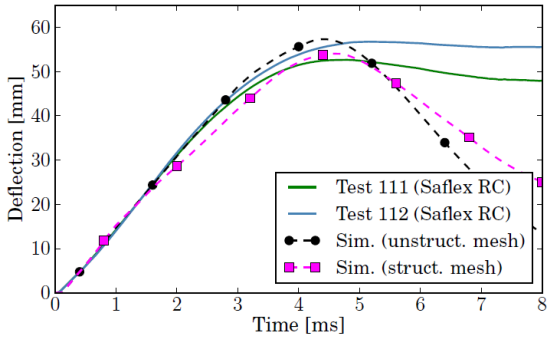

Figure 8-49 **Deflection at the centre of laminated glass plates in small-scale open air blast tests with 40 g C-4 at 250 mm: simulations vs. experiments.**

The simulated results, especially for the unstructured mesh, agree well with the test data for as long as the broken laminate is being stretched out of its frame. On the return stroke, however, the simulated glass panes clearly act more flexible than in reality. The return stroke is also where the responses in the experiments begin to differ. At that point, glass fragments come in contact and retain some compressive stiffness across the cracks. Subsequent deformation is determined predominantly by the extent of fracture and the crack topology, both of which may slightly differ for

each test panel. However, numerical models with element deletion cannot take account of this behaviour as the simulated cracks are as wide as the size of each element. As such, the technique does not seem capable of capturing the post-fracture behaviour entirely. Nonetheless, the fact that the initial deformation and the maximum deflection are simulated rather well leads to believe that the model does capture some of the features of post-fractured response that allow to evaluate the design of a laminated glass window, including an estimation of the maximum forces exerted on the frame and substructure.

In addition, the deformation of the entire horizontal centre line of the glass pane is given in Figure 8-50. It is seen that the deflection away from the centre is somewhat higher in reality than in the models. A possible explanation is found in the blast load being higher at these locations than the calculation by ConWep that does not account for the influence of earlier reflections. It has also been observed in the tests that a portion of the wool felt rings slips out of the frame. Although allowed for in the numerical model, this does not take place in the simulations.

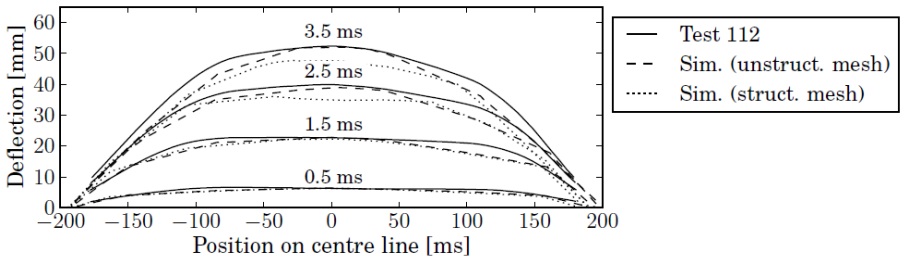

Figure 8-50 **Deflection of horizontal centre line of laminated glass plate in small-scale open air blast tests: simulation with unstructured and structured mesh versus experiment (outward deflection).**

8.5.2 Shock tube tests (see 8.3.2)

The shock tube test, with a C-4 charge of 15 g, is simulated with the ALE method by a 2D axisymmetric model with a uniform element length of 1.0 mm. In this case, symmetry conditions are applied at the open end of the tube, while the nodes at the other end and at the side are constrained in all directions. Again, the pressure field is mapped from a 1D model of the detonation. From then on, the shock wave is reflected multiple times until a planar shock front develops as shown in Figure 8-51.

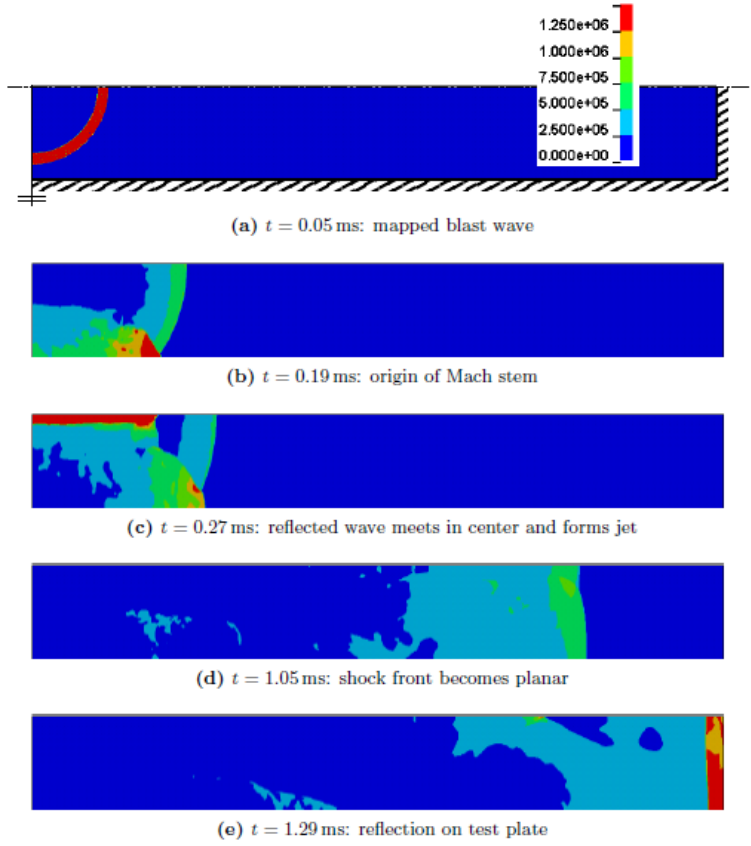

(a) $t = 0.05$ ms: mapped blast wave

(b) $t = 0.19$ ms: origin of Mach stem

(c) $t = 0.27$ ms: reflected wave meets in center and forms jet

(d) $t = 1.05$ ms: shock front becomes planar

(e) $t = 1.29$ ms: reflection on test plate

Figure 8-51 **ALE simulated evolution of blast wave in shock tube with 15 g charge of C-4.**

Unfortunately, the loading on the test plate is overpredicted in this ALE simulation. The average peak pressure in the simulations is 43.7 bar and the average specific impulse is 3021 kPa ms. The average measured peak pressure, however, was only 11.0 bar and the average pressure impulse was 558 kPa ms.

8.6 REFERENCES

[1] J. Pelfrene, "Numerical analysis of the post-fracture response of laminated glass under impact and blast loading," Doctor in de Ingenieurswetenschappen: Werktuigkunde-Elektrotechniek PhD, Department of Material Science and Engineering, Mechanics of Materials and Structures, Ghent University, Ghent, 2016.

[2] K. Spranghers, "Use of an inverse method (Finite Element Model Updating method) for the identification of the elasto-plastic material behavior of thin aluminum plates subjected to blast loading," Doctor in de Ingenieurswetenschappen: Bouwkunde, Mechanica van Materialen en Constructies, Vrije Universiteit Brussel, Brussel, 2014.

Chapter 9 BLAST: LARGE-SCALE TESTS

Overview

In this final research chapter a large-scale blast test series with industry-sized laminated glass panels is presented. A total of 12 tests were conducted, using a concrete shock tube. A comparison will be made for the blast resistance of panels laminated with a standard PVB interlayer and panels with a stiffer PVB. Such a test series requires a lot of preparations and these are described first. The final test set-up is discussed in detail, as well as the used instrumentation. The results, both qualitative and quantitative, are discussed. While the stiffer PVB laminates showed less deformation, they were propelled out of the clamping ring as a whole. The standard laminates experienced tearing of the interlayer but remained fixed in the testing area.

Up till now, all tests have been performed on relatively small samples, with only the EN 12600 impact tests having dimensions as used in actual glass constructions. The purpose of the large-scale blast test campaign was thus threefold:

- To investigate the scaling effect for blast tests, as some parameters of the interlayer might have a diminished effect on smaller samples.
- To be able to predict more precisely how industry-sized laminated glass panels behave during an explosion event.
- To gather information about scatter, as in literature little information is available on that. Typically, only a few tests are done and with different parameters each [1].

To accommodate the last point, only two test series of six identical, well equipped tests were performed. The dimensions of the samples were chosen as those prescribed by the EN 356 standard (1.1 by 0.9 m).

9.1 PREPARATIONS

9.1.1 Location

The blast tests were conducted in close collaboration with the Royal Military Academy of Belgium at their testing domain in Brasschaat. They already had experience with similar set-ups [2, 3]. At the military base two similar so-called sand chambers were available where the blast tests could take place.

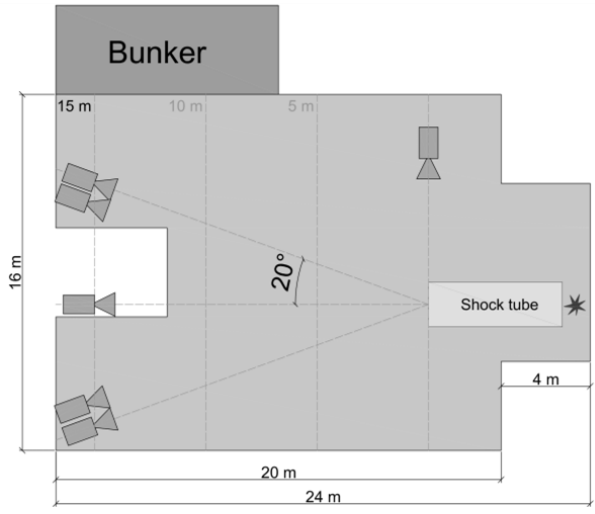

Figure 9-1 **Schematic of test set-up including shock tube and high-speed cameras.**

9.1.2 Shock tube

During the previous tests conducted by the RMA at this site [2], a shock tube had already been designed (see Figure 9-2). It was made of 6 square reinforced concrete sewer elements with inner dimensions of 2 x 2 m and each part measuring 1 m in length. Given its availability and practicality, it was decided to also use this shock tube for our experiments.

Figure 9-2 Test set-up used by De Reu [3].

However, an alternative method was needed to clamp the specimens. Several ideas, including using a large composite sandwich panel, an in situ cast concrete wall or a reinforced masonry wall, were investigated but ultimately the choice fell on a prefabricated concrete L-shaped wall (Figure 9-3). The advantages of this system are the guaranteed concrete quality and the precise location of the opening. The robustness of the wall is also an advantage.

At the location of the glass panel a small border is provided on which the panel can rest. This border is a bit higher at the top to ease the placement of the glass panel. Since the glass panel can rest on this border, it is also easier to install the steel clamping frame (see further). To protect the glass panel and to spread the load, rubber strips of 3 mm thick and 50 mm wide are glued to the concrete and the steel frame.. The only disadvantage of this system is the cost.

Since the concrete shock tube elements were damaged in some locations there was no perfect connection between the shock tube and the concrete. The gap between the shock tube and the concrete wall was filled with PUR foam.

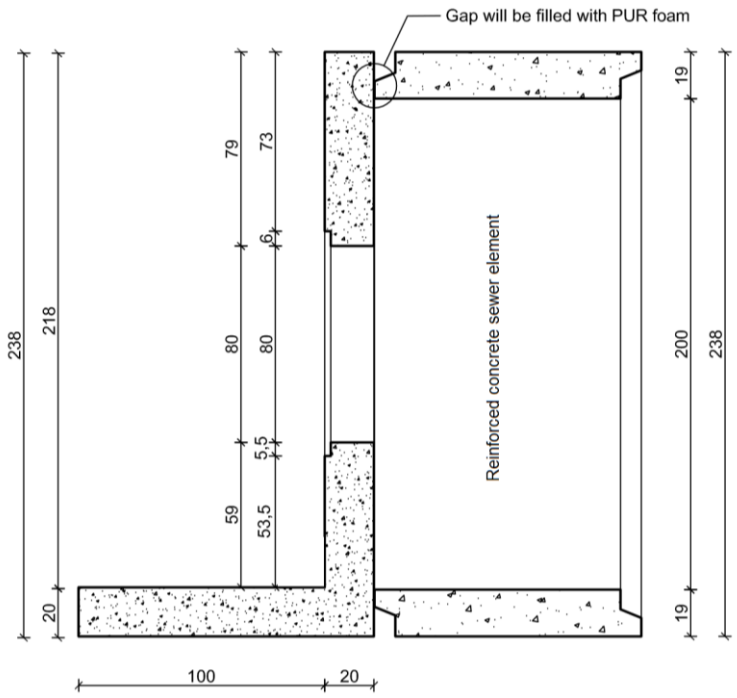

Figure 9-3 Prefabricated L-shaped concrete wall (dimensions in cm).

The wall's dimensions were increased to an even 2.5 x 2.5 m (as oppossed to 2.38 m, the outer dimension of the shock tube elements) and a 20 cm thickness and 1 m base length was thought to be sufficient to resist the explosive forces and minimize deflection.

To clamp the glass panel onto the wall, a system had to be found which is quick and easy to attach since the glass panel obviously has to be replaced after every test. For this clamping system a steel frame which is bolted on the wall was deemed the most efficient method, similar to the system used for the small-scale blast tests. The steel frame which was used is shown in Figure 9-4. The outer dimensions are 1220 mm x 1020 mm; the thickness is 12 mm and the width of the ring is 110 mm. This resulted into an inner area of 1000 x 800 mm. This implies that the glass panes were clamped to the rigid frame all around by 50 mm restraint. Since M12 bolts were used, the openings for the bolts were 14 mm diameter and were provided every 128.9 mm. Four openings were made to mount handles on the frame. The steel frame was custom made by a laser cutting machine.

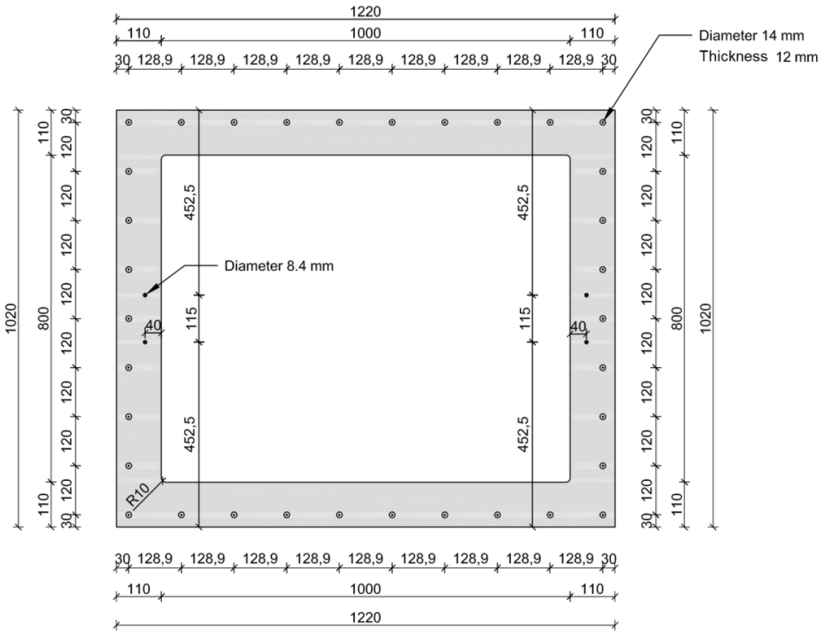

Figure 9-4 Steel clamping frame (dimensions in mm).

To be sure that the openings for the bolts are at the correct location, the steel frame was transported to the concrete contractor. The concrete wall was equipped with threaded sleeves for the bolts.

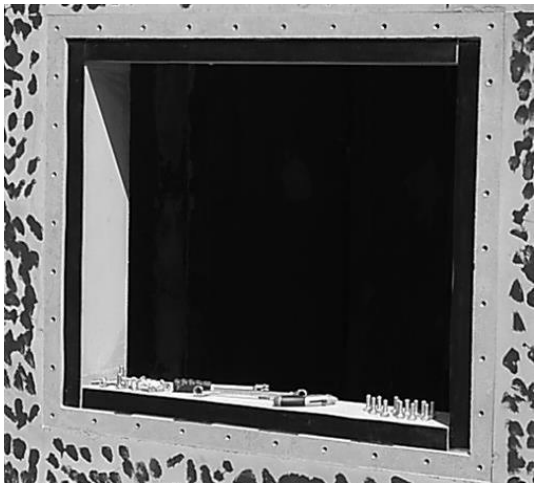

Figure 9-5 Window opening in concrete wall including rubber protective strips and embedded threaded sleeves.

In Figure 9-6 the finished shock tube with L-shaped prefabricated concrete wall is shown.

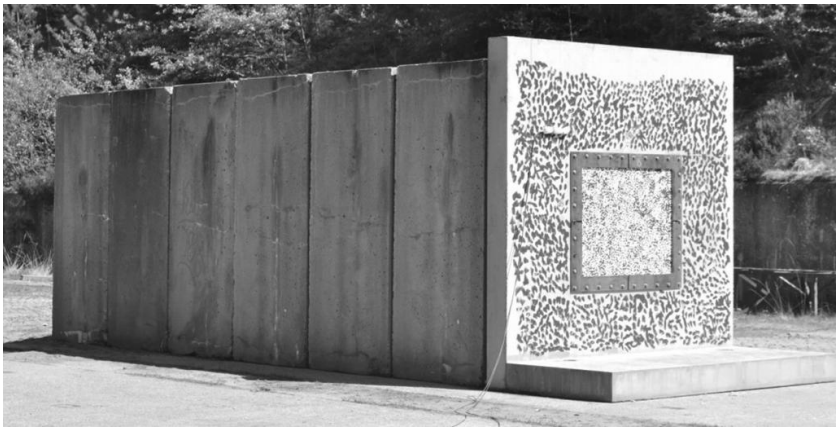

Figure 9-6 Shock tube and wall with glass panel installed, ready for testing.

9.1.3 Cameras

A total of 6 high-speed cameras was used, many in combination with the DIC technique. To measure the deformations during the test, two high-speed cameras filmed the glass panels (Photron Fastcam SA5), two other high-speed cameras filmed the movement of the frame (Photron Fastcam SA4), another high-speed camera filmed from the side of the shock tube (Photron Fastcam APX-RS) and a colour high-speed camera (Photron Fastcam SA3/CA3) was used to make additional pictures.

A test mock-up was executed, a few weeks prior to the actual testing, to check the wiring between the cameras and to detect possible problems. A problem which was encountered was that the tripods of the cameras are very sensitive to the wind. To get good calibration values it was important to have a wind shield. Two tents were used to protect the cameras from wind and rain (Figure 9-7). These tents had the additional advantage that it was possible to leave everything outside during the night.

Figure 9-7 Wind and rain protection for the high-speed cameras.

A flash detector was used to trigger the cameras. When the flash detector detects the flash of the explosion, a signal is sent to all cameras and blast measurement devices via BNC cable. This implies that the cameras and the measurements start at the same moment. A complete overview of all cables used to connect all devices is shown in Figure 9-8. The tents are indicated in orange, the armoured cabins are indicated in khaki. These cabins are used to protect the other cameras. In Figure 9-9 a picture of the test setup is given.

Light from the explosion can cause over-exposure of the cameras. To mitigate this problem, household aluminium foil was installed inside the shock tube, close to the glass panel, prior to each test. The back of the panels had also been painted black.

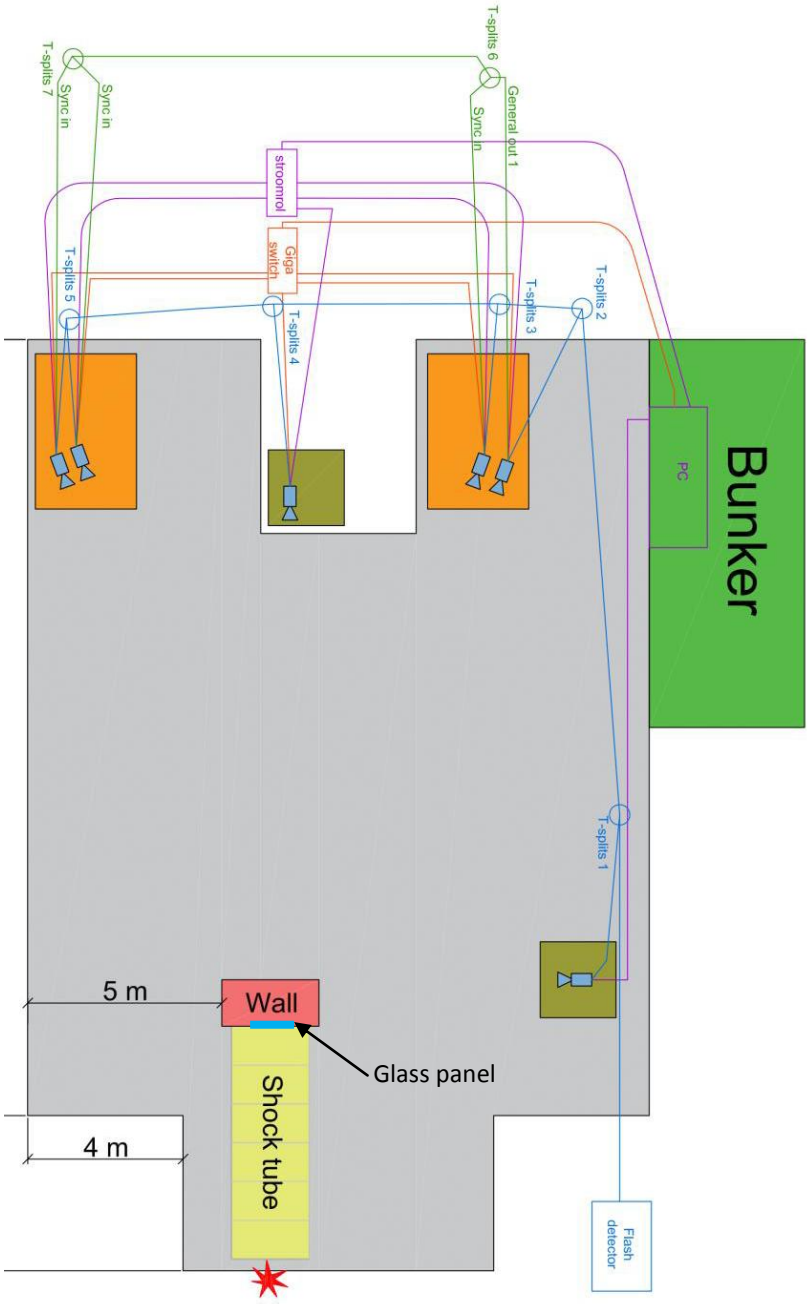

Figure 9-8 **Overview of all necessary cables (blue = BNC (triggering), green = BNC (synchronising), purple = electricity, orange = ethernet)**

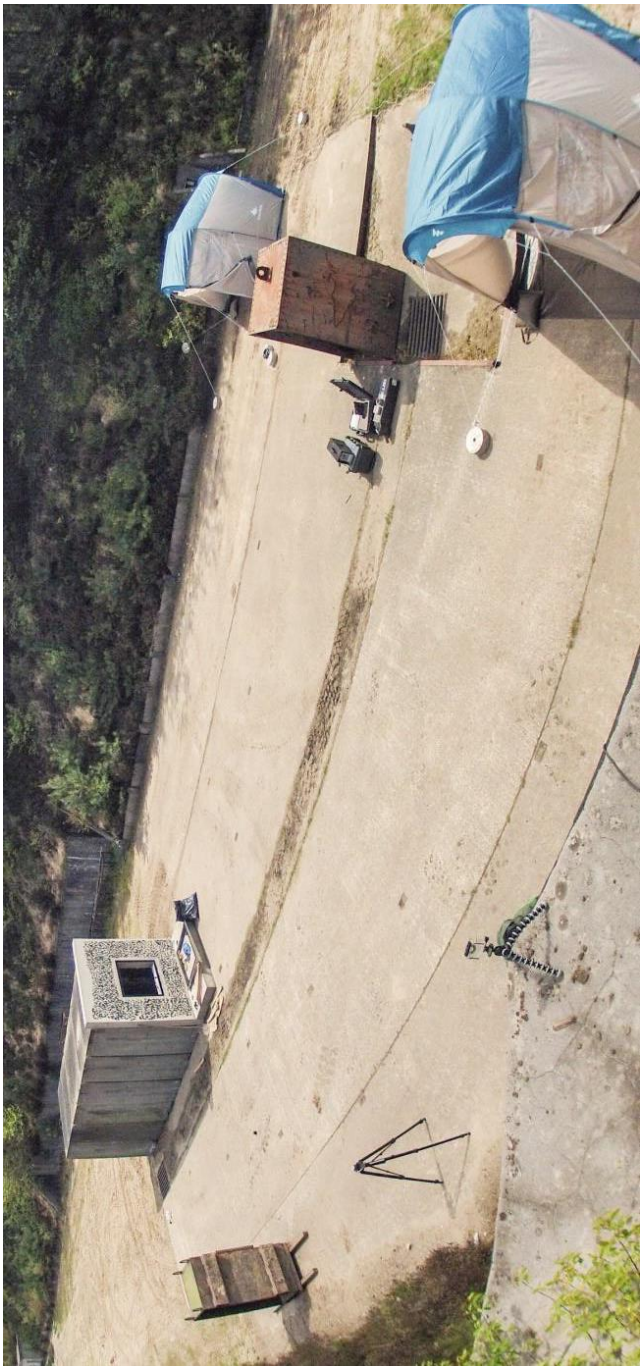

Figure 9-9 **Set-up ready for first test with shock tube, high-speed cameras and wind protection tents.**

9.1.3.a Lenses

The calculation of the lenses was done by a calculation tool provided by Photron, the camera manufacturer. Various working distances were studied since it was also possible to place the cameras on a concrete slab which was at 30 m from the explosion. Since this working distance leads to very heavy and expensive lenses (Table 9-1), the cameras were placed at 10-15 m from the glass panel, on the same concrete slab as the shock tube.

Table 9-1 Required focal lengths.

Working distance [m]	Required focal length glass panel [mm]	Required focal length concrete frame [mm]
30	768	307
20	512	205
15	384	154
10	256	102

Two zoom lenses were available from the Royal Military Academy:

- Tamron SP 60-300
- Nikon AF VR 80-400 1:4.5-5.6D ED

These lenses were used to film the glass panel. No other lenses were available which meet the required focal length, therefore two 105 mm (Nikon AF-S 105 f2,8 VR Macro) lenses with fixed focal length were hired.

The cameras for the glass panels were of highest importance, therefore the fastest cameras (SA5) were used to film the glass. The full resolution is 1024 x 800 pixels and the frame rate is 9300 fps. The cameras for the frame (SA4) operated at a full resolution of 1024 x 1024 pixels at a frame rate of 3600 fps. These frame rates are quite low but additional lighting, which would be necessary when using higher frame rates, could not be provided.

9.1.4 Materials

All specimens were composed of two plies of 4 mm (nominal) glass and a single interlayer with a thickness of 0.76 mm. The glass plies were produced by AGC Europe and the interlayers were produced by Eastman. The glass was laminated at Eastman. Two types of interlayer were compared, a common type with medium adhesion (Saflex RB) and a stiff interlayer (Saflex DG) which remains stiff after failure of the glass.

9.1.4.a Applying of the DIC speckle pattern

All the glass panels were first painted white to provide high contrast. However, since the panels were quite large, the common way of applying the speckles with laser tattoo paper would be too cumbersome. A cut-out of the full-size computer-generated ideal speckle pattern is shown in Figure 9-10 (left). The speckle pattern was projected on the painted glass panels to have an idea of the actual speckle size.

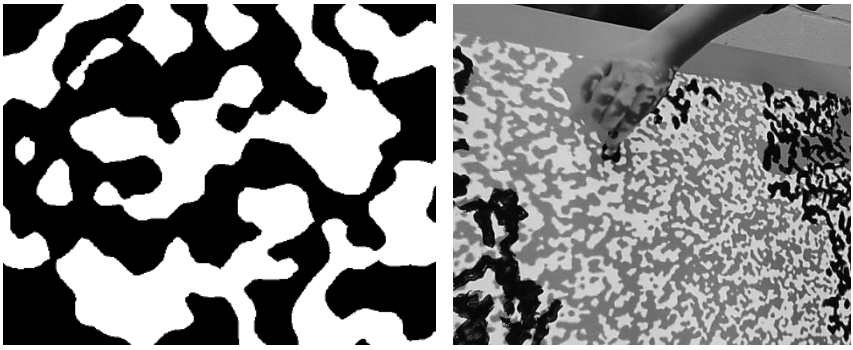

Figure 9-10 **Cut-out of full-size generated speckle pattern (left) and projected speckle pattern on glass panel (right).**

The first idea was to apply the speckles by swinging a (toilet) brush. The speckles which were created with this method were of a good size and shape but the paint was too thick and dripped down after a while. The second idea was to finger-paint the speckles (see also Figure 9-10 (right)). The result was very accurate but this method was too slow to use for 12 test specimens. The third idea was to use earplugs as a 'brush' and the method which is actually used is based on that idea: a stamp made of cardboard and earplugs.

A cardboard honeycomb core panel (Figure 9-11 (left)) is made of two sheets of board which are glued to paper honeycomb. By removing one of the sheets, the honeycomb pattern could be filled with the earplugs. A random pattern was made by turning the stamp and by applying variable pressure every time a print was made. A finished panel is shown in Figure 9-12.

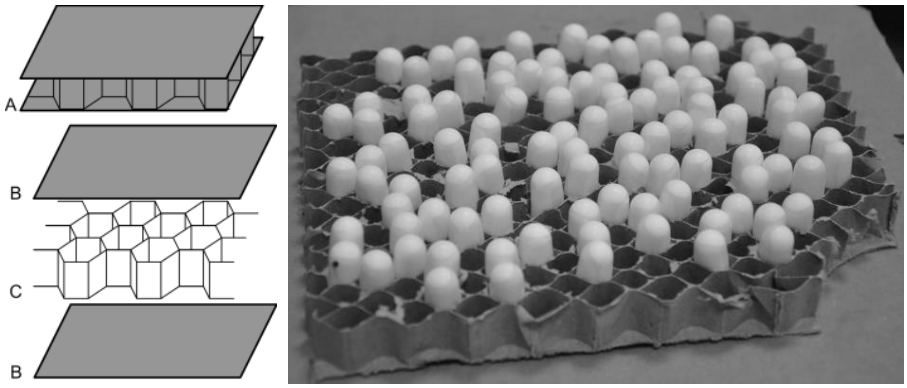

Figure 9-11 **Honeycomb cardboard panel (left) and stamp made of honeycomb cardboard and earplugs (right).**

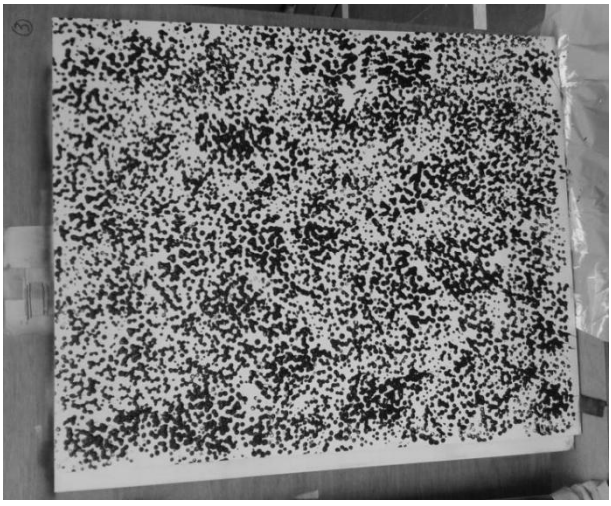

Figure 9-12 **Glass panel with applied DIC speckle pattern.**

The concrete frame was also equipped with a speckle pattern. This pattern was applied with a big paint brush, see Figure 9-13.

Figure 9-13 Applying the speckle pattern on the concrete L-shaped wall.

9.1.4.b Calibration target for DIC

It is important that the calibration target is printed on a stiff material since deformations will influence the calibration. Therefore the calibration target was made of concrete plex (formwork panel). There were two calibration targets, one for the glass panel (size A0) and one for the frame (size 2A0). The target was printed on a sticker and applied on the concrete plex panel. Two handles were provided on each side to make it possible to make the required motions during calibration. The calibration target is illustrated in Figure 9-14.

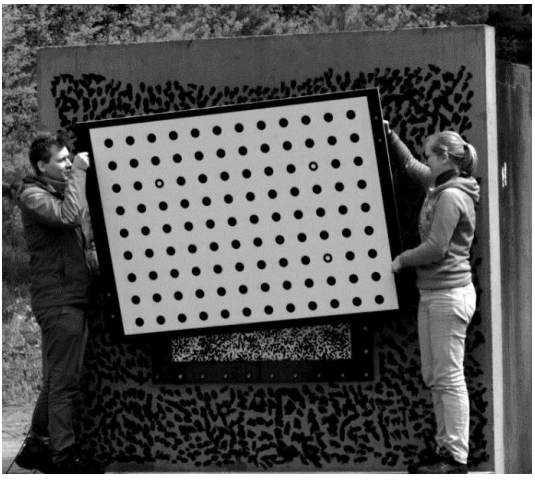

Figure 9-14 2A0 sized calibration target for the concrete wall.

9.1.5 Blast measurement devices

The pressure due to the shock wave was measured by two pressure sensors inside the shock tube and by two blast pencils outside.

One blast pencil was located in the camera tent the closest to the bunker, to determine the moment that the blast wave reaches the cameras. It is important to know that moment since the DIC measurements are not valid anymore from that moment. The other blast pencil was located at 6 m behind the explosion, to check the influence of the shock tube compared to an open air blast.

The pressure sensors were located inside the shock tube: one above the glass panel and one next to the glass panel. The locations are indicated at the outside, see Figure 9-15.

The coordinates (in mm) of the pressure sensors relative to the centre of the glass are (-704;109) for pressure sensor 1 and (27;619) for pressure sensor 2.

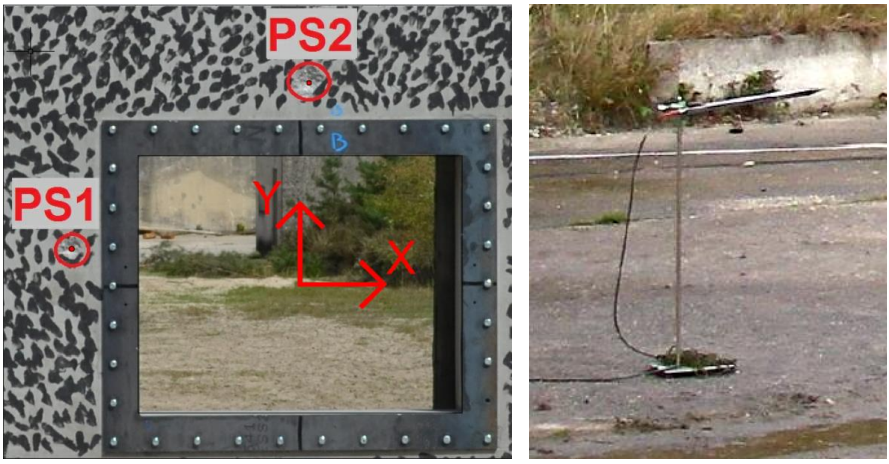

Figure 9-15 Location of pressure sensors (left) and blast pencil (right).

9.2 EXPERIMENTS

With everything – shock tube, instrumentation, high-speed cameras and glass panels – in place, testing could begin. In Figure 9-16 a panel ready for testing is shown.

Figure 9-16 Glass panel ready for testing.

9.2.1 List of performed tests

The test week ran from 27 to 30 April 2016. A total of twelve tests were performed, with the first day needed to set up everything. The first two tests were executed with a smaller charge, 140 g instead of 280 g. This was done to check the effect of the charge on the test setup. The value of 280 g was a convenient compromise, as the charges were pre-packaged in so-called 'loafs' of 560 g. This value was also in the same order as the value used by Kranzer [4]. The charges were manually moulded to a sphere. Care was taken to knead the material thoroughly.

Unfortunately, two plates already fractured (slightly, see also Figure 9-17) when tightening the bolts to clamp them to the frame. These tests are indicated in *grey italic* in Table 9-2.

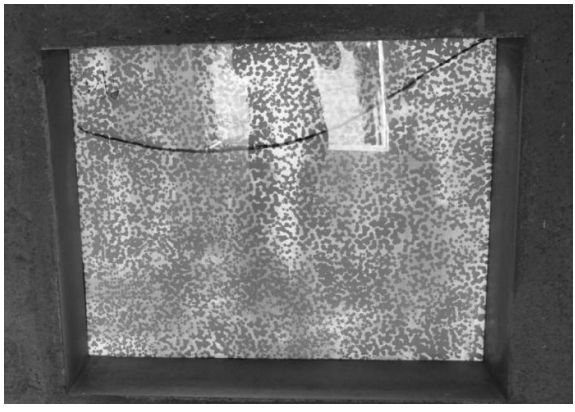

Figure 9-17 Panel with crack before testing (crack indicated with felt marker).

Table 9-2 Performed tests.

Test	Type	Date	Time	C4 [g]	Code
1	*RB*	*28/4*	*12u30*	*140*	*28-1-RB*
2	DG	28/4	15u00	140	28-2-DG
3	RB	29/4	9u30	280	29-1-RB
4	RB	29/4	10u30	280	29-2-RB
5	RB	26/4	11u20	280	29-3-RB
6	DG	29/4	12u10	280	29-4-DG
7	DG	29/4	13u30	280	29-5-DG
8	RB	29/4	14u40	280	29-6-RB
9	DG	30/4	9u30	280	30-1-DG
10	DG	30/4	10u20	280	30-2-DG
11	*RB*	*30/4*	*11u20*	*280*	*30-3-RB*
12	DG	30/4	12u00	280	30-4-DG

9.3 RESULTS

9.3.1 Qualitative assessment

9.3.1.a RB panels (medium adhesion)

In Table 9-3 images captured with the high-speed cameras are shown for each test with RB panels (except the first one with a lower charge weight), for four different time steps.

Unfortunately, for the last RB test, it is clear that the fracture which resulted from clamping the panel (as seen on Figure 9-17) has a big influence on the behaviour during the blast test. The panel almost immediately tears completely along this initial fracture, resulting in a much more damaged panel compared to the other tests. The results of this test will thus not be used in further discussions of the RB results. However, the bottom part of the panel remains attached to the rest of the panel via the bottom edge.

All panels experience interlayer tearing to a greater or lesser extent, with all but the third panel only having a tear along the top and/or bottom edge of the clamping ring. The third test resulted in more and larger tears all over the panel.

Table 9-3 Overview of the fracture of panels laminated with RB interlayer.

	20 ms	60 ms	120 ms	180 ms
29-1-RB	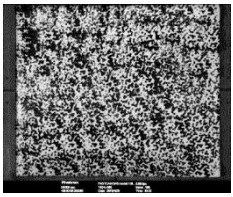	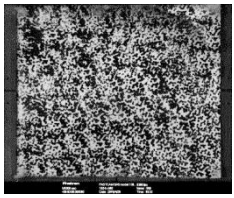	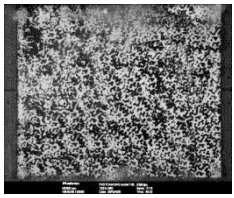	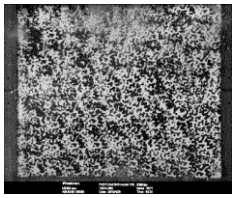
29-2-RB	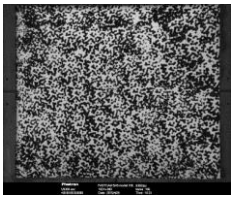	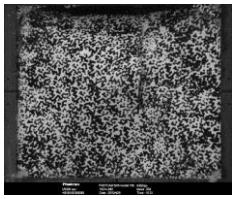	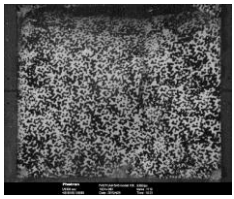	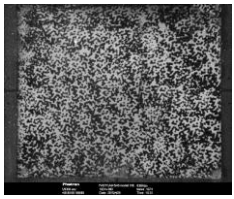
29-3-RB	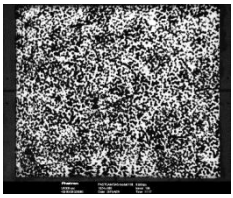	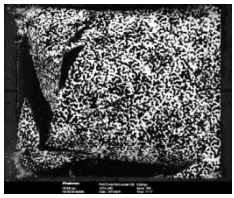	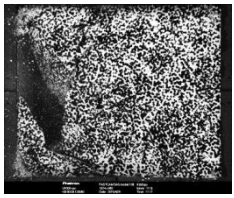	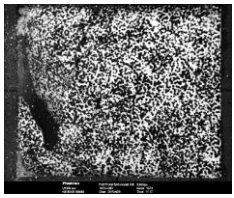
29-6-RB	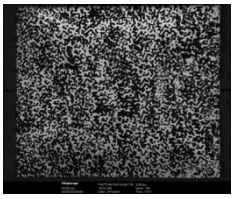		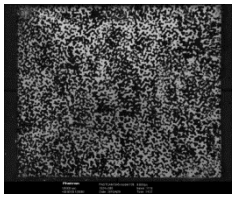	
30-3-RB	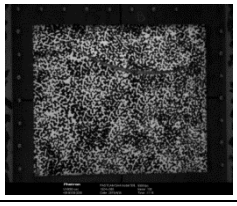	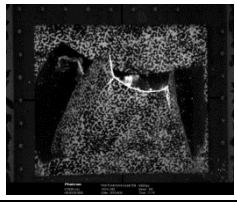	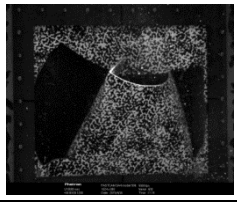	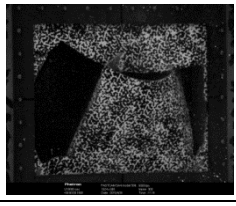

All panels showed the typical behaviour of having a convex surface after the test, as evidenced in Figure 9-18, much like during the small-scale tests.

Figure 9-18 Typical position of RB panels post-test, with outward curve.

In Figure 9-19 and Figure 9-20 some details of a panel after testing are shown, with typical damage for RB panels.

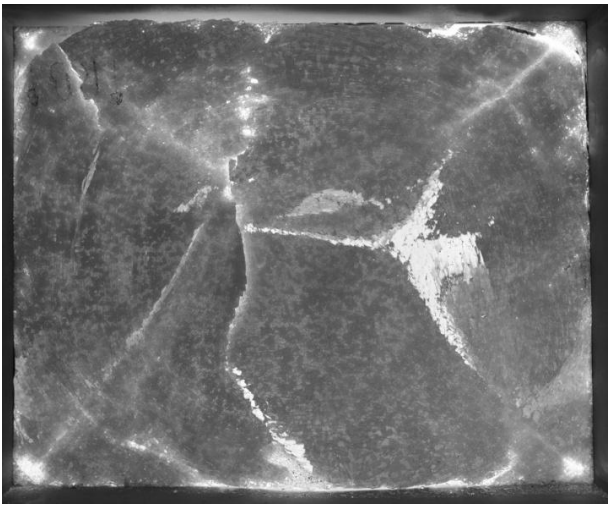

Figure 9-19 Back of RB panel after testing.

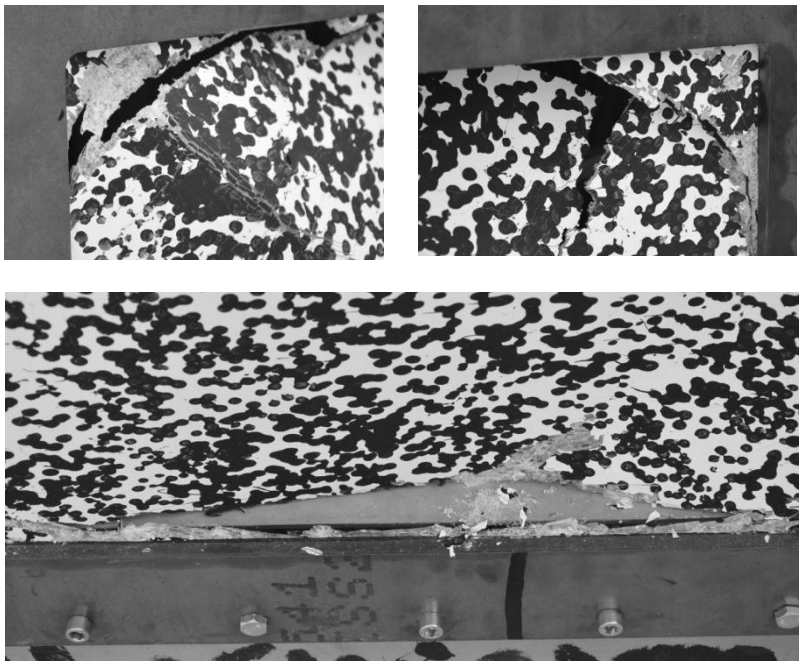

Figure 9-20 Details of damage to panel.

9.3.1.b DG panels (stiff interlayer)

Whereas the RB panels show some smaller tears along the upper edge and in the middle, but remain globally intact and attached to the glass 'ring' inside the clamping area, the DG panels' behaviour is completely the opposite. The panels tear very early on along the four clamping edges and they are blown out of the clamping area as a whole. An overview is shown in Table 9-4.

In four out of the five tests, the panel was completely torn along the clamping edges and blown out of the frame. For the third DG test, the panel was sucked back into the shock tube, due to the negative phase of the explosion. Four tests showed distinctive rotating of the panel in the same direction, with the left half of the panels turning towards the shock tube and the right half rotating towards the cameras.

Table 9-4 Overview of the fracture of panels laminated with stiff DG interlayer.

	20 ms	60 ms	120 ms	180 ms
29-4-DG	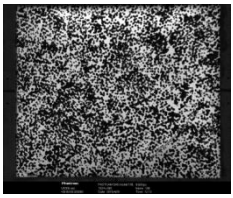	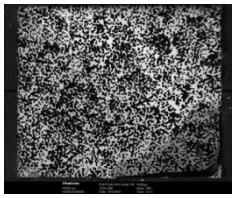	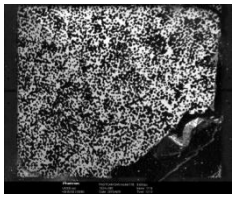	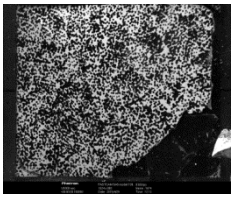
29-5-DG	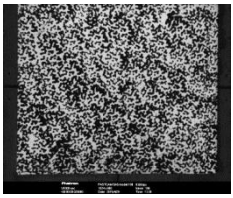	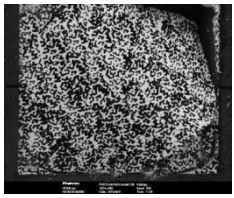	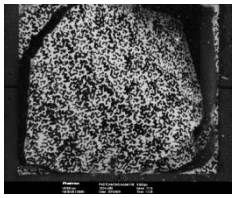	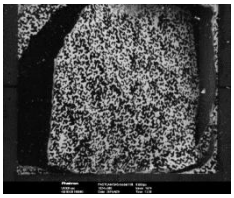
30-1-DG	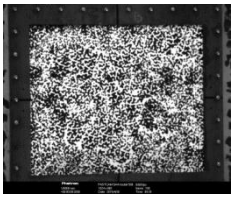	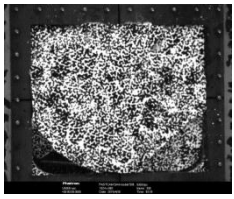	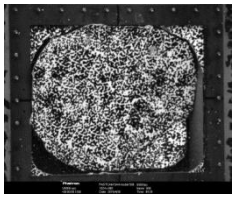	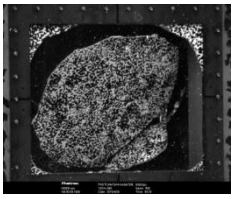
30-2-DG	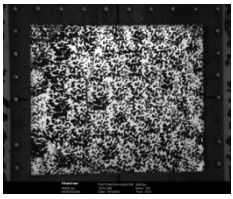	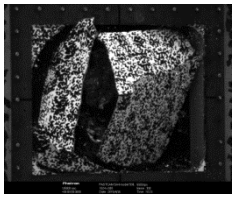	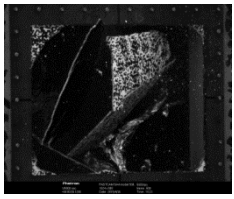	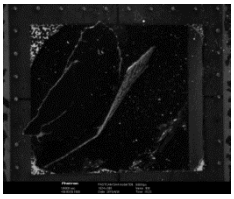
30-4-DG	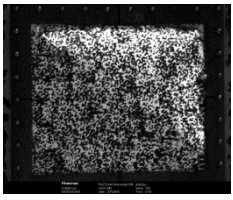	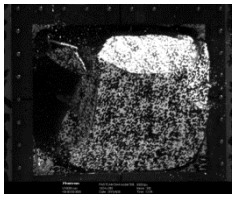	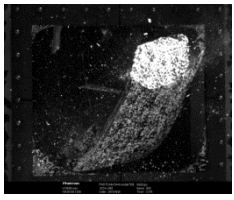	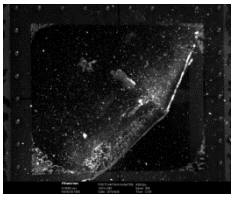

In Figure 9-21 and Figure 9-22 a close-up is shown of the remaining glass ‘ring’ and blown-out panel.

Figure 9-21 Detail of remaining pieces after test of a DG panel.

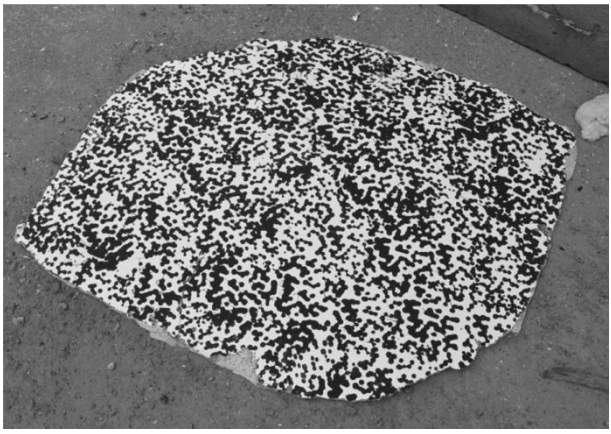

Figure 9-22 Detail of blown out DG panel after test.

9.3.2 Deflection

The DIC technique was used to obtain full-field measurements of all tests. All DIC processing was executed with a subset size of 27 pixels and a step size of 9 pixels.

The deflection of the midpoint in time is plotted in Figure 9-23. A comparison is made between the behaviour of the glass panels which are laminated with an RB interlayer (dashed lines) and those with a DG interlayer (full lines).

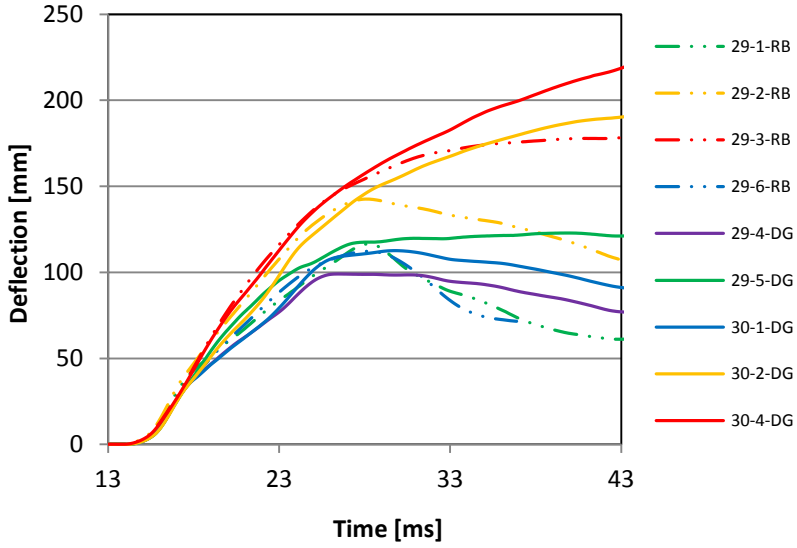

Figure 9-23 Comparison of RB & DG mid-point deflection in time.

The mid-point deflection is very similar for all tests, certainly in the very beginning. Given the fact that in the earliest stages only the properties of the glass, which is identical for all tests, influence the results, this is a good indicator of the reproducibility of the tests. Depending on when exactly the glass panels fracture and the (different types of) PVB begins to stretch, the results will start to deviate.

Overall, after reaching a maximum value at around 27 ms, the RB panels either maintain that maximum deflection (29-3-RB) or undergo a decrease of that value. The DG panels, on the other hand, will maintain that value or deflect even further. The DG panels blowing out of the clamping ring could not be tracked by DIC due to loss of correlation, what with such large displacements.

The main difference between RB and DG is not the deflection of the centre point but the behaviour of the whole glass panel. To illustrate this, the deflection of a horizontal line at mid height was plotted in Figure 9-24. The data of test 29-1-RB and test 30-1-DG were used. The position of the line is plotted every 5 ms, starting at 15 ms after the start of the explosion. Another position plot was added at 22.5 ms, because of the large difference in deflection between 20 and 25 ms.

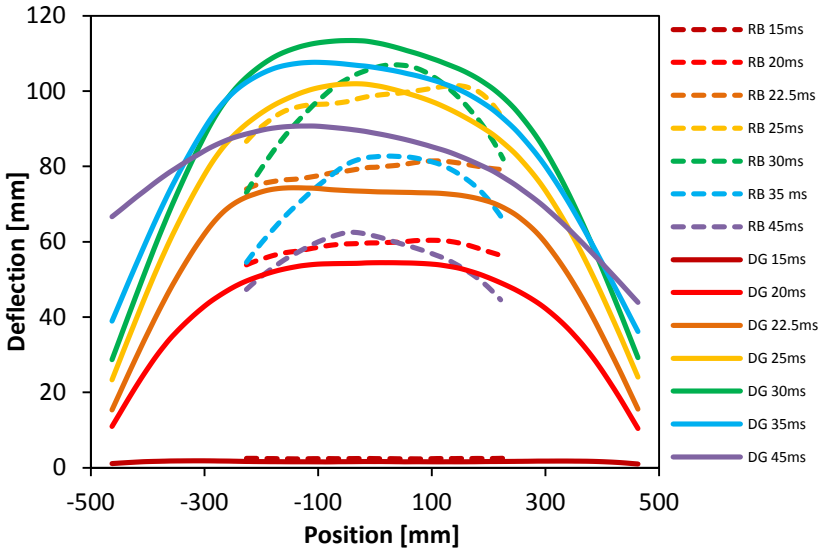

Figure 9-24 Comparison of the deflection of RB and DG panels.

The graph shows that the deflection for both interlayer types starts similar. The centre of the panel remains planar while the largest deformations can be seen at the sides. This can be seen for both types up to 25 ms, after which the behaviour starts to differ.

After 25 ms, the 29-1-RB panel will no longer show a 'planar' behaviour at the centre. The maximum deflection of the panel (116 mm) occurs at 28.17 ms, exactly at the centre of the plate. The curve at 30 ms shows a parabola-like shape of the deformed laminated glass panel. After that, the deformation decreases as the broken panel adopts its final deformed shape. As expected, the 30-1-DG panel shows a different behaviour. The centre of the panel barely changes shape as it reaches its maximum deflection (113.5 mm) at 36.40 ms. The interlayer at the sides of the panel fails between 18 and 25 ms. At that moment the shape of the centre part of the panel remains the same as at 15 ms, indicating a much stiffer behaviour than for the RB interlayer. As the deflection in the middle decreases, the sides of the panel are propelled outwards of the frame, thereby again obtaining a more planar shape.

In Table 9-5 some full-field DIC results are shown. Both deflection W and max. principal strain ε_1 during the elastic phase of the deformation correspond nicely with earlier results from the small-scale set-ups. Higher strains are located mainly along the edges. The middle of the panel clearly 'lags' behind, with hardly any strain in the middle.

Table 9-5 Deflection and strain (30-4-DG).

	W [mm]	e1 [-]
14.8 ms	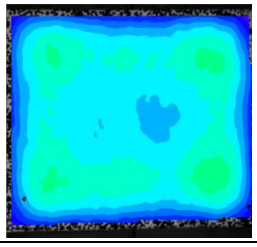	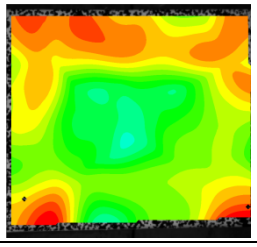
15.0 ms	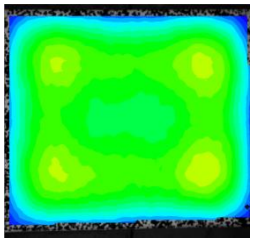	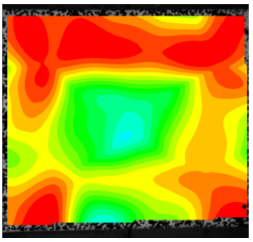
15.2 ms	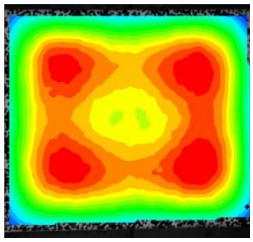	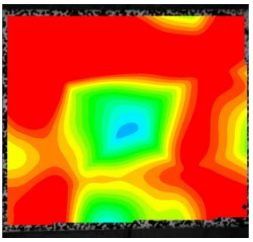

In Figure 9-25 the full-field deflection is shown for test 30-1-DG. Very early the glass panel starts to tear in both bottom corners and these parts are then sucked into the shock tube while the other part of the plate is moving away from the shock tube. The central part remains quite flat while it deflects.

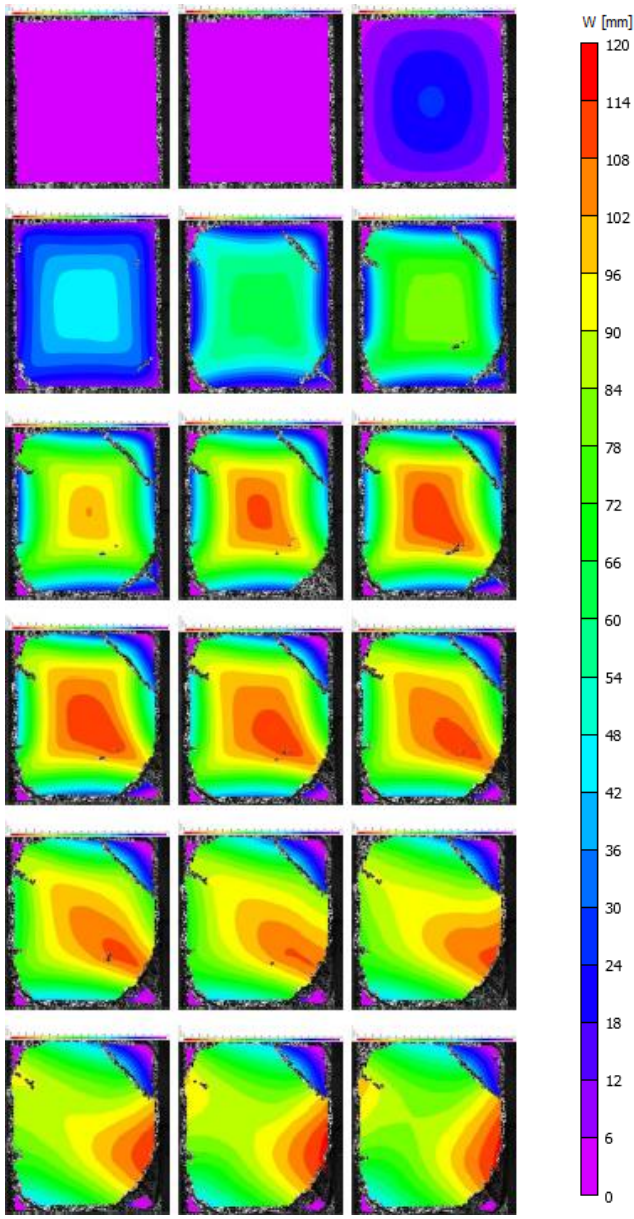

Figure 9-25 Evolution of the deflections 13 ms - 47 ms (every 2 ms) (30-1-DG).

This behaviour is also clearly visualised in the previous Table 9-4.

The pressure measurement of both sensors inside the shock tube and the mid-point deflection of a representative RB and DG panel are shown with the same time scale in Figure 9-26. The signals of the pressure sensors are filtered with a Butterworth filter at a cut-off-frequency of 1500 Hz. They result into an almost identical pressure time history; given that the sensors have a different distance to the centre, this indicates that the blast wave is planar when it reaches the glass panel.

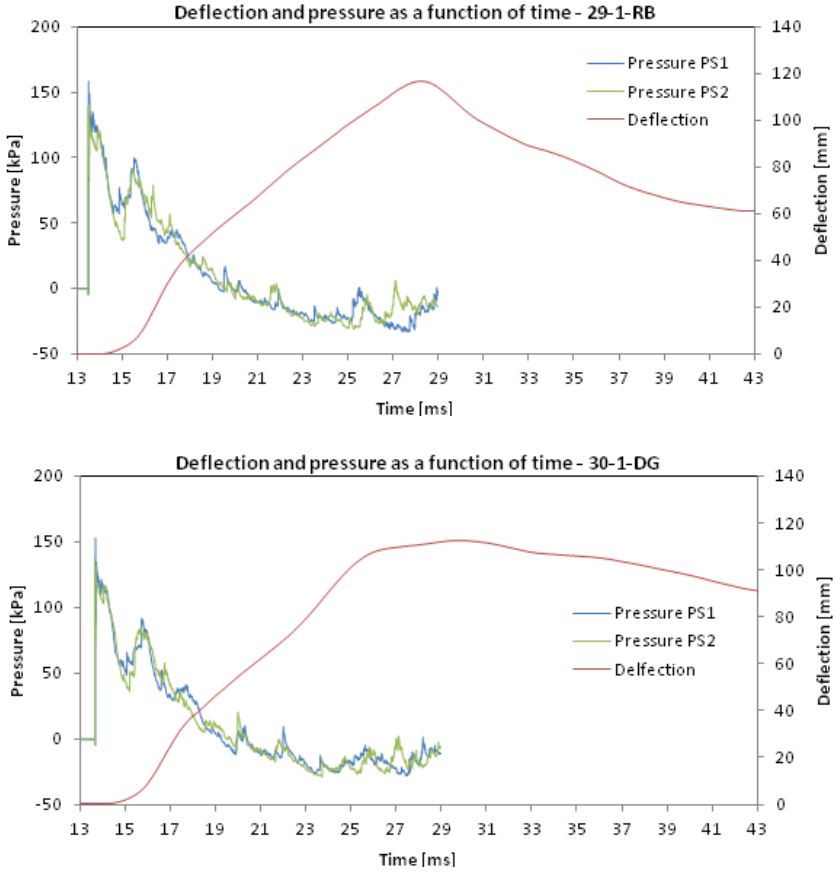

Figure 9-26 **Mid-point deflection and pressure as a function of time for (top) RB panel and (bottom) DG panel.**

In Figure 9-27 the pressure time history of the blast pencil in the camera tent is given for both tests. The pressure signal is filtered by a Butterworth filter at a cut-off-frequency of 3000 Hz.

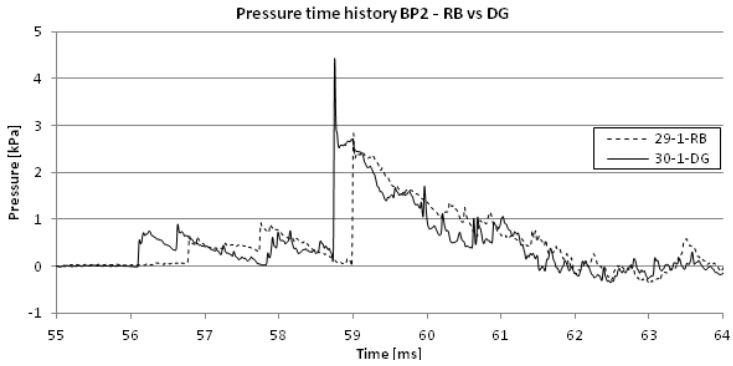

Figure 9-27 Pressure time history of blast pencil in camera tent.

The shock wave reaches the cameras in two steps, with a first, smaller peak in pressure, presumably from the initial explosion and with the pressure wave going around the outside of the shock tube, followed by a second, higher peak, presumably from the shock wave going through the shock tube and broken glass panel. From about 56 ms the calibration of the cameras is thus lost.

The scatter between the 10 measurements is quite low, with the arrival time for the second larger peak having only a scatter of about 0.7 ms.

9.3.3 Encountered problems

Synchronising six high-speed cameras of four different types proved to be difficult. After some initial troubles, and to not lose any more time, it was decided to go ahead with only the SA4 cameras filming the glass panel. This unfortunately meant a reduction in the frame rate from 9300 to 5000 fps. The other cameras were used to make additional un-synchronized images for qualitative purposes only.

As said before, test 30-3-RB already broke during the tightening of the bolts. In Figure 9-28 it is clearly visible that the glass failed along the initial crack. The ‘clean-cut’ fracture would have very neatly cut the PVB at the onset of bending.

Additionally, the steel clamping ring had deformed a little after some tests. Extra care was taken when tightening the bolts of tests thereafter.

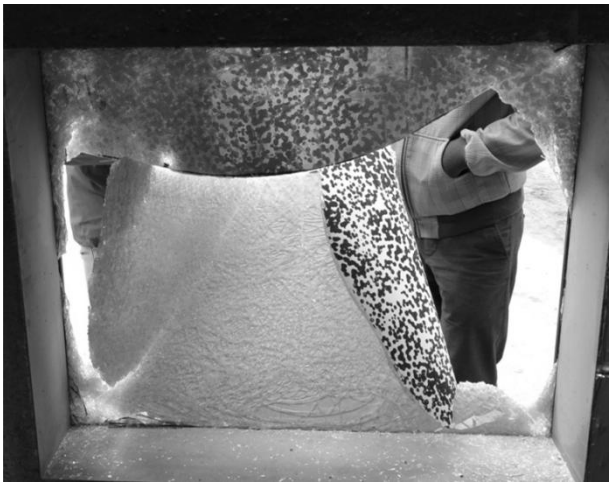

Figure 9-28 Panel 30-3-RB after testing.

9.4 CONCLUSIONS

A total of 12 large-scale blast tests on laminated glass panels were conducted. Two types of interlayer were tested: a medium adhesion 'standard' RB interlayer and a high adhesion stiffer DG interlayer. Due to the two first tests having a smaller charge weight and one panel being fractured before testing, 4 RB and 5 DG tests could be compared in the end.

Glass laminated with a DG interlayer proved to be much stiffer than glass with an RB interlayer. The combination of the stiffness and the high adhesion to the glass caused the interlayer to tear quickly at the edges by the incoming shock wave. In four of the five tests, the whole laminated glass panel was blown out of the frame, leaving only the clamped edges in place. In the fifth case, only a part of the panel was blown out and two of the four edges of the interlayer were torn. The pieces that were blown out of the frame, and the clamped area as well, remained very stiff.

On the contrary, the RB interlayer is clearly more flexible. Of the other four plates, the interlayer of three plates was torn. However, the way in which the panels deformed differed from the DG interlayer. Except for small glass shards, no parts were torn from the panel for any of the performed tests.

The main reason why the RB interlayer reacted better on the blast load was because the energy was dissipated by the deformation of the interlayer after the glass was broken. The flexible, medium adhesion interlayer allowed for large deformations without fully tearing apart, where the stiff DG interlayer with high

adhesion was torn soon after the impact of the shock wave. This behaviour was to be expected since the mechanism is the same as during the small-scale blast and impact tests.

The tests were reproducible in the initial phase, which attests the quality of the set-up. From the moment the glass fractured and subsequent PVB tearing start to play a role, the results differ. Despite the high cost, it is thus recommended to always perform at least 3 tests for every parameter one changes.

9.5 INTERACTION WITH MODELLING (PELFRENE [5])

Because the large-scale tests were only performed at the very end of this PhD study, Pelfrene already started simulations using data from Kuntsche [6], which was readily available. Apart from the exact blast load and composition of the panels, these proved to be very similar to the tests conducted in this study, be it that Kuntsche's tests completely adhered to the EN 13541 standard guidelines.

In early simulations, the criterion for glass fracture by element deletion consisted of a yield stress limit, followed by a short plastic phase. With this approach, the global deformation of the fractured panel could be matched fairly well, but not the local behaviour. It was seen that rather large zones of glass elements were being deleted from the analysis, especially around the corners of the plate. Also the strain in the interlayer material bridging the cracks remained much lower in the simulations than in reality. Consequently, tearing of the interlayer could never be predicted.

When these simulations were repeated with the crack delay model and the hyperviscoelastic material model for PVB interlayer, an improved cracking pattern could be obtained with finer cracks appearing in the correct locations. Without the modelling of delamination, this entails local interlayer strains that do come close to the tearing limit for the load case. Nonetheless, a more flexible response is observed in the numerical result as the deleted elements no longer possess any stiffness in compression.

An attempt has been made to model delamination as well by including cohesive zone elements at the interface, for which the simulation shows that the interlayer strains remain at a lower level than when delamination is not included. Even though this model shows credible elastic response and post-fracture deflection, a very high amount of delamination takes place in the simulation (see Figure 9-29). This rather unrealistic result is likely due to the coarse elements mesh.

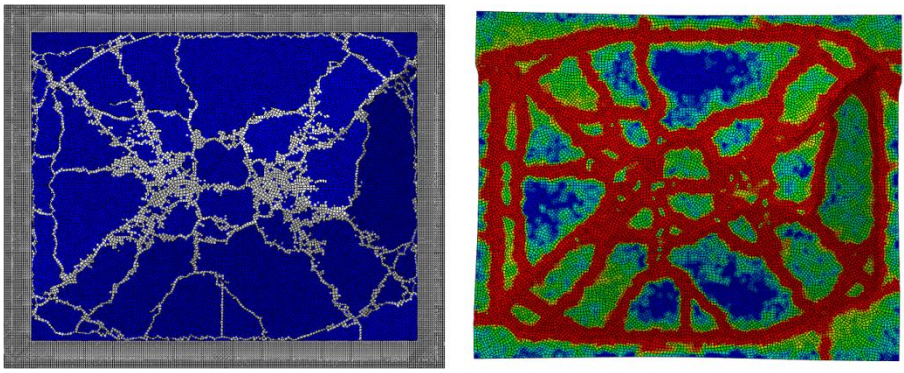

Figure 9-29 **Numerical simulation of cracked laminated glass panel with delamination: (left) cracking pattern and (right) contours of delamination in cohesive zone between interlayer and outward-facing glass ply (blue: no delamination, red: fully debonded).**

9.6 REFERENCES

[1] P. A. Hooper, R. A. M. Sukhram, B. R. K. Blackman, and J. P. Dear, "On the blast resistance of laminated glass," (in English), *International Journal of Solids and Structures*, vol. 49, no. 6, pp. 899-918, Mar 15 2012.

[2] J. Debroey, "Analyse van de interactie van schokgolven met gordijngevels," Royal Military Academy, Brussels, 2008.

[3] De Reu, D. Studie van de fragmentatie en scherven-uitworp van diverse types glas bij explosies. ASW, COBO (KMS), Brussel, 2008.

[4] C. Kranzer, G. Gürcke, and C. Mayrhofer, "Testing of Bomb Resistant Glazing Systems Experimental Investigation of the Time Depemdent Deflection of Blast Loaded 7.5 mm Laminated Glass," presented at the Glass Processing Days 2005, Tampere, Finland, 2005.

[5] J. Pelfrene, "Numerical analysis of the post-fracture response of laminated glass under impact and blast loading," Doctor in de Ingenieurswetenschappen: Werktuigkunde-Elektrotechniek PhD, Department of Material Science and Engineering, Mechanics of Materials and Structures, Ghent University, Ghent, 2016.

[6] J. Kuntsche. Mechanisches Verhalten von Verbundglas unter zeitabhängiger Belastung und Explosionsbeanspruchung. PhD thesis, Technische Universität Darmstadt, 2015.

Chapter 10 CONCLUSIONS AND OUTLOOK

Overview

In this final chapter the conclusions of all three major parts of the dissertation (material characterization, impact & blast) are presented, together with some recommendations for future work.

10.1 CONCLUSIONS

In this work, an experimental assessment has been made of laminated glass response to impact and blast loading, in close collaboration with Joren Pelfrene, who's PhD [1] focussed on numerical simulations of most tests presented in this work.

10.1.1 Part I – Introduction & Material characterization

In a first part, the constituent materials of laminated glass, PVB and glass, plus the interface between both, were studied. The nature of the two materials composing laminated glass could not be more different with on the one hand an elastic, brittle ceramic with a large scatter on flexural strength and a low failure strain, and on the other hand a visco-elastic polymer which can strain immensely and has a glass transition temperature around room temperature.

The fracture strength of glass was studied with both four-point and axisymmetrical bending test set-ups. Improvements were made to De Pauw's [2] numerical model of the axisymmetrical bending tests. A Weibull analysis was performed which, together with high-speed imaging, suggests the set-up is not edge-independent after all. Much higher fracture stress values (>200 MPa) were found for the axisymmetric specimens, where fracture started from the surface, than for the four-point bending specimens (average 64.4 MPa), where fracture typically starts from the edge.

Tensile tests on PVB, in both a quasi-static and dynamic regime, were performed. As expected, the material acted stiffer with a higher rate of deformation and the extension at failure also decreases with increasing test speeds.

An in-depth study was performed on Hooper's formula [3] for the deflection of a laminated beam under four-point bending. Through a combined analytical, experimental and numerical approach, it was shown that these formulas, are erroneous and we provided a correct solution.

The length of the cantilever section of a laminated beam (the part that extends beyond the supports) was shown to have an influence on the deflection in the middle of the beam. Contrary to the elastic beam theory, stress is also present in these sections. Furthermore, the stress between the loading points is not constant, which can explain why fracture more often starts near them.

Through-Cracked-Tension (TCT) tests were performed on samples with a variety of interlayers. For faster extension rates a steady state was obtained, and the strain in the interlayer was calculated using image post-processing.

While hardly any difference could be noticed in the steady-state force between high and low level adhesion samples, the tearing force, delamination rate,

strain and interface energy did show an influence of the adhesion level on their respective values.

Pull-off adhesion tests were performed but no strong conclusions can be deduced from their results.

10.1.2 Part II – Impact

In the second part the behaviour of laminated glass subjected to impact loading was investigated. It started with a description of the standards used in other chapters, and presented a literature study.

A small-scale drop weight (SSDW) test set-up was used to subject laminates to both hard and soft impact. Parameters such as glass and PVB thickness, PVB stiffness, adhesion level and boundary conditions were tried. Wherever possible, processing of the data obtained by all the sensors and high-speed images was automated.

A method was devised to automatically determine the time of fracture of both glass panels using the images from the high-speed camera, filming the specimens from below. Furthermore, a method was established to quantify the damage experienced by the samples in a so-called fracture number.

Numerous parameters, such as forces, velocities, deflections, etc. which were extracted from the sensors of the set-up, were studied but in the end no influence of the adhesion level on these results could be discerned. This was because the damage dealt to the specimens remained quite low and sufficient delamination of the interlayer did not yet take place to see an effect. However, reproducibility of the tests was proven to be very high.

Strains were measured and showed that even after fracture of a plate, stress was still transferred to it to a high degree.

Differences in boundary conditions did result in different fracture patterns being observed.

In a final test series on a different set-up, where the laminates were punctured and thus a higher degree of loading was experienced by the interlayer, a clear difference in behaviour for low and high level adhesion was found.

A second test campaign was performed on an EN 12600 set-up, which uses a twin-tyre pendulum to load the specimens. These tyres were characterised in great detail, through tensile and compression tests on several configurations (including the reinforcement fibers) and a micro-CT scan.

A pressure plate was used to measure the exact pressure distribution the tyres exerted during impact. The obtained pressure plots proved very useful for

validation of the models. The impactor acceleration during impact was also measured.

Tests were performed on laminated specimens with different glass and PVB thicknesses and different adhesion levels and, as it turned out, different lamination configurations.

Panels made with the smallest glass thickness all fractured whereas some panels with a higher thickness even withstood the impact from the highest drop height. Thicker glass also impeded deflection, due to mechanical interlocking of the larger shards. PVB thickness had a similar effect, with thicker interlayers resulting in lower deflections.

Influence of the adhesion was not so much visible in the deflection of the panels, but it was noticeable in the tearing behaviour, with higher adhesion leading to an earlier onset of tearing.

The lamination configuration (which side – air or tin – is laminated against the interlayer) proved to have a major influence on the fracture and subsequent deflection behaviour of the specimens, with 'tin-air' specimens having the lowest impact resistance.

10.1.3 Part III – Blast

Both small- and large-scale tests were performed in the final part, which dealt with blast loading of laminated glass. Their description was preceded by an introduction to blast including a literature study.

The preliminary small-scale tests, their problems, and subsequent steps to solve them can be summarized as follows. With the initial design of the set-up (open air blast and limited clamping), severe loading, needed to tear the PVB interlayer, resulted in the specimens being blown out of the frame. This was remediated in the second set-up with wider clamping rings. However, even with high charges very close to the specimen, no difference in behaviour, depending on adhesion level, could be discerned. Furthermore, this resulted in unpredictable pressures. The third set-up thus used a small-shock tube which could deliver a high load with reasonable precision. This concentrated force, however, resulted in immediate lateral cracking of the glass and subsequent problems with the correlation of the high-speed images.

A larger shock tube was constructed that overcame all aforementioned issues and could deliver a planar blast load that was high enough to obtain different responses from laminates with different adhesion levels.

Tearing of specimens with high adhesion was achieved, whereas specimens with lower adhesion were less likely to experience tearing.

Pressure measurements were conducted for the first (open air) and final (shock tube) test set-up and confirmed the reliability of both set-ups in producing good results.

In a final test campaign, 12 large-scale blast tests, with a shock tube, were performed on two types of laminates. The tests were reproducible in the initial phase, which attests the quality of the set-up. From the moment the glass fractured and subsequent PVB tearing start to play a role, the results differ.

Glass laminated with a DG interlayer proved to be much stiffer than glass with an RB interlayer. The combination of the stiffness and the high adhesion to the glass caused the interlayer to tear quickly at the edges by the incoming shock wave. Most often, the whole laminated glass panel was blown out of the frame, leaving only the clamped edges in place.

On the contrary, the RB interlayer is clearly more flexible. Three plates also experienced tearing of the interlayer; however, the way in which the panels deformed differed from the DG interlayer. Except for small glass shards, no parts were torn from the panel for any of the performed tests and the torn panels stayed inside the clamping area.

10.1.4 General

In the end, for each part, successful test campaigns have been designed, which could study the mechanical (post-fracture) behaviour of laminated glass, subjected to a variety of loading conditions. Often an iterative approach was employed to continuously improve on set-ups, to obtain a profound fundamental knowledge of the mechanisms at play. The role adhesion between a PVB interlayer and glass has on the dynamic response of laminated glass, was successfully characterised.

Most of these set-ups were extensively instrumented, which sometimes proved necessary to be able to extract the correct parameters to interpret the results. The most valuable TCT results, for example, were procured through post-processing of the images of the tests.

The instrumentation also provided a lot of data which could be used for the development, calibration and validation of the numerical work performed by Pelfrene [1]. The interaction was strongest for the twin-tyre pendulum of the EN 12600 set-up, which resulted in a very detailed, validated model of the tyres.

10.2 OUTLOOK

This research work has focussed on the mechanical behaviour (after breakage) of glass laminated with PVB interlayers with different adhesion levels. Some suggestions of the topics requiring further attention and areas for investigation that were not covered in this dissertation are given here.

10.2.1 Multilayer

A major development has been the creation of multilayer interlayers, such as the acoustic Saflex® Q-series. This is a three-layer system designed to decouple and disseminate sound waves for a better sound damping performance. A thin layer of PVB with a higher degree of plasticizer is sandwiched between two thicker outer layers of standard PVB.

While single layer PVB currently remains the industry standard, the need for such advanced multilayer films, where several properties – e.g. UV absorption and impact resistance – are combined, increases. An acoustic layer combined with one from the increased stiffness DG-series, could result in the possibility to use thinner glass, which is very attractive for the automotive industry due to the accompanying weight reduction.

However, current knowledge about the existing multilayer acoustic range is quite limited with clients reporting delamination taking place between the interlayers for some specific applications. Especially curved laminates (such as car windshields) have a high risk of interlaminar delamination.

The development of measurement techniques, in combination with numerical models, to obtain adhesion values between different PVB layers, can be a first step to further improving impact resistance of multilayer interlayers.

10.2.2 Tempered glass

All glass used in this study was common annealed float glass. More and more safety glass, however, is made using tempered glass panels.

Whereas the fracture pattern of annealed glass can seem arbitrary, and is very difficult to capture using numerical models, the distribution of cracks of a fractured tempered panel is more evenly distributed over the entire pane area. Furthermore, this cracking happens almost instantaneously. The behaviour of fractured tempered laminated glass is often characterized as that of a *'wet towel'* [4] (see also chapter cover image). Modelling could be reduced to finding an appropriate material law for this fractured cross-section as a whole (as opposed to different, complex material models for fractured glass and PVB separately). Only the fracture strength of the glass needs to be known with high precision to then model the post-fracture behaviour correctly.

10.2.3 EN 356 test campaign

Although an EN 356 set-up has been designed and constructed during this research (see Annex C), time constraints prevented a full experimental campaign being conducted on it. The nature of the loading, however, might prove to be beneficial for a study on several parameters – such as adhesion level – because it is quite high with possible penetration of the interlayer for higher drop heights.

10.3 REFERENCES

[1] J. Pelfrene, "Numerical analysis of the post-fracture response of laminated glass under impact and blast loading," Doctor in de Ingenieurswetenschappen: Werktuigkunde-Elektrotechniek PhD, Department of Material Science and Engineering, Mechanics of Materials and Structures, Ghent University, Ghent, 2016.

[2] S. De Pauw, "Experimental and Numerical Study of Impact on Window Glass Fitted with Safety Window Film," Doctor in de Ingenieurswetenschappen: Werktuigkunde-Elektrotechniek PhD, Department of Material Science and Engineering, Mechanics of Materials and Structures, Ghent University, Ghent, 2010.

[3] J. A. Hooper, "Bending of Architectural Laminated Glass," (in English), *International Journal of Mechanical Sciences*, vol. 15, no. 4, pp. 309-323, 1973.

[4] M. Haldimann, A. Luible, and M. Overend, *Structural Use of Glass* (Structural Engineering Documents, no. 10). Zürich: International Association for Bridge and Structural Engineering, 2008, p. 215.

ANNEXES

Three annexes are presented at the end of this work. The first gives an introduction to the Digital Image Correlation (DIC) technique. The second one presents in detail all results of the Small-Scale Drop Weight tests from Chapter 5. The third one details the building of an EN 356 set-up.

Annex A INTRODUCTION TO DIGITAL IMAGE CORRELATION

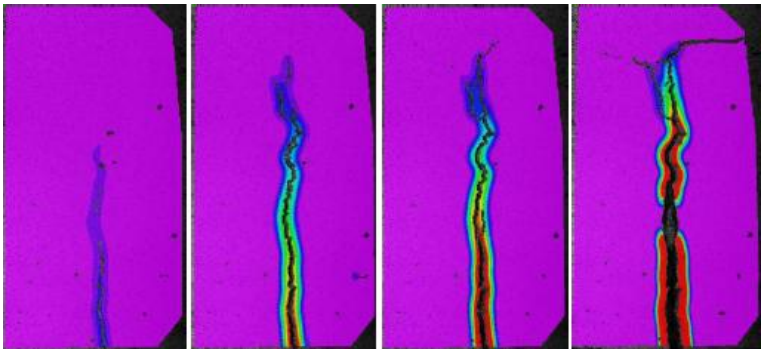

Overview

Throughout this work the Digital Image Correlation technique (DIC) is amply used. The basics needed for a proper understanding of this technique are explained in this annex. Several general concepts are introduced, as well as some more in-depth insights in the matter. The annex starts with the theoretical specifics of DIC, alternated with more practical know-how.

Most of the theory in this annex is based on the reference work of Sutton, Orteu and Schreier [1] and a practical course on how to perform good DIC measurements by Lava, Pierron and Reu [2], supplemented with material from frequently cited articles.

A.1 DIGITAL IMAGE CORRELATION (DIC)

Digital Image Correlation is a contactless optical measurement technique, capable of extracting full-field shape, deformation and motion measurements from an object under study. Advances in computer-vision-based measurement methods in the recent decades have caused an increasing interest in this technique which can, if used correctly, provide correct measurements in a detailed manner, trumping older methods like strain gauges, only providing data at one point.

At first, DIC's precursors photogrammetry and image correlation were mainly used for character recognition, microscopy, medicine and aerial photography, with engineering applications like deformation measurements non-existent. Next came an era of laser-based fringe analysis techniques, such as moiré interferometry, but these techniques required a laborious determination of estimates for fringe centre locations.

Nowadays, three-dimensional Digital Image Correlation is being used for a wide range of applications [3], ranging from large structures to nano-scale measurements, from engineering to biomedical science. The lowering cost and ever better capabilities of high speed imaging systems has also resulted in an abundance of research in that field using the DIC techniques.

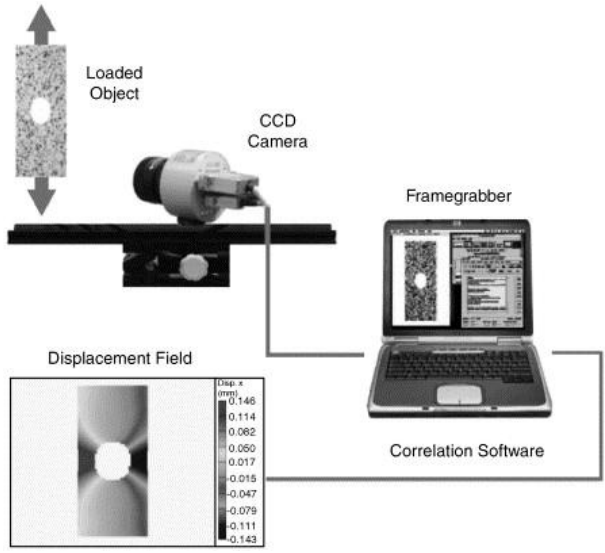

Figure A-1 Working principle of the DIC system [4].

The working principle (Figure A-1) of DIC is based on taking digital images of an object under loading, at different loading time steps and comparing small rectangular areas from images of the deformed object with a reference image of the

object without loading applied to it. To enable easy comparison between both images, a so-called speckle pattern is applied to the object's surface. To accommodate deformation of the rectangular area, shape functions are introduced. Information from the centre points of the rectangular areas is interpolated using special algorithms. In the end the software provides a displacement field. All these concepts are introduced in this chapter.

With the basics known, we can now take a look at how the DIC software will actually correlate the acquired images. To do so, it uses highly specialized algorithms with very stringent resolution requirements needed for an accurate estimation of strain.

Commercial DIC codes include ARAMIS (GOM), ISTRA 4D (Dantec Dynamics), StrainMaster (LaVision Inc.), Vic3D (Correlated Solutions) and MatchID (a spin-off company from University of Leuven) [9].

A.1.1 Speckle pattern

When trying to find a single pixel in a second image, this will be very hard as there are probably hundreds more with the same grey value and thousands more with a similar grey value. One way to solve this is to look at a neighbourhood of pixels or a so-called subset (Figure A-2). The solution may still not be unique, so it is important to have constraints on the minimum size of this neighbourhood.

A second problem arises when this neighbourhood can be found on several places in the image, when for example viewing a repeating structure. When a structure is textureless, no information from inside its boundaries can be determined.

To solve all these problems, in a unique manner, rules can be established for the object surface. The ideal surface texture should be isotropic, non-periodic and show a high degree of contrast. This inevitably leads to a so-called speckle-pattern.

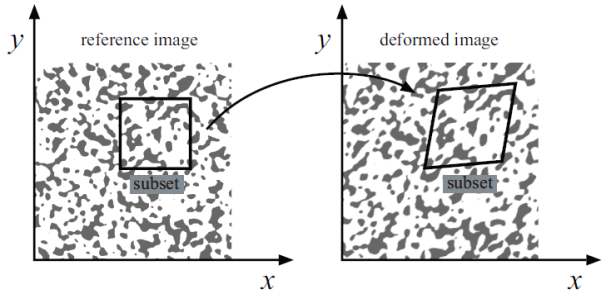

Figure A-2 **A subset in the undeformed (left) and deformed (right) speckle pattern [10].**

Ordinary paint is most often used to apply this speckle pattern. Matte paints should be used, to minimize possible specular reflection, and one usually starts by applying a thin white basecoat to the specimen surface. Black speckles can then be applied with a simple spray can, toner powder, using stencils and silk screen printing, or printing. Care should be taken that all speckles have a similar size, and that this size is in accordance with the desired spatial resolution.

Recently, advances have been made in generating optimized patterns for use with DIC [11]. No two speckle patterns applied by spray painting will be the same, compromising the reproducibility of the technique. In order to minimize this variability, the same generated pattern can be applied to each specimen. The speckle pattern is synthesized using a combination of morphological image processing and Fourier analysis, resulting in wide autocorrelation margins but with sharp autocorrelation peaks, which is ideal for DIC measurements.

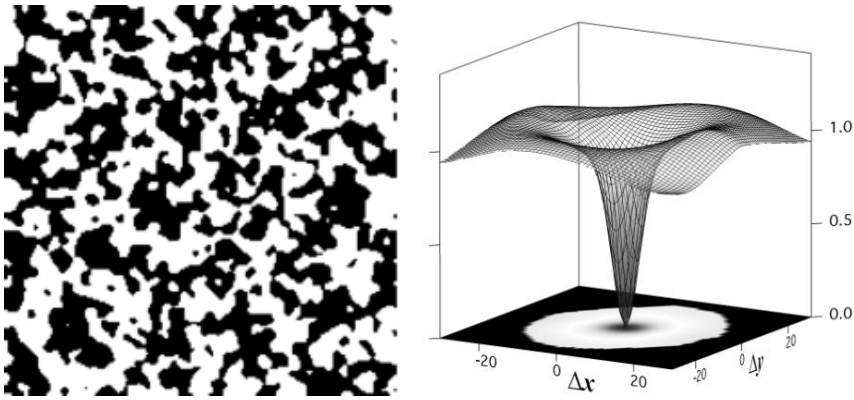

Figure A-3 **Optimized pattern (left) and its autocorrelation (right) (adapted from [11]).**

A.1.2 Correlation algorithms

The actual calculation of the displacement field depends on three separate algorithms, each with their own set of parameters. They are combined in a single iterative solution scheme.

A.1.2.a Subset shape functions

Basically, to derive the motion of such a subset, one can apply the sum of squares deviation (SSD) when comparing two images (see A.1.2.b). However, while this is

very simple for in-plane motions of an undeformed subset, the algorithm cannot cope with rotated or deformed subsets, which will most often be the case in engineering applications. To prevent this decorrelation, a subset shape function is introduced that transforms pixel coordinates in the reference subset into coordinates in an image after deformation.

Depending on the expected deformations, shape functions can range from very simple (rigid body) to very complex (quadratic), see Figure A-4. Most often, the deformation can be approximated by a first-order affine transformation, which accounts for translation and rotation, shear and normal straining.

Second-order shape functions introduce less systematic error for quickly varying displacement fields and should be used in the case of matching the left and right images recorded in a stereo DIC test [12].

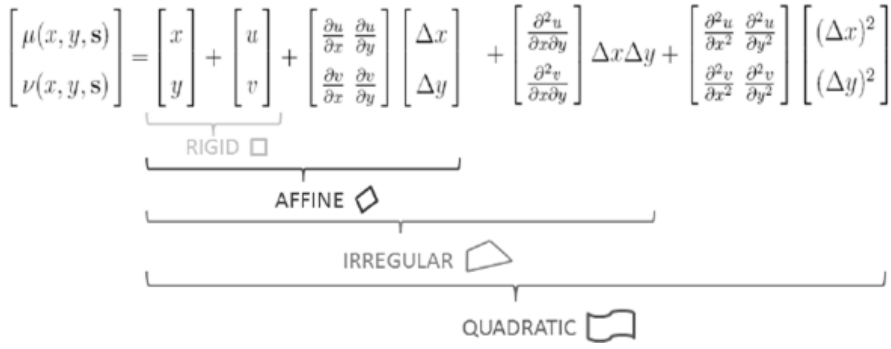

Figure A-4 Subset shape functions [2].

A.1.2.b Optimization criteria for pattern matching

To find a subset match in a different picture, an optimization criterion has to be used. Essentially, this involves minimizing a cost function. One problem which an adequate optimization criterion should resolve is changes in lighting conditions, especially for stereo images. A change in offset and/or scale of lighting is unavoidable even in near perfect lab conditions and this will inevitably result in changes in intensity (grey values) of the recorded images. For stereo-vision these changes will also be different for both cameras.

To address this issue, one can implement a zero-mean normalized sum of squared difference (ZNSSD) criterion. Despite the more complex equations behind this method, it can still be evaluated in a single pass (just like the SSD criterion) and it does not introduce a significant computational overhead compared to this criterion.

A.1.2.c Interpolation function

To obtain sub-pixel accuracy, interpolation between the gray values of the subset has to be applied. This will inevitably result in errors, as an interpolation can never perfectly match the values between two sample points. It is therefore important to choose filters that minimize this error.

A trade-off has to be made between bias and execution time. Generally speaking, the more coefficients used for interpolation, the better the result but the longer the computation time. However, methods applying the same number of coefficients can still result in large differences between their respective outcomes. One such example is cubic B-splines and cubic polynomial interpolation with the former having a much better performance.

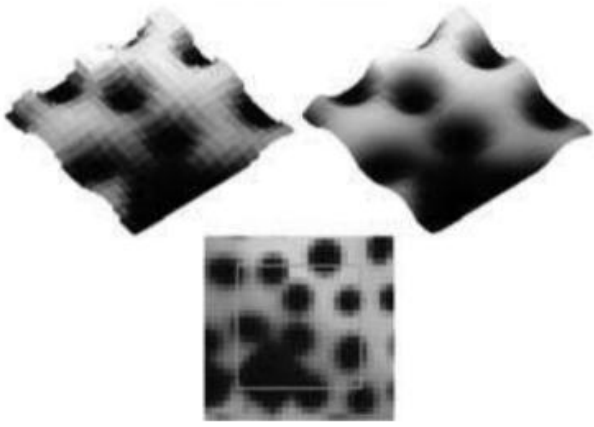

Figure A-5 Raw image data (left) and interpolated data (right) for a subset (bottom) [13].

In [14, 15] optimized filters have been developed. In particular the optimized six and eight-tap filters show very good results.

A.1.2.d Other parameters

Subset size

The size of the subset is one of the most important parameters to choose when correlating images. The spatial resolution is defined as half the subset size. Large subsets lead to a lower spatial resolution and they have problems matching a sharp corner. When the deformation field is quite homogeneous except for a single region, a smaller subset can be chosen to correlate that region, much like mesh refinement in numerical modelling.

Step size

Of course, one could perform this correlation for every pixel in the acquired image, but this would result in a massive amount of data which would also take a long time to compute. For this reason, displacement values are often only determined every 2, 5 or 10 pixels. As a rule of thumb, this so-called step size should be taken as one third of the subset size.

Resolution

The displacement resolution – the smallest value that can be detected above noise – is computed as the standard deviation of displacements in a self-correlation test. This can be done by correlating for example 10 images taken before the loading of the specimen.

The spatial resolution is the smallest distance between two independent measurement points; it is thus equal to the subset size (and not the step size, because that would not take the overlap of data points into account).

A.1.3 Strain field calculation

A full-field displacement array with sub-pixel precision contains all the information necessary to complete a full-field strain map. The deformation gradient needed for this calculation contains derivatives which are approximated by differentials. However, due to noise present in the displacement array, care has to be taken when performing a strain analysis. If the displacement resolution is 0.01 pixel, resolution on a finite difference is 0.02; if the strain is computed between two subset centres set 20 pixels apart, strain resolution will be 2.10^{-3} or 2000με.

To alleviate this, the displacement data is first smoothed before starting the differentiation process. A strain window of N by N data points (not pixels) is defined. Next, a surface smooths the experimental data in this "window". This is, in effect, equivalent to a low-pass spatial filter. Most often, bilinear (Q4) or biquadratic (Q9) Lagrange polynomials are used for this purpose. Large strain windows can be used when there is a homogeneous strain field, but they will miss large gradients as they smooth over these areas of rapidly changing strain.

The calculated strain is extremely sensitive to the virtual strain gauge size (VSG) and subset size. For a uniform strain, larger subsets and virtual gauges should be used but large subsets will mask strain gradients, even if the virtual gauge is small. When encountering gradients, use small subsets and virtual gauges.

Virtual Strain Gauge dimensions and the strain spatial resolution (SSR) can be calculated as:

$$VSG = [(StrainWindow - 1) \times Stepsize] + 1 \quad \text{(A.1)}$$

$$SSR = [(StrainWindow - 1) \times Stepsize] + Subsetsize \quad \text{(A.2)}$$

The resolution can once again be determined using the standard deviation of the reference image which is de facto strain-free.

A.2 2D-DIC

In order to get correct results when performing in-plane measurements with DIC, three assumptions have to be met by the specimen: i) the specimen should be nominally planar (flat) but may contain geometric discontinuities, ii) the object plane is parallel to the camera sensor plane and iii) the deformation predominantly takes place within the original planar surface.

Failing to meet these assumptions, especially the last one, will result in false strain measurements. If the object moves toward the camera, it will look like a uniform strain was applied to the specimen (Figure A-6). However, this can be mediated by using a telecentric lens or a stereo-vision set-up.

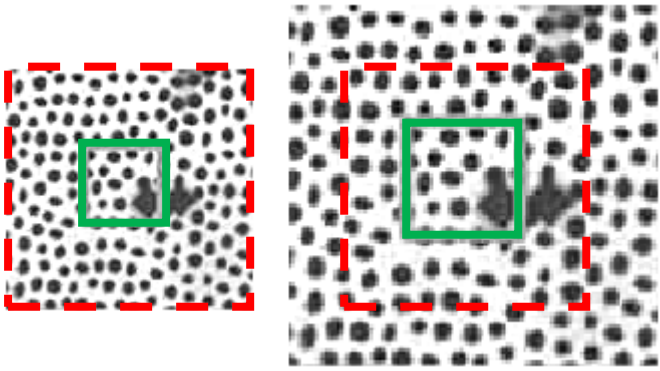

Figure A-6 **Reference image without strain (left) and same image moved closer to camera resulting in false strain (right) (adapted from [2]).**

Compared with regular uniaxial loading of planar specimens (e.g. dogbone tensile specimens) the use of DIC provides full-field data providing quantitative measurements of for example strain localization during necking. Furthermore, all three planar surface strains are obtained simultaneously. Because strain is unitless, any length dimension (millimetres or pixels) divides out, making calibration

unnecessary in a 2D set-up. However, in [16] Lava et al. do recommend to take the lens distortions explicitly into account, as this will substantially improve strain measurements.

A.3 HIGH-SPEED 3D-DIC

Extending this to the third dimension and high-speed imaging requires some adaptations. For an optimal spatial resolution the specimen should roughly fill the complete field-of-view (FOV). However, it is very important that the entire surface of the specimen should remain in the field of view of both cameras during the entire test as it may move substantially.

A.3.1 Stereo Angle

The angle between both cameras is an important parameter in stereo-vision measurements. In general an angle between 15 and 35 degrees is best. The narrower stereo-angles (shorter baseline) will improve the in-plane results at the cost of a higher out-of-plane uncertainty. Using a larger stereo-angle will improve out-of-plane results. For most experimental mechanics experiments, where strain is the desired measurement, a narrower stereo-angle is then generally preferred [17].

The uncertainty also varies with the location within the FOV and the lens focal length. Not entirely unexpected, the uncertainty increases with increasing distance from the centre of the image. However, this effect becomes less pronounced with increasing focal length [18].

A.3.2 Lighting considerations

Whenever possible, flat (or diffusive) lighting should be used. A direct path from the light to the camera should be avoided. However, should the object change shape during loading, it can become a bit trickier. Using diffusers and many light sources help create flat light. The possible loss of contrast, as evidenced in Figure A-7, does not have to pose a problem, as even a small amount of contrast is sufficient for the algorithms to find a correct match. Furthermore, darker images contain less noise.

Especially when recording at a high speed (and thus with a short shutter time), powerful lights may be needed for enough light to reach the sensor. Fluorescent lights should be avoided as they tend to flicker. Enduring exposure to lighting during the set-up may cause the specimen to heat up resulting in thermal strains. LED lighting can provide higher intensity with lower heat. One should also be careful to not saturate the images.

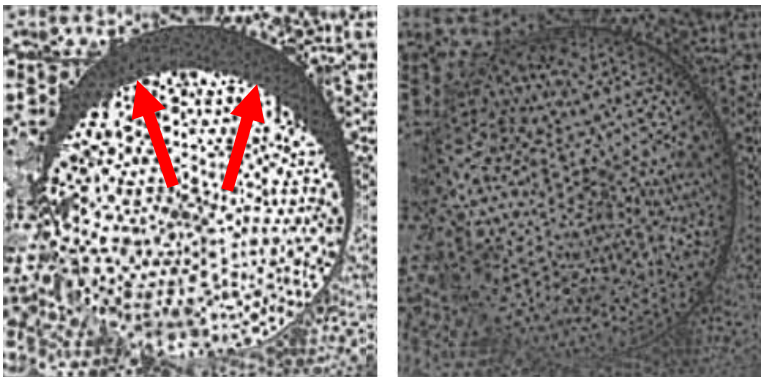

Figure A-7 **Direct illumination with undesired shadow (left) and flat illumination (right) (adapted from [2]).**

A.3.3 Calibration

Performing an excellent calibration is paramount to (having the possibility to) get good results. Pre-calibration routines include checking for dirt, aligning the stereo-rig, setting the focus, aperture and exposure and checking the calibration volume [19]. Having calibrated the system, there is no going back and the test must be executed swiftly. The focus, aperture, field-of-view and relative camera positions may not be altered.

Attributes of a good calibration image are (i) adequate and even illumination, (ii) be entirely in focus, (iii) have no motion blur, (iv) fill the measurement volume and the field-of-view and (v) be taken with synchronized cameras [20].

A.3.4 High-speed cameras used in this research

As there is a trade-off between the frame rate and the resolution a compromise needed to be found between the largest possible viewing window (determined by the resolution) and at the same time a sufficiently high frame rate to be able to capture the high-speed breakage phenomena.

APX-RS

The APX-RS was the first high-speed camera acquired by the department and it has a maximum framerate of 3 000 fps at a full resolution of 1 024 by 1 024 pixels. The maximal framerate is 250 000 fps at a reduced resolution of 128 by 16 pixels. It

features a 10-bit CMOS imaging sensor with 17 µm pixels. The shutter speed can be chosen between 16.7 ms to 2 µs. The interface relies on FireWire technology.

SA4

The maximal framerate is doubled compared to the APX-RS at the same reduced resolution of 128 by 16 pixels. At full resolution the maximal framerate is increased to 3600 fps. The maximum shutter speed is doubled to 1 µs. Two such cameras are available.

SA5

The RMA owns 2 upgraded versions, with slightly better specifications than the SA4. These cameras are used for the small-scale blast experiments in Chapter 9. All three types are used in the large-scale blast test campaign in Chapter 10.

A.4 CONCLUSIONS

The two defining characteristics of a lens are its focal length and aperture. Both should be chosen in accordance with the desired field of view and depth of field. Lens distortions can be accounted for using a bundle adjust calibration procedure.

DIC is an optical contactless method which can be applied to arbitrary geometries and loading conditions and which yields full-field displacement data with sub-pixel accuracy. It can cope with small strain levels up to a high plastic deformation, both in a 2D and 3D configuration.

It does so by taking synchronized pictures using CCD cameras and comparing the images of the deformed specimen with a reference image of an unloaded specimen. That being said, the DIC software is often considered as a black box and many parameters can be tuned to get the outcome one desires. To get correct and accurate results, special care has to be taken in every of its many steps. 3 basic rules are repeated here:

- Rule 1: Eeach speckle should be sampled by at least a 3 by 3 pixel array
- Rule 2: Each subset should contain at least 3 by 3 speckles
- Rule 3: The step size should be one third of the subset size

A random speckle pattern will be generated using software developed by Bossuyt in [11]. Affine subset shape functions can cope with most types of deformation, but quadratic functions are preferred when using stereo-vision. The ZNSSD criterion should be used too as it can cope with changes in lighting conditions. Six- and eight-

tap filters give the best interpolation results. Especially for high-speed imaging, adequate lighting should be provided.

A.5 REFERENCES

[1] M. A. Sutton, J.-J. Orteu, and H. Schreier, *Image Correlation for Shape, Motion and Deformation Measurements: Basic Concepts,Theory and Applications*: Springer Publishing Company, Incorporated, 2009.

[2] P. Lava, F. Pierron, and P. Reu, *Digital Image Correlation Course - Metrology beyond colors*. Ghent: MatchID, 2014.

[3] B. Pan, "Recent Progress in Digital Image Correlation," *Experimental Mechanics*, vol. 51, pp. 1223-1235, Sep 2011.

[4] D. Lecompte, A. Smits, S. Bossuyt, H. Sol, J. Vantomme, D. Van Hemelrijck, *et al.*, "Quality assessment of speckle patterns for digital image correlation," *Optics and Lasers in Engineering*, vol. 44, pp. 1132-1145, Nov 2006.

[5] P. Reu, "Stereo-rig Design: Lens Selection - Part 3," *Experimental Techniques*, vol. 37, pp. 1-3, Jan-Feb 2013.

[6] H. S. Sawhney and R. Kumar, "True multi-image alignment and its application to mosaicing and lens distortion correction," *Ieee Transactions on Pattern Analysis and Machine Intelligence*, vol. 21, pp. 235-243, Mar 1999.

[7] Correlated Solutions Incorporated. Calibrated sensor and method for calibrating same, 2006. Patent Filed 2/6/2003: Patent Issued 11/7/2006: US Patent No. 7,133,570.

[8] D. Garcia. Mesure de formes et de champs de déplacements tridimentionnels par stéréo-corrélation d'images. Ph.D. thesis, Institut National Polytechnique de Toulouse, France, December 2001.

[9] P. Reu, "Introduction to Digital Image Correlation: Best Practices and Applications," *Experimental Techniques*, vol. 36, pp. 3-4, Jan-Feb 2012.

[10] Lecompte, D., Elastic and Elasto-Plastic Material Parameter Identification by Inverse Modeling of Static Tests using Digital Image Correlation. Doctor of philosophy dissertation: Vrije Universiteit Brussel and Koninklijke Militaire School, Brussels (2007).

[11] Bossuyt, S., Optimized patterns for digital image correlation. In proceedings of SEM annual conference, Lombard, USA, June 3-5 (2013).

[12] Y. Gao, T. Cheng, Y. Su, X. H. Xu, Y. Zhang, and Q. C. Zhang, "High-efficiency and high-accuracy digital image correlation for three-dimensional measurement," *Optics and Lasers in Engineering*, vol. 65, pp. 73-80, Feb 2015.

[13] P. Reu, "Hidden Components of 3D-DIC: Interpolation and Matching - Part 2," *Experimental Techniques*, vol. 36, pp. 3-4, May-Jun 2012.

[14] M. Unser, A. Aldroubi, and M. Eden, "B-Spline Signal-Processing .1. Theory," *Ieee Transactions on Signal Processing*, vol. 41, pp. 821-833, Feb 1993.

[15] M. Unser, A. Aldroubi, and M. Eden, "B-Spline Signal-Processing .2. Efficient Design and Applications," *Ieee Transactions on Signal Processing*, vol. 41, pp. 834-848, Feb 1993.

[16] P. Lava, W. Van Paepegem, S. Coppieters, I. De Baere, Y. Wang, and D. Debruyne, "Impact of lens distortions on strain measurements obtained with 2D digital image correlation," *Optics and Lasers in Engineering*, vol. 51, pp. 576-584, May 2013.

[17] P. Reu, "Stereo-rig Design: Stereo-Angle Selection - Part 4," *Experimental Techniques*, vol. 37, pp. 1-2, Mar-Apr 2013.

[18] X. D. Ke, H. W. Schreier, M. A. Sutton, and Y. Q. Wang, "Error Assessment in Stereo-based Deformation Measurements Part II: Experimental Validation of Uncertainty and Bias Estimates," *Experimental Mechanics*, vol. 51, pp. 423-441, Apr 2011.

[19] P. Reu, "Calibration: Pre-Calibration Routines," *Experimental Techniques*, vol. 37, pp. 1-2, Jul 2013.

[20] P. Reu, "Calibration: A good calibration image," *Experimental Techniques*, vol. 37, pp. 1-3, Nov 2013.

Annex B SMALL-SCALE DROP WEIGHT (SSDW): ADDENDUM TO CHAPTER 5

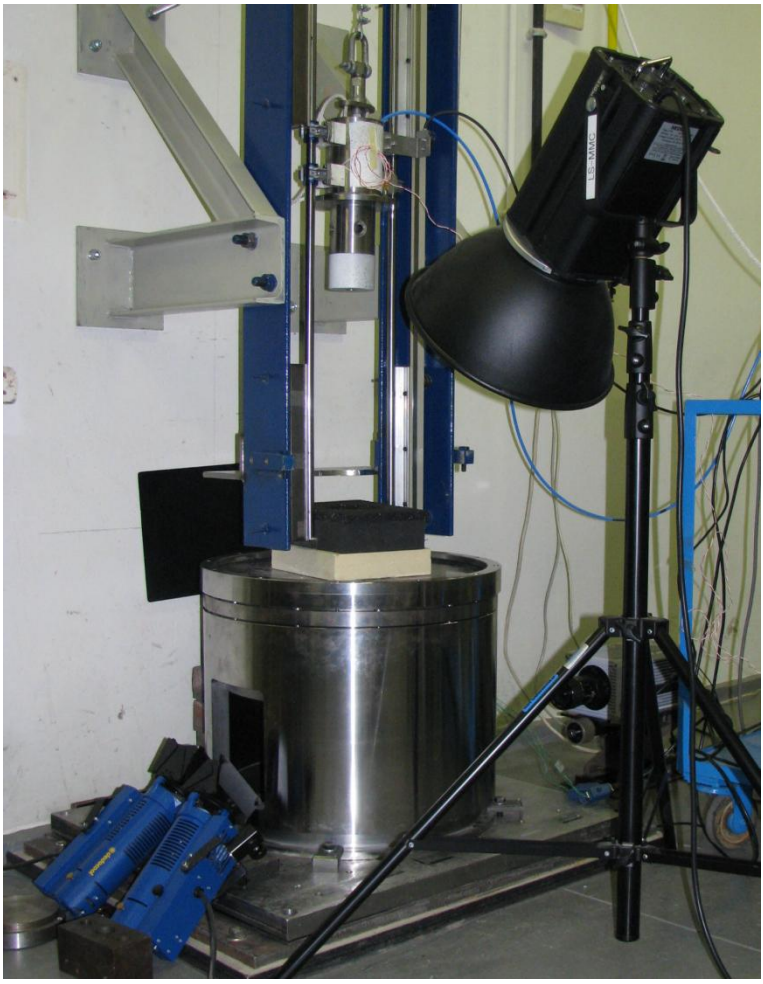

Overview

This annex serves as an addendum to Chapter 5. After detailing the instrumentation of the set-up, the results and their discussion, of both square and circular samples, is presented.

B.1 INSTRUMENTATION OF THE SSDW SET-UP

B.1.1 Displacement sensor

The displacement is measured by means of a Kübler linear measurement system (Limes). The system consists of the displacement sensor LI50 and a magnetic strip mounted parallel and next to the right guiding rail. Its measurement accuracy is 25 micron and valid for movement speeds smaller than 16.25m/s. For the readout of the high-frequent signal and in order to facilitate accurate setting of the drop height, an electronic counter type 572 by Kübler is installed near the test setup. It displays the impactor height permanently and can be easily reconfigured

B.1.2 Accelerometer

Depending on the sample glass thickness and the indentor material two different accelerometers were used during the tests. Their main properties are listed in Table B-1. Both types are integrated electronic piezoelectric (IEPE) axial accelerometers.

Table B-1 Accelerometer properties.

Property	**Type 1 [1]**	**Type 2 [2]**
Name	Kistler 8704B500	PCB 350 B02
Acceleration range [g]	±500	±10 000
Acceleration limit [g]	±1 000	±50 000
Sensitivity [mV/g]	9.84	0.103
Frequency range [Hz]	±5% : 1 - 10 000	±1dB : 4 - 10 000
Resonance frequency [kHz]	54	>100
IEPE type	Quartz	Ceramic
Internal signal filtering	No	Yes

The accelerometer was mounted on the top plate of the impactor. However, due to vibrations of the top plate the signal needed to be filtered.

B.1.3 Force sensor

Like the accelerometers, the force sensor is of the IEPE type. Its specifications are listed in Table B-2.

Table B-2 Force sensor properties [3].

Name	Endevco Isotron 2311
Measurement range [kN]	-2.2 - 22
Sensitivity [mV/N]	0.2293
Maximum force range [kN]	-2.2 - 66
Resonance frequency [kHz]	75
IEPE type	Quartz
Internal filtering	No

The force sensor is located directly above the indentor. Its structural housing ensures great rigidity and does not significantly influence the test results.

B.1.4 Data acquisition

The collection of the data originating from the different sensors was done by two different setups. For the square test samples a LabVIEW setup was used supported by National Instruments modules and the results of the circular test specimens were read out by an oscilloscope. The high-speed footage was processed with the help of the Photron Fastcam Viewer application on a PC. Both setups are described below.

B.1.4.a National Instruments & LabVIEW

The test setup is equipped with a NI cDAQ-9172 eight-slot USB chassis, designed to house NI C-series I/O modules. A total of 4 such modules were connected to perform the tests:

NI 9215 The module is used for reading out the displacement sensor via the counter device and is equipped with 4 BNC-connected channels. It has a ±10V input range and 16 bit resolution. It does not include an anti-aliasing filter.

NI 9234 The module is used for reading out the acceleration sensor and the force sensor. It is equipped with 4 BNC-connected Software-selectable IEPE signal conditioning channels. Operating on a ±5V input range and 24 bit resolution, it includes an anti-aliasing filter.

NI 9237 This module is used for reading out strain gauges. It is equipped with four 24-bit resolution, ±25 mV/V analog inputs with RJ50 connection. The module features a programmable half- and full-bridge completion and an anti-aliasing filter.

NI 9401 This module is used for triggering the high- speed camera and provided with an industry-standard 25-pin D-SUB connector. It is an 8-channel, TTL (5V) 100 ns bidirectional digital input module.

All of these modules have a maximal sample rate, but the sample rate has to be the same for all of the modules in the chassis. Therefore the sample rate is limited by the lowest maximum sample rate of the used modules: 51.2 kHz.

A LabVIEW script was written, which basically did two things: starting the test and collecting the test data. This is achieved by a USB 2.0 connection that links the PC to the DAQ chassis. Two scripts were used depending on the presence of strain gauges.

By pressing a single button the LabVIEW program sends out a pulse to the release system magnet that detaches the drop weight and also triggers the high-speed camera. Immediately afterwards, the National Instruments setup activates the data acquisition.

B.1.4.b Oscilloscope

The Genesis HighSpeed Gen5i oscilloscope was preferred. However, due to its low availability it was only used for the impact tests on the circular test specimens. The oscilloscope can read out the measurement sensors with a sample rate of 200 kHz. The data export from the Gen5i to a ".txt" file was done at a reduced sample rate of 100 kHz in order to decrease the data file size.

All of the sensors and also the camera are connected to the oscilloscope. The triggering is done by manually pressing a release button which activates the impactor release system. The triggering of the camera and the data acquisition of the sensors is done based on the displacement signal. If the displacement reaches a certain value the oscilloscope sends a pulse to the camera and records the sensor data in a specified timeframe.

B.2 SQUARE SPECIMENS

B.2.1 Test program

Table B-3 Test program I1 (left) and I2 (right).

Specimen	Height [cm]	Temp [°C]	Torque [Nm]
I1_1	25	20.9	15
I1_2	25	26.2	15
I1_3	15	22.6	10
I1_4	10	22.6	10
I1_5	25	24.4	10
I1_6	10	25.6	5
I1_7	15	25.8	5
I1_8	40	24.0	5
I1_9	45	23.4	5
I1_10	55	22.7	5
I1_11	55	23.1	5
I1_12	25	22.8	5

Specimen	Height [cm]	Temp [°C]	Torque [Nm]
I2_1	25	21.6	5
I2_2	25	21.2	5
I2_3	25	21.3	5
I2_4	25	21.5	5
I2_5	55	21.5	5
I2_6	55	21.5	5
I2_7	55	21.3	5
I2_8	55	21.9	5
I2_9	40	22.5	5
I2_10	40	22.1	5
I2_11	40	22.0	5
I2_12	40	22.2	5

Table B-4 Test program I3 (left) and I4 (right).

Specimen	Height [cm]	Temp [°C]	Torque [Nm]
I3_1	25	19.3	5
I3_2	40	19.7	5
I3_3	55	19.7	5
I3_4	40	20.1	5
I3_5	55	20.3	5
I3_6	55	20.3	5
I3_7	25	19.2	5
I3_8	25	19.5	5
I3_9	25	20.0	5
I3_10	25	20.2	5
I3_11	40	20.2	5
I3_12	40	20.2	5

Specimen	Height [cm]	Temp [°C]	Torque [Nm]
I4_1	25	21.4	5
I4_2	25	21.0	5
I4_3	25	21.9	5
I4_4	25	21.9	5
I4_5	40	22.1	5
I4_6	40	22.2	5
I4_7	40	23.1	5
I4_8	40	22.3	5
I4_9	55	22.3	5
I4_10	55	22.5	5
I4_11	55	22.4	5
I4_12	55	24.8	5

Table B-5 Test program for I5 (left) and I6 (right).

Specimen	Height [cm]	Temp. [°C]	Torque [Nm]	Boundary condition
I5_1	25	22.6	2	Filt
I5_2	25	23.9	/	Free
I5_7	10	24.1	5	Fixed
I5_8	25	24.7	/	Free
I5_9	25	25.1	/	Free
I5_10	25	24.9	5	Fixed
I5_11	25	25.2	5	Fixed
I5_12	25	25.0	5	Fixed

Specimen	Height [cm]	Temp. [°C]	Torque [Nm]	Boundary condition
I6_2	25	23.7	5	Fixed
I6_3	25	24.0	5	Fixed
I6_4	25	25.3	5	Fixed
I6_5	10	24.4	5	Fixed
I6_6	10	24.5	5	Fixed
I6_7	10	24.6	5	Fixed
I6_8	10	24.4	2	Filt
I6_9	25	24.6	2	Filt
I6_10	25	24.6	2	Filt
I6_11	25	24.3	/	Free

Table B-6 Test program for I7 (left) and I8 (right).

Specimen	Height [cm]	Temp. [°C]	Torque [Nm]	Boundary condition
I7_1	25	23.0	5	Fixed
I7_2	25	22.3	2	Filt
I7_3	25	25.0	5	Fixed
I7_4	25	25.1	5	Fixed
I7_5	25	25.1	/	Free
I7_6	25	25.1	/	Free
I7_7	25	25.1	2	Filt
I7_8	25	25.2	2	Filt

Specimen	Height [cm]	Temp. [°C]	Torque [Nm]	Boundary condition
I8_1	25	21.4	5	Fixed
I8_2	25	21.0	5	Fixed
I8_3	25	21.9	5	Fixed
I8_4	25	21.9	5	Fixed
I8_5	40	22.1	5	Fixed
I8_6	40	22.2	5	Fixed
I8_7	40	23.1	5	Fixed
I8_8	40	22.3	5	Fixed
I8_9	55	22.3	5	Fixed
I8_10	55	22.5	5	Fixed
I8_11	55	22.4	5	Fixed
I8_12	55	24.8	5	Fixed

B.2.2 Results and discussion: Specimens with 4 mm glass (I1, I2, I3, I4, I8)

B.2.2.a Initial response of the specimen (F_{max})

It can be observed that the initial force peak is higher, going from 3500 N to 4500 N and 5500 N for increasing drop height. These values are quasi constant for the first four test series, as can be seen on the graph below.

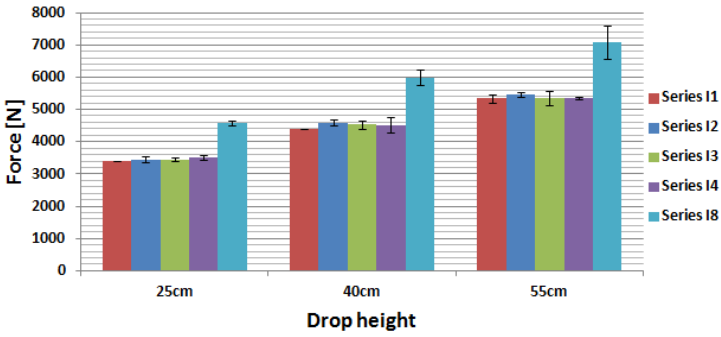

Figure B-1 Initial average force peak comparison.

There is no significant difference regarding the interlayer thickness and adhesion level. The independency of the adhesion level was to be expected because the specimen is still intact and no delamination has yet occurred.

Test series I8 manifests the same tendency of higher initial peak forces with increasing drop heights. However, the absolute values are 32% higher due to the presence of the stiffer DG-interlayer.

Figure B-2 shows a linear trend for the initial force peak in function of the impact velocity.

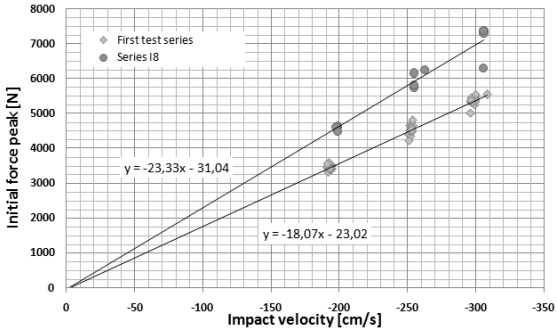

Figure B-2 Initial force peak in function of impact velocity.

B.2.2.b Time of fracture (t_1 & t_2)

Figure B-3 displays the time of fracture of the bottom plate t_1 in function of drop height. The standard deviations are large but still there is a certain trend noticeable: the higher the drop height the faster the bottom glass breaks. However, no consistent difference can be observed for adhesion level and interlayer thickness. For test series I8 bottom plate fracture occurs faster than for the other test series. These specimens generate higher forces due to their increased stiffness. A significant part of the I8 specimens break already at the first impact.

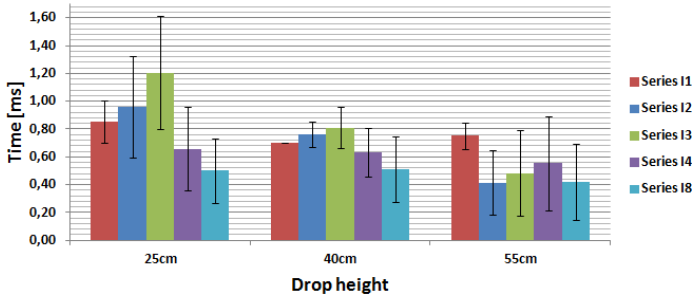

Figure B-3 Comparison of the average time of bottom plate fracture.

Figure B-4 displays the time of upper plate fracture t_2, the same conclusions can be made as for bottom plate fracture. However, the distinct difference for test series I8 is not present anymore. On the contrary, the time of upper plate fracture is postponed. The reason is that the specimens are stronger and more of the impact energy gets dissipated by bottom plate fracture. Test series I3 shows rather abnormal behaviour, especially for a drop height of 25cm. However, this is only a single specimen: the others manifested single plate fracture.

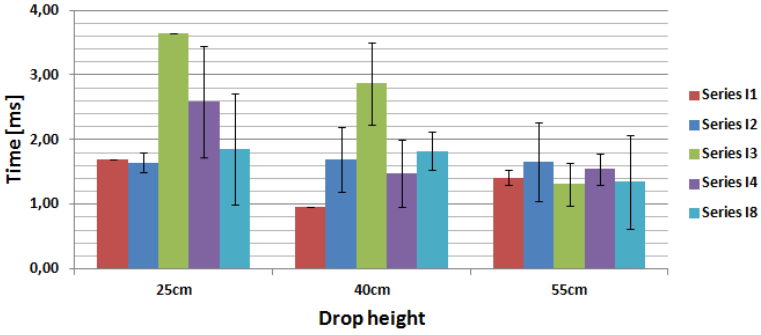

Figure B-4 Comparison of the average time of upper plate fracture (only for specimens with double fracture).

Figure B-5 compares the time between bottom and upper glass fracture (intertime) in function of the drop height. The larger the interlayer thickness the longer the intertime seems to be for low drop heights.

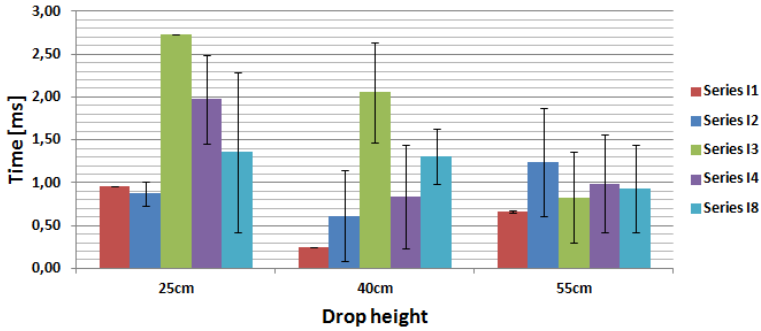

Figure B-5 Comparison of the average intertime (only for specimens with double fracture).

B.2.2.c Force at fracture (F_1 & F_2)

The average force of fracture of the bottom plate F_1 is displayed in Figure B-6. The standard deviations are very large and no real trend is visible. One could expect to see higher forces for higher drop heights and stiffer interlayers. However, fracture is not only determined by force but for example also by the work done before fracture and the glass surface flaw population.

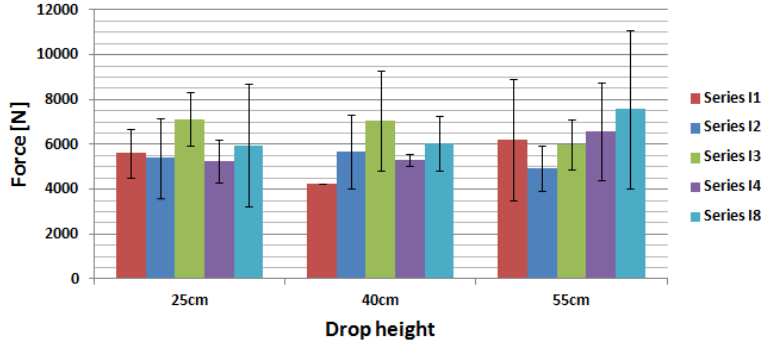

Figure B-6 Comparison of the average force at bottom plate fracture.

Figure B-7 shows the average force F_2 at the moment of upper plate fracture. Again, no consistent tendency can be found. However, the force of upper plate fracture is

lower than that of bottom plate fracture in 78% of the cases. This is to be expected because the flexural bending strength of the specimens is already reduced by the fracture of the bottom plate.

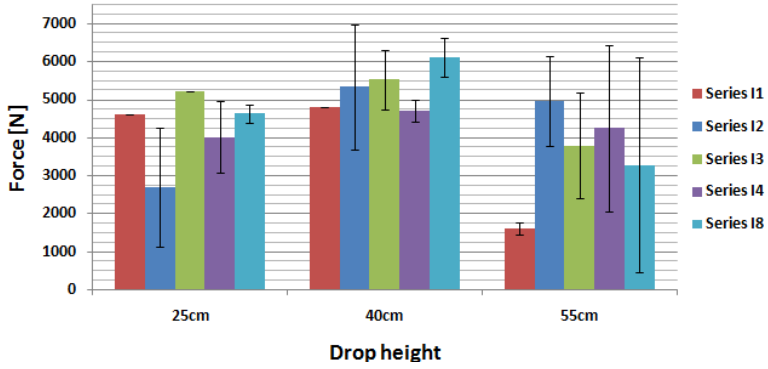

Figure B-7 **Comparison of the average force at upper plate fracture (only for specimens with double fracture).**

The time versus the force of fracture is displayed in Figure B-8 (test series I8 is not included because of its different composition). These data points follow the general course of a force history plot. It is observed that for a drop height of 25 cm, bottom plate fracture takes place in a great time interval. The strongest specimens survive until the third impact: because the forces and the work done by the second blow are still relatively low. Most of the specimens fail at the second impact. Except for the 55 cm drop height which delivers a strong initial impact; thus many of the specimens fail already at this point.

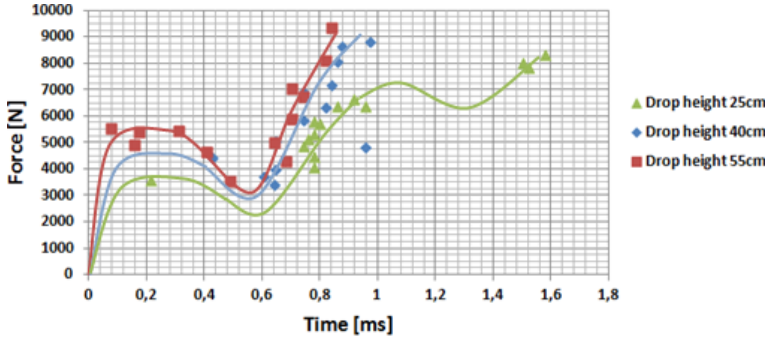

Figure B-8 **Force at bottom plate fracture in function of time of bottom plate fracture.**

If the above assumption about the impact principle is correct, the three specimens that correspond to the three failures at around 1.5 ms on the above graph must have a quasi identical force history course before the point of bottom plate fracture. This is verified on Figure B-9 where series I2 and I3 are represented. These series differ in adhesion as well as in interlayer thickness.

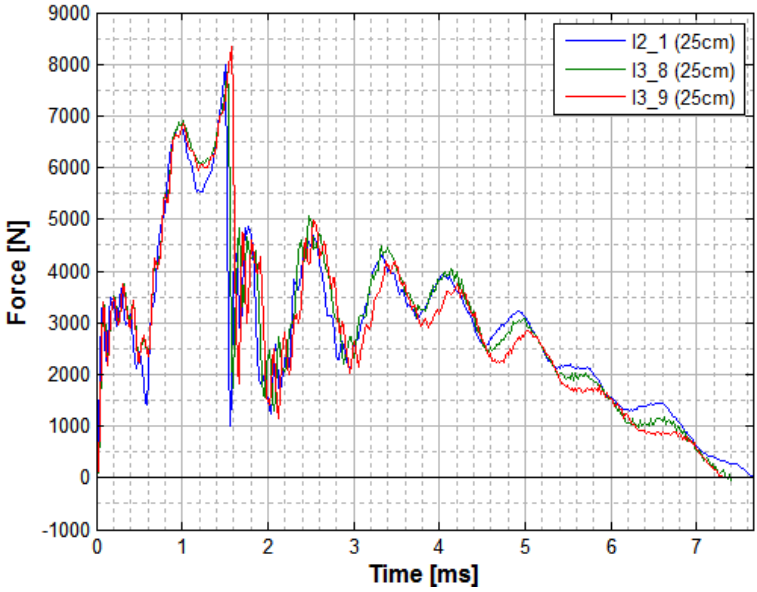

Figure B-9 **Force history plot for specimens with postponed bottom plate fracture.**

Indeed, the curves follow an almost identical path, certainly because no upper plate fracture takes place. The latter can be explained: the impactor has decelerated much due to the delayed time of fracture and does not possess enough kinetic energy to break the upper plate.

It can be concluded that the force history curve of each specimen is quasi identical before the point of fracture and that adhesion of the interlayer or the interlayer thickness has no influence on its course; even after bottom plate fracture.

B.2.2.d Duration of the impact

The global course of the force history for test series I2, tested at different drop heights, is displayed in Figure B-10. It is observed that the duration of the impact increases for higher drop heights; the deceleration of the impactor by the interlayer

takes a longer time because of its greater residual velocity. Furthermore, the force belly is most of the time initiated at quasi the same force.

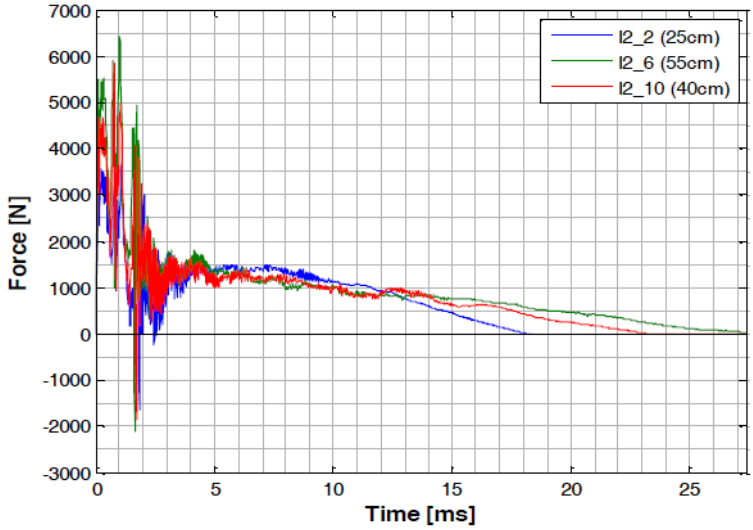

Figure B-10 Global response in function of the drop height.

Figure B-11 displays a quantitative representation of the results. One can see that test series I3 and I4 with double interlayer thickness manifest a smaller impact duration. This is to be expected because the thicker interlayer delivers more resistance and decelerates the impactor faster. Test series I8 is equipped with a stiffer structural interlayer which shows the shortest impact durations.

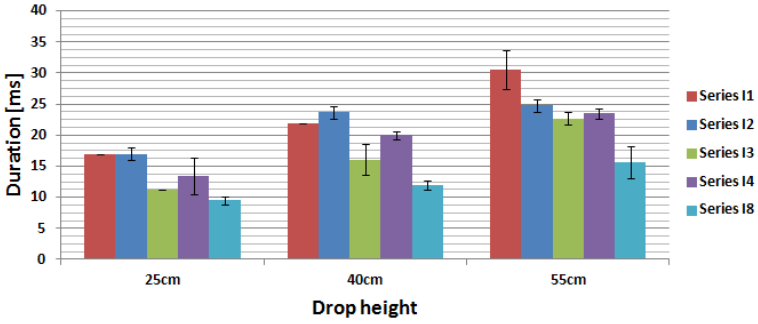

Figure B-11 Comparison of the average impact duration.

B.2.2.e Maximum displacement of the impactor

The average maximal displacement of the test specimens that have known double fracture is displayed in Figure B-12. The results are very similar to those of the impact duration and the same observations and explanations apply for the maximal displacement.

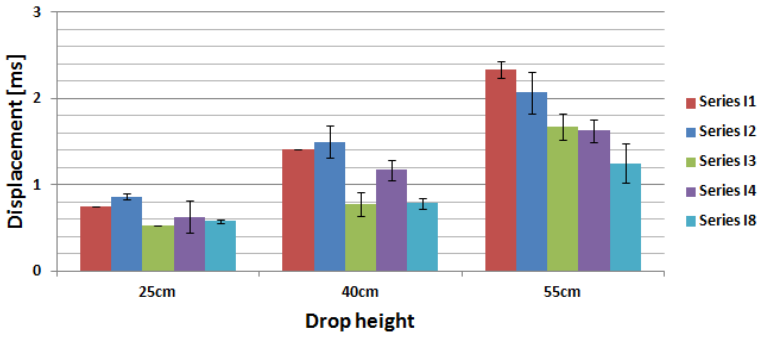

Figure B-12 Comparison of the average maximal displacement (only for specimens with double fracture).

There is a relationship between the duration of impact and the maximal displacement as represented by Figure B-13. Displacement and duration are linearly dependent.

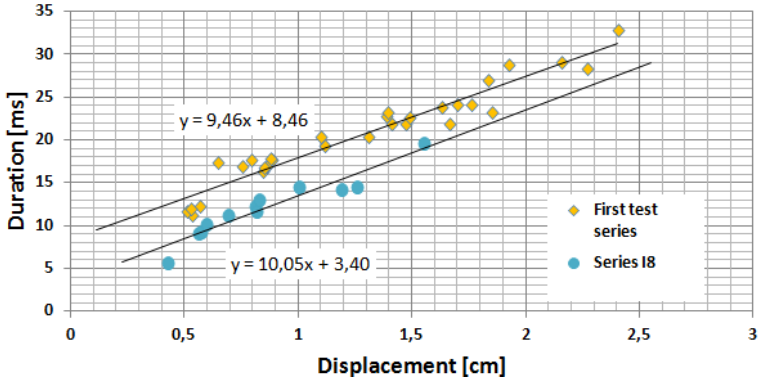

Figure B-13 Duration of impact vs. maximal displacement.

B.2.2.f Strain

Some of the specimens (I3_9, I4_7, I4_8 and I4_9) were equipped with strain gauges. The type used was CEA-06-250UN-350 by Vishay Micro-Measurements. They have a nominal grid resistance of 350 Ohm and a gauge factor of about 2.13 (depending on the used batch). The location of the strain gauges is represented on Figure B-14. Radial as well as tangential strain is measured both for the upper and the bottom plate.

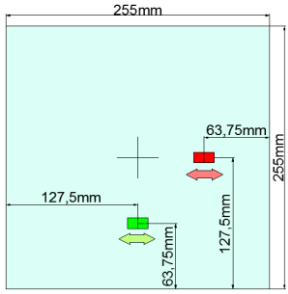

Figure B-14 Position of strain gauges.

In Figure B-15 the strain curves of specimen I4_7 are represented. To make comparison more straightforward, the sign of one curve is inverted. The tangential and radial strain is quasi identical before the point of fracture. There is no delay between both measurements: the impact is felt instantaneously on the top and bottom plate. This is a specimen that has known only fracture of the bottom plate as can be seen on the graph due to the strain drop at 0.7 ms.

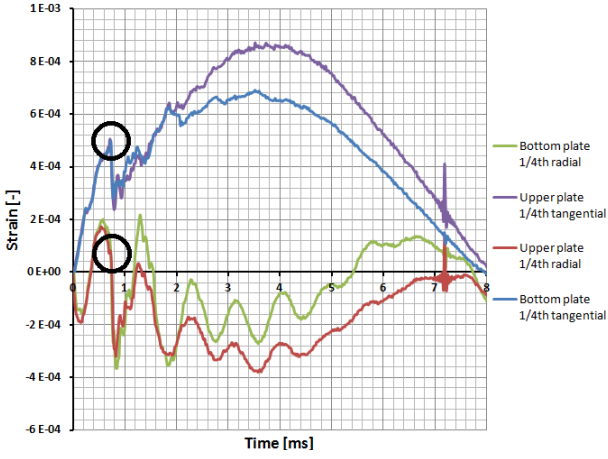

Figure B-15 Strain history plot.

Fracture of the bottom plate creates a drop in the tangential and radial strain for both the bottom and the upper glass plate. From this point the bottom plate tangential strain measurements are influenced by radial crack formation. The entire cracking pattern is already formed 0.1 ms after fracture, as evidenced by the high-speed footage.

After fracture, the tangential strain measurement of the bottom plate only differs some 20% from that of the upper plate. This means that the interlayer is still transferring 80% of the deformation and load of the upper plate to the bottom plate. Thus fracture of the bottom plate does not severely weaken the total specimen; that is why the force history plots still manifest quasi equal resistance of the specimen after fracture of the bottom plate.

Figure B-16 shows a comparison of the upper plate strains of specimens I4_7 and I3_9. Both specimens have known single fracture and have been tested at the same drop height of 25cm. One can see that the initial behaviour is very alike. The strain drop is bigger for a later time of fracture which was to be expected because a greater deformation was present at the time of fracture.

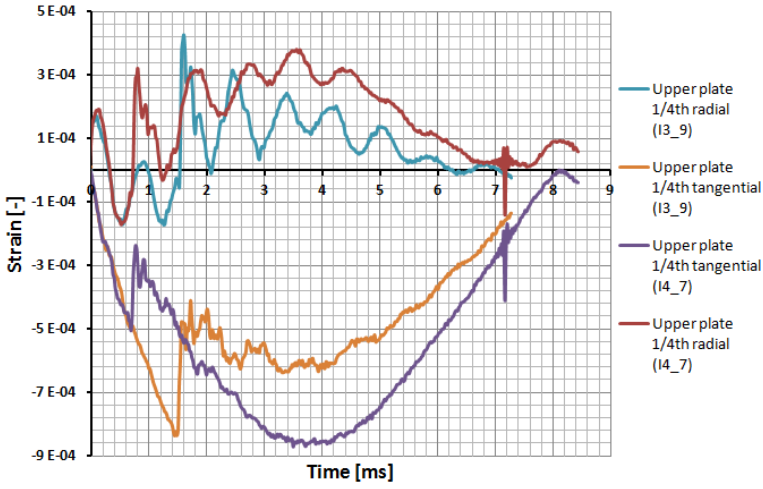

Figure B-16 Comparison bottom plate strains between specimens I3_9 and I4_7.

B.2.2.g Incurred damage

One expects to see higher damage for higher impact energies. The damage comparison is done based on the fracture number calculated by the processing script "samplescan.m". For this part only the specimens that have known complete failure were taken into account. The results are represented by Figure B-17.

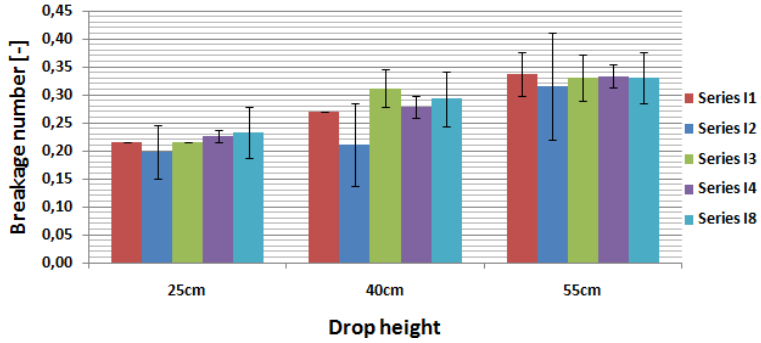

Figure B-17 Comparison of the average fracture number.

The made assumption is indeed correct; higher impact energy means higher damage. No significant difference is seen between the different test series.

There were several attempts made to correlate the incurred damage to other values (e.g. work performed until upper plate fracture, rebound velocity, time of fracture and force of fracture). Unfortunately no consistent correlations were found.

Another property is the ratio of the fracture number (B) and the number of centre fracture (CB). Following cases are to be distinguished.

Table B-7 Comparison of the average breaking ratio.

Cases	Explanation
$\frac{B}{CB} < 1$	Damage is concentrated in the center.
$\frac{B}{CB} \approx 1$	Damage is evenly distributed.
$\frac{B}{CB} > 1$	Damage is mainly concentrated at the edges.

Figure B-18 displays the average ratio distribution for the different test series.

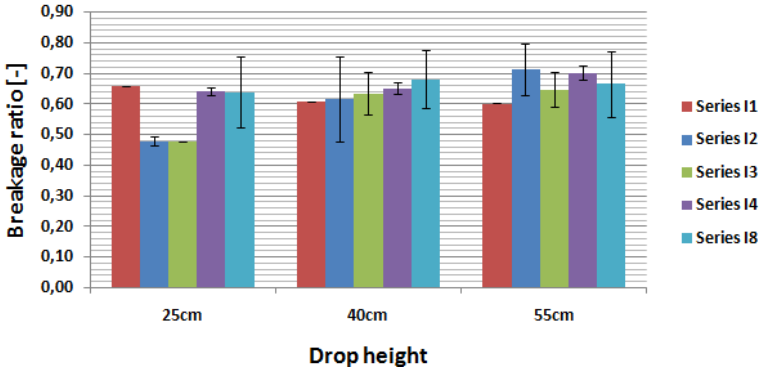

Figure B-18 Comparison average breaking ratio.

For 55 cm drop heights the upper glass plate gets locally crushed by the indentor. Additionally, interlayer penetration occurs for the single layered test series (I1, I2 and I8). Double layered test series are best capable of preventing small object penetration, even if compared to the structural series.

Furthermore, there is a more local upper penetration for the structural I8 test series. The indentor here creates a distinct circular piercing mark as seen on Figure B-19.

Also, it is observed that significantly more and larger glass fragments are detached from the bottom plate for I8 specimens. Two direct causes can be thought of: the more localized deformation of the specimen and the stiffer behaviour of the specimen.

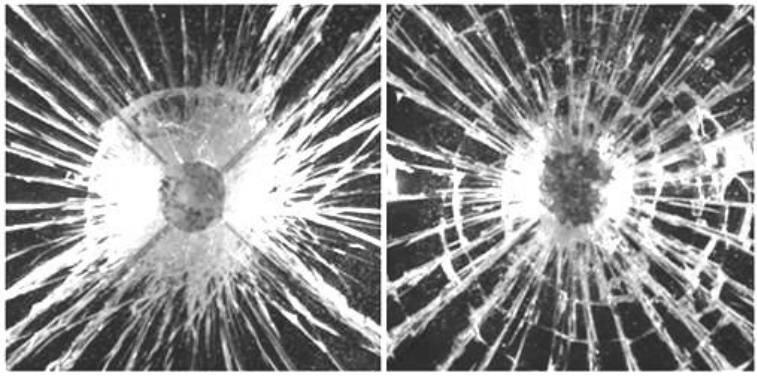

Figure B-19 Impactor penetration and crushing of glass for a drop height of 55 cm for specimen I8_9 with structural interlayer (left) and specimen I2_7 with normal interlayer (right).

B.2.3 Results and discussion: Specimens with 2 mm glass (I5, I6, I7)

Most of the specimens were tested at a drop height of 25cm. Unlike the first testing series, this parameter is thus quasi fixed. The results will be set out in function of the applied boundary conditions: fixed, felt and free.

B.2.3.a Initial response of the specimen

In Figure B-20 the initial average force peak for the different series is represented. It is observed that for the thinner glass plate series, much lower forces occur. This is a logical result since the specimen flexural stiffness is approximately reduced by a factor 8. Test series I7, equipped with the structural interlayer, generates the greatest force for the 2 mm glass plate samples.

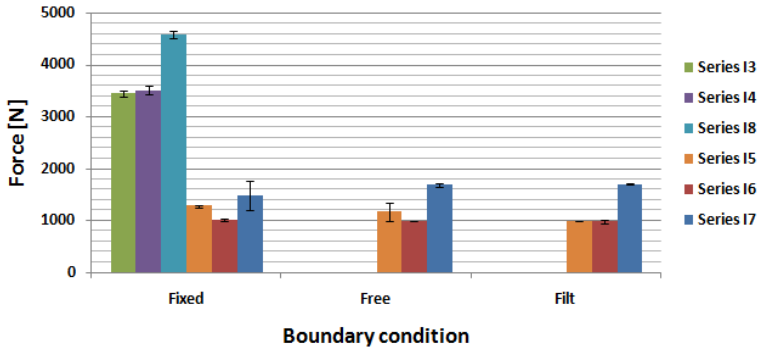

Figure B-20 Comparison of average initial peak force.

B.2.3.b Time of fracture

Figure B-21 displays the time of fracture of the bottom plate in function of the drop height. Again, no significant differences are to be seen between the different boundary conditions. Bottom plate fracture seems to occur slightly later for the thinner glass plate specimens (especially when comparing series I8 and I7). Again, specimens with lower flexural stiffness react slower and have postponed (average) breaking times. However, still there is no consistent difference between the adhesion levels noticeable.

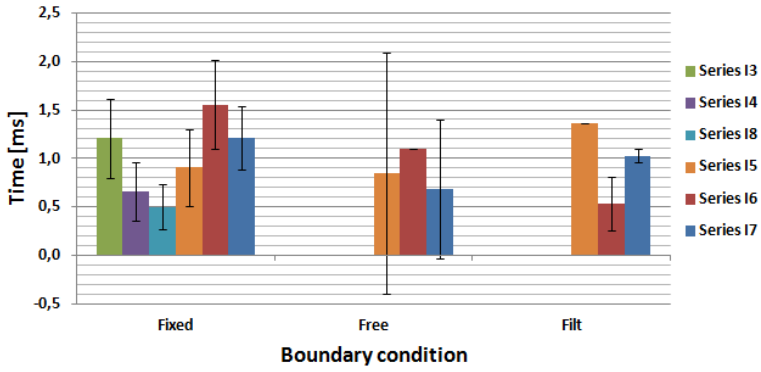

Figure B-21 Comparison of average time at bottom plate fracture.

No additional information can be drawn from the time of upper plate fracture or from the intertime.

B.2.3.c Force of fracture

Forces of bottom plate fracture are obviously much lower for the 2 mm glass plate specimens, as seen on Figure B-22. However, not much information is gained regarding interlayer adhesion or boundary condition influence.

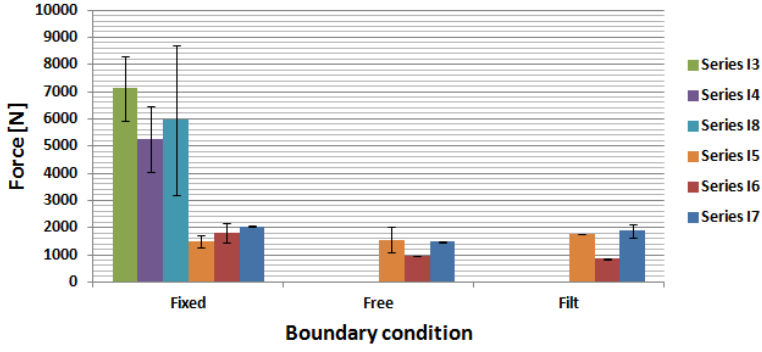

Figure B-22 Comparison of average force at bottom plate fracture.

B.2.3.d Duration of the impact

Durations are much longer for the thin glass plate test series. No consistent difference is observed regarding the boundary conditions or the adhesion bonding

strength of the interlayer. The structural series I7 and I8 manifest smaller impact durations due to their increased stiffness.

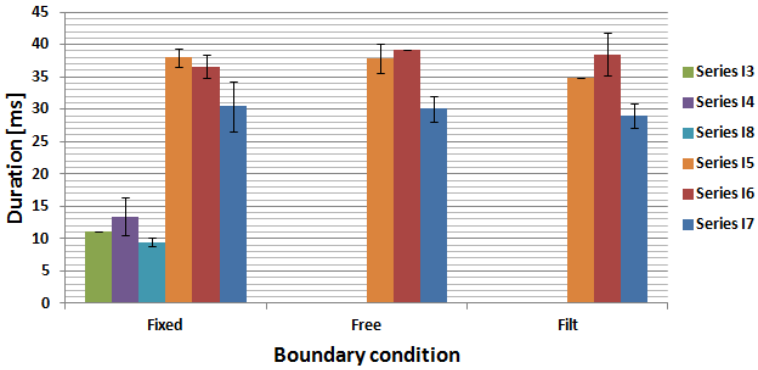

Figure B-23 **Comparison of average impact duration (only for specimens with double fracture).**

B.2.4 Fracture pattern analysis

Here, a brief overview is given regarding the different fracture patterns of the different post-test specimens.

Specimens that only had bottom plate fracture have a standard star shaped fracture pattern. The radial cracks have initiated in a cracking nucleus which is situated close to the impact point, following the weakest link principle (Figure B-24 (left)). It is plausible that around that point of impact some concentric cracks appear because of the locally very dense network of cracks.

Some specimens deviate from this pattern due to irregularities in the glass or possible multiple fragmentation (Figure B-24 (right)). The high-speed footage is not sufficiently accurate to record the simultaneous appearance of two such different cracking nuclei.

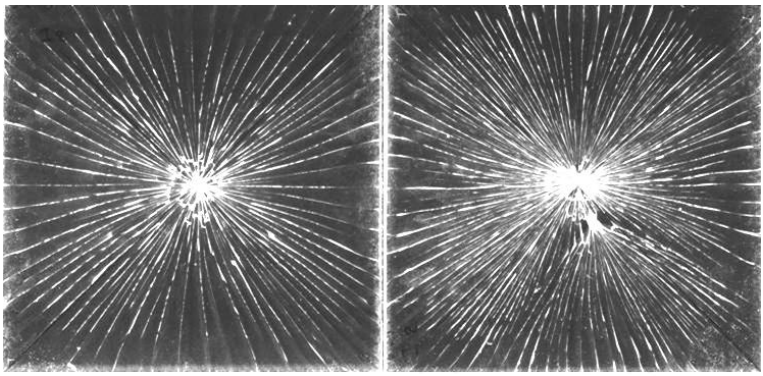

Figure B-24 **Fracture patterns for specimens with only bottom plate fracture; specimen I2_3 (left) and I2_1 (right).**

For specimens that have known complete failure (i.e. both plates are fractured), there are 3 main fracture patterns observed. The general fracture pattern is displayed in Figure B-25 (left); here radial and concentric cracks are symmetrically present. One can see that the radial cracks towards the corners of the specimens predominate. Furthermore, there are cracks close near the corners that are perpendicular with the radial cracks. These have formed due to the torsion stresses present here. These are logically not present for specimens tested with free end boundary conditions. Cracks that are parallel with the edges (Figure B-25 (right)) of the specimen are also caused due to the fixed end boundary condition and the stress distribution it brings with.

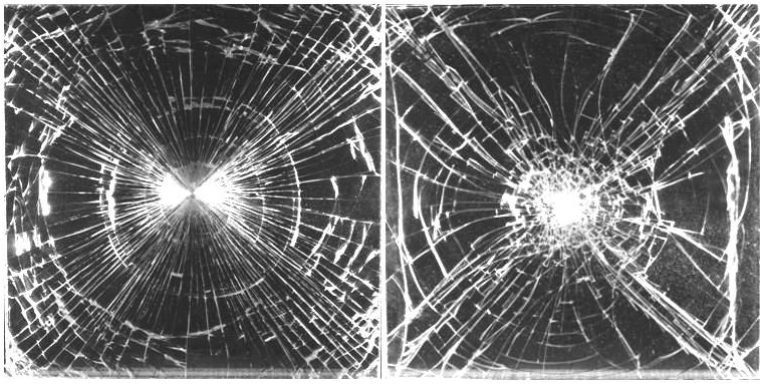

Figure B-25 **Fracture patterns for specimens with both plates broken: specimen I8_6 (left) and I6_9 (right).**

For specimens with free boundary conditions the fracture pattern is indeed different. Not only by the absence of corner and edge cracks but also by the presence of altered concentric cracks. These are not circular as for the fixed end and also semi fixed (felt) boundary conditions; they are square shaped with rounded corners (Figure B-26).

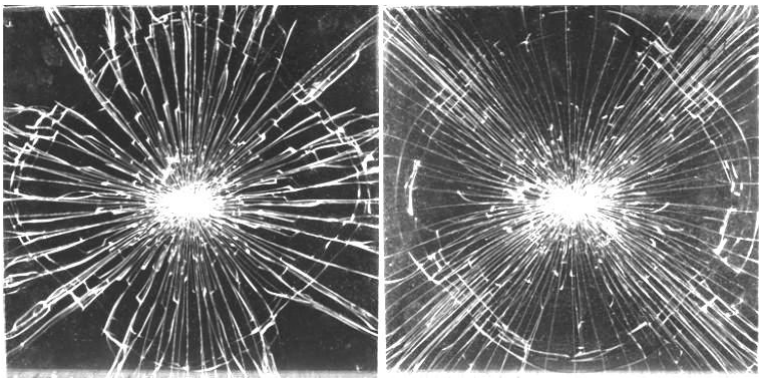

Figure B-26 **Fracture pattern for free end boundary conditions specimens: I5_8 (left) and I5_11 (right).**

The latter is proof that the fixed end boundary conditions and the free end conditions are clearly present, though this knowledge cannot be derived from the sensor data but only from the post-test pictures.

The third fracture pattern is represented by Figure B-27. Here the upper plate radial cracks deviate from the general cracking pattern, by the formation of little nerve shaped side-cracks. The form is comparable with a lightning bolt and these cracks will be referred to accordingly. This fracture pattern is formed if the upper glass plate generates radial cracking on the same places as the bottom plate.

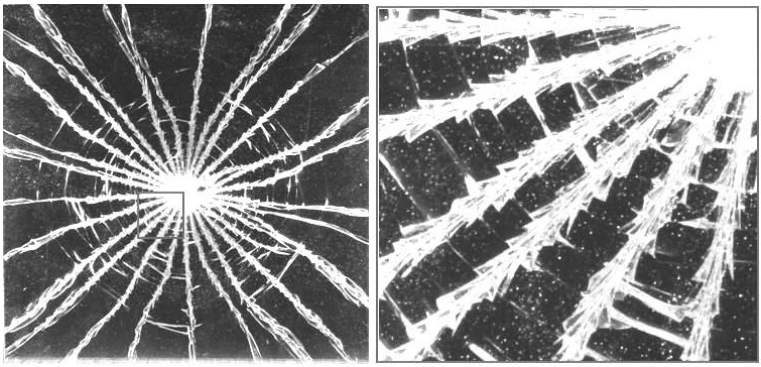

Figure B-27 Fracture pattern for specimen I7_6 (left) and detailed view (right).

There is no significant difference, regarding the sensor data, observed for the different fracture patterns.

Regarding the radial crack propagation velocity, several specimens were analyzed on the high-speed footage. The time needed for the radial cracks, originated from the central cracking nucleus, to reach the edge of the specimen is on average 0.08 ms. The crack propagation velocity is:

$$\frac{120\ mm}{0.08\ ms} = 1500\ {}^{m}/_{s}$$

This velocity is in accordance with values found in literature.

B.3 CIRCULAR SPECIMENS

B.3.1 Test program

There were some issues with the attachment of the indentor to the impactor; different solutions for this problem added mass and screws to the indentor itself. As these latter additions may change the impactor weight and its kinetic energy, the performed tests are listed in three different tables (Table B-8, Table B-9 and Table B-10) that correspond to the three different indentor designs used: i) the blue silicone glued to the impactor with double-sided tape ii) the silicone screwed to the impactor and iii) the silicone screwed to the impactor and with a lateral expansion impeding ring which prevented the screws from failing.

Table B-8 Tests performed on circular specimens with glued on indentor.

Test	Spec.	Sticker Orientation	Height [cm]	Torque [Nm]	Temp. [°C]	Fracture
C1_6	1	Up	15	5	20.3	No
C1_7	1	Up	25	5	20.3	No
C1_8	1	Up	35	5	20.3	No
C1_9	1	Up	45	5	20.4	No
C1_10	1	Up	55	5	20.4	No
C1_11	1	Up	65	5	20.4	Single
C1_12	2	Up	75	5	20.5	No
C1_13	2	Up	85	5	20.5	Single
C1_3	3	Up	100	5	20.8	Single
C1_4	4	Down	100	5	21.3	No
C1_4(2)	4	Down	100	5	21.3	No
C1_4(3)	4	Down	120	5	21.3	No
C1_4(4)	4	Down	140	5	21.4	No
C1_4(5)	4	Down	150	5	21.4	No
C1_4(6)	4	Down	160	5	21.4	No
C1_19	5	Up	120	5	21.3	Double
C1_20	6	Down	120	5	22.3	No
C1_21	6	Down	150	5	22.3	No

Table B-9 Tests performed on circular specimens with screwed on indentor.

Test	Spec.	Sticker Orientation	Height [cm]	Torque [Nm]	Temp. [°C]	Fracture
C2_1	7	Up	120	5	20.0	Single
C2_2	8	Down	120	5	20.4	No
C2_3	8	Down	150	5	20.4	No
C3_1	9	Down	100	2	20.4	No
C3_2	9	Down	100	4	20.6	No
C3_3	9	Down	100	6	20.8	No
C3_4	9	Down	100	8	20.7	No
C3_5	9	Down	100	10	20.7	No
C3_6	9	Down	100	12	20.7	Edge
C3_7	8	Up	120	5	20.9	Single
C3_8	6	Up	120	5	20.8	Single
C3_10	10	Up	120	5	20.8	Double
C3_11	11	Up	120	5	20.8	Single
C3_12	12	Up	120	5	19.8	Double
C3_13	13	Up	120	5	20.5	Double
C3_14	14	Up	120	5	20.2	Single
C3_15	15	Up	120	5	20.0	Double

Table B-10 **Tests performed on circular specimens with screwed on indentor and lateral expansion impeding ring.**

Test	Spec.	Sticker Orientation	Height [cm]	Torque [Nm]	Temp. [°C]	Fracture
C3_17	16	Down	20	5	20.3	No
C3_18	16	Down	30	5	20.3	No
C3_19	16	Down	40	5	20.4	No
C3_20	16	Down	50	5	20.5	No
C3_21	16	Down	60	5	20.6	No
C3_22	16	Down	70	5	20.7	No
C3_23	16	Down	80	5	20.9	No
C3_24	16	Down	90	5	21.0	No
C3_25	16	Down	100	5	21.1	No
C3_26	16	Down	110	5	21.2	No
C3_27	16	Down	120	5	21.3	No
C3_28	16	Down	130	5	21.4	No
C3_29	16	Down	140	5	21.5	No
C3_30	16	Down	150	5	21.6	No
C3_31	16	Down	160	5	21.6	No
C3_33	16	Up	20	5	21.3	Single
C3_34	17	Up	150	5	20.7	Double
C3_35	18	Up	150	5	21.0	Single
C3_37	4	Down	150	5	21.0	No

For a single test sample (sample 4) several strain measurements were performed for increasing drop heights. These tests were done with the Labview test setup and with the sticker side downwards. The final design for the indentor (with lateral expansion impeding ring) was used. Two strain gauges were present on the upper plate at r/2 from the side for tangential and radial measurements. The sample failed for a drop height of 80 cm. However, it had been tested multiple times before at drop heights of up to 160 cm.

Table B-11 Tests with strain gauges.

Test	Spec.	Sticker Orientation	Height [cm]	Torque [Nm]	Temp. [°C]	Fracture
C4_1	4	Down	20	5	19.4	No
C4_2	4	Down	30	5	19.6	No
C4_3	4	Down	40	5	19.9	No
C4_4	4	Down	50	5	19.7	No
C4_5	4	Down	60	5	19.6	No
C4_6	4	Down	70	5	19.7	No
C4_7	4	Down	80	5	19.7	Single

B.3.2 Fracture pattern analysis

In contrast to the square test series, the circular specimens describe a single fracture pattern (Figure B-28).

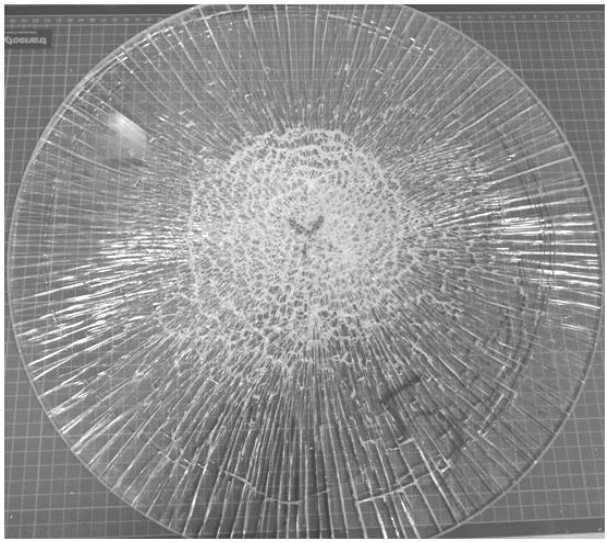

Figure B-28 Post-test specimen 5 (120 cm).

Bottom plate fracture is initiated from one or sometimes two central cracking nuclei (Figure B-29). After the radial cracks propagate towards the edge of the specimen, a

central, random and very dense crack pattern is formed at the contact area below the indentor.

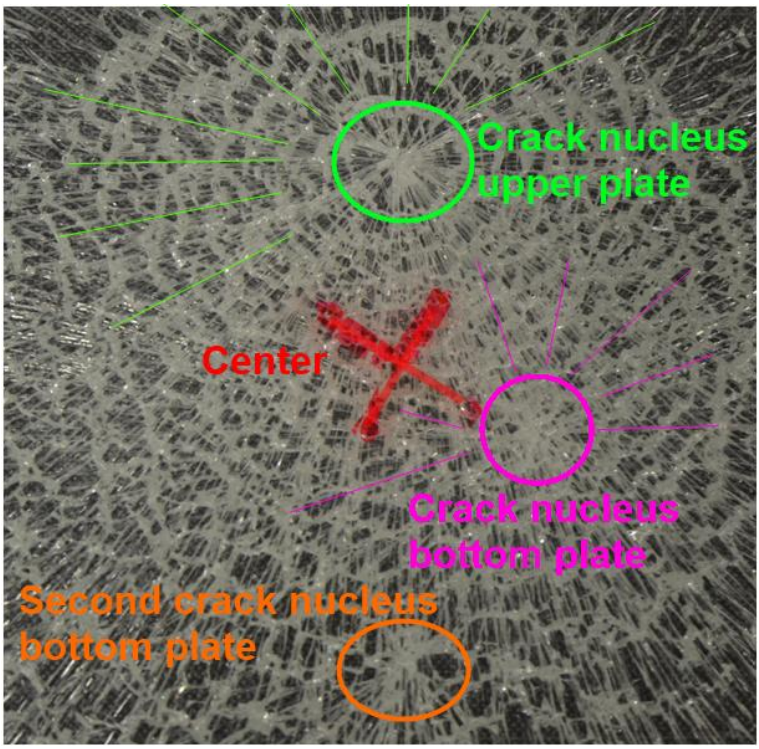

Figure B-29 Cracking nuclei of specimen 5 (120 cm).

The upper plate crack nucleus is not situated directly above the bottom plate nucleus because of the large load area, and none of them are necessarily in the centre of the specimen. This is caused by the distributed force over the area in contact with the indentor. The fracture process of the upper plate is equivalent to that of the bottom plate. The formation of concentric cracks takes place at the outer rim of the specimen for both plates.

B.4 REFERENCES

[1] Kistler 8704B500 data sheet.
[2] Vibration Division PCB Piezotronics product catalog.
[3] Endevco Isotron force sensor model 2311 data sheet.

ANNEX C DESIGN OF AN EN 356 SET-UP

Overview

In the framework of this PhD study a certified EN 356 set-up was designed and constructed. However, due to time constraints, only a handful of preliminary tests – to test the proper functioning of the set-up itself – were conducted. Nevertheless, its design is added in this annex for completeness.

The EN 356 standard has already been described in Chapter 5 which gives a review of impact research on laminated glass, together with the EN 12600 standard. Whereas an EN 12600 set-up was available (albeit in need of some slight modifications, see Chapter 7), no such set-up was available for EN 356 tests in this study. A fully functional set-up was available at Eastman, Solutia, but it was enclosed along three sides making it difficult to position high-speed cameras and other instrumentation. It was thus decided to design and construct our own set-up.

C.1 DESIGN OF THE SET-UP

The free-standing EN 356 set-up was designed in SolidWorks™. It consists of 3 main parts: i) a cube-like testing area with polycarbonate screens and metal fencing for security, ii) a support table to clamp the glass test panels and iii) guidance rails attached to a vertical steel beam with a motor on the top. Along these rails a cart, with three steel balls for the impact, can be moved up to 6 metres high.

C.1.1 Design of the support table

A secondary construction was designed to both clamp the glass panels during testing and contain the resulting glass fragments in a safe manner. It consists of three pivoting frames, connected to a rigid steel structure.

In Figure C-1 the different steps to remove a broken glass panel in an ergonomic way are shown.

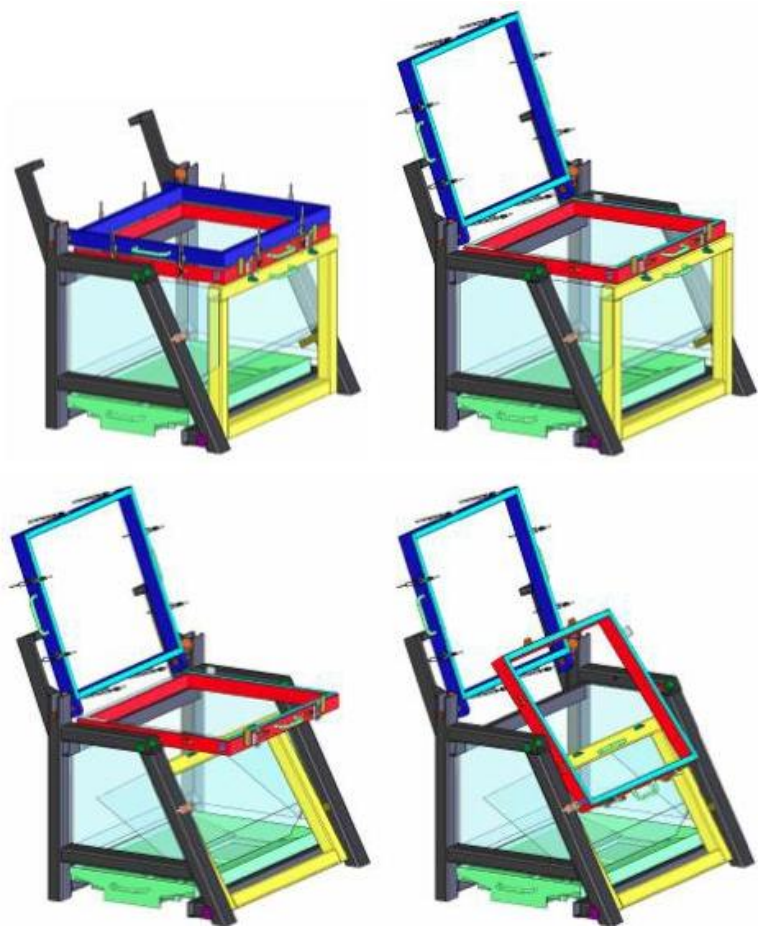

Figure C-1 **CAD design of support table showing in different steps how to replace a glass panel by rotating different parts (upper clamping ring (blue), base support (yellow) & lower clamping ring (red)).**

C.2 PICTURES OF THE CONSTRUCTED SET-UP

In Figure C-2 a complete overview of the constructed set-up is shown, including the testing area in which the support table is visible, the guidance rails with the motor on top to hoist the cart and the control panel, on the left. The next pictures (C-3 to C-6) highlight several details of the set-up.

Figure C-2 EN 356 set-up.

Figure C-3 **Testing area including support table and movable carriage with magnets to hold the three steel balls.**

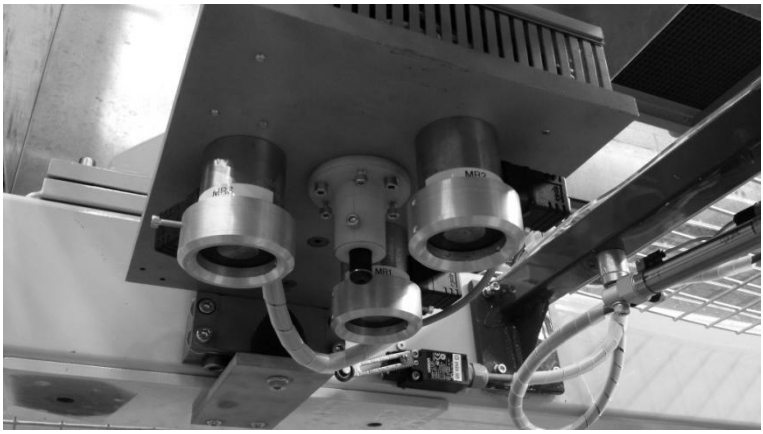

Figure C-4 **Detail of vertically movable carriage with three permanent electromagnets to hold the three steel spheres and laser pointer in the middle.**

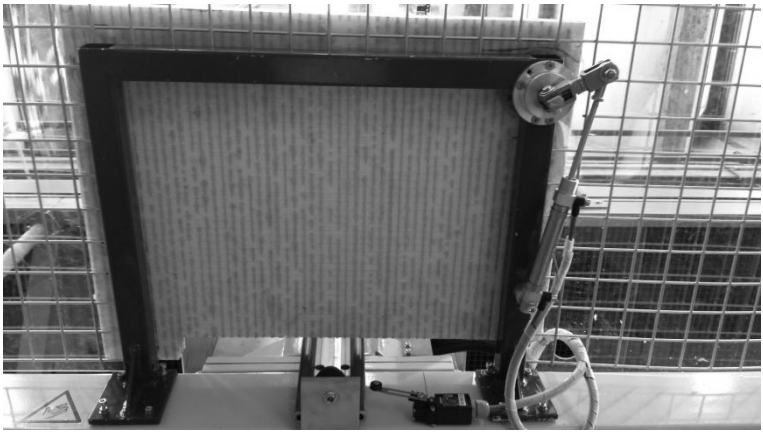

Figure C-5 **Detail of automatically closing Acrosoma panel to protect testing area from accidental drop of steel ball.**

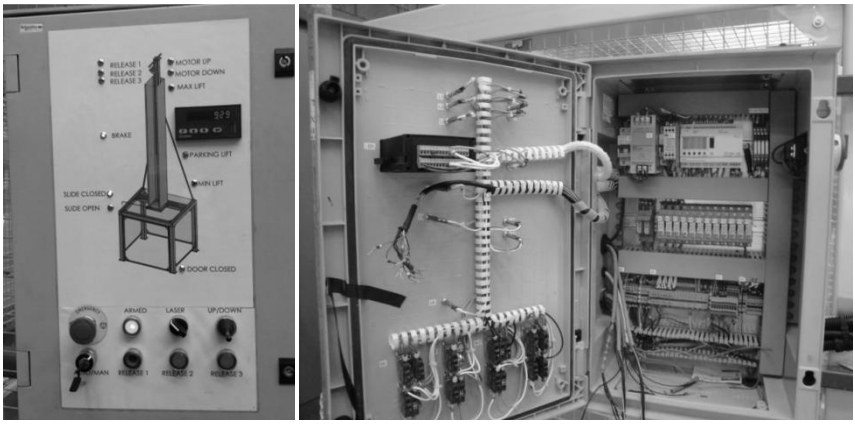

Figure C-6 **Details of operation switches including height indicator (left) and inside of electronic wiring (right).**

C.3 PRELIMINARY TESTS

Some panels that were left over from De Pauw's PhD [1] were used to test the proper functioning of the set-up. They bore no indication as to their composition, although most of them were equipped with some sort of Window Safety Film. While most of the panels' glass broke (but remained held together by the WSF) and only in some cases the steel balls penetrated the panel, some also exhibited no damage at all.

Below are a few pictures taken with high-speed cameras. The tests were considered successful.

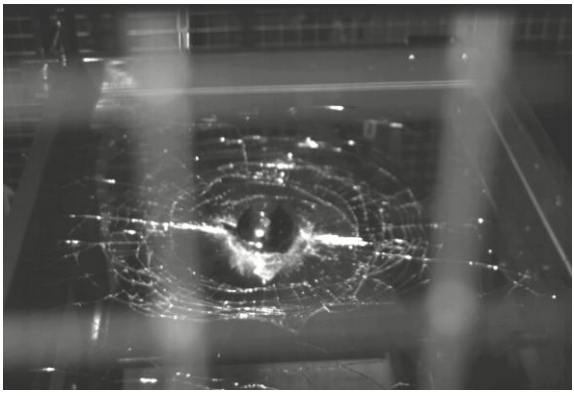

Figure C-7 **Steel ball puncturing through glass panel fitted with Window Safety Film. The protective steel fencing is visual as a blurry grid.**

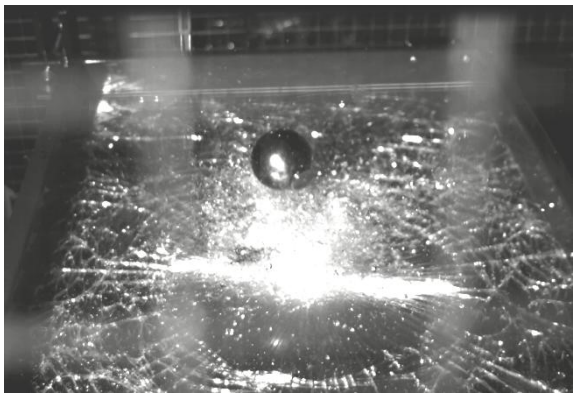

Figure C- 8 Rebound of third steel ball. The Window Safety Film remained intact.

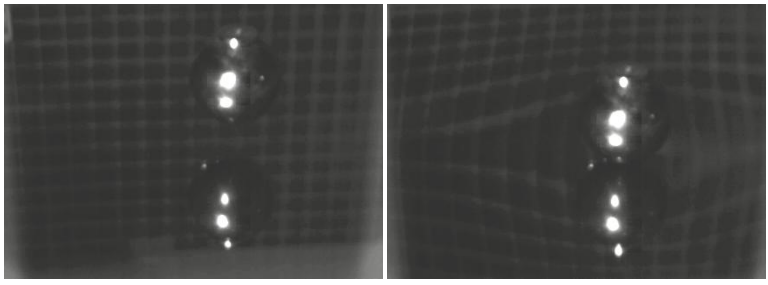

Figure C- 9 Glass panel which remained intact during testing. Notice the warped reflection of the safety fence due to the deflection of the panel in the picture on the right.

An operating manual, risk analysis and safety manual are available for the CE-certified set-up.

C.4 REFERENCES

[1] S. De Pauw, "Experimental and Numerical Study of Impact on Window Glass Fitted with Safety Window Film," Doctor in de Ingenieurswetenschappen: Werktuigkunde-Elektrotechniek PhD, Department of Material Science and Engineering Mechanics of Materials and Structures, Ghent University, Ghent, 2010.

JUSTIFICATION CHAPTER COVER IMAGES

Chapter 1 – Introduction
Shattered windows of the departure hall at Brussels Airport, Zaventem, after the March 22, 2016 attacks. Many injuries were due to the glass shards flying around after the explosions. Laminated glass has now been installed. Courtesy Belga.

Chapter 2 – Material selection & properties
Promotional image of laminated glass with polished edge finish, courtesy Urban Steel.

Chapter 3
Four-point bending monolithic specimens after testing, with fractures clearly visible.

Chapter 4 – Impact: Introduction
Still from a YouTube video of Tiltco Fenestrations, entitled '*TILTCO | Solutia Bat Test*', showing a panel of laminated glass being hit repeatedly with a baseball bat.

Chapter 5 – Impact: Small-scale drop weight (SSDW)
High-speed images of a specimen, filmed from the side, subjected to hard impact on the drop weight set-up. Radial cracks appear first and an early concentric crack is visible in the right hand bottom inside the circle.

Chapter 6 – Impact: EN 12600
When testing the – tempered – calibration plate at the highest drop height, the plate inexplicably failed, resulting in sudden glass fracture.

Chapter 7 – Blast: Introduction
Technician filling a barrel with a liquid explosive with a 100 kg TNT equivalent weight. See also Chapter 10.

Chapter 8 – Blast: Small-scale tests
Picture taken from the charge end of the small-shock tube, viewing an installed panel with the DIC speckle pattern visible because of the extra lighting on the other side.

Chapter 9 – Blast: Large-scale tests
Image of the fireball during detonation of the charge, captured with a GoPro, viewing the charge end of the shock tube during a large-scale test.

Chapter 10 – Conclusion and outlook
Picture taken at a large-scale blast test where different kinds of point or 'spider' connections were tested. Four different suppliers were tested, of which the third one performed the worst.

Annex A – DIC introduction
This picture actually is from my Master's Thesis and shows the DIC displacement field of a crack appearing in a reinforced concrete beam.

Annex B – Addendum to Chapter 5 (SSDW)
This was the initial configuration of the small-scale drop weight set-up, as designed by Stijn De Pauw.

Annex C – Design of an EN 365 set-up
Several safety signs which had to be applied to the set-up.

Ceterum censeo Carthaginem esse delendam